

Application of Heterojunction
Ni-Sb-SnO₂ Anodes for
Electrochemical Water Treatment

Thesis by
Yi (Sam) Zhang

In Partial Fulfillment of the Requirements for
the Degree of
Doctor of Philosophy

The logo for the California Institute of Technology (Caltech), featuring the word "Caltech" in a bold, orange, sans-serif font.

CALIFORNIA INSTITUTE OF TECHNOLOGY
Pasadena, California

2023
(Defended Feb 10, 2023)

© 2023

Yi (Sam) Zhang
ORCID: 0000-0002-9062-5201

ACKNOWLEDGMENTS

I want to thank my advisor, Professor Michael Hoffmann, for guiding me through the journey and giving me the freedom to explore different research directions. Thank you for all the random, weird, and/or interesting conversations we had on random, weird, and/or interesting stuff. I know you are very tough and will recover faster than anyone expected.

I want to thank my other committee members: Professor Philip Gschwend, Professor Kimberly See, Professor Alex Sessions, and Professor Christian Frankenberg. Thank you for all your advice and guidance on my thesis work. Thank you Phil for your questions and suggestions on my manuscripts and work in general. I learned a lot every time I talked with you. Thank you also to Christian and Professor Paul Wennberg for offering extra help at a time so close to my defense.

I want to thank Professor Mitchio Okumura for being my second project advisor during my first year. Thank you for accepting me into your lab, showing me diverse spectroscopy techniques, and introducing me to a great group of people.

I want to thank Dr. Nathan Dalleska for teaching me how to use all the instruments in the Water and Environmental Lab and for coming to my rescue when I ran into problems with, well, all the instruments again and again.

I want to thank my mentors: Professor Yang Yang, Professor Lei Guo, and Professor Sean McBeath. The work in this thesis would not have been possible without all of you. Thank you Yang for teaching me everything when I first got here, knowing nothing and not even having a clue how to assemble an electrochemical cell. Thank you Lei for leading me into the world of MOF to do something very different and exciting. Thank you Sean for offering to collaborate and introducing me to the ferrate work. I cherished the time we did experiments together and the conversations we had in the meantime on music, movies, books, and events happening around the world. And thank you for just being such a wonderful person.

I want to thank my lab members: Dr. Heng Dong (since your defense is two days earlier than mine), Dr. Alan Gu, Dr. Sean Kim, Dr. Clément Cid, and Léopold Dobelle. Thank you Heng for being my “trash buddy,” for all the McDonalds, In-N-Out, and other super cheap

food we bought for each other and for all the time we spent together talking about research, life, and other frustrating stuff.

I want to thank other friends from my year: (Dr. or soon-to-be Dr.) Yongzhao Guo, Yangcheng Luo, and Tian Zeng. Thank you Yangcheng for having so many meals with me and sharing your life with me (although maybe too much sharing sometimes). Thank you Tian for lending me your portable AC and saving my life when my room reached 45°C, and for simply being lovely and bringing happiness to everyone around you.

I want to thank the ESE and GPS staff: Nora Oshima, Bronagh Glaser, and Julie Lee. Thank you for your help on all things great and small.

I want to thank my fellow 5th year ESE students: Lily Dove, Sara Murphy, and Clare Singer. Thank you for all the work you did in the department and the changes you pushed for on new faculty hiring, student representatives in faculty meetings, quals reform, and so much more. I feel more than lucky to have three peer role models in the same year. I am certain you will continue to inspire people around you wherever you go.

I want to thank my undergraduate advisors: Professor Junping Shi and Professor Nathan Kidwell. Thank you for the help and support you provided in my college years. I would not have been here without you.

I want to thank two TV shows, *Person of Interest* and *Mrs. America*, and two books, *Sister Outsider* and *The Dialectic of Sex* (though it would be more precise to say Audre Lorde and Shulamith Firestone). Thanks for shaping my life and making me the person I am today.

I want to thank Joey Yung, whose songs got me through 8145 minutes just of 2022 (according to YouTube Music). Thank you for being a great singer and an even greater person.

I want to thank my family. And for my mom especially: thank you for watching TV shows with me (at a staggering pace!), reading with me (albeit occasionally reluctantly), being supportive of all my decisions (as unexpected and hard-to-understand as they sometimes may be), and loving me for who I am.

I want to thank the friends I met here: (All Dr.) Weimeng (aka Stephanie MenMen) Kong, Jing Li, Yujia Tao, and Yanzhe Zhu. Thank you MenMen for accommodating us whenever we went visiting and making me extravagant lunch and dinner all the time. I am

grateful for the sevenish pounds I gained each time at your place. Thank you Jing for being my first friend when I got here, telling me your stories at Chick-fil-A and Motto Tea Cafe, and for all the deep conversations we had on women (and for coercing me into watching Mrs. America and being coerced by me into watching Person of Interest). Thank you Yujia for agreeing to have lunch with me in April 2022 and sharing your life with me (almost) every following Thursday while eating Udon. Thank you Yanzhe for spending the most time with me and being there for me through everything.

I want to thank my best friend from college: Xiaoshi Zhang. Thank you for flying over from London to go on a road trip and spend the new year of 2019 together and for having quarterly video meetings with me. They helped me keep track of the days and years.

I want to thank my friends from high school: Siyu (Xiaoyu) Liu, Jingyan (Jián) Ma, Yongxian (Pi) Wang, Xiuwen (Wendy) Wu, Shuaiyao Liu (Chou), Qiaoqian Zhang (QianKun), and Yan Zhang (YanKun). Thank you for loving and supporting me over the past 10+ years, from near and far. I did not get to see you often (or at all...) in the past five years, and I missed you a lot.

Lastly, I want to thank all my friends once again. You are the most important things to me in the world. There are many more things I would like to do or at least try to do, but I believe the meaning of my life is getting to know and becoming friends with each and every one of you. I love you all.

ABSTRACT

Clean water supply and adequate sanitation services are critical for public health as well as for food production. Small-scale decentralized treatment represents an attractive alternative that can provide necessary water treatment in many parts of the developing world where centralized wastewater treatment facilities are not practical owing to financial, geographical, or political constraints. Electrochemical oxidation (EO) is a suitable technique for decentralized treatment settings since it does not require the addition of auxiliary chemicals and offers fast reaction kinetics and modular treatment capacity. EO is considered a versatile technology since it can degrade a wide array of contaminants and inactivate waterborne pathogens. The chemical composition of the anode, where EO takes place, is a key factor that controls reactive species production and thus treatment efficiency and energy consumption. Ideal anodes for wastewater treatment should have high overpotential for oxygen evolution (“nonactive” anodes) and favor complete organics oxidation through direct electron transfer and/or reactions with potent oxidants such as hydroxyl radical and ozone. Common nonactive anodes including antimony-doped tin oxide (Sb-SnO₂), lead oxide (PbO₂), and boron-doped diamond (BDD) have attracted wide research interests. The work presented in this thesis centered around a newly designed heterojunction Ni-Sb-SnO₂-based anode (NAT/AT) and its various applications in decentralized water and wastewater treatment. Direct treatment using NAT/AT has proved to be efficient for chemical oxygen demand removal, trace organic compound degradation, and microbial disinfection. Detailed investigation into pharmaceutical degradation kinetics and transformation products further established NAT/AT as a potential treatment alternative for the control of pharmaceuticals and their metabolites in hospital wastewaters. NAT/AT is also capable of synthesizing ferrates (e.g., FeO₄²⁻) in circumneutral conditions, the high oxidation state iron species that represents another group of powerful oxidants well-suited for decentralized treatment purposes. In an additional effort to tackle high concentrations of ammonium often present in latrine wastewaters, functionalized metal-organic framework (MOF), a class of materials featuring high porosity, abundant active sites, and highly tunable physical and chemical

properties, was used to recover the ammonium nitrogen. Various modifications of MOF-808, a highly water stable MOF, were designed and synthesized to achieve urea hydrolysis, ammonium capture, and real-time ammonium sensing in sequence. In combination, the described works provide a powerful toolkit that can be used in treating various waste streams before discharge and/or reuse.

PUBLISHED CONTENT AND CONTRIBUTIONS

Zhang, Y.;* Yang, Y.;* Yang, S.; Quispe-Cardenas, E.; Hoffmann, M. R. Application of Heterojunction Ni-Sb-SnO₂ Anodes for Electrochemical Water Treatment. *ACS EST Eng.* **2021**, *1* (8), 1236-1245. <https://doi.org/10.1021/acsestengg.1c00122>.

*These authors contributed equally. Y.Z. designed and conducted the experiments, analyzed the data, and wrote the manuscript for this project.

Zhang, Y.; Guo, L.; Hoffmann, M. R. Ozone- and Hydroxyl Radical-Mediated Oxidation of Pharmaceutical Compounds using Ni-doped Sb-SnO₂ Anodes: Degradation Kinetics and Transformation Products. *ACS EST Eng.* **2023**, *3* (3), 335-348. <https://doi.org/10.1021/acsestengg.2c00337>.

Y.Z. designed and conducted the experiments, analyzed the data, and wrote the manuscript for this project.

McBeath, S. T.;* **Zhang, Y.;*** Hoffmann, M. R. Novel Synthesis Pathways for Highly Oxidative Iron Species: Generation, Stability, and Treatment Applications of Ferrate(IV/V/VI). *Environ. Sci. Technol.* **2023**. <https://doi.org/10.1021/acs.est.2c09237>.

*These authors contributed equally. Y.Z. participated in experiment design, helped conduct the experiments, and assisted with data analysis.

Guo, L.;* **Zhang, Y.;*** Osella, S.; Webb, S. M.; Yang, X.; Goddard, W. A.; Hoffmann, M. R. Modular Metal-Organic Frameworks Functionalization Facilitating Nitrogen Recovery from Fresh Urine. To be submitted.

*These authors contributed equally. Y.Z. helped conduct the experiments and assisted with computational analysis.

TABLE OF CONTENTS

Acknowledgments	iii
Abstract	vi
Published Content and Contributions	viii
Table of Contents	ix
List of Illustrations.....	xi
List of Tables.....	xxiii
Introduction	1
1.1 Background and Motivation	1
1.2 Thesis Organization.....	3
1.3 References	5
Application of Heterojunction Ni-Sb-SnO ₂ Anodes for Electrochemical Water Treatment..	7
2.1 Abstract	7
2.2 Introduction	8
2.3 Materials and Methods	9
2.4 Results and Discussion	12
2.5 Conclusions	24
2.6 Acknowledgments	25
2.7 References	25
2.8 Supporting Information.....	28
Ozone- and Hydroxyl Radical-Mediated Oxidation of Pharmaceutical Compounds using Ni-doped Sb-SnO ₂ Anodes: Degradation Kinetics and Transformation Products	54
3.1 Abstract	54
3.2 Introduction	55
3.3 Materials and Methods	57
3.4 Results and Discussion	59
3.5 Conclusions	78
3.6 Acknowledgments	78
3.7 References	78
3.8 Supporting Information.....	82
3.9 Additional Notes.....	106
Novel Synthesis Pathways for Highly Oxidative Iron Species: Generation, Stability, and Treatment Applications of Ferrate(IV/V/VI)	107
4.1 Abstract	107
4.2 Introduction	108
4.3 Materials and Methods	110
4.4 Results and Discussion	112
4.5 Acknowledgments	124
4.6 References	124
4.7 Supporting Information.....	129

Modular Metal-Organic Frameworks Functionalization Facilitating Nitrogen Recovery from Fresh Urine	148
5.1 Abstract	148
5.2 Introduction	149
5.3 Results	151
5.4 Discussion	161
5.5 References	161
5.6 Supporting Information.....	166
Conclusions and Outlooks	192

LIST OF ILLUSTRATIONS

- Figure 2.1** (a) Cross-sectional SEM image for NAT/AT. (b) Ni/Sn and (c) Sb/Sn molar ratios for the seven sample points.....13
- Figure 2.2** (a) EIS spectra, (b) cyclic voltammograms, and (c) charging currents as functions of scan rate by AT, NAT/AT, and NAT electrodes. Dashed lines in (a) represent fitting results based on a Randles circuit (inset).....14
- Figure 2.3** (a) Chlorine evolution rate and current efficiency measured in 30 mM NaCl electrolytes. (b) Dissolved O₃ detected in NaClO₄ electrolytes during electrolysis by NAT/AT and NAT. Test “w/ Cl” was performed in 30 mM NaCl electrolyte. Test “w/ BA” was conducted in 30 mM NaClO₄ spiked with 1 mM BA. Dashed lines represent kinetic modeling results. (c) Overall ozone evolution rates for NAT in 100 mM NaClO₄, and NAT/AT in 100 mM NaClO₄ and 30 mM NaCl. Current efficiencies were marked on the bar diagram. Anode surface area = 6 cm², current density = 10 mA/cm², electrolyte volume = 25 mL.15
- Figure 2.4** (a) Electrochemical oxidation of BA by AT, NAT/AT, and NAT electrodes in 30 mM NaClO₄ electrolytes in the presence or absence of 100 mM tBuOH or 100 mM MeOH. (b) Electrochemical oxidation of BA by NAT/AT in chloride-bearing electrolytes (30 and 60 mM NaCl). Dashed lines represent kinetic modeling results. Anode surface area = 6 cm², current density = 10 mA/cm², electrolyte volume = 25 mL.17
- Figure 2.5** (a) Differences of pH values on the NAT/AT anode surface (hollow) and in the bulk electrolyte (solid). (b) Schematic illustration of two indirect pathways for the production of ·OH from O₃.....18
- Figure 2.6** Removal of (a) 30 μM carbamazepine (CBZ) and inactivation of (b) *E. coli* and (c) MS2 by different electrodes in 30 mM NaClO₄ electrolytes. Anode surface area = 6 cm², current density = 10 mA/cm², electrolyte volume = 25 mL.22

Figure 2.7 Electrochemical oxidation by NAT/AT of (a) pharmaceuticals (10 μ M each) and (b) <i>E. coli</i> and MS2 spiked into latrine wastewater. Anode surface area = 6 cm ² , current density = 10 mA/cm ² , wastewater volume = 25 mL.....	23
Figure 2.S1 Stability test of Ni (1 atom-%)-SnO ₂ electrode at 10 mA/cm ² in 100 mM NaClO ₄	31
Figure 2.S2 Sheet resistance measurements of (a) NAT and (b) AT.....	31
Figure 2.S3 Accelerated lifetime tests of anodes.....	32
Figure 2.S4 Cyclic voltammograms at scan rates of 5, 10, 25, 50, 100, 200, 400, and 800 mV/s of AT, NAT/AT, NAT, IrO ₂ , and BDD electrodes and charging currents as functions of scan rate of IrO ₂ and BDD electrodes.	33
Figure 2.S5 Leaching of Sb and Ni by AT and NAT/AT electrodes.....	34
Figure 2.S6 Evolution rates of O ₃ in the gas phase during electrolysis in NaCl and NaClO ₄ electrolytes. Anode surface area = 6 cm ² , current density = 10 mA/cm ² , electrolyte volume = 25 mL.	35
Figure 2.S7 Apparent O ₃ production with different concentrations of malonic acid (MA) added to quench free chlorine. Anode surface area = 6 cm ² , current density = 10 mA/cm ² , electrolyte volume = 25 mL.....	35
Figure 2.S8 Linear sweep voltammograms (LSV) of NAT/AT in 30 mM NaClO ₄ electrolytes in the absence and presence of 1 mM benzoic acid (BA).....	36
Figure 2.S9 BA degradation by NAT/AT in 30 mM NaClO ₄ electrolytes.	36
Figure 2.S10 Experimental current vs. applied potential of NAT/AT with and without stirring.	37
Figure 2.S11 Benzoic acid (BA) degradation by homogeneous ozonation.	38
Figure 2.S12 Impacts of the organic radical quenchers benzoic acid (BA), nitrobenzene (NB), and tert-butanol (tBuOH) on the production of O ₃ by NAT/AT anode in 30 mM NaClO ₄ . Anode surface area = 6 cm ² , current density = 10 mA/cm ² , electrolyte volume = 25 mL.	39
Figure 2.S13 Effect of pH on the BA degradation kinetics by NAT/AT. Anode surface area = 6 cm ² , current density = 10 mA/cm ² , electrolyte volume = 25 mL.	39

Figure 2.S14 EO treatment of (a) nitrobenzene (NB), (b) phenol (Ph), and (c) ibuprofen (IBP) in 30 mM NaClO ₄ . The dashed red line in (c) represents kinetic model prediction of IBP degradation, taking into account reaction with both O ₃ and ·OH. Anode surface area = 6 cm ² , current density = 10 mA/cm ² , electrolyte volume = 25 mL.....	40
Figure 2.S15 Radical contributions to BA degradation by NAT/AT in NaClO ₄ and NaCl electrolytes.....	40
Figure 2.S16 Carbamazepine (CBZ) degradation by NAT/AT in 30 mM NaClO ₄ electrolytes.....	41
Figure 2.S17 Removal of 30 μM carbamazepine (CBZ) by (a) NAT/AT in 30 mM NaClO ₄ and NaCl and (b) different electrodes in 30 mM NaCl. Inactivation of (c) <i>E. coli</i> and (d) MS2 by NAT/AT in 30 mM NaClO ₄ and NaCl electrolytes. Anode surface area = 6 cm ² , current density = 10 mA/cm ² , electrolyte volume = 25 mL.....	41
Figure 2.S18 Formation of disinfection byproducts (DBPs) during electrolysis of latrine wastewater by NAT/AT electrode.	42
Figure 3.1 Electrochemical oxidation of carbamazepine (CBZ) by (a) NAT/AT and (b) BDD, and of fluconazole (FCZ) by (c) NAT/AT and (d) BDD in ClO ₄ : 50 mM NaClO ₄ , SO ₄ ClO ₄ : 5 mM Na ₂ SO ₄ + 50 mM NaClO ₄ , Cl: 50 mM NaCl, and SO ₄ Cl: 5 mM Na ₂ SO ₄ + 50 mM NaCl electrolytes.....	61
Figure 3.2 (a) FCZ degradation by NAT/AT under different chloride concentrations (50, 10, and 5 mM NaCl, 5 mM NaClO ₄ was added to 5 mM NaCl to compensate for lower conductivity). Influence of pH on FCZ degradation by (b) BDD and (c) NAT/AT in 50 mM NaCl electrolytes. For degradation under pH 9 (no adjustment), no phosphate buffer was added.....	63
Figure 3.3 Proposed carbamazepine (CBZ) transformation pathways. Blue structures mark products detected during electrolysis in NaClO ₄ electrolytes. Green structures mark products with higher confidence levels/higher uncertainties and thus more tentative structures and pathways.....	69
Figure 3.4 CBZ transformation product evolution in NaClO ₄ electrolytes at (a) NAT/AT and (b) BDD.....	72

Figure 3.5 Major CBZ transformation product evolution in NaCl electrolytes at (a) NAT/AT and (b) BDD.....	74
Figure 3.6 (a) Proposed formation pathway and (b) evolution of FCZ transformation product TP224 at NAT/AT and BDD.....	76
Figure 3.7 Removal of spiked pharmaceutical compounds (2 μ M each) during electrolysis of (a) latrine wastewater and (b) secondary effluent by NAT/AT.....	77
Figure 3.S1 Experimental results and kinetic modeling predictions (dashed lines) for CBZ degradation by NAT/AT in (a) ClO ₄ : 50 mM NaClO ₄ and SO ₄ ClO ₄ : 5 mM Na ₂ SO ₄ + 50 mM NaClO ₄ and (b) Cl: 50 mM NaCl and SO ₄ Cl: 5 mM Na ₂ SO ₄ + 50 mM NaCl electrolytes.....	83
Figure 3.S2 Experimental results and kinetic modeling predictions (dashed lines) for FCZ degradation by NAT/AT in (a) ClO ₄ : 50 mM NaClO ₄ and SO ₄ ClO ₄ : 5 mM Na ₂ SO ₄ + 50 mM NaClO ₄ and (b) Cl: 50 mM NaCl and SO ₄ Cl: 5 mM Na ₂ SO ₄ + 50 mM NaCl electrolytes.....	83
Figure 3.S3 Linear sweep voltammograms (LSV) of (a) BDD in 50 mM NaClO ₄ , (b) BDD in 50 mM NaCl, and (c) NAT/AT in 50 mM NaCl electrolytes in the absence and presence of 20 μ M CBZ or FCZ.....	83
Figure 3.S4 FCZ degradation by (a) NAT/AT and (b) BDD in 50 mM NaClO ₄ electrolytes with pH adjusted to 5, 7, and 9 in phosphate buffers. For degradation under pH 5 (no adjustment), no phosphate buffer was added.	84
Figure 3.S5 Chlorine evolution rate and current efficiency measured in 50 mM NaCl electrolytes during electrolysis by (a) BDD and (b) NAT/AT.	85
Figure 3.S6 Dissolved O ₃ concentrations measured under different pHs in 50 mM NaCl electrolytes during electrolysis by NAT/AT.	85
Figure 3.S7 Possible structures for TP253a.	85
Figure 3.S8 Mass spectra of TP278, TP181, TP301, TP289, TP285, TP273, and TP230.	87
Figure 3.S9 A zoomed-in look at CBZ transformation product evolution (excluding TP251) in NaClO ₄ electrolytes at (a) NAT/AT and (b) BDD.	87

- Figure 3.S10** Responses of (a) TP267, (b) TP301, (c) TP224, (d) TP226, and (e) TP271 and TP253a of CBZ at NAT/AT in the absence (left) and presence (right) of 5 mM Na₂SO₄ in 50 mM NaCl electrolytes.....88
- Figure 3.S11** CBZ transformation product evolution (all) in NaCl electrolytes at (a) NAT/AT and (b) BDD.....89
- Figure 3.S12** Peak concentrations and calibration curves of TP180 (acridine), TP253b (carbamazepine 10,11-epoxide), and TP224 (9-acridinecarboxylic acid) at NAT/AT and BDD in different electrolytes.....90
- Figure 3.S13** Electrochemical oxidation and transformation product evolution of 20 μM TP253b (CBZ-EP) at (a) NAT/AT and (b) BDD in 50 mM NaClO₄ and NaCl electrolytes.....90
- Figure 3.S14** Electrochemical oxidation and transformation product evolution of 20 μM TP224 (9-acridinecarboxylic acid) at (a) NAT/AT and (b) BDD in 50 mM NaClO₄ and NaCl electrolytes.....92
- Figure 3.S15** Experimental results and kinetic modeling predictions (dashed lines) for (a) atenolol (ATL), (b) gabapentin (GBP), and (c) ibuprofen (IBP) degradation by NAT/AT in 50 mM NaClO₄ electrolytes.93
- Figure 3.S16** COD removal during treatment of latrine wastewater spiked with pharmaceuticals.93
- Figure 3.S17** Transformation product evolution for (a) CBZ, (b) a zoomed-in look for CBZ excluding TP251, and (c) FCZ during treatment of secondary effluent spiked with pharmaceuticals by NAT/AT.....94
- Figure 3.S18** Removal of spiked pharmaceutical compounds (2 μM each) during electrolysis of (a) latrine wastewater and (b) secondary effluent by BDD.94
- Figure 3.S19** Transformation product evolution for (a) CBZ, and (b) a zoomed-in look for CBZ excluding TP285 during treatment of secondary effluent spiked with pharmaceuticals by BDD. TP224 of FCZ was not detected.....94
- Figure 4.1** (A) Ferrate(IV/V/VI) generation using BDD, NAT and AT electrodes with a Fe³⁺₀ = 10 mM and 10 mA cm⁻². Fe(VI)_{Eq} = Equivalent oxidative capacity of Fe(VI) with

ABTS (1:1 molar ratio). (B) Faradaic efficiency of ferrate (IV/V/VI) generation at 5, 10 and 15 mA cm ⁻² and with a Fe ³⁺ ₀ = 10 mM.	114
Figure 4.2 Ferrate(IV/V/VI) generation with a Fe ³⁺ ₀ = 10 mM at 5, 10 and 20 mA cm ⁻² using (A) NAT electrode, and (B) BDD electrode. Inset figures are final ferrate solutions after 90 min of electrolysis. Fe(VI) _{Eq} = Equivalent oxidative capacity of Fe(VI) with ABTS (1:1 molar ratio).....	115
Figure 4.3 UV-spectra (left) and cyclic voltammograms (right) of final BDD and NAT ferrate solutions after 90 min of electrolysis at 10 mA cm ⁻² and an initial FeCl ₃ concentration of 10 mM (CV condition: scan rate 50 mV s ⁻¹ , 0.0 V vs. E _{OC} to -1.3 V vs. ref.).....	117
Figure 4.4 ABTS (415 nm) and direct (530 nm) UV-vis spectrophotometric results from NAT electrolysis at 10 mA cm ⁻² and FeCl ₃ of 15 mM (left), and O ₃ oxidation with an initial FeCl ₃ of 15 mM (right).....	120
Figure 4.5 Normalized ferrate degradation with (A) BDD derived ferrate(IV/V) (Fe(VI) _{Eq} = 13.6 mM), and (B) NAT derived ferrate(VI) (Fe(VI) = 3.9 mM).	121
Figure 4.6 Ferrate(IV/V) oxidation experiments with O ₃ post and during electrolysis to form ferrate(VI).....	123
Figure 4.S1 Cyclic voltammograms of BDD with OER potential at ~2.7 V _{RHE} . CV condition: scan rate 50 mV s ⁻¹ , 0.0 V vs. E _{OC} to +3.0 V vs. ref.....	129
Figure 4.S2 Ferrate(VI) ABTS calibration curves using K ₂ SO ₄ (Element 26) in phosphate buffer (pH = 7.0), yielding a molar absorption coefficient of 0.043 mM ⁻¹ cm ⁻¹	130
Figure 4.S3 ABTS absorbance during BDD ferrate (5 mA cm ² , 10 mM FeCl ₃) and control (5 mA cm ² , 30 mM NaCl) experiments.	131
Figure 4.S4 ABTS absorbance during BDD ferrate (10 mA cm ² , 10 mM FeCl ₃) and control (10 mA cm ² , 30 mM NaCl) experiments.	131
Figure 4.S5 ABTS absorbance during BDD ferrate (20 mA cm ² , 10 mM FeCl ₃) and control (20 mA cm ² , 30 mM NaCl) experiments.	132
Figure 4.S6 ABTS absorbance during NAT ferrate (5 mA cm ² , 10 mM FeCl ₃) and control (5 mA cm ² , 30 mM NaCl) experiments.	132

Figure 4.S7 ABTS absorbance during NAT ferrate (10 mA cm ² , 10 mM FeCl ₃) and control (10 mA cm ² , 30 mM NaCl) experiments.	133
Figure 4.S8 ABTS absorbance during NAT ferrate (20 mA cm ² , 10 mM FeCl ₃) and control (20 mA cm ² , 30 mM NaCl) experiments.	133
Figure 4.S9 ABTS absorbance during NAT ferrate (5 mA cm ² , 15 mM FeCl ₃) and control (5 mA cm ² , 45 mM NaCl) experiments.	134
Figure 4.S10 ABTS absorbance during NAT ferrate (10 mA cm ² , 15 mM FeCl ₃) and control (10 mA cm ² , 45 mM NaCl) experiments.	134
Figure 4.S11 ABTS absorbance during NAT ferrate (20 mA cm ² , 15 mM FeCl ₃) and control (20 mA cm ² , 45 mM NaCl) experiments.	135
Figure 4.S12 ABTS absorbance during AT ferrate (10 mA cm ² , 10 mM FeCl ₃) and control (10 mA cm ² , 30 mM NaCl) experiments.	135
Figure 4.S13 Ferrate(VI) generation using an NAT electrodes with a Fe ³⁺ ₀ = 15 mM and current densities of at 5, 10 and 20 mA cm ⁻²	136
Figure 4.S14 Raman spectra graph of final BDD and NAT ferrate solutions after 90 min of electrolysis at 10 mA cm ⁻² and an initial FeCl ₃ concentration of 10 mM.	137
Figure 4.S15 FTIR spectra graph of final BDD and NAT ferrate solutions after 90 min of electrolysis at 10 mA cm ⁻² and an initial FeCl ₃ concentration of 10 mM.	137
Figure 4.S16 Nitrobenzene degradation using NAT derived ferrate(VI) and NaCl control solutions (NB ₀ = 0.1 mM, Fe(VI) = 1.52 mM).	138
Figure 4.S17 Nitrobenzene degradation using BDD derived ferrate(IV/V) and NaCl control solutions (NB ₀ = 0.1 mM, Fe(VI) _{Eq} = 3.83 mM).	138
Figure 4.S18 Nitrobenzene degradation using BDD derived ferrate(IV/V) and NaCl control solutions (NB ₀ = 0.1 mM, Fe(VI) _{Eq} = 3.83 mM).	139
Figure 4.S19 CBZ degradation using NAT derived ferrate(VI) and NaCl control solutions (CBZ ₀ = 10 μM).	139
Figure 4.S20 Second-order reaction rate determination of CBZ and NAT derived ferrate(VI) (CBZ ₀ = 10 μM, Fe(VI) ₀ = 1.66 mM).....	140
Figure 4.S21 CBZ degradation using BDD derived ferrate(IV/V) and NaCl control solutions (CBZ ₀ = 10 μM).	140

Figure 4.S22 CBZ degradation using AT derived ferrate(IV/V) and NaCl control solutions (CBZ ₀ = 10 μM).....	141
Figure 4.S23 FCZ degradation using NAT derived ferrate(VI) and NaCl control solutions (FCZ ₀ = 10 μM).....	141
Figure 4.S24 FCZ degradation using BDD derived ferrate(IV/V) and NaCl control solutions (FCZ ₀ = 10 μM).....	142
Figure 4.S25 ABTS absorbance data for ferrate(IV/V) degradation long term study (Fe(VI) _{Eq} = 13.6 mM).....	142
Figure 4.S26 ABTS absorbance data for ferrate(VI) degradation long term study (Fe(VI) = 3.9 mM).....	143
Figure 4.S27 Fe(VI) _{Eq} data for ferrate(IV/V) degradation long term study (Fe(VI) _{Eq} = 13.6 mM). Fe(VI) _{Eq} = Equivalent oxidative capacity of Fe(VI) with ABTS (1:1 molar ratio).....	143
Figure 4.S28 Fe(VI) data for ferrate(VI) degradation long term study (Fe(VI) = 3.9 mM).	144
Figure 4.S29 Cyclic voltammograms of BDD derived ferrate(IV/V) solution over 6 week stability test. CV condition: scan rate 50 mV s ⁻¹ , 0.0 V vs. E _{oc} to -1.3 V vs. ref. .	144
Figure 4.S30 Cyclic voltammograms of NAT derived ferrate(VI) solution over 6 week stability test. CV condition: scan rate 50 mV s ⁻¹ , 0.0 V vs. E _{oc} to -1.3 V vs. ref. .	145
Figure 4.S31 ABTS absorbance during BDD electrolysis and O ₃ purging (10 mA cm ² , 15 mM FeCl ₃).....	146
Figure 4.S32 Ferrate(IV/V) oxidation experiments with O ₃ during electrolysis to form ferrate(VI) (full set of photos).....	146
Figure 4.S33 ABTS absorbance of control ozonation of NaCl and PBS solution.....	146
Figure 4.S34 ABTS absorbance during O ₃ purging on ferrate(IV/V) solution produced with BDD electrolysis (10 mA cm ² , 15 mM FeCl ₃) and control (10 mA cm ² , 45 mM NaCl).....	147
Figure 4.S35 UV-absorption spectra of ferrate(VI) from K ₂ FeO ₄ , K ₂ FeO ₄ and Fe(III) (dosed using FeCl ₃) and NAT-generated ferrate(VI).....	147

Scheme 5.1 Newly developed nitrogen recovery from *fresh* urine facilitated with functionalized MOFs.151

Figure 5.1 (a) Synthesis scheme for MOF-808-U. Urease structure from pdb 4H9M. (b) PXRD patterns of MOF-808-U and pristine MOF-808. Almost identical PXRD patterns indicates that the crystallinity of MOF structure was well-maintained during the incorporation of urease. (c) Michaelis–Menten kinetic measurement of MOF-808-U and free urease. MOF-808-U exhibited near-identical enzymatic activity as that of free urease. (d) Stability tests of MOF-808-U and free urease, where MOF-808-U demonstrated its stability (up to 6 days) compared to free urease.153

Figure 5.2 (a) Synthesis scheme of MOF-808-based ammonium adsorbents. (b) PXRD patterns, (c) ammonium uptake isotherms, and (d) ammonium capture kinetics experiments of MOF-808, MOF-808-OA, MOF-808-MA, and MOF-808-SA. While all four MOF materials shared identical structure, modification of interior pore environment has a direct and significant impact on their ammonium capture performances. (e) Cumulative RDF analysis for the nitrogen-oxygen distance for all the studied MOF systems. (f) Ammonium uptake capacity and (g) recovery efficiency of MOF-808-OA with 10 cycles of regeneration, where sodium nitrate solution was used as the regeneration reagent and ammonium nitrate as the recovery product.....156

Figure 5.3 (a) PXRD patterns of pristine MOF-808, MOF-808-Cu, and MOF-808-Cu exposed with $[\text{NH}_4^+\text{-N}]$ of 2000 ppm. (b) SEM-EDS images of MOF-808-Cu. (c) Linear relationship between the readout of the R channel of an image of MOF-808-Cu suspension and $[\text{NH}_4^+\text{-N}]$. Inset: an image of MOF-808-Cu suspended in a series of solutions with different $[\text{NH}_4^+\text{-N}]$ levels. Concentrations from top left to bottom right are: 40000, 20000, 8000, 4000, 2000, 800, 400, 200, 80, and 40 ppm. Single vial on the right was MOF-808-Cu suspended in water. (d) Readout of the R channel of MOF-808-Cu after 5 cycles of regeneration. Inset: an image of regenerated MOF-808-Cu suspended in a solution of 2000 ppm $[\text{NH}_4^+\text{-N}]$158

Figure 5.4 (a) Schematic diagram of fresh urine treatment integrating the functionalized MOF materials designed in this work. (b) Total nitrogen removal and recovery

efficiency of five cycles of entire treatment. (c) MOF-808-Cu suspended in the treated solution after MOF-808-U (top) and MOF-808-OA (bottom) in each of the five cycles, demonstrating efficiency of each treatment steps (urea conversion, ammonium capture, and regeneration of ammonium adsorbent).	160
Figure 5.S1 FT-IR spectra of MOF-808, free urease, and MOF-808-U.	169
Figure 5.S2. FT-IR spectra of MOF-808 and the dicarboxylate functionalized derivatives.	169
Figure 5.S3 FT-IR spectra of MOF-808 and MOF-808-Cu.	170
Figure 5.S4 ¹ H NMR spectrum of digested MOF-808. Peak with the chemical shift of 8.08 ppm is assigned to formic acid (FA). Ratio of BTC and FA was determined as 2:2.82.	170
Figure 5.S5 ¹ H NMR spectrum of digested MOF-808-OA.	171
Figure 5.S6 ¹ H NMR spectrum of digested MOF-808-MA. Peak with the chemical shift of 3.23 ppm is assigned to malonic acid (MA). Ratio of BTC and MA was determined as 2:5.78.	171
Figure 5.S7 ¹ H NMR spectrum of digested MOF-808-SA. Peak with the chemical shift of 2.40 ppm is assigned to succinic acid (SA). Ratio of BTC and SA was determined as 2:5.30.	172
Figure 5.S8 SEM image of MOF-808.	172
Figure 5.S9 SEM image of MOF-808-U.	173
Figure 5.S10 SEM image of MOF-808-OA.	173
Figure 5.S11 SEM image of MOF-808-MA.	174
Figure 5.S12 SEM image of MOF-808-SA.	174
Figure 5.S13 SEM image of MOF-808-Cu.	175
Figure 5.S14 Comparison of Langmuir, Freundlich, and Langmuir–Freundlich models of MOF-808 for fitting the experimental uptake data.	177
Figure 5.S15 Comparison of Langmuir, Freundlich, and Langmuir–Freundlich models of MOF-808-OA for fitting the experimental uptake data.	177
Figure 5.S16 Comparison of Langmuir, Freundlich, and Langmuir–Freundlich models of MOF-808-MA for fitting the experimental uptake data.	178

Figure 5.S17 Comparison of Langmuir, Freundlich, and Langmuir–Freundlich models of MOF-808-SA for fitting the experimental uptake data.	178
Figure 5.S18 Cumulative distribution function (CDF) analyses of four MOF systems. For MOF-808-OA, MOF-808-MA, and MOF-808-SA, RDF intensity of carboxylate oxygen and ammonium nitrogen was integrated, whereas for MOF-808, RDF intensity of formate hydrogen and ammonium nitrogen was integrated.....	182
Figure 5.S19 Histogram of the RDF analysis for each ammonium-H pair present in the MOF-808 system.	182
Figure 5.S20 Histogram of the RDF analysis for each ammonium-oxygen pair present in the MOF-808-OA system.	183
Figure 5.S21 Histogram of the RDF analysis for each ammonium-oxygen pair present in the MOF-808-MA system.	183
Figure 5.S22 Histogram of the RDF analysis for each ammonium-oxygen pair present in the MOF-808-SA system.....	184
Figure 5.S23 Histogram of the adsorption free energy (absolute value) of all MOF systems.	185
Figure 5.S24 Free energy of different amount of ammonium ions in water solution. High linearity of the curve indicates the high validity of the 2PT analysis.	185
Figure 5.S25 UV–vis diffuse reflectance spectra for MOF-808-Cu after exposing to ammonium hydroxide solutions of different concentrations.	186
Figure 5.S26 Relationship between ammonium concentrations vs. R value of MOF-808-Cu upon exposure to ammonium hydroxide solutions.....	187
Figure 5.S27 Relationship between ammonium concentrations vs. G value of MOF-808-Cu upon exposure to ammonium hydroxide solutions.....	187
Figure 5.S28 Relationship between ammonium concentrations vs. B value of MOF-808-Cu upon exposure to ammonium hydroxide solutions.....	188
Figure 5.S29 Catalytic activity of MOF-808-U in five successive cycles.	189
Figure 5.S30 Ammonium and total nitrogen (including urea) capture capacity of MOF-808-OA in five cycles of treatment.	189

Figure 5.S31 Nitrogen recovery efficiency of MOF-808-OA in five cycles of treatment.

.....190

LIST OF TABLES

Table 2.S1 Target compound properties.	42
Table 2.S2 Principle reactions in the kinetic model.....	42
Table 2.S3 Rate constants estimated by kinetic modeling.....	47
Table 2.S4 Carbamazepine transformation products.....	48
Table 2.S5 Composition of latrine wastewater.....	49
Table 2.S6 Energy consumption for pharmaceuticals/pathogens removal by common electrodes.....	49
Table 3.1 Carbamazepine (CBZ) transformation products.....	64
Table 3.S1 Principle reactions in the kinetic model.....	95
Table 3.S2 Fragmentation analyses of TP244, 278, 253a, 267, 253c, and 205 of CBZ.....	99
Table 3.S3 Sorted carbamazepine (CBZ) transformation product response ^a at NAT/AT and BDD.....	100
Table 3.S4 Target pharmaceutical compound properties.....	101
Table 3.S5 Composition of latrine wastewater and secondary effluent.....	101
Table 5.S1 Enzymatic kinetic parameters determined from the Michaelis–Menten plot.....	175
Table 5.S2 Fitting parameters of three different models for MOF-808-based adsorbents.....	178
Table 5.S3 Adsorption free energies of all MOF systems.....	184
Table 5.S4 Pore size analysis of all MOF systems.....	186

Chapter 1

INTRODUCTION

1.1 Background and Motivation

Clean water supply is critical for public health as well as for food production. Currently, over 2 billion people around the world use drinking water sources that are contaminated with fecal matter.¹ Meanwhile, more than 1.7 billion people lack basic sanitation facilities including latrines and private toilets.² Inadequate sanitation services and the continued practice of open defecation in developing regions of the world have led to the spread of water-borne diseases and millions of attributed deaths each year.³ While centralized wastewater treatment facilities are not practical in many parts of the developing world owing to financial, geographical, or political constraints, small-scale decentralized treatment represents an attractive alternative that can provide necessary water treatment for discharge and/or reuse.

Electrochemical oxidation (EO) is an attractive technique that does not require the addition of chemical reagents. EO provides for fast reaction kinetics, modular treatment capacity, and easy modes of operation.^{4,5} It has been demonstrated to be particularly useful for the purpose of decentralized onsite treatment.^{4,5} EO redox systems are suitable for removing chemical oxygen demand (COD), treating recalcitrant chemical contaminants, and inactivating pathogens in concentrated wastewater streams.^{4,5}

In the built environment, viruses can survive in toilet wastewater and be transmitted via aerosols produced during flushing and aeration.⁶ Moreover, toilet wastewater can be a major sink of micro-pollutants such as pharmaceuticals and personal care products (PPCPs), as a significant amount of ingested pharmaceuticals is excreted either partially metabolized or unmetabolized through urine and fecal matter.^{7,8} In previous studies, EO wastewater treatment has also been shown to be cost-effective for microbial disinfection and PPCPs removal in bench-top prototypes and full-scale applications.⁹⁻¹¹

In electrochemical processes, treatment is achieved through reactions with the oxidizing species (e.g. hydroxyl radicals, free chlorine, and ozone) generated at the anode as well as in some cases direct electrolysis on the electrode surface. The chemical composition of the anodes is a key factor that controls reactive species production and thus the relative treatment efficiency and overall energy consumption during electrochemical oxidation. Electrodes that do not depend on the use of platinum-group metals are essential in reducing capital costs. Anodes can be categorized into two classes – “active” and “nonactive” – depending on the nature of the materials.⁴ Examples of “active” and “nonactive” anodes include iridium oxide (IrO_2) and boron-doped diamond (BDD), which are often used for chlorine evolution and free radical production, respectively. However, IrO_2 and other active anodes are not ideal for organic degradation since, with oxidation largely dependent on active chlorine, they do not facilitate complete contaminant oxidation.⁴ Nonactive anodes, on the other hand, are more suitable for wastewater treatment since they have high oxygen evolution overpotential and favor complete oxidation of organics to CO_2 .⁴ In the specific case of BDD electrodes, however, the high capital cost (e.g., $>\$7000/\text{m}^2$ for BDD) and poor mechanical strength (e.g., brittle substrate) of the material prohibit economical large-scale applications.^{5,12}

Similar to BDD, antimony-doped tin oxide (Sb-SnO_2 , AT) is also a nonactive anode. Pristine SnO_2 is a wide bandgap ($E_{\text{bg}} = 3.6 \text{ eV}$) n-type semiconductor, and antimony is commonly used to increase its conductivity.^{13,14} It is easy to prepare (by dip- or brush-coating methods with annealing at $400\text{-}600^\circ\text{C}$) and can generate a variety of oxidizing species. It is often used under high anodic potentials to oxidize an array of chemical contaminants.^{15,16} Moreover, multiple metal precursors can be homogeneously blended into the precursor coating solutions to generate metal-doped Sb-SnO_2 electrodes. On modification of Sb-SnO_2 , nickel and antimony-doped tin oxide (Ni-Sb-SnO_2 , NAT), has been reported to produce ozone (O_3) during electrolysis in acidic electrolytes and could potentially be used to produce O_3 gas at lower DC voltages as an alternative to the high-voltage ozonator.¹⁷ Ni-Sb-SnO_2 anodes have also been used in the electrochemical oxidation of organic compounds in water and O_3 produced during electrolysis has been found to enhanced target compound degradation.¹⁸

Hydroxyl radical ($\cdot\text{OH}$) is a key oxidant produced during oxygen evolution reaction (OER) in the absence of chloride. However, the reported current efficiency (CE) for $\cdot\text{OH}$ production using a boron-doped diamond electrode is $<0.05\%$.¹⁹ The majority of the anodic current is applied toward achieving oxygen production, which does not contribute to the oxidation of target chemical species. However, a nickel and antimony-doped tin oxide electrode can oxidize water to O_3 along with $\cdot\text{OH}$ at high current density. Thus, *in situ* O_3 production at Ni-Sb-SnO₂ provides another oxidation pathway as well as an additional source of $\cdot\text{OH}$ due to O_3 transformation.²⁰

Given that AT has excellent electron shuttling capability to serve as an ohmic contact,²¹ and that NAT shows superior EO reactivity coupled with a lower potential for Sb leaching, a heterojunction anode was constructed with NAT on top of AT coated on the titanium base-metal substrate. The work presented in this thesis thus centered around this newly designed heterojunction Ni-Sb-SnO₂-based anode (NAT/AT) and its various applications in decentralized water and wastewater treatment.

1.2 Thesis Organization

Chapter 2 describes the electrode design, characterization, mechanistic investigation, and performance evaluation. NAT/AT was found to be durable and can reduce Sb leaching due to the lower Sb concentration in the top layer. It was also demonstrated to be efficient for microbial disinfection, waste pharmaceutical degradation, and onsite human wastewater treatment. Experimental and computational methods were combined to provide a new mechanism for O_3 activation to $\cdot\text{OH}$ at the electrode/electrolyte interface. Results from this work showed that NAT/AT holds great potential in treating trace organic compounds including pharmaceuticals in wastewater streams, given that compounds with both fast and slow reaction rate constants with O_3 could potentially be removed at fast rates.

Chapter 3, following the work in Chapter 2, further probes the applicability of NAT/AT in treating pharmaceuticals, an important group of emerging environmental contaminants. Degradation kinetics and transformation products (TPs) were studied for carbamazepine (CBZ) and fluconazole (FCZ), two of the top 100 commonly used pharmaceuticals with significantly different reaction rates with O_3 . The NAT/AT anode demonstrated promising

performance in degrading a range of pharmaceutical compounds as well as their transformation products. NAT/AT, compared to BDD, could achieve similar or better removal with lower energy consumption. It could represent a more economical and efficient method for water treatment practices that is capable of large-scale implementation. Moreover, treatment of a similar waste stream suggested that electrolytic oxidation with NAT/AT could also provide a suitable treatment alternative for the control of pharmaceuticals in hospital wastewaters.

Chapter 4, instead of focusing on treatment using NAT/AT directly, reports on the application of NAT/AT in the circumneutral electrosynthesis of the high oxidation state iron species ferrates, another group of powerful oxidant. Ferrates are also well-suited for decentralized treatment purposes, since they are not known to form toxic disinfection byproducts and Fe^{3+} , their reduced product, is non-toxic and can function as a coagulant. Investigation into generation kinetics and stability and speciation of the formed iron species indicated NAT/AT as a potential alternative to the conventional and costly BDD electrodes.

Chapter 5, while still dealing with the broader topic of decentralized treatment, shifts the focus from NAT/AT anode itself to ammonium (NH_4^+), one commonly occurring component that often poses as a problem especially during latrine wastewater treatment. In all works described in the above chapters, removal of NH_4^+ from latrine wastewater proved to be very difficult using both NAT/AT and BDD. Waste streams high in NH_4^+ , when discharged, can lead to serious problems such as eutrophication. It also represents a huge waste of nitrogen that can potentially be recovered as a source for fertilizers. The work in this chapter thus explored another possibility to recover nitrogen from urine using functionalized metal-organic frameworks (MOFs), a class of materials featuring high porosity, abundant active sites, and highly tunable physical and chemical properties. Specifically, various target-oriented modifications of MOF-808, a highly water stable MOF, were designed and synthesized. By incorporating different functional groups onto the MOF-808 backbone, urea hydrolysis, ammonium capture, and real-time ammonium sensing can be achieved in sequence.

1.3 References

- (1) *Drinking-water*. <https://www.who.int/news-room/fact-sheets/detail/drinking-water> (accessed 2022-10-21).
- (2) *Sanitation*. <https://www.who.int/news-room/fact-sheets/detail/sanitation> (accessed 2022-10-21).
- (3) Programme, U. N. E. *Sick Water?: The Central Role of Wastewater Management in Sustainable Development: A Rapid Response Assessment*; UNEP/Earthprint, 2010.
- (4) Panizza, M.; Cerisola, G. Direct And Mediated Anodic Oxidation of Organic Pollutants. *Chem. Rev.* **2009**, *109* (12), 6541–6569.
- (5) Radjenovic, J.; Sedlak, D. L. Challenges and Opportunities for Electrochemical Processes as Next-Generation Technologies for the Treatment of Contaminated Water. *Environ. Sci. Technol.* **2015**, *49* (19), 11292–11302.
- (6) Lin, K.; Marr, L. C. Aerosolization of Ebola Virus Surrogates in Wastewater Systems. *Environ. Sci. Technol.* **2017**, *51* (5), 2669–2675.
- (7) Zuccato, E.; Calamari, D.; Natangelo, M.; Fanelli, R. Presence of Therapeutic Drugs in the Environment. *The Lancet* **2000**, *355* (9217), 1789–1790.
- (8) Patel, M.; Kumar, R.; Kishor, K.; Mlsna, T.; Pittman, C. U.; Mohan, D. Pharmaceuticals of Emerging Concern in Aquatic Systems: Chemistry, Occurrence, Effects, and Removal Methods. *Chem. Rev.* **2019**, *119* (6), 3510–3673.
- (9) A. Cid, C.; Qu, Y.; R. Hoffmann, M. Design and Preliminary Implementation of Onsite Electrochemical Wastewater Treatment and Recycling Toilets for the Developing World. *Environ. Sci.: Water Res. Technol.* **2018**, *4* (10), 1439–1450.
- (10) Jasper, J. T.; Shafaat, O. S.; Hoffmann, M. R. Electrochemical Transformation of Trace Organic Contaminants in Latrine Wastewater. *Environ. Sci. Technol.* **2016**, *50* (18), 10198–10208.
- (11) Huang, X.; Qu, Y.; Cid, C. A.; Finke, C.; Hoffmann, M. R.; Lim, K.; Jiang, S. C. Electrochemical Disinfection of Toilet Wastewater Using Wastewater Electrolysis Cell. *Water Res.* **2016**, *92*, 164–172.
- (12) Chaplin, B. P. The Prospect of Electrochemical Technologies Advancing Worldwide Water Treatment. *Acc. Chem. Res.* **2019**, *52* (3), 596–604.
- (13) Shanthi, E.; Dutta, V.; Banerjee, A.; Chopra, K. L. Electrical and Optical Properties of Undoped and Antimony-doped Tin Oxide Films. *J. Appl. Phys.* **1980**, *51* (12), 6243–6251.
- (14) Elangovan, E.; Ramamurthi, K. A Study on Low Cost-High Conducting Fluorine and Antimony-Doped Tin Oxide Thin Films. *Appl. Surf. Sci.* **2005**, *249* (1), 183–196.
- (15) Zhuo, Q.; Deng, S.; Yang, B.; Huang, J.; Yu, G. Efficient Electrochemical Oxidation of Perfluorooctanoate Using a Ti/SnO₂-Sb-Bi Anode. *Environ. Sci. Technol.* **2011**, *45* (7), 2973–2979.
- (16) Zhuo, Q.; Wang, J.; Niu, J.; Yang, B.; Yang, Y. Electrochemical Oxidation of Perfluorooctane Sulfonate (PFOS) Substitute by Modified Boron Doped Diamond (BDD) Anodes. *Chem. Eng. J.* **2020**, *379*, 122280.
- (17) Christensen, P. A.; Attidekou, P. S.; Egdell, R. G.; Maneelok, S.; Manning, D. A. C.; Palgrave, R. Identification of the Mechanism of Electrocatalytic Ozone Generation on Ni/Sb-SnO₂. *J. Phys. Chem. C* **2017**, *121* (2), 1188–1199.

- (18) Yang, S. Y.; Kim, D.; Park, H. Shift of the Reactive Species in the Sb–SnO₂-Electrocatalyzed Inactivation of E. Coli and Degradation of Phenol: Effects of Nickel Doping and Electrolytes. *Environ. Sci. Technol.* **2014**, *48* (5), 2877–2884.
- (19) Henke, A. H.; Saunders, T. P.; Pedersen, J. A.; Hamers, R. J. Enhancing Electrochemical Efficiency of Hydroxyl Radical Formation on Diamond Electrodes by Functionalization with Hydrophobic Monolayers. *Langmuir* **2019**, *35* (6), 2153–2163.
- (20) Lesko, T. M.; Colussi, A. J.; Hoffmann, M. R. Hydrogen Isotope Effects and Mechanism of Aqueous Ozone and Peroxone Decompositions. *J. Am. Chem. Soc.* **2004**, *126* (13), 4432–4436.
- (21) Hong, H.-G.; Song, J.-O.; Na, H.; Kim, H.; Kim, K.-K.; Seong, T.-Y. Formation of Sb-Doped SnO₂ p-Type Ohmic Contact for Near-UV GaN -Based LEDs by a ClO Interlayer. *Electrochem. Solid-State Lett.* **2007**, *10* (9), H254.

APPLICATION OF HETEROJUNCTION NI-SB-SNO₂ ANODES FOR ELECTROCHEMICAL WATER TREATMENT

Zhang, Y.; Yang, Y.; Yang, S.; Quispe-Cardenas, E.; Hoffmann, M. R. Application of Heterojunction Ni-Sb-SnO₂ Anodes for Electrochemical Water Treatment. *ACS EST Eng.* **2021**, *1* (8), 1236-1245. <https://doi.org/10.1021/acsestengg.1c00122>.

2.1 Abstract

Electrochemical oxidation can be used for decentralized wastewater treatment without the addition of chemicals. Antimony-doped tin oxide (Sb-SnO₂: AT) provides a catalytic anode coating that is easily prepared at a relatively low cost. However, there is the potential of Sb leaching during use. To overcome this problem, a heterojunction anode is developed that uses an AT oxide layer as ohmic contact and a nickel-doped AT oxide layer (NAT) with a substantially lower Sb content as an outer catalytic layer (NAT/AT). The two-layer NAT/AT anode has significantly longer operational lifetimes, lower Sb leaching potential, and higher activities for free radical generation and ozone production than either layer when used alone. Based on experimental results in combination with theory, an anodic ozone activation pathway at the acidic electrode/electrolyte interface is identified as a key ·OH source coupled with direct ·OH production via water electrolysis. The NAT/AT anode outperforms commercial anodes (e.g., boron-doped diamond and IrO₂) for organic compound destruction and for microbial disinfection. One-log removal of carbamazepine (surface area-normalized first-order rate constant $k_{CBZ,SA} = 1.13 \times 10^{-3}$ m/s) and five-log inactivation of *E. coli* and MS2 virus is achieved within 60 s in synthetic electrolytes. Even though electrochemical efficiency is lower in the case of latrine wastewater treatment, the energy consumption (e.g., 3.9-14.0 kWh/m³) is low compared to previously reported values.

Keywords: Double-layer Ni-Sb-SnO₂ anodes, Anodic ozone activation, Organic compound degradation, Microbial disinfection, Wastewater treatment

2.2 Introduction

Electrochemical oxidation (EO) is useful for small-scale, decentralized wastewater treatment systems that do not require the addition of chemical reagents, but provides for fast reaction kinetics, modular treatment capacity, and easy modes of operation.^{1,2} EO redox systems are also suitable for treating recalcitrant chemical wastes and inactivating pathogens in concentrated wastewater streams.

In developing regions of the world, inadequate sanitation facilities and the continued practice of open defecation have led to the spread of water-borne diseases and millions of attributed deaths each year.³ In the built environment, viruses can survive in toilet wastewater and be transmitted via aerosols produced during flushing and aeration.⁴ Moreover, toilet wastewater can be a major sink of micro-pollutants such as pharmaceuticals and personal care products (PPCPs) as a significant amount of ingested pharmaceuticals is excreted either metabolized or unmetabolized through urine and fecal matter.^{5,6} In previous studies, EO wastewater treatment has been shown to be cost-effective for microbial disinfection and PPCPs removal in bench-top prototypes and full-scale applications.⁷⁻⁹

The chemical composition of the anodes and, to a lesser extent, the cathodes is a key factor that often controls the relative treatment efficiency and the overall energy consumption during electrochemical oxidation and reduction. Electrodes that do not depend on the use of platinum-group metal are essential in reducing capital and operational costs. Iridium oxide (IrO_2) and boron-doped diamond (BDD) electrodes are often used for chlorine evolution and free radical production, respectively. However, in the specific case of BDD electrodes, the high cost (e.g., \$7000/m²) of the material prohibits economical large-scale applications.¹⁰ As an alternative to Pt-group metal oxide anodes, sub-stoichiometric Ti_4O_7 coatings on Ti metal may provide a lower-cost alternative for the degradation of recalcitrant chemical contaminants. However, a limitation in the use of Ti_4O_7 coated anodes arises from a production process that requires the reduction of TiO_2 at high temperature in pure H_2 .^{12,13}

The antimony-doped tin oxide (AT: Sb-SnO_2) anodes are prepared by dip- or brush-coating methods with annealing at 400-600°C. They are often used under high anodic potentials to oxidize an array of chemical contaminants.^{14,15} Moreover, multiple metal precursors can be homogeneously blended into the precursor coating solutions to generate

metal-doped AT electrodes. Christensen *et al.*¹⁶ reported that nickel-doped AT (NAT: Ni-Sb-SnO₂) produced ozone (O₃) during electrolysis in an acidic electrolyte and then proposed that a NAT anode could be used to produce O₃ gas at lower DC voltages as an alternative to the high-voltage ozonator. Yang *et al.*¹⁷ used NAT anodes to electrochemically oxidize organic compounds in water (e.g., phenol) and reported that O₃ produced during electrolysis enhanced the oxidation of target compounds.

Hydroxyl radical ($\cdot\text{OH}$) is a key oxidant produced during oxygen evolution reaction (OER) in the absence of chloride. However, the reported current efficiency (CE) for $\cdot\text{OH}$ production using a boron-doped diamond electrode is <0.05%.¹⁸ The majority of the anodic current is applied toward achieving OER, resulting in a minimal contribution to the oxidation of target chemical species. However, a nickel-doped AT oxide electrode can oxidize water to O₃ along with $\cdot\text{OH}$ at high current density. Thus, *in situ* O₃ production provides an additional source of $\cdot\text{OH}$ due to O₃ transformation.¹⁹

Herein, we report on the development and application of a new heterojunction, SnO₂-based anode that minimizes Sb leaching, is durable, efficient for microbial disinfection, waste pharmaceutical products degradation, and for onsite human wastewater treatment. Experimental and computational methods are combined to provide a new mechanism for O₃ activation to $\cdot\text{OH}$ at the electrode/electrolyte interface.

2.3 Materials and Methods

Electrode preparation and physicochemical characterization. Three types of electrodes were prepared: electrodes containing a single-layer AT coating, a single-layer NAT coating, and a double-layer coating with a NAT layer on top of the base metal (i.e., Ti metal) AT coating (NAT/AT). Clean titanium (Ti) plates (2 cm × 3 cm) were etched in a 1:4 HF:HNO₃ solution for 1 min before use. Deposition of the metal oxide coatings on the Ti plate was achieved by dip-coating in aqueous precursor solutions followed by calcination. The precursor solution for AT contained 360 mM SnCl₄·5H₂O (98%, Aldrich) and 40 mM SbCl₃ (>99.0%, Aldrich), while precursor solution for NAT contained 360 mM SnCl₄·5H₂O, 15 mM SbCl₃, and 4 mM Ni(OCOCH₃)₂·4H₂O (98%, Aldrich). The Ti plate was dipped in the coating solution for 20 s, dried under room temperature, and annealed at 600°C for 10

min. This cycle was repeated until a desired mass loading level was attained, after which the plate was annealed at 600°C for 1.5 h. The mass loading level of the two single-layer electrodes was 1.3 mg/cm². For the heterojunction anode, NAT(1.3)/AT(1.3 mg/cm²) was used for activity evaluations and accelerated lifetime tests. NAT(0.6)/AT(0.6 mg/cm²) was prepared exclusively for accelerated lifetime testing. IrO₂ and BDD electrodes were purchased from Ecosan (China) and NeoCoat (Switzerland), respectively.

Physiochemical characterization of the prepared electrodes was obtained using a scanning electron microscope (SEM, Zeiss 1550 VP) equipped with an Oxford X-Max SDD X-ray energy dispersive spectrometer (EDS) system for elemental distribution.

Electrochemical characterization. All electrochemical tests were performed in an undivided electrolysis cell. An anode (6 cm²) was coupled to a stainless steel cathode (6 cm²) at a spacing of 5 mm. At the same spacing close to the anode, an Ag/AgCl reference electrode (BASI Inc.) was installed. Cyclic voltammetry (CV) and electrochemical impedance spectroscopy (EIS) were characterized using a Biologic VSP-300 potentiostat. CVs were measured in 100 mM sodium perchlorate (NaClO₄) solutions using a scan rate of 0.05 V/s. The uncompensated resistance (R_u) in relevant electrolytes was determined by the impedance method at 100 kHz with a 20 mV sine wave. All anodic potentials (E_a) were corrected by the product of current (i) and R_u drop using equation $E_a - iR_u$. EIS measurements were performed in aqueous solutions containing 350 mM K₃Fe(CN)₆, 350 mM K₄Fe(CN)₆, and 1.0 M KCl over the frequency range of 100 kHz to 0.1 Hz with a 10 mV sine wave.²⁰ Perchloric acid (HClO₄) or sodium hydroxide (NaOH) solutions were used to adjust pH.

Electrolysis and analytical methods. All tests were conducted at a constant current density of 10 mA/cm² in 25 mL solutions (specific surface area = 24 m²/m³). Both NAT/AT and NAT produced O₃ during electrolysis. The dissolved O₃ was measured using the indigo method.²¹ Headspace O₃ concentrations were determined using an ambient ozone monitor (Horiba APOA-360). For O₃ generation in NaCl solutions, malonic acid (MA) was added to selectively quench reactive chlorine species.²¹ Chlorine evolution (CER) rate measurements were performed in 30 mM NaCl solutions. Chlorine concentrations were measured by DPD (N,N-diethyl-p-phenylenediamine) reagent (Hach DPD Method 10102). Current efficiencies (η) for free chlorine and O₃ generation were calculated using the following equation:

$$\eta = \frac{nVF dC}{I dt}$$

where n is the electrons required to form one mole of Cl_2 from Cl^- ($n = 2$) or O_3 from O^{2-} ($n = 6$), V is the volume of electrolyte (25 mL), F is Faraday constant (96,485 C/mol), and I is the current (A). The mass transfer rate constant for NAT/AT was determined using the limiting current technique.²²

Benzoic acid (BA, 1 mM), nitrobenzene (NB, 1mM), phenol (Ph, 1 mM), and ibuprofen (IBP, 20 μM) were used as radical probes.²³ The substrates were quantified using high-performance liquid chromatography coupled with a UV detector (HPLC-UV). Carbamazepine, alone or in combination with four other common pharmaceutical products, was treated in both synthetic electrolyte solutions and human wastewater samples collected on campus. Parent pharmaceutical compound and transformation products were identified by an ultrahigh performance liquid chromatography system (Waters Acquity UPLC) coupled to a time-of-flight mass spectrometer (Waters Xevo GS-2 TOF). Metal (Sb and Ni) concentrations in electrolytes were quantified by inductively coupled plasma mass spectrometry (Thermo Scientific iCAP RQ ICP-MS). Details of analytical procedures are provided in [SI Text 2.S1](#).

E. coli was cultured in Luria-Bertani (LB) broth (BD Difco) and grown at 37°C for 15 h.⁹ The bacterial suspension was centrifuged at 5000 rcf for 5 min and resuspended in 30 mM NaClO_4 or 30 mM NaCl electrolyte solutions. The resulting microbial suspensions had concentrations of $\sim 10^9$ CFU/mL determined by optical density at 600 nm (OD_{600}).²⁴ The suspensions were subsequently used as bacterial stock solutions. For electrolysis, the freshly-prepared stock was seeded into the electrolyte to an approximate concentration of 10^5 - 10^6 CFU/mL, a value typically observed in environmental waters. Samples taken during experiments were spread evenly onto LB agar (BD Difco) plates. The plates were then incubated at 37°C for 15 h, after which colonies were counted to obtain concentrations. MS2 was also seeded into the electrolyte to reach 10^5 - 10^6 PFU/mL. Sample concentrations were determined using the double agar layer method.²⁵

Human wastewater was obtained from an electrochemical toilet prototype on the Caltech campus (Pasadena, CA). Prior to treatment, wastewater samples were filtered (0.45 μm) and spiked with pharmaceuticals, *E. coli.*, and MS2.

Theoretical modeling. A kinetic model containing 102 elementary reactions obtained from literature was developed using the chemical kinetics software package, Kintecus 6.80.²⁶ Unknown rate constants were estimated by fitting the model with experimental data (more details provided in [SI Text 2.S2](#)). The model was evaluated in both NaClO_4 and NaCl electrolytes to investigate the influence of chlorine species on O_3 and $\cdot\text{OH}$ generation and subsequent transformations.

2.4 Results and Discussion

Electrode characterization. Pristine SnO_2 is a wide bandgap ($E_{\text{bg}} = 3.6 \text{ eV}$) n-type semiconductor. Antimony is commonly used to increase its conductivity.^{27,28} However, leaching of Sb from AT anodes could be a concern for water treatment application for leaching levels greater than the WHO recommended drinking water quality guideline value of 20 ppb ($20 \mu\text{g L}^{-1}$).²⁹ Ni- and Sb- doping both increase the conductivity of SnO_2 and facilitate the production of ozone.^{17,30} Furthermore, Sb doping also increases the stability of Ni- SnO_2 , which, in the absence of Sb, rapidly deactivated at 2.7 V_{RHE} (potential versus reversible hydrogen electrode) within one minute ([Figure 2.S1](#)). Co-doping with Ni reduces the minimum required Sb doping level to 4 atom-%. As shown in [Figure 2.S2](#), the conductivity of NAT (4 atom-% Sb) is comparable to AT (10 atom-% Sb). However, NAT appears to deactivate faster than AT during accelerated lifetime tests ([Figure 2.S3](#)). This result is most likely due to slow electron transfer kinetics from NAT to the Ti substrate and to the formation of a passivation layer between the two phases. Given that AT has excellent electron shuttling capability to serve as an ohmic contact,³¹ and that NAT shows superior EO reactivity coupled with a lower potential for Sb leaching (*vide infra*), a heterojunction anode was constructed with NAT on top of AT coated on the Ti base-metal substrate.

A cross-sectional image of the resulting heterojunction NAT/AT electrode is shown in [Figure 2.1a](#). EDS point analysis reveals that Ni is well-dispersed throughout the NAT top

layer (**Figure 2.1b**), and the top NAT layer appears to have less Sb than the AT interlayer (**Figure 2.1c**).

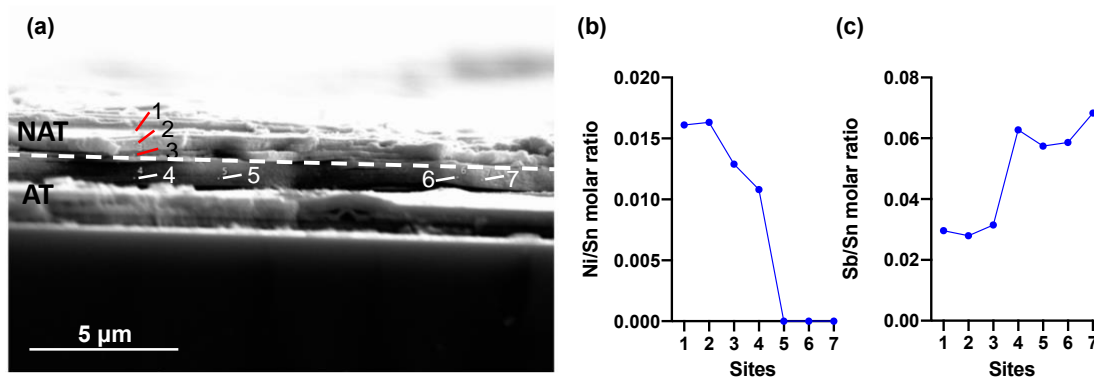


Figure 2.1 (a) Cross-sectional SEM image for NAT/AT. (b) Ni/Sn and (c) Sb/Sn molar ratios for the seven sample points.

Charge transfer resistance (R_{ct}) was determined using electrochemical impedance spectroscopy (EIS). The EIS spectra were fitted using the Randles equivalent circuit model, and the R_{ct} for AT was fitted to be 0.058 ohm, as shown in **Figure 2.2a**. In comparison to NAT (0.30 ohm), the heterojunction coating of NAT/AT (0.068 ohm) gave an order of magnitude reduction in R_{ct} and an increase in electron transfer kinetics.

Figure 2.2b shows cyclic voltammetry analysis of the three electrodes in 100 mM NaClO₄. Each of the electrodes had a high oxygen evolution potential at ~2.4 V, which is comparable to the state-of-the-art BDD and TiO_{2-x} electrodes for EO water treatment.¹¹ The electrochemically active surface areas (ECSA) were measured by a current charging method reported previously (**Figure 2.S4**).³² The slopes of the charging curves give capacitances (mF/cm²) that are proportional to the ECSA (**Figure 2.2c**). Dividing the capacitances by a general specific capacitance for metal oxide (0.04 mF/cm²)³² gives ECSA values for AT and NAT of 201 and 70 cm², respectively. NAT/AT with NAT built on a rough AT layer has an ECSA of 130 cm².

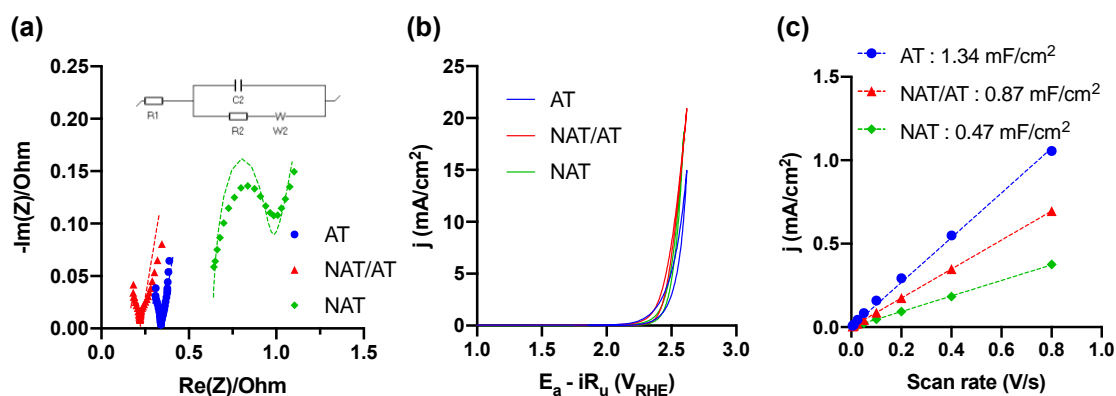


Figure 2.2 (a) EIS spectra, (b) cyclic voltammograms, and (c) charging currents as functions of scan rate by AT, NAT/AT, and NAT electrodes. Dashed lines in (a) represent fitting results based on a Randles circuit (inset).

The stability of anodes was assessed using accelerated lifetime tests based on electrolysis at a current density of 200 mA/cm² (Figure 2.S3). The results were then used to estimate the lifetime at lower operational current densities. The estimated lifetime at 10 mA/cm² of NAT/AT (5373 h) was significantly longer than that of AT (342 h) and NAT (260 h) alone. In order to establish a fair comparison, electrodes composed of NAT(0.6)/AT(0.6) were made with a 50% mass reduction of each layer to match the total 1.3 mg/cm² mass loading of a single layer each of AT and NAT. The reduced mass electrode formulation of NAT(0.6)/AT(0.6) produced a lifetime of 1156 h, which was still better than the AT and NAT electrodes alone. The lifetime of the bilayer NAT/AT electrode is significantly longer than those reported for either the NAT or AT electrodes (2-20 h at 12 mA/cm²).¹⁷

The leaching of metals during electrolysis was determined using ICP-MS (Figure 2.S5). The Sb concentrations found in the NaClO₄ electrolyte after 90 min electrolysis at 10 mA/cm² due to leaching from the AT and NAT/AT electrodes were 31 and 5 μg-Sb/L, respectively. The heterojunction structure of NAT/AT results in a lower level of Sb leaching or loss combined with the relatively high electrochemical activity of NAT.

Electrochemical production of chlorine and ozone. The electrochemical production of chlorine at a current density of 10 mA/cm² was quantified in 30 mM NaCl solutions.⁷ The AT electrode had a current efficiency (CE) of 50% (Figure 2.3a), which is similar to the

total chlorine production efficiency obtained with either IrO_2 or TiO_{2-x} anodes.^{33,34} Doping AT with Ni results in lower reactive chlorine evolution rates for NAT/AT and NAT electrodes (CE of 34% and 35%, respectively) but was compensated by O_3 production. The electrochemical production of O_3 on NAT requires a six-electron water oxidation reaction ($E^\circ = 1.51 \text{ V}_{\text{RHE}}$) that involves the combination of adsorbed oxygen species: O_2 is generated at surficial Ni sites and reacts with $\cdot\text{OH}$ produced from neighboring Sb- SnO_2 surficial sites to form $\cdot\text{HO}_3$, which is then converted into O_3 .^{16,35,36} The heterojunction NAT/AT electrode produces more O_3 than does the NAT electrode alone (i.e., the aqueous-phase $[\text{O}_3]$ increases faster on NAT/AT than on NAT, as shown in **Figure 2.3b**). This is probably because NAT/AT has a larger ECSA than NAT, promoting the interplay among adsorbed oxygen species.

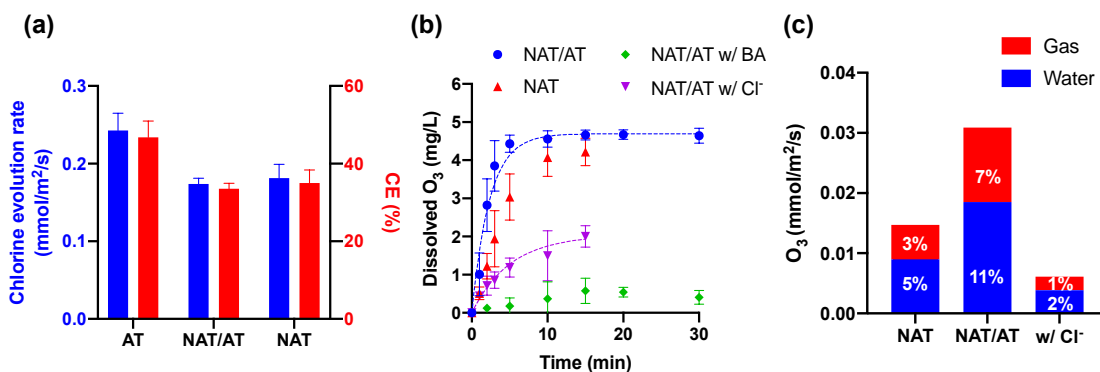


Figure 2.3 (a) Chlorine evolution rate and current efficiency measured in 30 mM NaCl electrolytes. (b) Dissolved O_3 detected in NaClO_4 electrolytes during electrolysis by NAT/AT and NAT. Test “w/ Cl⁻” was performed in 30 mM NaCl electrolyte. Test “w/ BA” was conducted in 30 mM NaClO_4 spiked with 1 mM BA. Dashed lines represent kinetic modeling results. (c) Overall ozone evolution rates for NAT in 100 mM NaClO_4 , and NAT/AT in 100 mM NaClO_4 and 30 mM NaCl. Current efficiencies were marked on the bar diagram. Anode surface area = 6 cm², current density = 10 mA/cm², electrolyte volume = 25 mL.

Ozone released to the headspace of the electrolysis cell was quantified using an online ozone monitor. Current efficiencies were calculated using the combined evolution rates in

both aqueous and gas phases. As shown in **Figure 2.3c**, higher current efficiencies for O₃ production were obtained using the NAT/AT electrode than single-layer NAT electrode (e.g., 18 vs. 8%). After 10 min of electrolysis, [O₃] reached a plateau value of ~4.7 mg/L for both the NAT and NAT/AT electrodes (**Figure 2.3b**). Gaseous O₃ evolution also reached a steady-state concentration (**Figure 2.S6**).

Ozone production in the presence of Cl⁻ was also investigated. Malonic acid was added to the water samples collected during electrolysis to mask free chlorine interference on dissolved O₃ measurement (**Figure 2.S7**). Results show that Cl⁻ inhibits O₃ production (**Figure 2.3b and 2.S6**).

The homogeneous reactions among O₃, Cl⁻, and free reactive chlorine can be considered to be negligible due to relatively slow reaction rates (e.g., $k_{O_3,Cl^-} = 3.0 \times 10^{-3} \text{ M}^{-1}\text{s}^{-1}$, $k_{O_3,HOCl} \cong 2.0 \times 10^{-3} \text{ M}^{-1}\text{s}^{-1}$, $k_{O_3,OCl^-} = 1.2 \times 10^2 \text{ M}^{-1}\text{s}^{-1}$) coupled with low [O₃].³⁷ Thus, the inhibitory impact of Cl⁻ on O₃ production is most likely due to the competition for active sites on the anode surface. Chloride competes for active surface sites that would normally initiate the OER, since the initial reaction steps involving Cl⁻ adsorption and subsequent electron transfer to the electrode surface are similar to the one-electron oxidation of OH⁻.^{38,39} In addition, Cl⁻ quenching by reaction with ·OH is also likely.³³ In 30 mM NaCl electrolyte solutions, ozone production and chlorine generation account for 4 and 38% of the overall current efficiency, respectively.

Direct and indirect pathways for radical production. Benzoic acid (BA) was used as a probe molecule to explore electrochemical free radical production since BA reacts readily with ·OH, O^{·-}, Cl^{·-}, and Cl₂^{·-}, but does not react readily with free chlorine and O₃.^{23,40} Since BA is unlikely to be oxidized by direct electron transfer to the electrode under the applied potential (**Figure 2.S8**),³⁴ BA oxidation in NaClO₄ solutions should occur by reaction with ·OH (e.g., $k_{BA,·OH} = 4.3 \times 10^9 \text{ M}^{-1}\text{s}^{-1}$). As shown in **Figure 2.4a**, the heterojunction NAT/AT electrode produced the fastest BA transformation rate, followed by the single-layer anodes, NAT and AT. Assuming pseudo-first-order kinetics, the rate constant for BA degradation by NAT/AT (normalized by specific surface area) was calculated to be $k_{BA,SA} = 2.83 \times 10^{-5} \text{ m/s}$ (**Figure 2.S9**), close to the mass transfer rate constant with stirring estimated by the current

limiting method ($k_{m,BA} = 3.31 \times 10^{-5}$ m/s, **Figure 2.S10**). The applied current (60 mA, above $I_{lim,BA}$) and the first-order exponential BA removal trend both indicate that BA degradation was under mass transport control during electrolysis.

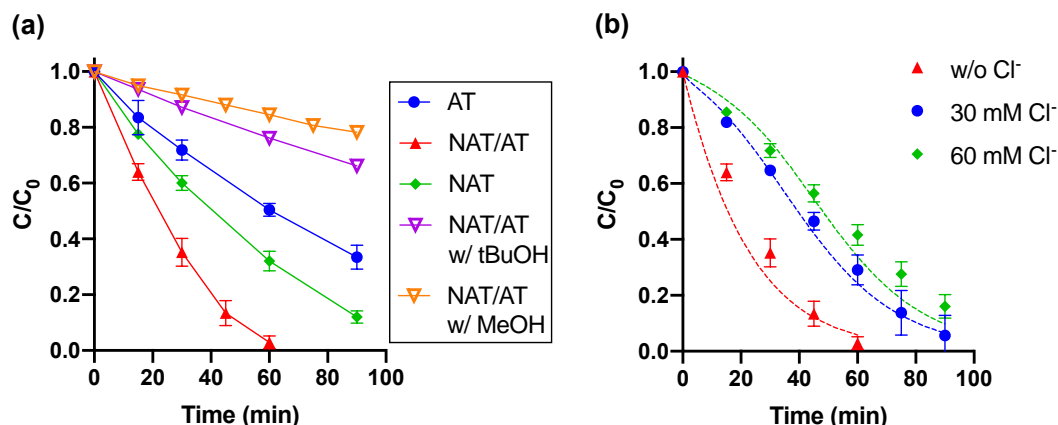


Figure 2.4 (a) Electrochemical oxidation of BA by AT, NAT/AT, and NAT electrodes in 30 mM NaClO₄ electrolytes in the presence or absence of 100 mM tBuOH or 100 mM MeOH. (b) Electrochemical oxidation of BA by NAT/AT in chloride-bearing electrolytes (30 and 60 mM NaCl). Dashed lines represent kinetic modeling results. Anode surface area = 6 cm², current density = 10 mA/cm², electrolyte volume = 25 mL.

Addition of the known $\cdot\text{OH}$ radical quenchers, tert-butanol (tBuOH, $k_{\cdot\text{OH}} = 6.0 \times 10^8 \text{ M}^{-1}\text{s}^{-1}$) and methanol (MeOH, $k_{\cdot\text{OH}} = 9.7 \times 10^8 \text{ M}^{-1}\text{s}^{-1}$), significantly retarded BA transformation kinetics (**Figure 2.4a**).⁴¹ MeOH, which is known to scavenge $\cdot\text{OH}$ on anode surfaces,⁴² slowed the oxidation of BA more than tBuOH. These results indicate that $\cdot\text{OH}$ radical-mediated oxidation within the electrical double layer close to the anode surface is the primary pathway for the electrochemical oxidation of BA.

Even though BA does not readily react with ozone at circum-neutral pH, as illustrated in **Figure 2.S11**, BA oxidation on NAT/AT and NAT anodes was found to be consistent with their respective O₃ production activity (**Figure 2.4a vs. 2.3c**). Furthermore, residual O₃ concentrations were very low during the electrochemical oxidation of BA (**Figure 2.3b**). These results suggest that either (1) O₃ production was inhibited by BA or (2) O₃ reacted with BA via a new path. In order to verify assumption (1), tBuOH, which has a similar $\cdot\text{OH}$

quenching activity to BA, was added during electrolysis using the NAT/AT anode. However, the dissolved $[O_3]$ detected in the presence of 100 mM tBuOH was found to be higher than that measured in the presence of 1 mM BA (**Figure 2.S12**). This result indicates that BA does not inhibit the electrochemical O_3 production via $\cdot OH$ quenching and thus is consistent with assumption (2) that BA reacts indirectly with the electrochemically produced O_3 .

The conversion of O_3 to $\cdot OH$ is facilitated either by catalysts, natural organic matter, or at high pH (≈ 11).^{19,42,43} A more plausible explanation for O_3 decomposition to $\cdot OH$ at pH close to the electrode surface must consider the micro-environment within the electrical double layer (EDL). Water splitting taking place at the anode rapidly lowers the pH within the EDL. We propose that acidic EDL facilitates the decomposition of O_3 to $\cdot OH$ in the presence of BA.

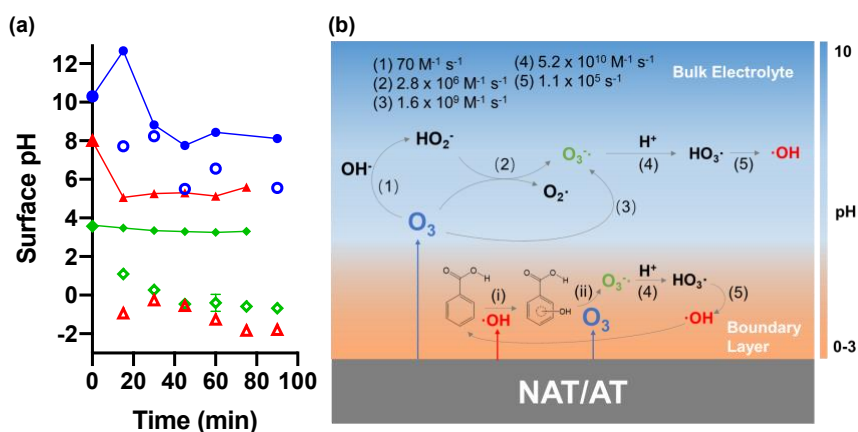


Figure 2.5 (a) Differences of pH values on the NAT/AT anode surface (hollow) and in the bulk electrolyte (solid). (b) Schematic illustration of two indirect pathways for the production of $\cdot OH$ from O_3 .

A micro pH probe (Thermo ScientificTM 8220BNWP, the diameter of the hemispherical probe tip is 2 mm) was used to measure the surficial pH of NAT/AT operated at 10 mA/cm^2 . The diffusion layer thickness was determined as ~ 27 and $270 \text{ }\mu\text{m}$ for stirred and static conditions, respectively (**Figure 2.S10**). These values are comparable to $10\text{-}100 \text{ }\mu\text{m}$ reported

on plate-type electrodes.^{11,22} The pH probe was placed ~ 500 μm above the anode surface. Even though this approach could not measure the pH within the diffusion layer, low surface pH (< 2) was still observed, even when the initial bulk pH was adjusted to 8 (**Figure 2.5a**). Note that rapid BA degradation was observed at initial pH of 4 and 8 (**Figure 2.S13**). We propose that BA first reacts with $\cdot\text{OH}$ via ring insertion forming an $\cdot\text{OH}$ -BA adduct as a reaction intermediate, which in turn reacts with O_3 to form hydroxybenzoic acid and ozonide ($\text{O}_3^{\cdot-}$). Thus, an acidic boundary layer favors the transformation of $\text{O}_3^{\cdot-}$ to $\cdot\text{OH}$ (reactions 4 and 5 in **Figure 2.5b**). This mechanism is supported by results presented in a previous study of $\text{O}_3 + \text{BA}$ reaction at pH 2.3, which also showed that hydroxybenzoic acid served as a reaction intermediate.⁴⁴ For BA degradation at pH 10 (**Figure 2.5a and 2.S13**), base-catalyzed O_3 activation (reaction 1 in **Figure 2.5b**) in the bulk electrolyte leads directly to $\cdot\text{OH}$ radical formation.

The efficacy of anodic O_3 activation depends on the structure of the target aromatic substrate. We note that anodic O_3 activation promoted the degradation of ibuprofen (IBP) but did not appear to impact the degradation of nitrobenzene (NB) and phenol (Ph) (**Figure 2.S14**). Upon initial examination, whether a compound is promoted by anodic O_3 activation cannot be simply explained using the electron-withdrawing/donating capacity of the ring substituent or the log K_{ow} value of the target compound (**Table 2.S1**). More investigation is needed to determine the structure-activity relationship.

Benzoic acid oxidation was also carried out in NaCl electrolytes to investigate the impact of Cl^- on radical speciation. Previous EO studies showed that Cl^- promotes BA degradation due to the production of $\text{Cl}\cdot$ and $\text{Cl}_2^{\cdot-}$ as reaction intermediates.^{33,45} However, we observed that Cl^- retards electrochemical BA oxidation on NAT/AT (**Figure 2.4b**) by competitively inhibiting O_3 production, limiting the anodic activation of O_3 . As a result, the lower $\cdot\text{OH}$ input offsets the positive effects due to $\text{Cl}\cdot$ and $\text{Cl}_2^{\cdot-}$.

Kinetic modeling. Kinetic models were developed to quantify reactive species generation at the surface of NAT/AT and help with the interpretation of experimental results. A total of 102 reactions were considered, including details of aqueous-phase O_3 chemistry (eqs. 58-69 of **Table 2.S2**), radical species $\text{O}_3^{\cdot-}$ reactions (eqs. 70-73 of **Table 2.S2**), and $\text{O}_2^{\cdot-}$ reactions (eqs. 74-81 of **Table 2.S2**).

To calibrate the kinetic model, zero-order reaction rates for electrochemical O₃ production (r_{O_3} , M/s) on NAT/AT (eq. 9 of **Table 2.S2**) in NaClO₄ and NaCl were obtained by fitting to experimental results for dissolved [O₃] as shown in **Figure 2.3b**. The steady-state concentrations of dissolved O₃ as predicted by the model fitting were 9.8×10^{-5} M (4.7 mg/L) in NaClO₄ solutions and 4.3×10^{-5} M (2.1 mg/L) in NaCl solutions. The predicted concentrations are consistent with the experimentally determined concentrations. Given the rates of electrochemical O₃ production, the rate of ·OH production, $r_{\cdot OH}$ (M/s), (eq. 10 of **Table 2.S2**) was subsequently calibrated using BA degradation kinetic data in NaClO₄, assuming that ·OH was the sole contributor to oxidation. Enhancements in BA oxidation via anodic O₃ activation (reactions i and ii in **Figure 2.5b**) were taken into account according to eqs. 97 and 101 of **Table 2.S2**.

For reactions in the NaCl electrolyte, the number of active sites and ·OH production rate were assumed to be the same as in the case of NaClO₄. However, the production rates of chlorine radical and free chlorine species were calibrated using BA oxidation data obtained in 30 mM NaCl solutions. For both NaClO₄ and NaCl electrolytes, the calibrated model successfully reproduced the experimentally observed transformation kinetics (red and blue lines in **Figure 2.4b**). All model fittings had $R^2 > 0.95$. A list of the fitted rate constants is presented in **Table 2.S3**.

The constrained model predicted a steady-state ·OH concentration, $[\cdot OH]_{ss}$, of 1.6×10^{-13} M in NaClO₄. This compares well with the value of 1.58×10^{-13} M obtained from BA degradation, as shown in **Figure 2.S9**. In addition, the kinetic model predicts slower BA removal rates with higher Cl⁻ concentrations. This latter result agrees well with the experimental results obtained for reactions in 60 mM NaCl solutions, as illustrated by the green line in **Figure 2.4b**.

Our validated kinetic model is then used for additional mechanistic insight into pathways for the EO of BA and for quantifying the relative contributions of the reactive species toward the overall oxidation of BA. The relative contributions from each of the radical species (·OH, O⁻, Cl⁻, and Cl₂⁻) reacting with BA were estimated by including only their independent reactions with BA in the model calculation (eqs. 97-100 of **Table 2.S2**). The anodic activation of O₃ was estimated by turning on and off ·OH production (eq. 10 of **Table 2.S2**).

In both electrolytes, model results show that the contribution to BA oxidation by $O\cdot^-$ was negligible due to its low steady-state concentration ($\sim 10^{-20}$ M) and its relatively slow bimolecular reaction rate constant with BA ($k_{BA,O\cdot^-} = 4.00 \times 10^7 \text{ M}^{-1}\text{s}^{-1}$). Model results show that $\cdot\text{OH}$ contributes the most to the degradation of BA in NaClO_4 , accounting for close to 100% of total removal in which $\sim 32\%$ of total $\cdot\text{OH}$ is produced from the anodic activation of O_3 . In NaCl solutions, $\cdot\text{OH}$ contributes $>95\%$ of total BA removal, while only $\sim 17\%$ of $\cdot\text{OH}$ comes from the anodic activation of O_3 (**Figure 2.S15**). Furthermore, the contributions of $\text{Cl}\cdot$ and $\text{Cl}_2\cdot^-$ toward BA oxidation in NaCl account for $<5\%$ and $\ll 1\%$ to the total degradation of BA, respectively.

Environmental applications. An optimized NAT/AT anode was tested for the oxidative removal of several pharmaceutical compounds. Carbamazepine (CBZ, $30 \mu\text{M}$) was used as a model compound due to its high persistence in the advanced oxidation processes.⁴⁶ As shown in **Figure 2.6a**, the complete electrochemical oxidation of $30 \mu\text{M}$ CBZ on a NAT/AT anode is achieved in less than 60 s in NaClO_4 electrolytes. The approximate rate constant for CBZ degradation (normalized by specific surface area) was calculated to be $k_{\text{CBZ,SA}} = 1.13 \times 10^{-3} \text{ m/s}$ (**Figure 2.S16**). The high EO activity obtained using a NAT/AT anode clearly outperforms the AT, IrO_2 , and BDD anodes (70-80% removal in 5 min) operated at identical current densities of 10 mA/cm^2 . The higher EO activity of NAT/AT is ascribed to the higher yields of $\cdot\text{OH}$ that are obtained via water electrolysis coupled with the direct oxidation of CBZ by electrochemically produced O_3 . In the latter case, 1-(2-benzaldehyde)-4-hydro-(1H,3H)-quinazoline-2-one (BQM) is detected as the direct ozonation product (**Table 2.S4**).⁴⁷

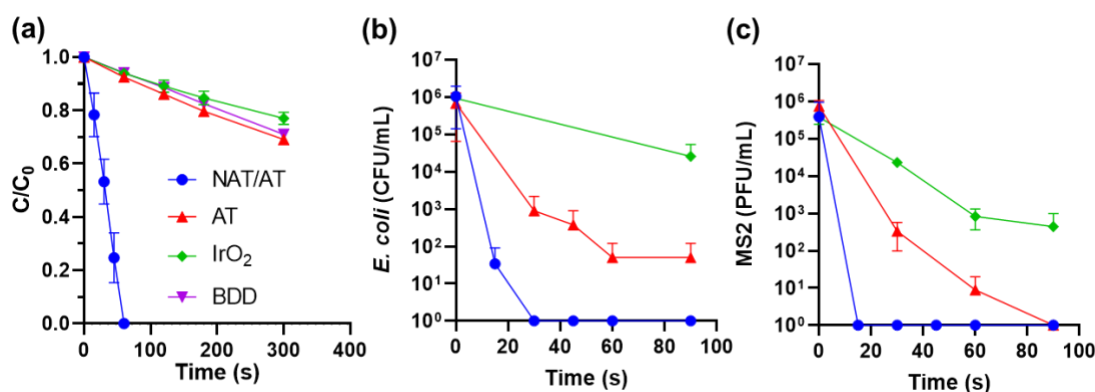


Figure 2.6 Removal of (a) 30 μM carbamazepine (CBZ) and inactivation of (b) *E. coli* and (c) MS2 by different electrodes in 30 mM NaClO_4 electrolytes. Anode surface area = 6 cm^2 , current density = 10 mA/cm^2 , electrolyte volume = 25 mL.

Degradation of CBZ is also obtained via EO in NaCl electrolytes. However, CBZ appears to be biphasic with fast oxidation over the first 15s followed by a slower rate, as shown in [Figure 2.S17a](#). Even though O_3 was generated at a slower rate, the apparent faster removal during the first 15 s phase in NaCl solutions are most likely due to reactions of CBZ with radical species such as $\text{Cl}_2\cdot^-$. Accelerated CBZ removal rates in electrolytes containing Cl^- were reported by Chiron *et al.*⁴⁸ They estimated a rate constant for $\text{CBZ} + \text{Cl}_2\cdot^-$ of $k = 2.6 \times 10^9 \text{ M}^{-1}\text{s}^{-1}$ to explain a faster CBZ EO rate in the presence of Cl^- . In this case, due to the generation of chlorine radicals, similar CBZ removal kinetics were observed at all four tested electrodes (NAT/AT, AT, IrO_2 , and BDD), with IrO_2 being slightly faster than the other three. Complete oxidation of 30 μM CBZ can be achieved in less than 5 min ([Figure 2.S17b](#)). In addition to BQM, four other transformation products of CBZ were detected at NAT/AT in NaCl solutions ([Table 2.S4](#)). These products result from chlorine-mediated oxidation, as reported for the EO of CBZ using IrO_2 -based anodes.⁸ Overall, these results demonstrated the superior performance of NAT/AT both in the absence and presence of Cl^- and thus its potential applicability in removing trace organic contaminants in wastewater streams where $[\text{Cl}^-]$ is low (e.g., primary and secondary effluent, typical $[\text{Cl}^-] = 1\text{-}10 \text{ mM}$ ⁴⁹).

Electrochemical disinfection using a NAT/AT anode was explored in NaClO_4 electrolytes ([Figure 2.6b and c](#)) using *E. coli* and coliphage MS2 as surrogates for bacteria

and viruses.⁹ With EO on NAT/AT, 5- \log_{10} reductions in the number of *E. coli* and MS2 are obtained in less than 30 s. Most likely, electrochemically generated O_3 is the primary driving force for disinfection on NAT/AT anodes. Moreover, when Cl^- is present, EO on NAT/AT resulted in faster disinfection (**Figure 2.S17c and d**) due to the co-generation of ozone and reactive chlorine species.

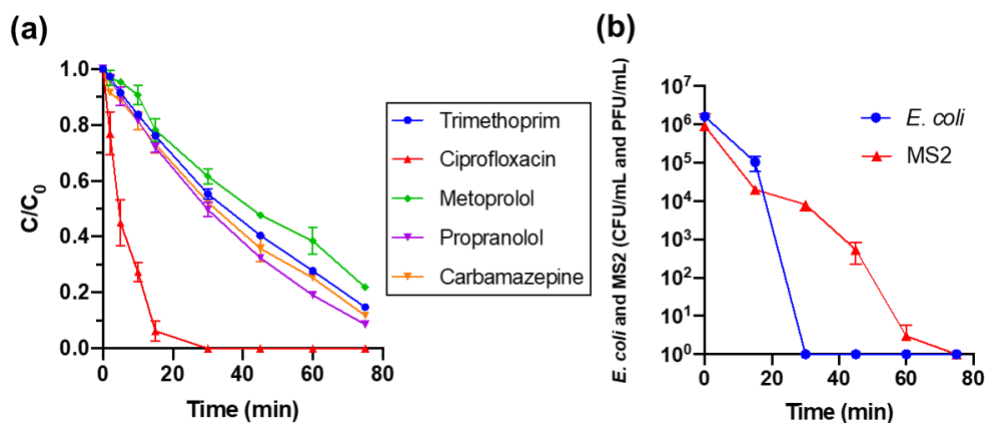


Figure 2.7 Electrochemical oxidation by NAT/AT of (a) pharmaceuticals (10 μ M each) and (b) *E. coli* and MS2 spiked into latrine wastewater. Anode surface area = 6 cm^2 , current density = 10 mA/cm^2 , wastewater volume = 25 mL.

The performance of NAT/AT on pharmaceutical product removal and disinfection was further explored during the treatment of latrine wastewater. Five representative pharmaceuticals, which were frequently reported to be present in the wastewater treatment plant effluents,⁶ were spiked in latrine wastewater, which was collected on the Caltech campus. The chemical composition, COD removal, and ammonium-N removal of the wastewater are given in **Table 2.S5**. As shown in **Figure 2.7a**, due to the high background COD of the wastewater (300 mg/L) and NH_4^+ (80 mM), degradation of CBZ and the other pharmaceuticals is slower due to the competitive consumption of the electrochemically-produced oxidants. The half-life for CBZ is reduced from 30 s in $NaClO_4$ to approximately 30 min in latrine wastewater. Slower disinfection kinetics were also observed during tests using latrine wastewater (**Figure 2.7b**), where the times required for 5- \log_{10} reductions of *E.*

coli and MS2 were <30 and 60 min, respectively. However, the performance of the NAT/AT anodes is better than the IrO₂-based electrodes used in our previous reports (e.g., $t_{1/2} = 75$ min for CBZ) while 5-log₁₀ reductions in *E. coli* and MS2 numbers were obtained at 10 and 60 min, respectively, since our initial *E. coli* and MS2 concentrations are ~1-log₁₀ higher.^{8,9} The energy consumption required to achieve 1-log₁₀ removal of pharmaceuticals and 5-log₁₀ reductions in the number of target pathogens in latrine wastewater ranges from 3.9 to 14 kWh/m³ (Table 2.S6).

The formation of disinfection byproducts (DBPs) during EO treatment of latrine wastewater was also investigated (Figure 2.S18). The total concentrations of trihalomethanes (THMs) and haloacetic acids (HAAs) after 90 min of electrolysis were 0.007 and 65 µg/L, respectively. These values are below or close to the EPA drinking water limit (THMs 80, HAAs 60 µg/L), though the treated effluent is not for potable reuse. Chloroform was detected as the only THM, while mono- and di-chloroacetic acids were the primary HAAs. Chlorate (ClO₃⁻) and perchlorate (ClO₄⁻) concentrations after 90 min of electrolysis were 1.7 and 0.16 mM, respectively. Overall, lower concentrations of ClO₃⁻ (1.7 mM) and ClO₄⁻ (0.16 mM) were observed at 90 min electrolysis on NAT/AT anodes compared to BDD ([ClO₃⁻]_{90 min} = 5 mM, [ClO₄⁻]_{90 min} = 0.5 mM) operated at the same current density and [electrode area]/[electrolyte volume] ratio by our group.³⁴ The minimum DBP formation observed in this study is because pathogens and pharmaceuticals were readily removed before the chlorination breakpoint. The dominant reactive chlorine species were chloramines, which have lower DBP formation potentials than free chlorine.⁵⁰ The THMs and HAAs could also be readily eliminated by O₃.⁵¹

2.5 Conclusions

In summary, the NAT/AT anodes are durable with high reactivities for chlorine, ozone, and ·OH production. They are cost-effective for treating pharmaceutical compounds and pathogens in electrolyte solutions and latrine wastewater. Scaled-up demonstrations of EO treatment units using this novel electrode for decentralized wastewater treatment systems are currently underway. The anodic O₃ activation mechanism presented in this study lays the groundwork for developing electrochemically assisted ozonation processes.

2.6 Acknowledgments

This research was supported by an investment grant made by the Bill and Melinda Gates Foundation (INV-003227). We are grateful to our program officers, Dr. Carl Hensman and Dr. Doulaye Kone, for their suggestions and guidance. We also thank Dr. Yuanlong Huang for help with headspace ozone measurements and Dr. Nathan Dalleska for help on sample analysis.

2.7 References

- (1) Panizza, M.; Cerisola, G. Direct And Mediated Anodic Oxidation of Organic Pollutants. *Chem. Rev.* **2009**, *109* (12), 6541–6569.
- (2) Radjenovic, J.; Sedlak, D. L. Challenges and Opportunities for Electrochemical Processes as Next-Generation Technologies for the Treatment of Contaminated Water. *Environ. Sci. Technol.* **2015**, *49* (19), 11292–11302.
- (3) Programme, U. N. E. *Sick Water?: The Central Role of Wastewater Management in Sustainable Development : A Rapid Response Assessment*; UNEP/Earthprint, 2010.
- (4) Lin, K.; Marr, L. C. Aerosolization of Ebola Virus Surrogates in Wastewater Systems. *Environ. Sci. Technol.* **2017**, *51* (5), 2669–2675.
- (5) Zuccato, E.; Calamari, D.; Natangelo, M.; Fanelli, R. Presence of Therapeutic Drugs in the Environment. *Lancet* **2000**, *355* (9217), 1789–1790.
- (6) Patel, M.; Kumar, R.; Kishor, K.; Mlsna, T.; Pittman, C. U.; Mohan, D. Pharmaceuticals of Emerging Concern in Aquatic Systems: Chemistry, Occurrence, Effects, and Removal Methods. *Chem. Rev.* **2019**, *119* (6), 3510–3673.
- (7) A. Cid, C.; Qu, Y.; R. Hoffmann, M. Design and Preliminary Implementation of Onsite Electrochemical Wastewater Treatment and Recycling Toilets for the Developing World. *Environ. Sci.: Water Res. Technol.* **2018**, *4* (10), 1439–1450.
- (8) Jasper, J. T.; Shafaat, O. S.; Hoffmann, M. R. Electrochemical Transformation of Trace Organic Contaminants in Latrine Wastewater. *Environ. Sci. Technol.* **2016**, *50* (18), 10198–10208.
- (9) Huang, X.; Qu, Y.; Cid, C. A.; Finke, C.; Hoffmann, M. R.; Lim, K.; Jiang, S. C. Electrochemical Disinfection of Toilet Wastewater Using Wastewater Electrolysis Cell. *Water Res.* **2016**, *92*, 164–172.
- (10) Chaplin, B. P. The Prospect of Electrochemical Technologies Advancing Worldwide Water Treatment. *Acc. Chem. Res.* **2019**, *52* (3), 596–604.
- (11) Trellu, C.; Chaplin, B. P.; Coetsier, C.; Esmilaire, R.; Cerneaux, S.; Causserand, C.; Cretin, M. Electro-Oxidation of Organic Pollutants by Reactive Electrochemical Membranes. *Chemosphere* **2018**, *208*, 159–175.
- (12) Nayak, S.; Chaplin, B. P. Fabrication and Characterization of Porous, Conductive, Monolithic Ti₄O₇ Electrodes. *Electrochim. Acta* **2018**, *263*, 299–310.

- (13) Radjenovic, J.; Duinslaeger, N.; Avval, S. S.; Chaplin, B. P. Facing the Challenge of Poly- and Perfluoroalkyl Substances in Water: Is Electrochemical Oxidation the Answer? *Environ. Sci. Technol.* **2020**, *54* (23), 14815–14829.
- (14) Zhuo, Q.; Deng, S.; Yang, B.; Huang, J.; Yu, G. Efficient Electrochemical Oxidation of Perfluorooctanoate Using a Ti/SnO₂-Sb-Bi Anode. *Environ. Sci. Technol.* **2011**, *45* (7), 2973–2979.
- (15) Zhuo, Q.; Wang, J.; Niu, J.; Yang, B.; Yang, Y. Electrochemical Oxidation of Perfluorooctane Sulfonate (PFOS) Substitute by Modified Boron Doped Diamond (BDD) Anodes. *Chem. Eng. J.* **2020**, *379*, 122280.
- (16) Christensen, P. A.; Attidekou, P. S.; Egdell, R. G.; Maneelok, S.; Manning, D. A. C.; Palgrave, R. Identification of the Mechanism of Electrocatalytic Ozone Generation on Ni/Sb-SnO₂. *J. Phys. Chem. C* **2017**, *121* (2), 1188–1199.
- (17) Yang, S. Y.; Kim, D.; Park, H. Shift of the Reactive Species in the Sb-SnO₂-Electrocatalyzed Inactivation of E. Coli and Degradation of Phenol: Effects of Nickel Doping and Electrolytes. *Environ. Sci. Technol.* **2014**, *48* (5), 2877–2884.
- (18) Henke, A. H.; Saunders, T. P.; Pedersen, J. A.; Hamers, R. J. Enhancing Electrochemical Efficiency of Hydroxyl Radical Formation on Diamond Electrodes by Functionalization with Hydrophobic Monolayers. *Langmuir* **2019**, *35* (6), 2153–2163.
- (19) Lesko, T. M.; Colussi, A. J.; Hoffmann, M. R. Hydrogen Isotope Effects and Mechanism of Aqueous Ozone and Peroxone Decompositions. *J. Am. Chem. Soc.* **2004**, *126* (13), 4432–4436.
- (20) Yang, Y.; Kao, L. C.; Liu, Y.; Sun, K.; Yu, H.; Guo, J.; Liou, S. Y. H.; Hoffmann, M. R. Cobalt-Doped Black TiO₂ Nanotube Array as a Stable Anode for Oxygen Evolution and Electrochemical Wastewater Treatment. *ACS Catal.* **2018**, *8* (5), 4278–4287.
- (21) Bader, H.; Hoigné, J. Determination of Ozone in Water by the Indigo Method. *Water Res.* **1981**, *15* (4), 449–456.
- (22) Cañizares, P.; García-Gómez, J.; Fernández de Marcos, I.; Rodrigo, M. A.; Lobato, J. Measurement of Mass-Transfer Coefficients by an Electrochemical Technique. *J. Chem. Educ.* **2006**, *83* (8), 1204.
- (23) Fang, J.; Fu, Y.; Shang, C. The Roles of Reactive Species in Micropollutant Degradation in the UV/Free Chlorine System. *Environ. Sci. Technol.* **2014**, *48* (3), 1859–1868.
- (24) Volkmer, B.; Heinemann, M. Condition-Dependent Cell Volume and Concentration of Escherichia Coli to Facilitate Data Conversion for Systems Biology Modeling. *PLoS One* **2011**, *6* (7).
- (25) *Bacteriophages: Methods and Protocols, Volume 1: Isolation, Characterization, and Interactions*; Clokie, M. R. J., Kropinski, A., Eds.; Methods in Molecular Biology; Humana Press, 2009.
- (26) Ianni, J. C., *Kintecus*, Windows Version 6.80. www.kintecus.com.
- (27) Shanthi, E.; Dutta, V.; Banerjee, A.; Chopra, K. L. Electrical and Optical Properties of Undoped and Antimony-doped Tin Oxide Films. *J. Appl. Phys.* **1980**, *51* (12), 6243–6251.
- (28) Elangovan, E.; Ramamurthi, K. A Study on Low Cost-High Conducting Fluorine and Antimony-Doped Tin Oxide Thin Films. *Appl. Surf. Sci.* **2005**, *249* (1), 183–196.

- (29) WHO 2003. Ammonia in drinking-water. Background document for preparation of WHO Guidelines for drinking-water quality. Geneva, World Health Organization (WHO/SDE/WSH/03.04/1).
- (30) Azam, A.; Ahmed, A. S.; Ansari, M. S.; Shafeeq M, M.; Naqvi, A. H. Study of Electrical Properties of Nickel Doped SnO₂ Ceramic Nanoparticles. *J. Alloys Compd.* **2010**, *506* (1), 237–242.
- (31) Hong, H.-G.; Song, J.-O.; Na, H.; Kim, H.; Kim, K.-K.; Seong, T.-Y. Formation of Sb-Doped SnO₂ p-Type Ohmic Contact for Near-UV GaN -Based LEDs by a ClO Interlayer. *Electrochem. Solid-State Lett.* **2007**, *10* (9), H254.
- (32) McCrory, C. C. L.; Jung, S.; Peters, J. C.; Jaramillo, T. F. Benchmarking Heterogeneous Electrocatalysts for the Oxygen Evolution Reaction. *J. Am. Chem. Soc.* **2013**, *135* (45), 16977–16987.
- (33) Yang, Y.; Shin, J.; Jasper, J. T.; Hoffmann, M. R. Multilayer Heterojunction Anodes for Saline Wastewater Treatment: Design Strategies and Reactive Species Generation Mechanisms. *Environ. Sci. Technol.* **2016**, *50* (16), 8780–8787.
- (34) Yang, Y.; Hoffmann, M. R. Synthesis and Stabilization of Blue-Black TiO₂ Nanotube Arrays for Electrochemical Oxidant Generation and Wastewater Treatment. *Environ. Sci. Technol.* **2016**, *50* (21), 11888–11894.
- (35) Christensen, P. A.; Yonar, T.; Zakaria, K. The Electrochemical Generation of Ozone: A Review. *Ozone: Sci. Eng.* **2013**, *35* (3), 149–167.
- (36) Wang, Y.-H.; Chen, Q.-Y. Anodic Materials for Electrocatalytic Ozone Generation. *Int. J. of Electrochem.* **2013**, *2013*, e128248.
- (37) Hoigné, J.; Bader, H.; Haag, W. R.; Staehelin, J. Rate Constants of Reactions of Ozone with Organic and Inorganic Compounds in Water—III. Inorganic Compounds and Radicals. *Water Res.* **1985**, *19* (8), 993–1004.
- (38) Trasatti, S. Progress in the Understanding of the Mechanism of Chlorine Evolution at Oxide Electrodes. *Electrochim. Acta* **1987**, *32* (3), 369–382.
- (39) Trasatti, S. Electrocatalysis in the Anodic Evolution of Oxygen and Chlorine. *Electrochim. Acta* **1984**, *29* (11), 1503–1512.
- (40) Hoigné, J.; Bader, H. Rate Constants of Reactions of Ozone with Organic and Inorganic Compounds in Water—I: Non-Dissociating Organic Compounds. *Water Res.* **1983**, *17* (2), 173–183.
- (41) Buxton, G. V.; Greenstock, C. L.; Helman, W. P.; Ross, A. B. Critical Review of Rate Constants for Reactions of Hydrated Electrons, Hydrogen Atoms and Hydroxyl Radicals ($\cdot\text{OH}/\cdot\text{O}^-$ in Aqueous Solution. *J. Phys. Chem. Ref. Data* **1988**, *17* (2), 513–886.
- (42) Yu, G.; Wang, Y.; Cao, H.; Zhao, H.; Xie, Y. Reactive Oxygen Species and Catalytic Active Sites in Heterogeneous Catalytic Ozonation for Water Purification. *Environ. Sci. Technol.* **2020**, *54* (10), 5931–5946.
- (43) Crittenden, J. C.; Trussell, R. R.; Hand, D. W.; Howe, K. J.; Tchobanoglous, G. *MWH's Water Treatment: Principles and Design*; John Wiley & Sons, 2012.
- (44) Huang, X.; Li, X.; Pan, B.; Li, H.; Zhang, Y.; Xie, B. Self-Enhanced Ozonation of Benzoic Acid at Acidic PHs. *Water Res.* **2015**, *73*, 9–16.

- (45) Yang, S.; Fernando, S.; Holsen, T. M.; Yang, Y. Inhibition of Perchlorate Formation during the Electrochemical Oxidation of Perfluoroalkyl Acid in Groundwater. *Environ. Sci. Technol. Lett.* **2019**, *6* (12), 775–780.
- (46) Wang, W.-L.; Wu, Q.-Y.; Huang, N.; Wang, T.; Hu, H.-Y. Synergistic Effect between UV and Chlorine (UV/Chlorine) on the Degradation of Carbamazepine: Influence Factors and Radical Species. *Water Res.* **2016**, *98*, 190–198.
- (47) McDowell, D. C.; Huber, M. M.; Wagner, M.; von Gunten, U.; Ternes, T. A. Ozonation of Carbamazepine in Drinking Water: Identification and Kinetic Study of Major Oxidation Products. *Environ. Sci. Technol.* **2005**, *39* (20), 8014–8022.
- (48) Chiron, S.; Minero, C.; Vione, D. Photodegradation Processes of the Antiepileptic Drug Carbamazepine, Relevant To Estuarine Waters. *Environ. Sci. Technol.* **2006**, *40* (19), 5977–5983.
- (49) Pérez, G.; Gómez, P.; Ibañez, R.; Ortiz, I.; Urriaga, A. M. Electrochemical Disinfection of Secondary Wastewater Treatment Plant (WWTP) Effluent. *Water Sci. Technol.* **2010**, *62* (4), 892–897.
- (50) Bougeard, C. M. M.; Goslan, E. H.; Jefferson, B.; Parsons, S. A. Comparison of the Disinfection By-Product Formation Potential of Treated Waters Exposed to Chlorine and Monochloramine. *Water Res.* **2010**, *44* (3), 729–740.
- (51) Mohd Zainudin, F.; Abu Hasan, H.; Sheikh Abdullah, S. R. An Overview of the Technology Used to Remove Trihalomethane (THM), Trihalomethane Precursors, and Trihalomethane Formation Potential (THMFP) from Water and Wastewater. *J. Ind. Eng. Chem.* **2018**, *57*, 1–14.

2.8 Supporting Information

Text 2.S1 Analytical methods.

Benzoic acid (BA), nitrobenzene (NB), and phenol (Ph) were quantified by high-performance liquid chromatography (HPLC) equipped with an XDB-Phenyl column (Agilent, 2.1 × 50 mm, 5 μm particles) at 226 and 250 nm. The eluent had a flow rate of 0.5 mL/min and consisted of 10% acetonitrile (ACN) and 90% water with 0.1% formic acid.

Pharmaceutical degradation was analyzed using HPLC with an XDB-C18 column (Agilent, 2.1 × 50 mm, 3.5 μm particles), the eluent flowed at 0.5 mL/min and consisted of ACN and water with 0.1% formic acid. A gradient was used to resolve peaks: 0 min, 5% ACN; 0.6 min, 5% ACN; 9.6 min, 95% ACN; 10.5 min, 95% ACN; 10.8 min, 5% ACN; 15 min, 5% ACN.

Model compound transformation products were identified using an ultrahigh performance liquid chromatography system (Waters Acquity UPLC) with an Acquity BEH C18 column (2.1 × 50 mm, 1.7 μm particles) coupled to a time-of-flight mass spectrometer

(Waters Xevo GS-2 TOF). Eluent consisting of ACN and water with 0.1% formic acid flowed at 0.5 mL/min. The gradient was: 0 min, 5% ACN; 0.2 min, 5% ACN; 3.2 min, 95% ACN; 3.5 min, 95% ACN; 3.6 min, 5% ACN; 5 min, 5% ACN. Conditions used for mass spectrometer were: carbamazepine (CBZ) – positive electrospray ionization (ESI+) in resolution mode, capillary voltage 0.2 kV; ibuprofen (IBP) – negative electrospray ionization (ESI-) in resolution mode, capillary voltage 1.0 kV. Cone voltage 50 V, source offset 80 V, source temperature 120°C, desolvation temperature 400°C, cone gas 40 L/h, desolvation gas 800 L/h, 0.3 s scan time in continuum mode, collision energy 1.0 eV, and second acquisition channel collision energy scanned from 0 to 30 eV. A leucine lock-mass was used to correct for accurate mass values.

Trihalomethanes (THMs) and haloacetic acids (HAAs) were extracted using a previously reported method.¹ Briefly, THMs were extracted in pentane and collected after centrifugation (5000 rpm, 5 min). HAAs (1 mL water sample) were extracted in 2 mL methyl *tert*-butyl ether (MTBE) following adjustment of pH (0.1 mL concentrated sulfuric acid) and ionic strength (0.5 g sodium sulfate). Sample methylation was completed with acidic methanol (1 mL 10% sulfuric acid in methanol) at 50°C for 2 hours. Formed HAA-esters were cleaned using 10% sodium sulfate in water (4 mL), and the upper ether layer was collected for analysis.

THMs and HAAs extracts were analyzed by gas chromatography equipped with an electron capture detector (GC/ECD, Agilent 7890). Helium was used as a detector makeup gas in constant makeup mode at 30 mL/min. Separation was performed on a 30 m Rxi-5ms column (0.25 mm i.d., 0.25 µm film thickness, RESTEK). Helium was used as the carrier gas in constant flow mode at 1 mL/min. For THMs, the oven was initially set to 30°C (hold for 2 min), then programmed as follows: 5°C/min to 50°C (hold for 2 min), 35°C/min to 150°C (hold for 5 min), 25°C/min to 185°C and hold for 5 min. For HAAs, the oven was initially set to 40°C (hold for 10 min), then ramped as following: 2.5°C/min to 65°C, then 10°C/min to 85°C, then 20°C/min to 205°C and hold for 7 min. The injector temperature was set to 200°C for both methods.

Metal leaching (Sb, Ni, Sn, Ti) from anodes was analyzed by an Inductively Coupled Plasma Mass Spectrometry (Thermo Scientific, iCAP™ RQ ICP-MS). Samples were first

aerosolized by a nebulizer and then introduced into a radiofrequency Argon plasma, causing atomization and ionization to be separated based on their mass-to-charge ratio (m/z ratio) by a single quadrupole mass spectrometer. Experiments were performed using acid-washed and air-dried glass beakers (nitric acid optima grade) using 40 mL NaClO_4 (100 mM) as the electrolyte solution with a current density of 10 mA/cm^2 . The solution was mixed continuously during the EC experiment using clean magnetic stirrers (experiment time 90 min), and samples were collected using acid-washed pipette tips and microcentrifuge tubes (using 10% nitric acid). Samples were diluted using 2% optima-grade nitric acid and spiked with 1 mg/L internal standard (Yttrium, Scandium, and Cerium) for quality assurance and quality control (QA/QC). The lower limit of quantification (LOQ) was 10 ng/L based on the background levels of the compounds. Calibration standards and instrument and method blanks (2% nitric acid and Milli-Q water used to prepare electrolyte, respectively) were injected to validate experimental conditions and determine background levels. Finally, a standard was reinjected during the sequence to validate the instrument response. A calibration curve with an $R > 0.9998$ was used to determine the metal concentrations in all replicates.

Text 2.S2 Kinetic modeling.

Kinetic modeling was performed using the chemical kinetics software Kintecus 6.80.² A total of 102 elementary reactions were included in the model. pH was set to 2 in all fitting scenarios. Rate constants were obtained from literature or calibrated from experimental and fitting results. The reactions implemented in the model were provided below in Table 2.S1.

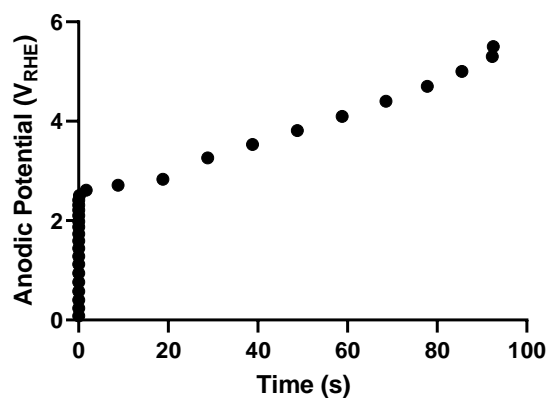


Figure 2.S1 Stability test of Ni (1 atom-%)-SnO₂ electrode at 10 mA/cm² in 100 mM NaClO₄.

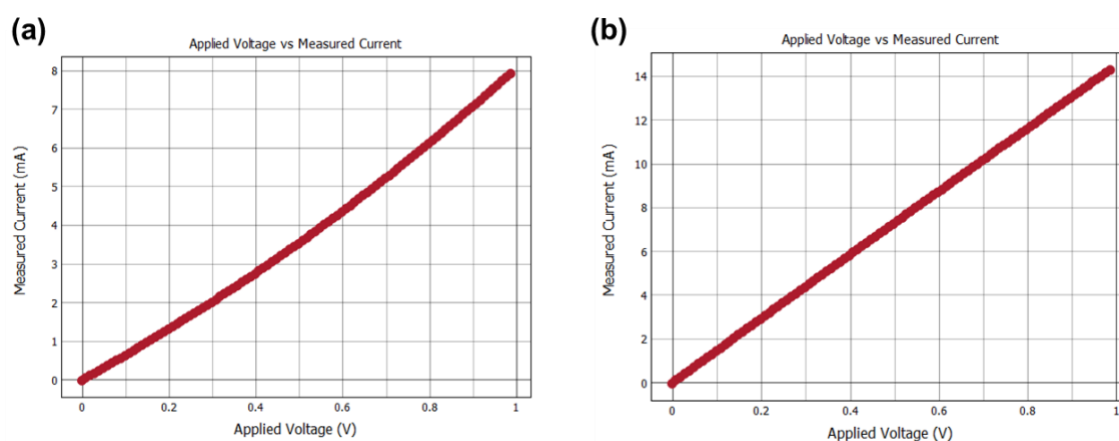


Figure 2.S2 Sheet resistance measurements of (a) NAT and (b) AT.

The tests were performed on an Ossila[®] four-point probe. NAT and AT have much lower sheet resistance than the indium-tin-oxide glass standard sample (17 ohm/square provided by Ossila[®]). They are both considered as metallic conductive with no specific sheet resistance given. Comparing the slopes of current-voltage curves of the outer forced connections gives a qualitative conclusion that NAT has a conductivity similar to AT.

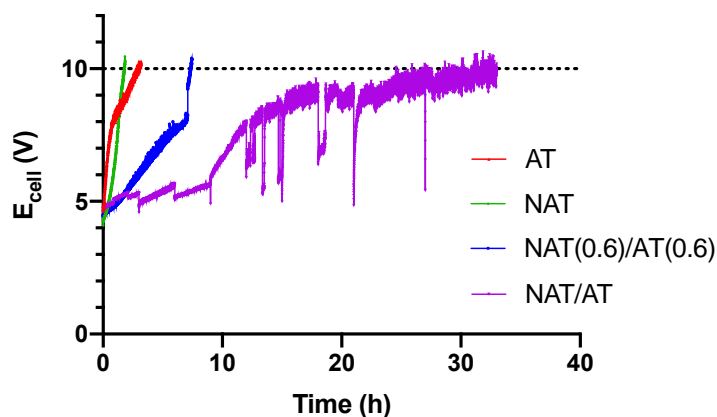


Figure 2.S3 Accelerated lifetime tests of anodes.

In the accelerated lifetime tests, anodes with a surface area of 0.5 cm^2 were subjected to 100 mA current (current density 200 mA/cm^2). Deactivation is reflected in the cell voltage (E_{cell}) vs. time plot by the increase of E_{cell} to above 10 V , at which point the titanium metal base starts to be corroded.³⁵ The actual lifetime (t_{oc}) of an electrode at a specific operating current (I_{oc}) can be estimated using the lifetime (t_{alt}) under high current (I_{alt}) based on the empirical equation^{3,4}:

$$t_{\text{oc}} = \frac{I_{\text{alt}}^{1.7} t_{\text{alt}}}{I_{\text{oc}}^{1.7}}$$

Lifetimes under high current for AT, NAT, and NAT/AT were 2.1, 1.6, and 33 h, which correspond to the lifetimes at 10 mA/cm^2 as 342, 260, and 5373 h, respectively. Lifetime for NAT(0.6)/AT(0.6) at 10 mA/cm^2 was calculated to be 1156 h.

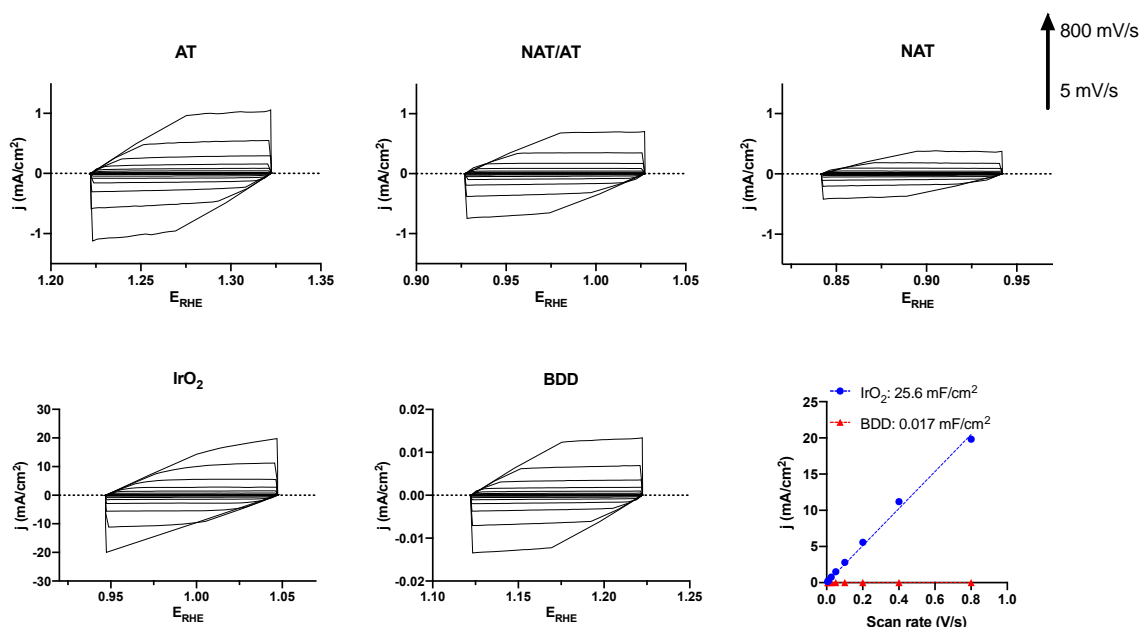


Figure 2.S4 Cyclic voltammograms at scan rates of 5, 10, 25, 50, 100, 200, 400, and 800 mV/s of AT, NAT/AT, NAT, IrO₂, and BDD electrodes and charging currents as functions of scan rate of IrO₂ and BDD electrodes.

The slopes of the charging curves give capacitances (mF/cm²) that are proportional to the ECSA. Multiplying by the electrode geometric area (6 cm²) and dividing by a general specific capacitance for metal oxide (0.04 mF/cm²) gave ECSA values for AT, NAT/AT, NAT, IrO₂, and BDD of 201, 130, 70, 3840, and 2.5 cm², respectively. The commercial IrO₂ anode demonstrated a very large ECSA. The reason is unclear due to the proprietary manufacturing procedure. Possibly explanation lies in the porous structure and high mass loading of catalyst (10 mg/cm² according to the supplier). On the other hand, BDD had a smaller ECSA than its geometric surface area (2.5 vs. 6 cm²), likely due to the heterogeneous distribution of electro-active sites on the BDD surface. Not all the crystal facets of BDD have activity towards redox couples used in the ECSA measurement.⁵

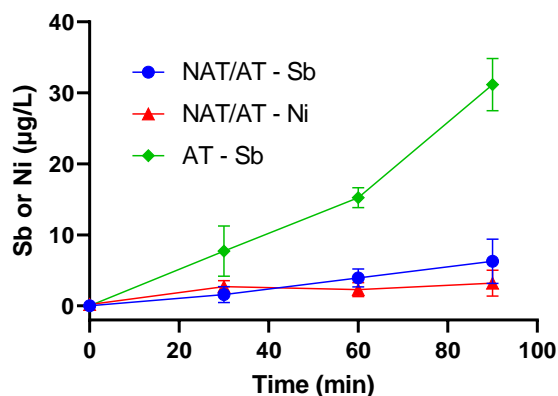


Figure 2.S5 Leaching of Sb and Ni by AT and NAT/AT electrodes.

All electrodes were subjected to 90 min aging at 10 mA/cm² before the leaching tests. The 90 min leaching tests were performed three times for each electrode. Fresh electrolyte (100 mM NaClO₄) was used in each run. Averages of triplicate experiments are shown. Error bars represent standard deviations.

Based on the precursor composition and the average mass loading of 1.3 mg/cm² of the layer exposed to the electrolyte, the total mass of Sb in the form of Sb₂O₃ are 378 and 757 µg for NAT/AT and AT, respectively. A 90 min electrolysis tested by AT released 31 µg/L of Sb in 25 mL electrolyte, equivalent to 0.93 µg Sb₂O₃. This accounts for 0.1% loss of the total Sb₂O₃ from the AT electrode. Similarly, the leaching test indicates that NAT/AT loss 0.05% of Sb₂O₃ after 90 min electrolysis.

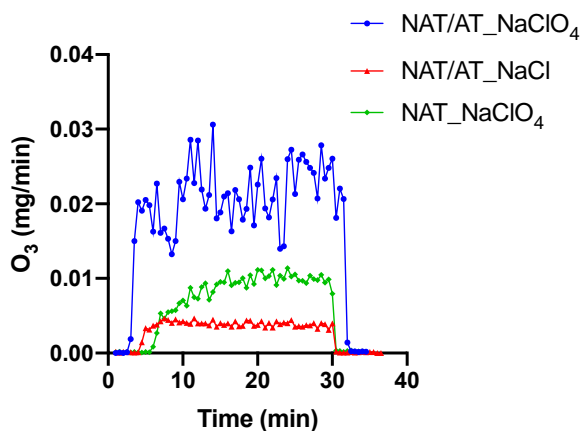


Figure 2.S6 Evolution rates of O_3 in the gas phase during electrolysis in NaCl and NaClO₄ electrolytes. Anode surface area = 6 cm², current density = 10 mA/cm², electrolyte volume = 25 mL.

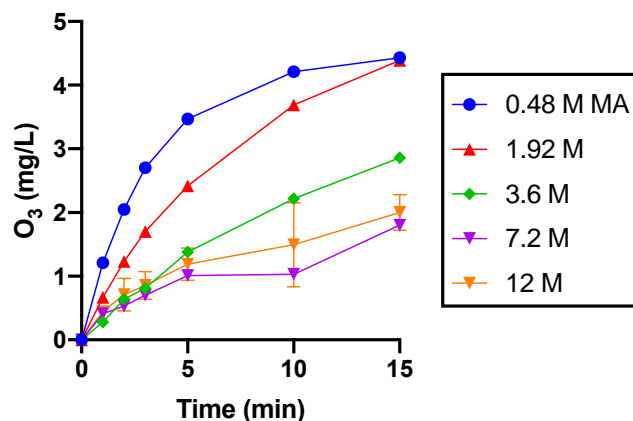


Figure 2.S7 Apparent O_3 production with different concentrations of malonic acid (MA) added to quench free chlorine. Anode surface area = 6 cm², current density = 10 mA/cm², electrolyte volume = 25 mL.

The result for O_3 production contradicts that from a previous study on Ni-Sb-SnO₂, which reported enhanced ozone production in the presence of Cl⁻.⁶ The authors likely arrived at their conclusion because the amount of malonic acid (MA) added was insufficient to mask chlorine. During electrolysis, when a small amount of MA (0.48 M) was added, O_3 appeared to be produced faster due to decolorization caused by unmasked chlorine species. However, with increased MA concentrations, the rate of O_3 generation inferred by decolorization of potassium indigo trisulfonate decreased and gradually approached a specific level that is slower compared to electrolysis in NaClO₄ solution.

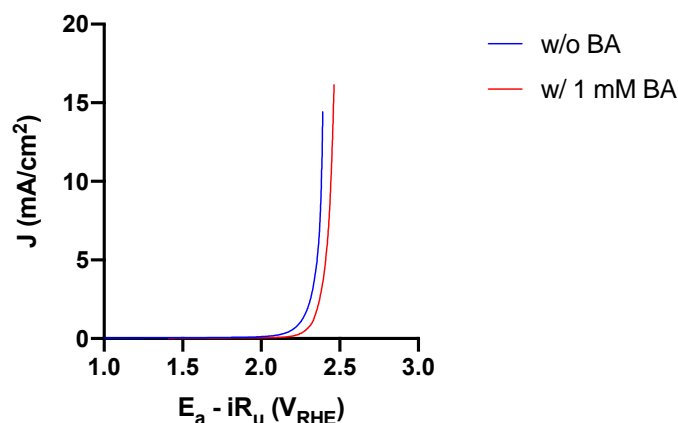


Figure 2.S8 Linear sweep voltammograms (LSV) of NAT/AT in 30 mM NaClO₄ electrolytes in the absence and presence of 1 mM benzoic acid (BA).

Direct electron transfer (DET) to the electrode would be indicated by a redox peak in the presence of BA. Such signal was not observed on NAT/AT, thus ruling out the contribution to BA degradation by DET.

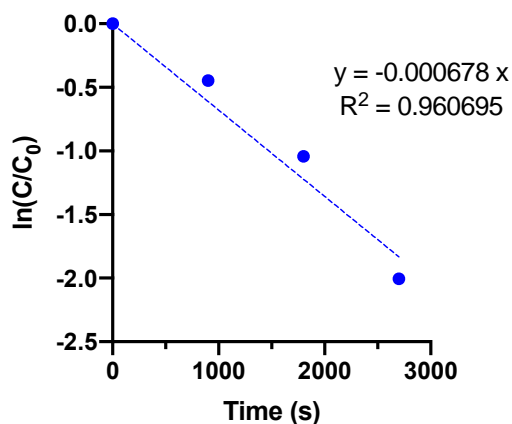


Figure 2.S9 BA degradation by NAT/AT in 30 mM NaClO₄ electrolytes.

Assuming that BA degradation follows pseudo first-order kinetics, the fitted rate constant was $k_{BA} = 0.000678 \text{ s}^{-1}$, which, normalized by the specific surface area ($24 \text{ m}^2/\text{m}^3$), is $k_{BA,SA} = 2.83 \times 10^{-5} \text{ m/s}$.

The steady-state concentration of $\cdot\text{OH}$ ($[\cdot\text{OH}]_{ss}$) can be estimated using k_{BA} :

$$\frac{d[\text{BA}]}{dt} = k_{BA,H\text{O}}[\text{BA}][\cdot\text{OH}]_{ss} = k_{BA}[\text{BA}]$$

$$[\cdot\text{OH}]_{\text{ss}} = \frac{k_{\text{BA}}}{k_{\text{BA,OH}}} = 1.58 \times 10^{-13} \text{ M}$$

where k_{BA} is the pseudo-first-order rate constant and $k_{\text{BA,OH}}$ is the second-order rate constant for BA and $\cdot\text{OH}$. The number matches that predicted by the kinetic model, which is $\sim 1.6 \times 10^{-13} \text{ M}$ in NaClO_4 solutions.

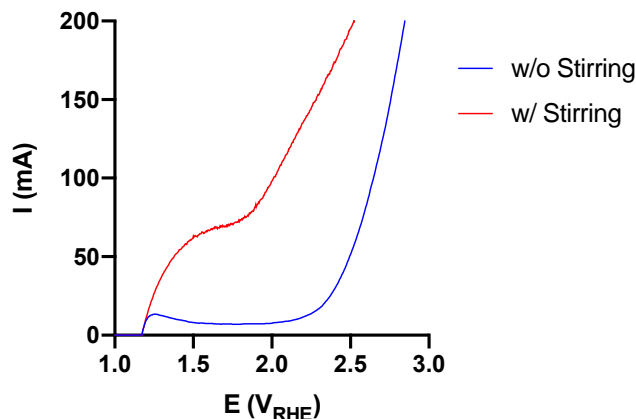


Figure 2.S10 Experimental current vs. applied potential of NAT/AT with and without stirring.

The experiment was measured in 0.5 M Na_2CO_3 , 0.05 M $\text{K}_4\text{Fe}(\text{CN})_6$, and 0.1 M $\text{K}_3\text{Fe}(\text{CN})_6$. The limiting currents (I_{lim}) with and without stirring were ~ 70 and 7 mA, respectively. The mass transfer rate constants (k_{m}) can then be calculated⁷:

$$\begin{aligned} k_{\text{m}} &= \frac{I_{\text{lim}}}{nFAC} = \frac{0.07 \text{ A or } 0.007 \text{ A}}{1(96485 \times 1000 \text{ C/kmol})(0.0006 \text{ m}^2)(0.05 \text{ kmol/m}^3)} \\ &= 2.42 \times 10^{-5} \text{ m/s or } 2.42 \times 10^{-6} \text{ m/s} \end{aligned}$$

where I_{lim} is the limiting current (plateau region), n is the number of electrons exchanged, F is Faraday constant (96,485 C/mol), A is the electrode surface area, and C is the concentration of the compound of interest in the bulk solution.

Knowing the diffusion coefficient for $\text{Fe}(\text{CN})_6^{4-}$ $D = 6.58 \times 10^{-10} \text{ m}^2/\text{s}$,⁸ the diffusion layer thickness (δ) can be calculated:

$$\delta = \frac{D}{k_{\text{m}}} = \frac{6.58 \times 10^{-10} \text{ m}^2/\text{s}}{0.0000242 \text{ m/s or } 0.00000242 \text{ m/s}} = 2.72 \times 10^{-5} \text{ m or } 2.72 \times 10^{-4} \text{ m}$$

that is, the diffusion layer thickness (δ) is $\sim 27 \mu\text{m}$ (with stirring) or $\sim 270 \mu\text{m}$ (without stirring).

Assuming the same diffusion layer thickness (δ) for benzoic acid (BA) systems and knowing the diffusion coefficient $D_{\text{BA}} = 0.9 \times 10^{-9} \text{ m}^2/\text{s}$ for BA at 25°C ,⁹ a more accurate mass transfer rate constant for BA ($k_{\text{m,BA}}$) can be estimated as follows:

$$k_{\text{m,BA}} = \frac{D_{\text{BA}}}{\delta} = \frac{0.9 \times 10^{-9} \text{ m}^2/\text{s}}{2.72 \times 10^{-5} \text{ m}} = 3.31 \times 10^{-5} \text{ m/s}$$

The limiting current (assuming mineralization of BA) in this system initially can then be estimated:

$$\begin{aligned} I_{\text{lim,BA}} &= nFAk_{\text{m,BA}}C_{\text{BA}} = (4x + y - 2z)FAk_{\text{m,BA}}C_{\text{BA}} \\ &= (28 + 6 - 4)(96485 \times 1000 \text{ C/kmol})(0.0006 \text{ m}^2)(3.31 \\ &\quad \times 10^{-5} \text{ m/s})(0.001 \text{ kmol/m}^3) \\ &= 0.057 \text{ A} \end{aligned}$$

where x , y , and z are the number of C, H, and O in BA ($\text{C}_7\text{H}_6\text{O}_2$), respectively. $I_{\text{lim,BA}}$ drops during treatment as C_{BA} drops. BA degradation is under mass transport control during the course of electrolysis.

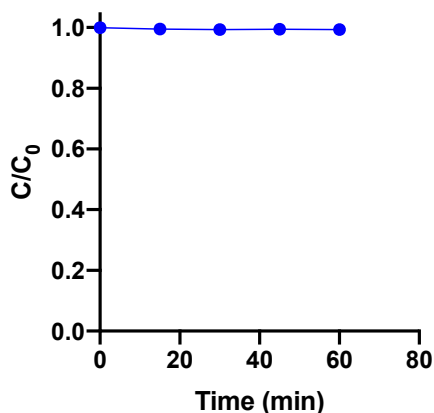


Figure 2.S11 Benzoic acid (BA) degradation by homogeneous ozonation.

In order to exclude the contribution to BA degradation by the direct reaction between O_3 and BA and to mimic the produced O_3 concentration in actual electrolysis experiments, O_3 in the headspace of the electrolysis cell using NAT/AT in 100 mM NaClO_4 electrolyte ($\sim 40\%$

of total O₃ generated) was purged by N₂ gas into another beaker containing 1 mM BA solution. No BA removal was observed during one-hour electrolysis, confirming our hypothesis that direct reaction between O₃ and BA did not contribute to BA degradation.

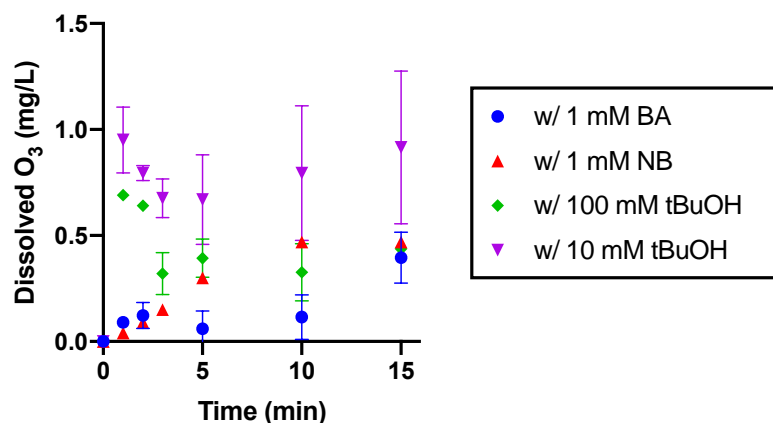


Figure 2.S12 Impacts of the organic radical quenchers benzoic acid (BA), nitrobenzene (NB), and tert-butanol (tBuOH) on the production of O₃ by NAT/AT anode in 30 mM NaClO₄. Anode surface area = 6 cm², current density = 10 mA/cm², electrolyte volume = 25 mL.

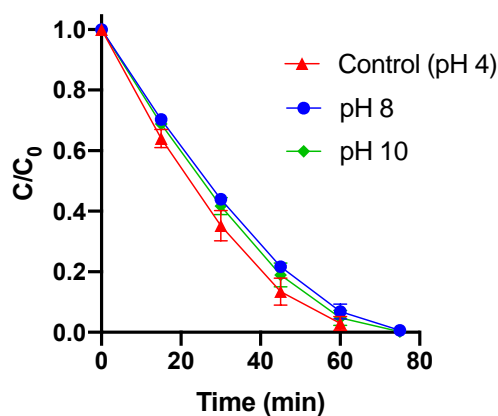


Figure 2.S13 Effect of pH on the BA degradation kinetics by NAT/AT. Anode surface area = 6 cm², current density = 10 mA/cm², electrolyte volume = 25 mL.

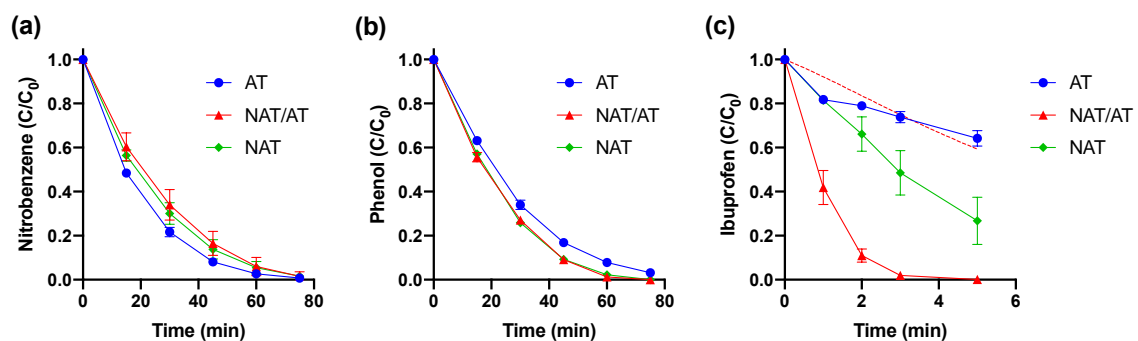


Figure 2.S14 EO treatment of (a) nitrobenzene (NB), (b) phenol (Ph), and (c) ibuprofen (IBP) in 30 mM NaClO_4 . The dashed red line in (c) represents kinetic model prediction of IBP degradation, taking into account reaction with both O_3 and $\cdot\text{OH}$. Anode surface area = 6 cm^2 , current density = 10 mA/cm^2 , electrolyte volume = 25 mL.

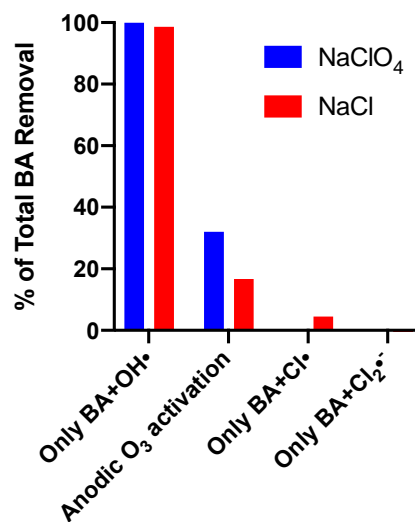


Figure 2.S15 Radical contributions to BA degradation by NAT/AT in NaClO_4 and NaCl electrolytes.

The model predicted that total BA removal in NaClO_4 and NaCl electrolytes at 1 h were *ca.* 94% and 76%, respectively. Contributions from specific radical species were quantified by turning on only its reaction with BA and excluding the others. In both electrolytes, contributions from $\text{O}\cdot^-$ were negligible (no BA removal was predicted with only BA + $\text{O}\cdot^-$) and thus not shown. Inside the contribution from $\cdot\text{OH}$, by turning on/off electrochemical $\cdot\text{OH}$ production (reaction 10 in Table 2.S1), sub-contributions from anodic O_3 activation

were estimated to be *ca.* 32% and 17%, respectively, in NaClO₄ and NaCl electrolytes. Contributions from Cl[·] and Cl₂^{·-} in NaCl were not important, responsible for <5% and <<1% of total removal, respectively.

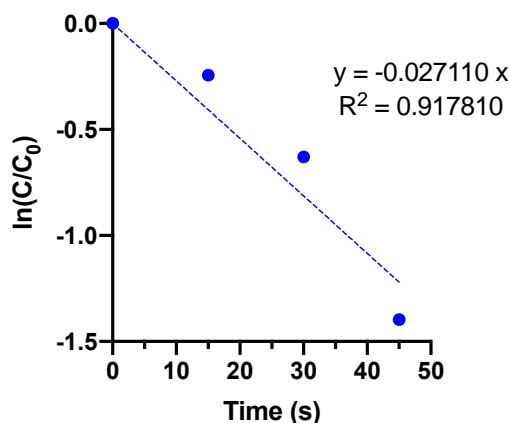


Figure 2.S16 Carbamazepine (CBZ) degradation by NAT/AT in 30 mM NaClO₄ electrolytes.

Assuming that CBZ degradation follows pseudo-first-order kinetics, the fitted rate constant was $k_{CBZ} = 0.027110 \text{ s}^{-1}$, which, normalized by the specific surface area ($24 \text{ m}^2/\text{m}^3$), is $k_{CBZ,SA} = 1.13 \times 10^{-3} \text{ m/s}$. Comparing to that for BA, this assumption is less accurate due to the reaction between CBZ and O₃ in the aqueous phase, which is also manifested in the rate constant that is two orders of magnitude higher than the mass transfer rate constants.

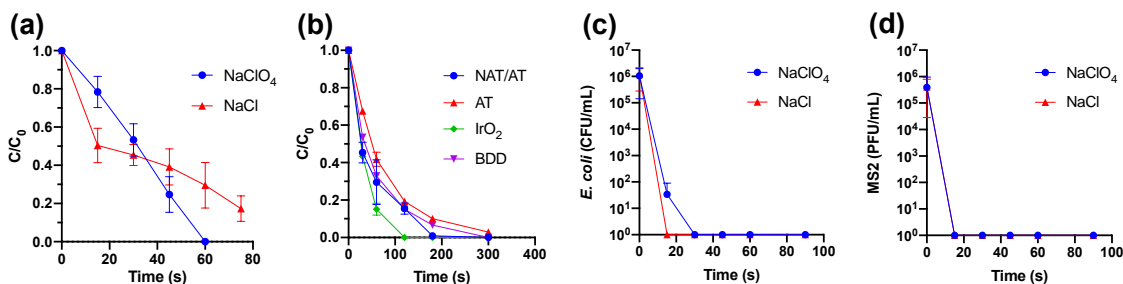


Figure 2.S17 Removal of 30 μM carbamazepine (CBZ) by (a) NAT/AT in 30 mM NaClO₄ and NaCl and (b) different electrodes in 30 mM NaCl. Inactivation of (c) *E. coli* and (d) MS2 by NAT/AT in 30 mM NaClO₄ and NaCl electrolytes. Anode surface area = 6 cm^2 , current density = $10 \text{ mA}/\text{cm}^2$, electrolyte volume = 25 mL.

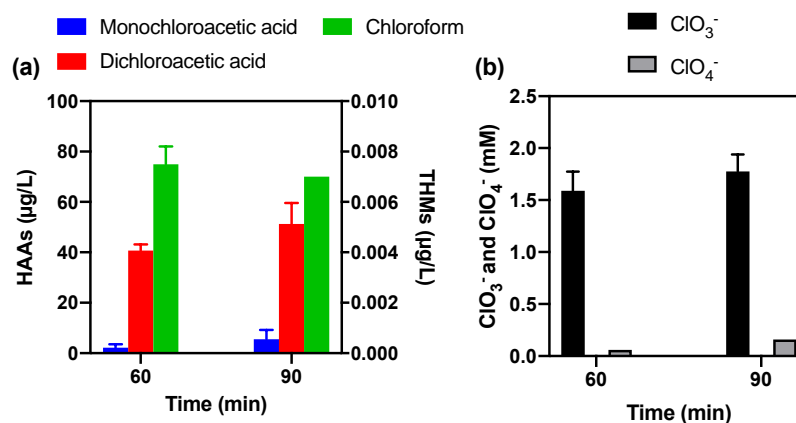


Figure 2.S18 Formation of disinfection byproducts (DBPs) during electrolysis of latrine wastewater by NAT/AT electrode.

Table 2.S1 Target compound properties.

	Hammett constant (δ) ^a	$k_{\text{-OH}}$ (M ⁻¹ s ⁻¹) ¹	logK _{ow} ^b	pKa	Reference
Benzoic acid (BA)	-	4.3×10^9	1.89	4.19	10
Nitrobenzene (NB)	0.78 (-NO ₂)	3.9×10^9	1.85	n.a.	10
Phenol (Ph)	-0.36 (-OH)	6.6×10^9	1.44	9.95	10
Ibuprofen (IBP)	-	7.2×10^9	2.48-3.97	5.3	11

- NB has an electron-withdrawing ring substituent with a Hammett constant of $\sigma = 0.78$, while the hydroxyl group on phenol has a $\sigma = -0.36$, yet either compound was promoted by anodic O₃ activation, suggesting there is no clear correlation between electron-withdrawing/donating capacity of the ring substituent and activation.
- BA and NB share really close logK_{ow}, but one was promoted and the other was not, indicating there is no clear correlation between logK_{ow} and activation.

Table 2.S2 Principle reactions in the kinetic model.

No.	Reaction	Rate constant	Reference
-----	----------	---------------	-----------

1	$\text{H}^+ + \text{OH}^- \rightarrow \text{H}_2\text{O}$	$1.00 \times 10^{11} \text{ M}^{-1}\text{s}^{-1}$	12
2	$\text{H}_2\text{O} \rightarrow \text{H}^+ + \text{OH}^-$	$1.00 \times 10^{-3} \text{ s}^{-1}$	12
3	$\text{H}^+ + \text{HO}_2^- \rightarrow \text{H}_2\text{O}_2$	$5.00 \times 10^{10} \text{ M}^{-1}\text{s}^{-1}$	12
4	$\text{H}_2\text{O}_2 \rightarrow \text{H}^+ + \text{HO}_2^-$	$1.30 \times 10^{-1} \text{ s}^{-1}$	12
5	$\text{H}^+ + \text{Cl}^- \rightarrow \text{HCl}$	$5.00 \times 10^{10} \text{ M}^{-1}\text{s}^{-1}$	12
6	$\text{HCl} \rightarrow \text{H}^+ + \text{Cl}^-$	$8.60 \times 10^{16} \text{ s}^{-1}$	12
7	$\text{H}^+ + \text{OCl}^- \rightarrow \text{HOCl}$	$5.00 \times 10^{10} \text{ M}^{-1}\text{s}^{-1}$	12
8	$\text{HOCl} \rightarrow \text{H}^+ + \text{OCl}^-$	$1.40 \times 10^3 \text{ s}^{-1}$	12
9	$\text{MO} \rightarrow \text{O}_3$	$6.92/1.42 \times 10^{-7} \text{ s}^{-1}$	Fitted ^a
10	$\text{MO} \rightarrow \text{HO}\cdot$	$1.69 \times 10^{-6} \text{ s}^{-1}$	Fitted
11	$\text{MO} + \text{Cl}^- \rightarrow \text{Cl}\cdot$	$1.50 \times 10^{-5} \text{ s}^{-1}$	Fitted
12	$\text{MO} + 2\text{Cl}^- \rightarrow \text{Cl}_2$	$8.05 \times 10^{-1} \text{ s}^{-1}$	Fitted
13	$\text{MO} + \text{OCl}^- \rightarrow \text{OCl}\cdot$	$3.89 \times 10^2 \text{ s}^{-1}$	Fitted
14	$\text{MO} + \text{OCl}^- \rightarrow \text{ClO}_3^-$	Not important ^b	
15	$\text{MO} + \text{ClO}_3^- \rightarrow \text{ClO}_4^-$	Not important ^b	
16	$\text{HO}\cdot + \text{H}_2\text{O}_2 \rightarrow \text{HO}_2\cdot + \text{H}_2\text{O}$	$2.70 \times 10^7 \text{ M}^{-1}\text{s}^{-1}$	10
17	$\text{HO}\cdot + \text{OH}^- \rightarrow \text{O}\cdot^- + \text{H}_2\text{O}$	$1.20 \times 10^{10} \text{ M}^{-1}\text{s}^{-1}$	13
18	$\text{HO}\cdot + \text{HO}\cdot \rightarrow \text{H}_2\text{O}_2$	$5.50 \times 10^9 \text{ M}^{-1}\text{s}^{-1}$	10
19	$\text{HO}\cdot + \text{Cl}^- \rightarrow \text{ClOH}\cdot^-$	$4.30 \times 10^9 \text{ M}^{-1}\text{s}^{-1}$	14
20	$\text{HO}\cdot \rightarrow \text{Products}$	$1.00 \times 10^7 \text{ s}^{-1}$	Assumed ^c
21	$\text{ClOH}\cdot^- \rightarrow \text{Cl}^- + \text{HO}\cdot$	$6.10 \times 10^9 \text{ s}^{-1}$	14
22	$\text{ClOH}\cdot^- + \text{H}^+ \rightarrow \text{Cl}\cdot + \text{H}_2\text{O}$	$2.10 \times 10^{10} \text{ M}^{-1}\text{s}^{-1}$	14
23	$\text{ClOH}\cdot^- + \text{Cl}^- \rightarrow \text{Cl}_2\cdot^- + \text{OH}^-$	$1.00 \times 10^4 \text{ M}^{-1}\text{s}^{-1}$	15
24	$\text{Cl}\cdot + \text{H}_2\text{O} \rightarrow \text{ClOH}\cdot^- + \text{H}^+$	$2.50 \times 10^5 \text{ M}^{-1}\text{s}^{-1}$	16
25	$\text{Cl}\cdot + \text{H}_2\text{O}_2 \rightarrow \text{HO}_2\cdot + \text{Cl}^- + \text{H}^+$	$2.00 \times 10^9 \text{ M}^{-1}\text{s}^{-1}$	17
26	$\text{Cl}\cdot + \text{OH}^- \rightarrow \text{ClOH}\cdot^-$	$1.80 \times 10^{10} \text{ M}^{-1}\text{s}^{-1}$	18
27	$\text{Cl}\cdot + \text{Cl}^- \rightarrow \text{Cl}_2\cdot^-$	$8.00 \times 10^9 \text{ M}^{-1}\text{s}^{-1}$	19

28	$\text{Cl}_2\cdot^- + \text{H}_2\text{O} \rightarrow \text{Cl}\cdot + \text{HClOH}$	$1.30 \times 10^3 \text{ M}^{-1}\text{s}^{-1}$	16
29	$\text{Cl}_2\cdot^- + \text{H}_2\text{O}_2 \rightarrow \text{HO}_2\cdot + 2\text{Cl}^- + \text{H}^+$	$1.40 \times 10^5 \text{ M}^{-1}\text{s}^{-1}$	20
30	$\text{Cl}_2\cdot^- + \text{OH}^- \rightarrow \text{ClOH}\cdot^- + \text{Cl}^-$	$4.50 \times 10^7 \text{ M}^{-1}\text{s}^{-1}$	15
31	$\text{Cl}_2\cdot^- \rightarrow \text{Cl}\cdot + \text{Cl}^-$	$6.00 \times 10^4 \text{ s}^{-1}$	19
32	$\text{HClOH} \rightarrow \text{Cl}\cdot + \text{H}_2\text{O}$	$1.00 \times 10^2 \text{ s}^{-1}$	16
33	$\text{HClOH} \rightarrow \text{ClOH}\cdot^- + \text{H}^+$	$1.00 \times 10^8 \text{ s}^{-1}$	16
34	$\text{HClOH} + \text{Cl}^- \rightarrow \text{Cl}_2\cdot^- + \text{H}_2\text{O}$	$5.00 \times 10^9 \text{ M}^{-1}\text{s}^{-1}$	16
35	$\text{Cl}\cdot + \text{Cl}\cdot \rightarrow \text{Cl}_2$	$8.80 \times 10^7 \text{ M}^{-1}\text{s}^{-1}$	21
36	$\text{Cl}\cdot + \text{Cl}_2\cdot^- \rightarrow \text{Cl}^- + \text{Cl}_2$	$2.10 \times 10^9 \text{ M}^{-1}\text{s}^{-1}$	17
37	$\text{Cl}_2\cdot^- + \text{HO}\cdot \rightarrow \text{HOCl} + \text{Cl}^-$	$1.00 \times 10^9 \text{ M}^{-1}\text{s}^{-1}$	22
38	$\text{Cl}_2\cdot^- + \text{Cl}_2\cdot^- \rightarrow 2\text{Cl}^- + \text{Cl}_2$	$9.00 \times 10^8 \text{ M}^{-1}\text{s}^{-1}$	17
39	$\text{Cl}_2 + \text{H}_2\text{O} \rightarrow \text{HOCl} + \text{Cl}^- + \text{H}^+$	$1.50 \times 10^1 \text{ M}^{-1}\text{s}^{-1}$	23
40	$\text{Cl}_2 + \text{H}_2\text{O}_2 \rightarrow \text{O}_2 + 2\text{HCl}$	$1.30 \times 10^4 \text{ M}^{-1}\text{s}^{-1}$	20
41	$\text{Cl}_2 + \text{O}_2\cdot^- \rightarrow \text{O}_2 + \text{Cl}_2\cdot^-$	$1.00 \times 10^9 \text{ M}^{-1}\text{s}^{-1}$	20
42	$\text{Cl}_2 + \text{HO}_2\cdot \rightarrow \text{O}_2 + \text{Cl}_2\cdot^- + \text{H}^+$	$1.00 \times 10^9 \text{ M}^{-1}\text{s}^{-1}$	24
43	$\text{Cl}_2 + \text{Cl}^- \rightarrow \text{Cl}_3^-$	$2.00 \times 10^4 \text{ M}^{-1}\text{s}^{-1}$	25
44	$\text{Cl}_3^- + \text{O}_2\cdot^- \rightarrow \text{Cl}_2\cdot^- + \text{Cl}^- + \text{O}_2$	$3.80 \times 10^9 \text{ M}^{-1}\text{s}^{-1}$	20
45	$\text{Cl}_3^- + \text{HO}_2\cdot \rightarrow \text{Cl}_2\cdot^- + \text{HCl} + \text{O}_2$	$1.00 \times 10^9 \text{ M}^{-1}\text{s}^{-1}$	24
46	$\text{Cl}_3^- \rightarrow \text{Cl}_2 + \text{Cl}^-$	$1.10 \times 10^5 \text{ s}^{-1}$	25
47	$\text{HOCl} + \text{H}_2\text{O}_2 \rightarrow \text{HCl} + \text{H}_2\text{O} + \text{O}_2$	$1.10 \times 10^4 \text{ M}^{-1}\text{s}^{-1}$	26
48	$\text{HOCl} + \text{HO}\cdot \rightarrow \text{OCl}\cdot + \text{H}_2\text{O}$	$2.00 \times 10^9 \text{ M}^{-1}\text{s}^{-1}$	20
49	$\text{HOCl} + \text{O}_2\cdot^- \rightarrow \text{Cl}\cdot + \text{OH}^- + \text{O}_2$	$7.50 \times 10^6 \text{ M}^{-1}\text{s}^{-1}$	20
50	$\text{HOCl} + \text{HO}_2\cdot \rightarrow \text{Cl}\cdot + \text{H}_2\text{O} + \text{O}_2$	$7.50 \times 10^6 \text{ M}^{-1}\text{s}^{-1}$	20
51	$\text{HOCl} + \text{Cl}\cdot \rightarrow \text{OCl}\cdot + \text{Cl}^- + \text{H}^+$	$3.00 \times 10^9 \text{ M}^{-1}\text{s}^{-1}$	18
52	$\text{HOCl} + \text{Cl}^- + \text{H}^+ \rightarrow \text{Cl}_2 + \text{H}_2\text{O}$	$1.82 \times 10^4 \text{ M}^{-2}\text{s}^{-1}$	23
53	$\text{OCl}^- + \text{H}_2\text{O}_2 \rightarrow \text{Cl}^- + \text{H}_2\text{O} + \text{O}_2$	$1.70 \times 10^5 \text{ M}^{-1}\text{s}^{-1}$	26

54	$\text{OCl}^\cdot + \text{HO}^\cdot \rightarrow \text{OCl}^\cdot + \text{OH}^-$	$8.80 \times 10^9 \text{ M}^{-1}\text{s}^{-1}$	20
55	$\text{OCl}^\cdot + \text{O}_2^{\cdot-} + \text{H}_2\text{O} \rightarrow \text{Cl}^\cdot + 2\text{OH}^- + \text{O}_2$	$2.00 \times 10^8 \text{ M}^{-2}\text{s}^{-1}$	20
56	$\text{OCl}^\cdot + \text{Cl}^\cdot \rightarrow \text{OCl}^\cdot + \text{Cl}^\cdot + \text{H}^+$	$8.20 \times 10^9 \text{ M}^{-1}\text{s}^{-1}$	18
57	$\text{OCl}^\cdot + \text{OCl}^\cdot \rightarrow \text{P3}$	$7.50 \times 10^9 \text{ M}^{-1}\text{s}^{-1}$	27
58	$\text{O}_3 + \text{H}_2\text{O}_2 \rightarrow \text{O}_2 + \text{HO}^\cdot + \text{HO}_2^\cdot$	$6.50 \times 10^{-3} \text{ M}^{-1}\text{s}^{-1}$	28
59	$\text{O}_3 + \text{OH}^- \rightarrow \text{O}_2 + \text{HO}_2^\cdot$	$7.00 \times 10^1 \text{ M}^{-1}\text{s}^{-1}$	29
60	$\text{O}_3 + \text{HO}^\cdot \rightarrow \text{O}_2 + \text{HO}_2^\cdot$	$1.10 \times 10^8 \text{ M}^{-1}\text{s}^{-1}$	29
61	$\text{O}_3 + \text{O}_2^{\cdot-} \rightarrow \text{O}_3^{\cdot-} + \text{O}_2$	$1.60 \times 10^9 \text{ M}^{-1}\text{s}^{-1}$	30
62	$\text{O}_3 + \text{HO}_2^\cdot \rightarrow \text{O}_2 + \text{HO}^\cdot + \text{O}_2^{\cdot-}$	$2.80 \times 10^6 \text{ M}^{-1}\text{s}^{-1}$	28
63	$\text{O}_3 + \text{Cl}^- \rightarrow \text{O}_2 + \text{OCl}^-$	$3.00 \times 10^{-3} \text{ M}^{-1}\text{s}^{-1}$	31
64	$\text{O}_3 + \text{HOCl} \rightarrow \text{Products}$	$2.00 \times 10^{-3} \text{ M}^{-1}\text{s}^{-1}$	31
65	$\text{O}_3 + \text{OCl}^- \rightarrow \text{Products}$	$1.20 \times 10^2 \text{ M}^{-1}\text{s}^{-1}$	31
66	$\text{O}_3 + \text{ClO}_3^- \rightarrow \text{Products}$	$1.00 \times 10^{-4} \text{ M}^{-1}\text{s}^{-1}$	31
67	$\text{O}_3 + \text{ClO}_4^- \rightarrow \text{Products}$	$2.00 \times 10^{-5} \text{ M}^{-1}\text{s}^{-1}$	31
68	$\text{O}_3 + \text{Cl}_2^{\cdot-} \rightarrow \text{Products}$	$9.00 \times 10^7 \text{ M}^{-1}\text{s}^{-1}$	32
69	$\text{O}_3 \rightarrow \text{Products}$	$7.04/3.28 \times 10^{-3} \text{ s}^{-1}$	Fitted ^d
70	$\text{O}_3^{\cdot-} + \text{H}^+ \rightarrow \text{HO}_3^\cdot$	$5.20 \times 10^{10} \text{ M}^{-1}\text{s}^{-1}$	30
71	$\text{O}_3^{\cdot-} + \text{HO}^\cdot \rightarrow \text{HO}_2^\cdot + \text{O}_2^{\cdot-}$	$8.50 \times 10^9 \text{ M}^{-1}\text{s}^{-1}$	33
72	$\text{O}_3^{\cdot-} + \text{O}^\cdot \rightarrow 2\text{O}_2^{\cdot-}$	$7.00 \times 10^8 \text{ M}^{-1}\text{s}^{-1}$	34
73	$\text{O}_3^{\cdot-} \rightarrow \text{O}_2 + \text{O}^\cdot$	$3.30 \times 10^3 \text{ s}^{-1}$	35
74	$\text{O}_2^{\cdot-} + \text{H}_2\text{O}_2 \rightarrow \text{O}_2 + \text{HO}^\cdot + \text{OH}^-$	$1.30 \times 10^{-1} \text{ M}^{-1}\text{s}^{-1}$	36
75	$\text{O}_2^{\cdot-} + \text{H}^+ \rightarrow \text{HO}_2^\cdot$	$7.20 \times 10^{10} \text{ M}^{-1}\text{s}^{-1}$	37
76	$\text{O}_2^{\cdot-} + \text{HO}^\cdot \rightarrow \text{O}_2 + \text{OH}^-$	$7.00 \times 10^9 \text{ M}^{-1}\text{s}^{-1}$	36
77	$\text{O}_2^{\cdot-} + \text{O}^\cdot + \text{H}_2\text{O} \rightarrow \text{O}_2 + 2\text{OH}^-$	$6.00 \times 10^8 \text{ M}^{-2}\text{s}^{-1}$	34
78	$\text{O}_2^{\cdot-} + \text{HO}_2^\cdot \rightarrow \text{HO}_2^- + \text{O}_2$	$9.70 \times 10^7 \text{ M}^{-1}\text{s}^{-1}$	36
79	$\text{O}_2^{\cdot-} + \text{Cl}_2^{\cdot-} \rightarrow \text{O}_2 + 2\text{Cl}^-$	$2.00 \times 10^9 \text{ M}^{-1}\text{s}^{-1}$	20
80	$\text{O}_2^{\cdot-} + \text{Cl}^- \rightarrow \text{Products}$	$1.40 \times 10^{-2} \text{ M}^{-1}\text{s}^{-1}$	38
81	$\text{O}_2^{\cdot-} + \text{HOCl} \rightarrow \text{O}_2 + \text{Cl}^- + \text{HO}^\cdot$	$7.50 \times 10^6 \text{ M}^{-1}\text{s}^{-1}$	38

82	$O\cdot^- + O_2 \rightarrow O_3\cdot^-$	$3.60 \times 10^9 M^{-1}s^{-1}$	10
83	$O\cdot^- + H_2O \rightarrow HO\cdot + OH^-$	$1.70 \times 10^6 M^{-1}s^{-1}$	10
84	$O\cdot^- + HO\cdot \rightarrow HO_2^-$	$2.00 \times 10^{10} M^{-1}s^{-1}$	10
85	$O\cdot^- + HO_2^- \rightarrow OH^- + O_2\cdot^-$	$4.00 \times 10^8 M^{-1}s^{-1}$	10
86	$O\cdot^- + OCl^- \rightarrow OCl\cdot + OH^-$	$2.30 \times 10^8 M^{-1}s^{-1}$	10
87	$HO_2\cdot + H_2O + O_2\cdot^- \rightarrow O_2 + H_2O_2 + OH^-$	$9.70 \times 10^7 M^{-2}s^{-1}$	38
88	$HO_2\cdot + H_2O_2 \rightarrow O_2 + H_2O + HO\cdot$	$3.00 \times 10^9 M^{-1}s^{-1}$	36
89	$HO_2\cdot + HO\cdot \rightarrow O_2 + H_2O$	$6.60 \times 10^9 M^{-1}s^{-1}$	36
90	$HO_2\cdot + HO_2\cdot \rightarrow O_2 + H_2O_2$	$8.30 \times 10^5 M^{-1}s^{-1}$	36
91	$HO_2\cdot + Cl_2\cdot^- \rightarrow O_2 + 2Cl^- + H^+$	$3.00 \times 10^9 M^{-1}s^{-1}$	20
92	$HO_2\cdot + Cl_2 \rightarrow Cl_2\cdot^- + O_2 + H^+$	$1.00 \times 10^9 M^{-1}s^{-1}$	24
93	$HO_2\cdot \rightarrow H^+ + O_2\cdot^-$	$7.90 \times 10^5 s^{-1}$	12
94	$HO_2^- + HO\cdot \rightarrow HO_2\cdot + OH^-$	$7.50 \times 10^9 M^{-1}s^{-1}$	10
95	$HO_3\cdot \rightarrow HO\cdot + O_2$	$1.10 \times 10^5 s^{-1}$	30
96	$HO_3\cdot \rightarrow O_3\cdot^- + H^+$	$3.70 \times 10^4 s^{-1}$	30
97	$BA + HO\cdot \rightarrow P1$	$4.30 \times 10^9 M^{-1}s^{-1}$	10
98	$BA + O\cdot^- \rightarrow P2$	$4.00 \times 10^7 M^{-1}s^{-1}$	10
99	$BA + Cl\cdot \rightarrow P3$	$1.80 \times 10^{10} M^{-1}s^{-1}$	39
100	$BA + Cl_2\cdot^- \rightarrow P4$	$2.00 \times 10^6 M^{-1}s^{-1}$	40
101	$P1 + O_3 \rightarrow P5 + O_3\cdot^-$	$1.00 \times 10^5 M^{-1}s^{-1}$	Assumed ^e
102	$P5 + 3O_3 \rightarrow P6 + O_3\cdot^-$	Not important ^f	

- a. The concentration of active sites MO was set as unity.
- b. No significant amounts of ClO_3^- and ClO_4^- were detected through the course of electrolysis experiments. These two reactions were therefore not taken into account in this model.

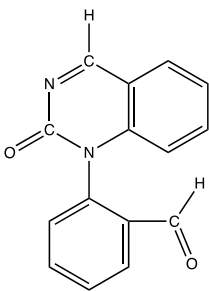
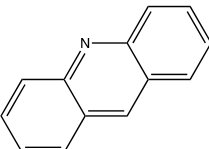
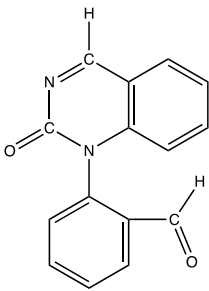
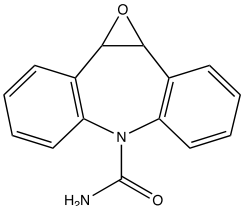
- c. Reaction 20 accounted for unknown HO· quenching pathways in the solution matrix. The rate was set the same as that assumed in Yang *et al.*⁴¹ where a more detailed explanation was provided. It was assumed that the quenching pathways were similar in the two systems. This assumption also enabled easier comparison between NAT/AT and BDD.
- d. Reaction 69 was incorporated into the kinetic model to account for the escape of O₃ from the aqueous to the gas phase and depletion of aqueous O₃ through unknown transformation pathways in the solution matrix.
- e. The actual rate constant between the transient OH-adduct radical (OH-BA, P1) and O₃ is not quantified in this study and needs further investigation. We chose $1.00 \times 10^5 \text{ M}^{-1}\text{s}^{-1}$ for our model with two considerations: (1) assuming numbers between 1.00×10^3 and $1.00 \times 10^9 \text{ M}^{-1}\text{s}^{-1}$ did not significantly affect the fitted HO· production rate (reaction 10), probably because O₃·⁻ formed in this step is limited by the amount and rate of P1 formed, that is, the rate of reaction 97; (2) aqueous O₃ concentrations predicted using rate constants $\geq 1.00 \times 10^5$ matched better to experimentally measured values in the first 5 min. Predicted O₃ concentrations became higher than experimental ones for two potential reasons: (1) the excess O₃ got transformed in the bulk electrolyte where the assumption of pH = 2 no longer holds, and/or (2) unknown reactions between O₃ and BA degradation products.
- f. Changing the rate constant for reaction 102 (proposed in Huang *et al.*⁴²) did not affect the fitting outcome. Due to the fact that this reaction involves the product of reaction 101 as well as three O₃ molecules, it is likely not important in yielding O₃·⁻ and thus HO· to facilitate BA degradation.

Table 2.S3 Rate constants estimated by kinetic modeling.

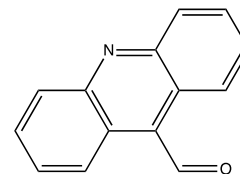
	In NaClO ₄	Avg RMSD ^a /R ²	In NaCl	Avg RMSD/R ²
r _{O3}	$6.92 \times 10^{-7} \text{ s}^{-1}$	0.036/99.4	$1.42 \times 10^{-7} \text{ s}^{-1}$	0.045/99.6
r _{HO·} ^b	$1.69 \times 10^{-6} \text{ s}^{-1}$	3.48/96.8	$1.69 \times 10^{-6} \text{ s}^{-1}$	3.48/96.8
k _{Cl·}	-	-	$1.50 \times 10^{-5} \text{ s}^{-1}$	0.058/99.5
k _{Cl2}	-	-	$8.05 \times 10^{-1} \text{ s}^{-1}$	0.057/99.5
k _{OCl·}	-	-	$3.89 \times 10^2 \text{ s}^{-1}$	0.057/99.5
k ₆₉	$7.04 \times 10^{-3} \text{ s}^{-1}$	0.036/99.4	$3.28 \times 10^{-3} \text{ s}^{-1}$	0.045/99.6

- Root-mean-square-deviation (RMSD), a value of 0 indicates a perfect fit.
- Comparing to a previously reported SbSn/CoTi/Ir anode,⁴³ NAT/AT showed two-order-of-magnitude higher $r_{HO\cdot}$ and a lot faster benzoic acid BA degradation (~70% removal in 30 mM NaCl after 4 h at 25 mA/cm² vs. ~100% removal in 30 mM NaCl after 75 min at 10 mA/cm²) and COD removal from toilet wastewater. The fitted $r_{HO\cdot}$ and $k_{Cl\cdot}$ values were on the same order of magnitude as those fitted for BDD in another study.⁴¹

Table 2.S4 Carbamazepine transformation products.

Electrolyte	RT (min)	TP m/z (Name)	Major fragment ions m/z	Calculated formula	Mass error (mDa)	Structure	Ref
NaClO ₄	1.51	251 (BQM)	180.08	C ₁₅ H ₁₁ N ₂ O ₂	0.2		44
			208.077				
NaCl	1.16	180	152.0612	C ₁₃ H ₁₀ N	0.6		45
			208.077				
NaCl	1.51	251 (BQM)	180.08	C ₁₅ H ₁₁ N ₂ O ₂	0.5		44
			208.077				
NaCl	1.59	253	180.0803	C ₁₅ H ₁₃ N ₂ O ₂	0.4		45
			210.0912				

2.09 208 180.0804 C₁₄H₁₀NO 0.6



2.43 205 139.9873 C₁₄H₉N₂ 0.6
141.9825

Structure unknown

Table 2.S5 Composition of latrine wastewater.

Property	Before EO	After EO (75 min)
pH		8.5-8.8
Conductivity (mS cm ⁻¹)		13.3
COD (mg O ₂ L ⁻¹)	307 ± 13	94 ± 14
[NH ₄ ⁺] (mM)	84 ± 6	71 ± 1
[Cl ⁻] (mM)	65 ± 8	56 ± 3
Average voltage (V)		3.9

Table 2.S6 Energy consumption for pharmaceuticals/pathogens removal by common electrodes.

Electrode	Solution type ^a	Pharmaceuticals (kWh/m ³)	E. coli (kWh/m ³)	MS2 (kWh/m ³)	All (kWh/m ³)
NAT/AT	30 mM NaClO ₄ /NaCl	~0.8 for 1-log removal of 5 pharmaceuticals (10 μM each)	<0.04 for 5-log removal	<0.04 for 5-log removal	~0.8
	Latrine wastewater	14.0 for 1-log removal of 5 pharmaceuticals (10 μM each)	3.9 for 5-log removal	7.8 for 5-log removal	14.0
Bismuth-doped TiO ₂ (Nanopac)	Latrine wastewater ^b	~14.0 for 1-log removal of 8 pharmaceuticals ^c (1 μM each) ⁴⁵		2.0 for 5-log removal ⁴⁶	
BDD	Secondary effluent		1-4 for 4-log removal ^{47,48}		
Ti/BDD	2.8 mM Na ₂ SO ₄	>11.3 for >0.3-log removal of 43.2 μM carbamazepine ⁴⁹			

Ti/PbO ₂	2.8 mM Na ₂ SO ₄	>12.4 for >0.3-log removal of 43.2 μM carbamazepine ⁴⁹		
SS/PbO ₂	10-120 mM NaCl		0.017 for 3.3- log removal ⁵⁰	
Pb/PbO ₂	10-120 mM NaCl		0.096 for 3.3- log removal ⁵⁰	
Platinum	10-120 mM NaCl		0.11 for 3.3- log removal ⁵⁰	
Graphite	10-120 mM NaCl		0.14 for 3.3- log removal ⁵⁰	
Platinum clad niobium mesh	30 mM Na ₂ SO ₄		6.3 for 4-log removal ⁵¹	7.8 for 6-log removal ⁵¹

- a. While few studies investigated pharmaceutical removal and *E. coli* and MS2 inactivation together, one or two aspects examined in various solutions were selected for comparison purposes. All initial *E. coli* and MS2 concentrations range from 10⁴-10⁶ CFU or PFU/mL.
- b. Toilet wastewater used in these two studies had different compositions than the one used in our experiments, with lower [NH₄⁺] and [Cl⁻] (<20 and 30 mM comparing to *ca.* 84 and 65 mM). By converting free chlorine to chloramines, ammonia can retard disinfection efficiency.
- c. The 5 pharmaceuticals used in our study overlapped with the 8 used in this study.

References

- (1) Jasper, J. T.; Yang, Y.; Hoffmann, M. R. Toxic Byproduct Formation during Electrochemical Treatment of Latrine Wastewater. *Environ. Sci. Technol.* **2017**, *51* (12), 7111–7119.
- (2) Ianni, J. C., *Kintecus*, Windows Version 6.80. www.kintecus.com.
- (3) Cho, K.; Hoffmann, M. R. Bi_xTi_{1-x}O₂ Functionalized Heterojunction Anode with an Enhanced Reactive Chlorine Generation Efficiency in Dilute Aqueous Solutions. *Chem. Mater.* **2015**, *27* (6), 2224–2233.
- (4) Chen, X.; Chen, G.; Yue, P. L. Stable Ti/IrO_x-Sb₂O₅-SnO₂ Anode for O₂ Evolution with Low Ir Content. *J. Phys. Chem. B* **2001**, *105* (20), 4623–4628.
- (5) P. Chaplin, B. Critical Review of Electrochemical Advanced Oxidation Processes for Water Treatment Applications. *Environ. Sci.: Process. Impacts* **2014**, *16* (6), 1182–1203.
- (6) Yang, S. Y.; Kim, D.; Park, H. Shift of the Reactive Species in the Sb-SnO₂-Electrocatalyzed Inactivation of *E. Coli* and Degradation of Phenol: Effects of Nickel Doping and Electrolytes. *Environ. Sci. Technol.* **2014**, *48* (5), 2877–2884.

- (7) Cañizares, P.; García-Gómez, J.; Fernández de Marcos, I.; Rodrigo, M. A.; Lobato, J. Measurement of Mass-Transfer Coefficients by an Electrochemical Technique. *J. Chem. Educ.* **2006**, *83* (8), 1204.
- (8) Klymenko, O. V.; Evans, R. G.; Hardacre, C.; Svir, I. B.; Compton, R. G. Double Potential Step Chronoamperometry at Microdisk Electrodes: Simulating the Case of Unequal Diffusion Coefficients. *J. Electroanal. Chem.* **2004**, *571* (2), 211–221.
- (9) Noulty, R. A.; Leaist, D. G. Diffusion Coefficient of Aqueous Benzoic Acid at 25.Degree.C. *J. Chem. Eng. Data* **1987**, *32* (4), 418–420.
- (10) Buxton, G. V.; Greenstock, C. L.; Helman, W. P.; Ross, A. B. Critical Review of Rate Constants for Reactions of Hydrated Electrons, Hydrogen Atoms and Hydroxyl Radicals ($\cdot\text{OH}/\cdot\text{O}^-$ in Aqueous Solution. *J. Phys. Chem. Ref. Data* **1988**, *17* (2), 513–886.
- (11) Huber, M. M.; Canonica, S.; Park, G.-Y.; von Gunten, U. Oxidation of Pharmaceuticals during Ozonation and Advanced Oxidation Processes. *Environ. Sci. Technol.* **2003**, *37* (5), 1016–1024.
- (12) Yang, Y.; Pignatello, J. J.; Ma, J.; Mitch, W. A. Comparison of Halide Impacts on the Efficiency of Contaminant Degradation by Sulfate and Hydroxyl Radical-Based Advanced Oxidation Processes (AOPs). *Environ. Sci. Technol.* **2014**, *48* (4), 2344–2351.
- (13) V. Buxton, G. Pulse Radiolysis of Aqueous Solutions. Rate of Reaction of OH with OH⁻. *Trans. Faraday Soc.* **1970**, *66* (0), 1656–1660.
- (14) G. Jayson, G.; J. Parsons, B.; J. Swallow, A. Some Simple, Highly Reactive, Inorganic Chlorine Derivatives in Aqueous Solution. Their Formation Using Pulses of Radiation and Their Role in the Mechanism of the Fricke Dosimeter. *J. Chem. Soc. Faraday Trans. 1: Physical Chemistry in Condensed Phases* **1973**, *69* (0), 1597–1607.
- (15) Grigor'ev, A. E.; Makarov, I. E.; Pikaev, A. K. Formation of Cl₂⁻ in the Bulk of Solution during Radiolysis of Concentrated Aqueous Solutions of Chlorides. *Khimiya Vysokikh Ehnergij* **1987**, *21* (2), 123–126.
- (16) McElroy, W. John. A Laser Photolysis Study of the Reaction of Sulfate(1-) with Chloride and the Subsequent Decay of Chlorine(1-) in Aqueous Solution. *J. Phys. Chem.* **1990**, *94* (6), 2435–2441.
- (17) Yu, X.-Y.; Barker, J. R. Hydrogen Peroxide Photolysis in Acidic Aqueous Solutions Containing Chloride Ions. II. Quantum Yield of HO•(Aq) Radicals. *J. Phys. Chem. A* **2003**, *107* (9), 1325–1332.
- (18) Kläning, U. K.; Wolff, T. Laser Flash Photolysis of HClO, ClO⁻, HBrO, and BrO⁻ in Aqueous Solution. Reactions of Cl- and Br-Atoms. *Berichte der Bunsengesellschaft für physikalische Chemie* **1985**, *89* (3), 243–245.
- (19) Nagarajan, V.; Fessenden, R. W. Flash Photolysis of Transient Radicals. 1. X₂⁻ with X = Cl, Br, I, and SCN. *J. Phys. Chem.* **1985**, *89* (11), 2330–2335.
- (20) Matthew, B. M.; Anastasio, C. A Chemical Probe Technique for the Determination of Reactive Halogen Species in Aqueous Solution: Part 1? Bromide Solutions. *Atmospheric Chem. Phys. Discussions* **2006**, *6* (1), 899–940.
- (21) Wu, D.; Wong, D.; Di Bartolo, B. Evolution of Cl₂⁻ in Aqueous NaCl Solutions. *J. Photochem.* **1980**, *14* (4), 303–310.

- (22) Wagner, I.; Karthäuser, J.; Strehlow, H. On the Decay of the Dichloride Anion Cl⁻² in Aqueous Solution. *Berichte der Bunsengesellschaft für physikalische Chemie* **1986**, *90* (10), 861–867.
- (23) Wang, T. X.; Margerum, D. W. Kinetics of Reversible Chlorine Hydrolysis: Temperature Dependence and General-Acid/Base-Assisted Mechanisms. *Inorg. Chem.* **1994**, *33* (6), 1050–1055.
- (24) Bjergbakke, E.; Navaratnam, S.; Parsons, B. J.; Swallow, A. J. Reaction between Hydroperoxo Radicals and Chlorine in Aqueous Solution. *J. Am. Chem. Soc.* **1981**, *103* (19), 5926–5928.
- (25) Ershov, B. G. Kinetics, Mechanism and Intermediates of Some Radiation-Induced Reactions in Aqueous Solutions. *Russ. Chem. Rev.* **2004**, *73* (1), 101–113.
- (26) Connick, R. E. The Interaction of Hydrogen Peroxide and Hypochlorous Acid in Acidic Solutions Containing Chloride Ion. *J. Am. Chem. Soc.* **1947**, *69* (6), 1509–1514.
- (27) V. Buxton, G.; S. Subhani, M. Radiation Chemistry and Photochemistry of Oxychlorine Ions. Part 1.—Radiolysis of Aqueous Solutions of Hypochlorite and Chlorite Ions. *J. Chem. Soc., Faraday Trans. 1: Physical Chemistry in Condensed Phases* **1972**, *68* (0), 947–957.
- (28) Staehelin, Johannes.; Hoigne, Juerg. Decomposition of Ozone in Water: Rate of Initiation by Hydroxide Ions and Hydrogen Peroxide. *Environ. Sci. Technol.* **1982**, *16* (10), 676–681.
- (29) Lesko, T. M.; Colussi, A. J.; Hoffmann, M. R. Hydrogen Isotope Effects and Mechanism of Aqueous Ozone and Peroxone Decompositions. *J. Am. Chem. Soc.* **2004**, *126* (13), 4432–4436.
- (30) Buehler, R. E.; Staehelin, J.; Hoigne, J. Ozone Decomposition in Water Studied by Pulse Radiolysis. 1. Perhydroxyl (HO₂)/Hyperoxide (O₂⁻) and HO₃/O₃⁻ as Intermediates. *J. Phys. Chem.* **1984**, *88* (12), 2560–2564.
- (31) Hoigné, J.; Bader, H.; Haag, W. R.; Staehelin, J. Rate Constants of Reactions of Ozone with Organic and Inorganic Compounds in Water—III. Inorganic Compounds and Radicals. *Water Res.* **1985**, *19* (8), 993–1004.
- (32) Bielski, B. H. J. A Pulse Radiolysis Study of the Reaction of Ozone with Cl⁻² in Aqueous Solutions. *Radiat. Phys. Chem.* **1993**, *41* (3), 527–530.
- (33) Sehested, K.; Holcman, J.; Bjergbakke, E.; Hart, E. J. Formation of Ozone in the Reaction of Hydroxyl with O₃⁻ and the Decay of the Ozonide Ion Radical at PH 10–13. *J. Phys. Chem.* **1984**, *88* (2), 269–273.
- (34) Sehested, K.; Holcman, J.; Bjergbakke, E.; Hart, E. J. Ultraviolet Spectrum and Decay of the Ozonide Ion Radical, O₃⁻, in Strong Alkaline Solution. *J. Phys. Chem.* **1982**, *86* (11), 2066–2069.
- (35) Gall, B. L.; Dorfman, L. M. Pulse Radiolysis Studies. XV. Reactivity of the Oxide Radical Ion and of the Ozonide Ion in Aqueous Solution. *J. Am. Chem. Soc.* **1969**, *91* (9), 2199–2204.
- (36) Crittenden, J. C.; Hu, S.; Hand, D. W.; Green, S. A. A Kinetic Model for H₂O₂/UV Process in a Completely Mixed Batch Reactor. *Water Res.* **1999**, *33* (10), 2315–2328.
- (37) Field, R. J.; Noyes, R. M.; Postlethwaite, D. Photoreduction of Hydrogen Peroxide by Hydrogen. *J. Phys. Chem.* **1976**, *80* (3), 223–229.

- (38) Bielski, B. H. J.; Cabelli, D. E.; Arudi, R. L.; Ross, A. B. Reactivity of HO₂/O⁻² Radicals in Aqueous Solution. *J. Phys. Chem. Ref. Data* **1985**, *14* (4), 1041–1100.
- (39) Mártire, D. O.; Rosso, J. A.; Bertolotti, S.; Le Roux, G. C.; Braun, A. M.; Gonzalez, M. C. Kinetic Study of the Reactions of Chlorine Atoms and Cl₂^{•-} Radical Anions in Aqueous Solutions. II. Toluene, Benzoic Acid, and Chlorobenzene. *J. Phys. Chem. A* **2001**, *105* (22), 5385–5392.
- (40) Hasegawa, K.; Neta, P. Rate Constants and Mechanisms of Reaction of Chloride (Cl⁻) Radicals. *J. Phys. Chem.* **1978**, *82* (8), 854–857.
- (41) Yang, S.; Fernando, S.; Holsen, T. M.; Yang, Y. Inhibition of Perchlorate Formation during the Electrochemical Oxidation of Perfluoroalkyl Acid in Groundwater. *Environ. Sci. Technol. Lett.* **2019**, *6* (12), 775–780.
- (42) Huang, X.; Li, X.; Pan, B.; Li, H.; Zhang, Y.; Xie, B. Self-Enhanced Ozonation of Benzoic Acid at Acidic PHs. *Water Res.* **2015**, *73*, 9–16.
- (43) Yang, Y.; Shin, J.; Jasper, J. T.; Hoffmann, M. R. Multilayer Heterojunction Anodes for Saline Wastewater Treatment: Design Strategies and Reactive Species Generation Mechanisms. *Environ. Sci. Technol.* **2016**, *50* (16), 8780–8787.
- (44) McDowell, D. C.; Huber, M. M.; Wagner, M.; von Gunten, U.; Ternes, T. A. Ozonation of Carbamazepine in Drinking Water: Identification and Kinetic Study of Major Oxidation Products. *Environ. Sci. Technol.* **2005**, *39* (20), 8014–8022.
- (45) Jasper, J. T.; Shafaat, O. S.; Hoffmann, M. R. Electrochemical Transformation of Trace Organic Contaminants in Latrine Wastewater. *Environ. Sci. Technol.* **2016**, *50* (18), 10198–10208.
- (46) Huang, X.; Qu, Y.; Cid, C. A.; Finke, C.; Hoffmann, M. R.; Lim, K.; Jiang, S. C. Electrochemical Disinfection of Toilet Wastewater Using Wastewater Electrolysis Cell. *Water Res.* **2016**, *92*, 164–172.
- (47) Schmalz, V.; Dittmar, T.; Haaken, D.; Worch, E. Electrochemical Disinfection of Biologically Treated Wastewater from Small Treatment Systems by Using Boron-Doped Diamond (BDD) Electrodes – Contribution for Direct Reuse of Domestic Wastewater. *Water Res.* **2009**, *43* (20), 5260–5266.
- (48) Haaken, D.; Dittmar, T.; Schmalz, V.; Worch, E. Influence of Operating Conditions and Wastewater-Specific Parameters on the Electrochemical Bulk Disinfection of Biologically Treated Sewage at Boron-Doped Diamond (BDD) Electrodes. *Desalination Water Treat.* **2012**, *46* (1–3), 160–167.
- (49) García-Gómez, C.; Droguí, P.; Zaviska, F.; Seyhi, B.; Gortáres-Moroyoqui, P.; Buelna, G.; Neira-Sáenz, C.; Estrada-alvarado, M.; Ulloa-Mercado, R. G. Experimental Design Methodology Applied to Electrochemical Oxidation of Carbamazepine Using Ti/PbO₂ and Ti/BDD Electrodes. *J. Electroanal. Chem.* **2014**, *732*, 1–10.
- (50) Rahmani, A. R.; Samarghandi, M. R.; Nematollahi, D.; Zamani, F. A Comprehensive Study of Electrochemical Disinfection of Water Using Direct and Indirect Oxidation Processes. *J. Environ. Chem. Eng.* **2019**, *7* (1), 102785.
- (51) Kerwick, M. I.; Reddy, S. M.; Chamberlain, A. H. L.; Holt, D. M. Electrochemical Disinfection, an Environmentally Acceptable Method of Drinking Water Disinfection? *Electrochim. Acta* **2005**, *50* (25), 5270–5277.

OZONE- AND HYDROXYL RADICAL-MEDIATED OXIDATION OF PHARMACEUTICAL COMPOUNDS USING NI-DOPED SB-SNO₂ ANODES: DEGRADATION KINETICS AND TRANSFORMATION PRODUCTS

Zhang, Y.; Guo, L.; Hoffmann, M. R. Ozone- and Hydroxyl Radical-Mediated Oxidation of Pharmaceutical Compounds using Ni-doped Sb-SnO₂ Anodes: Degradation Kinetics and Transformation Products. *ACS EST Eng.* **2023**, *3* (3), 335-348. <https://doi.org/10.1021/acsestengg.2c00337>.

3.1 Abstract

Electrochemical oxidation provides a versatile technique for treating wastewater streams onsite. We previously reported that a two-layer heterojunction Ni-Sb-SnO₂ anode (NAT/AT) can produce both ozone (O₃) and hydroxyl radical (\cdot OH). In this study, we explore further the applicability of NAT/AT anodes for oxidizing pharmaceutical compounds using carbamazepine (CBZ) and fluconazole (FCZ) as model probe compounds. Details of the oxidation reaction kinetics and subsequent reaction products are investigated in the absence and presence of chloride (Cl⁻) and sulfate (SO₄²⁻). In all cases, faster or comparable degradation kinetics of CBZ and FCZ are achieved using the double-layered NAT/AT anode coupled with a stainless steel (SS) cathode in direct comparison to an identical setup using a boron-doped diamond anode. Production of O₃ on NAT/AT enhances the elimination of both parent compounds and their transformation products (TPs). Very fast CBZ degradation is observed during NAT/AT-SS electrolysis in both NaClO₄ and NaCl electrolytes. However, more reaction products are identified in the presence of Cl⁻ than ClO₄⁻ (23 TPs vs. 6). Rapid removal of FCZ is observed in NaClO₄, while the degradation rate is retarded in NaCl depending on the [Cl⁻]. In SO₄²⁻-containing electrolytes, altered reaction pathways and transformation product distributions are observed due to sulfate radical generation. SO₄⁻ oxidation produces fewer hydroxylated products and promotes the oxidation of aldehydes to

carboxylic acids. Similar trend in treatment performance is observed in mixtures of CBZ and FCZ with other pharmaceutical compounds in latrine wastewater and secondary WWTP effluent.

Keywords: Ozone- and hydroxyl radical-mediated oxidation, Ni-doped Sb-SnO₂ anodes, pharmaceuticals, degradation kinetics, transformation products

3.2 Introduction

Pharmaceuticals represent an important group of emerging environmental contaminants due to excretion of ingested medicines in urine and feces and through the intentional disposal of unused or expired medicines.¹ Depending on the specific drug types, more than 90% of consumed pharmaceuticals can be excreted unmetabolized. Thus, residual pharmaceutical products have been detected in virtually all environmental waters including groundwater, surface water, and wastewater treatment plant (WWTP) influents and effluents.¹⁻⁴ This level of discharge of untreated or partially treated pharmaceutical products is problematic for aquatic systems and drinking water supplies. While traditional WWTPs are inadequate for degrading many commonly used pharmaceutical compounds,⁵⁻⁷ advanced oxidation processes (AOPs) involving reactive species such as ozone (O₃), hydroxyl radicals (\cdot OH), and free reactive chlorine provide an attractive alternative for compound degradation.⁸⁻¹⁰ Meanwhile, transformation products of pharmaceuticals also are an area of increasing research interest. The identification of specific transformation products allows us to further understand their ultimate environmental fates, including formation of transformation products that are more toxic than their parent compounds.^{1,11-13}

Electrochemical oxidation (EO) is applied in decentralized and small-scale wastewater treatment systems when preceded by a biological pretreatment step.^{14,15} The composition of the electro-active anode materials is a key factor in determining energy consumption and electrolytic treatment efficiency. Ideal nonactive electrodes suitable for wastewater treatment that promote complete oxidation of organic pollutants include boron-doped diamond (BDD) and antimony-doped tin oxide (AT: Sb-SnO₂) anodes.^{14,16,17} While large-scale application of BDD electrodes is hindered by high manufacturing costs, typical AT electrodes offer a less expensive option due to the absence of platinum-group metal components and lower

production costs. Moreover, when nickel is co-doped with AT (NAT: Ni-Sb-SnO₂), the NAT anodes produce ozone,^{18,19} which provides an additional anodic oxidation pathway.

Electrochemical oxidation has been investigated for various pharmaceutical compounds using dimensionally stable anodes (Ti/Pt/PbO₂),²⁰ mixed metal-oxide (Ti/Ir_xTa_yO₂/[Bi₂O₃]_z[TiO₂]_{1-z}),¹⁵ and mostly BDD electrodes²⁰⁻²² in pure electrolytes, latrine wastewater, and biologically-treated hospital wastewater. However, degradation with Sb-SnO₂-based anodes has not been well studied, and transformation product analysis is limited. In our previous study, a heterojunction Ni-Sb-SnO₂ anode (NAT/AT) was prepared that simultaneously produces ozone (O₃) and hydroxyl radical (\cdot OH) at the anode.²³ NAT/AT electrolysis was shown to be effective for treating a mixture of pharmaceutical compounds in toilet wastewater. An anodic O₃ activation mechanism was proposed by Zhang et al. to explain the accelerated degradation kinetics of some aromatic compounds that are not highly reactive with O₃ (e.g., ibuprofen, IBP, $k_{O_3,IBP} = 9.6 \text{ M}^{-1}\text{s}^{-1}$)⁸. Since aromatic rings and/or N and S atoms with nonbonded electrons are ubiquitous in pharmaceutical compounds, NAT/AT electrolysis should prove to be effective for treating pharmaceuticals in waste effluents.

The primary goal of this study is to investigate both the kinetics and the possible mechanistic pathways for product formation via NAT/AT-SS electrolysis in undivided cells as a promising AOP for pharmaceutical compound treatment in contaminated water. Degradation kinetics and transformation products (TPs) formation are studied in detail for carbamazepine (CBZ) and fluconazole (FCZ). CBZ and FCZ are persistently found in natural water bodies around the world.^{24,25} They are also excellent probes for studying reaction mechanisms and evaluating treatment efficiencies due to their different bimolecular rate constants with O₃ ($k_{O_3,CBZ} = 3.0 \times 10^5 \text{ M}^{-1}\text{s}^{-1}$ vs. $k_{O_3,FCZ} = 2.0 \text{ M}^{-1}\text{s}^{-1}$).^{8,26} The added impact of electrochemical O₃ production on the observed degradation kinetics and pathways in the NAT/AT system is compared to degradation using BDD electrodes as a reference anode material. The influence of pH and common ions present in wastewaters (Cl⁻ and SO₄²⁻)^{27,28} is investigated. Kinetic models to predict overall reaction kinetics and removal efficiencies are presented. Furthermore, pharmaceutical degradation at the NAT/AT anode is evaluated

in actual toilet wastewater and secondary effluent where the occurrence of these compounds is frequently reported.

3.3 Materials and Methods

Reagents and wastewater. All pharmaceutical compounds, acridine, carbamazepine 10,11-epoxide, and 9-acridinecarboxylic acid standards were purchased from Sigma-Aldrich. Actual latrine wastewater was collected from a public electrochemical toilet prototype on the campus of Caltech (Pasadena, CA). Secondary effluent was obtained from Sanitation Districts of Los Angeles County (Whittier, CA) and stored in the dark at 4°C for less than 1 month prior to use.

Stock solutions of individual pharmaceuticals were prepared at 20 μM in relevant electrolytes and stored under room temperature in the dark. Wastewater samples were filtered with 0.45 μm glass fiber membranes (Tisch) and amended with pharmaceuticals (2 μM) before treatment.

Electrolysis experiments. Two types of electrodes were used in this study. NAT/AT anodes were prepared by a dip-coating method as previously described.²³ BDD electrodes were purchased from NeoCoat (Switzerland). All electrochemical tests were performed in an undivided electrolysis cell. A stainless-steel cathode (6 cm^2) was coupled in parallel to an NAT/AT or BDD anode (6 cm^2) with a 5 mm separation. An Ag/AgCl/Sat. NaCl reference electrode (BASI Inc.) was placed at the same spacing close to the anode. Electrolysis experiments were conducted in 25 mL solutions at a fixed current density of 10 mA/cm^2 (specific surface area = 24 m^2/m^3).

Linear sweep voltammetry (LSV) was conducted using a Biologic VSP-300 potentiostat in relevant solutions using a scan rate of 0.05 V/s. For some experiments, solutions were buffered with 5 mM phosphate and pH was adjusted with perchloric acid (HClO_4), hydrochloric acid (HCl), or sodium hydroxide (NaOH).

Analytical methods and transformation product identification. Free chlorine concentrations were measured by DPD (N,N-diethyl-*p*-phenylenediamine) reagent (Hach DPD Method 10102). Dissolved O_3 produced by NAT/AT was quantified using the indigo

method.²⁹ Current efficiencies (η) for chlorine and O₃ evolution were calculated using the equation:

$$\eta = \frac{nVF dC}{I dt}$$

where n is the number of electrons required for one mole formation of Cl₂ from Cl⁻ ($n = 2$) or O₃ from O²⁻ ($n = 6$), V is the electrolyte volume (25 mL), F is Faraday constant (96,485 C/mol), and I is the current (A). Common wastewater ions (NH₄⁺, Cl⁻, Na⁺, K⁺, and Mg²⁺) were quantified by ion chromatography.

Carbamazepine (CBZ), fluconazole (FCZ), and other pharmaceutical compounds were quantified using high-performance liquid chromatography coupled with a UV detector (HPLC-UV) and equipped with an XDB-C18 column (ZORBAX, 2.1 × 50 mm, 1.8 μm particles). CBZ and FCZ were monitored at 285 and 205 nm, respectively. Eluent flowed at 0.4 mL/min and consisted of acetonitrile (ACN) and water with 0.1% formic acid. A gradient was used to resolve peaks: 0 min, 5% ACN; 2 min, 5% ACN; 6 min, 95% ACN; 8 min, 95% ACN; 9 min, 5% ACN; 12 min, 5% ACN.

For transformation product identification, electrolysis of CBZ and FCZ was conducted at elevated compound concentration (20 μM) and in solutions containing: NaClO₄ (50 mM), Na₂SO₄ (5 mM) + NaClO₄ (50 mM), NaCl (50 mM), or Na₂SO₄ (5 mM) + NaCl (50 mM). Products were analyzed using an ultrahigh performance liquid chromatography system (Waters Acquity UPLC) coupled to a time-of-flight mass spectrometer (Waters Xevo GS-2 TOF) equipped with an Acquity BEH C18 column (2.1 × 50 mm, 1.7 μm particles). Eluent consisting of ACN and water with 0.1% formic acid flowed at 0.5 mL/min. The applied ACN/H₂O gradient profile was as follows: 0 min, 5% ACN; 0.2 min, 5% ACN; 3.2 min, 95% ACN; 3.5 min, 95% ACN; 3.6 min, 5% ACN; 5 min, 5% ACN. Products were monitored under positive electrospray ionization (ESI⁺) in resolution mode (measurement accuracy better than 1 ppm RMS) with 0.2 kV capillary voltage. Other mass spectrometer conditions include: cone voltage 50 V, source offset 80 V, source temperature 120°C, desolvation temperature 400°C, cone gas 40 L/h, desolvation gas 800 L/h, 0.3 s scan time in continuum mode, collision energy 1.0 eV, and second acquisition channel collision energy

scanned from 0 to 30 eV. A leucine lock-mass ($m/z = 556.2771$) was used to correct for accurate mass values.

Parent compounds and transformation products (TPs) were identified with the Masslynx software (Waters) and quantified with Quanlynx. TP chemical formulas were obtained using accurate mass determinations and known parent compound elemental compositions. Tentative structures were proposed based on fragmentation patterns, isotopic patterns (when chloride present), authentic standards (when available), and comparison to literature.

Theoretical modeling. Kinetic modeling and prediction of pharmaceutical degradation kinetics were achieved using the chemical kinetics computational program, Kintecus 6.80.³⁰ A total of 117 elementary reactions were considered with rate constants obtained from the literature. The model was evaluated in all electrolytes to examine the influence of salts on degradation kinetics (more details in [Text 3.S1](#) and [Table 3.S1](#)).

3.4 Results and Discussion

Degradation kinetics. Degradation was investigated in detail for carbamazepine (CBZ, 20 μM) and fluconazole (FCZ, 20 μM).

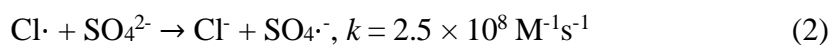
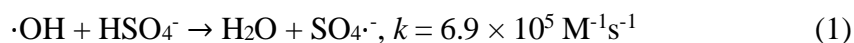
CBZ. Fast degradation of CBZ was observed using the NAT/AT anode ([Figure 3.1a](#)). For example, complete removal was achieved in less than 30 s in NaClO_4 electrolytes, which appears to be due to direct oxidation by O_3 . Our kinetic model also predicted complete removal in 30 s ([Figure 3.S1a](#)). When Cl^- is present in the system, O_3 production is inhibited due to competition for active sites between Cl^- and OH^- ,²³ although rapid removal is achieved with 100% removal in less than 1 min in NaCl electrolytes. Despite lower aqueous-phase O_3 concentrations, a similar CBZ removal efficiency is achieved due to the formation of the chlorine radical anion $\text{Cl}_2^{\cdot-}$ ($E^0 = 2.1 \text{ V}_{\text{NHE}}$, estimated $k_{\text{Cl}_2^{\cdot-}, \text{CBZ}} = 2.6 \times 10^9 \text{ M}^{-1}\text{s}^{-1}$).¹¹ Prediction using the kinetic model also gave similar results taking into account the kinetics of the chlorine radical anion ([Figure 3.S1b](#)).

Degradation of CBZ with BDD was slower in both electrolytes compared to that with NAT/AT due to the absence of O_3 production ([Figure 3.1b](#)). Reaction retardation was greater in NaClO_4 electrolytes, in which ~60% removal was obtained within 20 min. In NaCl , however, the differences in degradation kinetics were less pronounced, with complete

removal achieved after 5 min of electrolysis, which is consistent with oxidation of CBZ by the chlorine radical species. For both NAT/AT and BDD anodes in NaClO₄ and NaCl electrolyte solutions, there was no discernible impact of the sulfate radical anion, SO₄^{•-}, on the observed degradation kinetics. The reaction rate constant between SO₄^{•-} and CBZ is smaller than that between •OH and CBZ but on the same order of magnitude ($k_{\text{SO}_4^{\bullet-}, \text{CBZ}} = 1.9 \times 10^9 \text{ M}^{-1}\text{s}^{-1}$ vs. $k_{\text{OH}, \text{CBZ}} = 8.8 \times 10^9 \text{ M}^{-1}\text{s}^{-1}$).⁷ However, due to the low concentration of SO₄²⁻ and thus SO₄^{•-} present, CBZ degradation was dominated by O₃, chlorine radical species, and •OH.

FCZ. Very different degradation rates were obtained using the NAT/AT anode in NaClO₄ vs. NaCl electrolytes (**Figure 3.1c**). The rate constant between FCZ and O₃ is five orders of magnitude lower than that of CBZ. However, faster-than-expected degradation was again observed with NAT/AT in NaClO₄ electrolytes. 100% removal was attained in 5 min, which is notably faster than the predicted degradation rates considering reactions with both O₃ and •OH (**Figure 3.S2a**). This result suggests that, similar to ibuprofen,²³ FCZ degradation is promoted by anodic O₃ activation on the NAT/AT anode. In NaCl solutions, on the other hand, FCZ removal was retarded compared to that in NaClO₄ given that only 60-70% removal was observed after 1 h of electrolysis. This removal rate did not deviate significantly from our kinetic model predictions (**Figure 3.S2b**), indicating that anodic O₃ activation had little impact in this case.

Electrolysis using the BDD anode resulted in ~80% FCZ removal in 20 min in NaClO₄ and 80-90% removal in 1 h in NaCl electrolytes (**Figure 3.1d**). Higher removal efficiencies for BDD than NAT/AT in NaCl electrolytes are consistent with higher •OH production levels at BDD coupled with an added contribution from direct electron transfer (*vide infra*). For FCZ, degradation with both electrodes was enhanced in the presence of SO₄²⁻ in NaCl electrolytes. We propose that such enhancement in removal kinetics results from oxidation by sulfate radicals (SO₄^{•-}), which have a comparable or slightly higher redox potential ($E^0 = 2.5\text{-}3.1 \text{ V}_{\text{NHE}}$)³¹ than that of •OH ($E^0 = 2.7 \text{ V}_{\text{NHE}}$).³² Formation of SO₄^{•-} occurs via the following two pathways:^{32,33}



with the second reaction, eq. 2, occurring only when $\text{Cl}\cdot$ ($E^0 = 2.4 \text{ V}_{\text{NHE}}$)³⁴ forms from Cl^- in solution. Even though $[\text{HSO}_4^-]$ ($\text{pK}_a = 1.92$)³⁵ is negligible in the bulk solution at $\text{pH} \sim 9$, sulfate radical production via eq. 1 could actually take place within the acidic ($\text{pH} < 2$) electrical double-layer very close to the anode surface. Compared to $\cdot\text{OH}$, $\text{SO}_4^{\cdot-}$ is a more selective oxidant that reacts primarily via electron transfer.^{7,31,36} While $\cdot\text{OH}$ also reacts readily and rapidly via addition and H-abstraction pathways, $\text{SO}_4^{\cdot-}$ generally has lower rate constants for those reactions. For many pharmaceutical compounds, however, reactions rates with $\text{SO}_4^{\cdot-}$ are comparable to or occasionally faster than those with $\cdot\text{OH}$.⁷ In addition to FCZ, the presence of SO_4^{2-} in wastewater matrices has been reported to accelerate removal of other pharmaceutical compounds including ciprofloxacin, sulfamethoxazole,²² and ketoprofen²¹ using BDD anodes. With FCZ, the effect of SO_4^{2-} was prominent in NaCl electrolytes. This result suggests that $\text{SO}_4^{\cdot-}$ played a more important role in cases where O_3 and/or $\cdot\text{OH}$ -mediated oxidation was less important. In NaClO_4 electrolytes, in contrast, FCZ removal appeared to be unaffected in the presence of SO_4^{2-} .

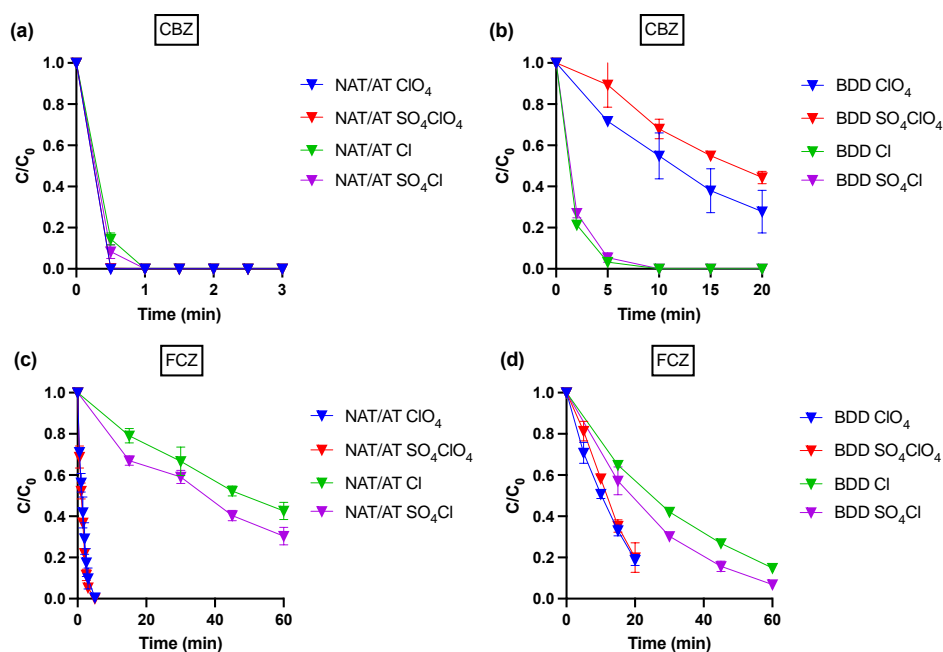


Figure 3.1 Electrochemical oxidation of carbamazepine (CBZ) by (a) NAT/AT and (b) BDD, and of fluconazole (FCZ) by (c) NAT/AT and (d) BDD in ClO_4^- : 50 mM NaClO_4 ,

SO₄ClO₄: 5 mM Na₂SO₄ + 50 mM NaClO₄, Cl: 50 mM NaCl, and SO₄Cl: 5 mM Na₂SO₄ + 50 mM NaCl electrolytes.

The higher removal percentage of FCZ than CBZ at BDD over 20 min even though the reaction rate constant between FCZ and ·OH is slightly lower ($k_{\text{FCZ},\cdot\text{OH}} = 4.4 \times 10^9 \text{ M}^{-1}\text{s}^{-1}$ vs. $k_{\text{CBZ},\cdot\text{OH}} = 8.8 \times 10^9 \text{ M}^{-1}\text{s}^{-1}$)^{8,26} suggests that additional oxidation pathways are operative. Given that direct electron transfer (DET) is known to happen at the surface of BDD (but not NAT/AT), it was suspected that DET made a substantial contribution to the removal of FCZ. DET from FCZ to BDD was confirmed using linear sweep voltammetry (LSV) in 50 mM NaClO₄ (control) and in 50 mM NaClO₄ containing 20 μM CBZ or FCZ (**Figure 3.S3**). While no obvious feature is observed for CBZ comparing to the NaClO₄ control, a notable peak was recorded at ~3.0 V_{NHE} in the FCZ voltammogram, which implies that DET is taking place.

The FCZ degradation results on both anodes in NaCl electrolytes indicate that FCZ is relatively resistant to oxidation by both free chlorine and chlorine radical species. This hypothesis is supported by a separate control experiment using a NaOCl solution (<30% removal in 2 h with excess NaOCl, data not shown) as well as experiments at NAT/AT with variable Cl⁻ concentrations. When [Cl⁻] is decreased from 50 to 5 mM, removal of FCZ after 1 h increased from 60 to >80% (**Figure 3.2a**), which results from higher O₃ production with lower [Cl⁻].²³

The influence of pH on FCZ degradation was also investigated using both electrolytes with pH adjusted to 5, 7, and 9 in phosphate buffers. In some cases, pH 2 was also examined for trend elucidation. In NaClO₄, pH had negligible influence on FCZ removal for NAT/AT and BDD (**Figure 3.S4**). Similar degradation kinetics at all pH values indicate a consistent ·OH production on the anode surface coupled with O₃ production on NAT/AT. In NaCl, different kinetic profiles for BDD compared to NAT/AT were observed. For example, degradation on BDD anode was not influenced by the variation in electrolyte pH in that similar removal levels were observed as pH was lowered from 9 to 2 (**Figure 3.2b**). This result, along with the similar result in **Figure 3.S4**, also suggested that phosphate buffer did not influence degradation kinetics. On the NAT/AT anode, on the other hand, faster FCZ

degradation was recorded as pH was lowered from 9 to 5 (e.g., ~60% degradation at pH 9 to >90% degradation at pH 5 after 1 h of electrolysis). However, the trend did not continue to pH 2, where the slowest removal was observed (**Figure 3.2c**).

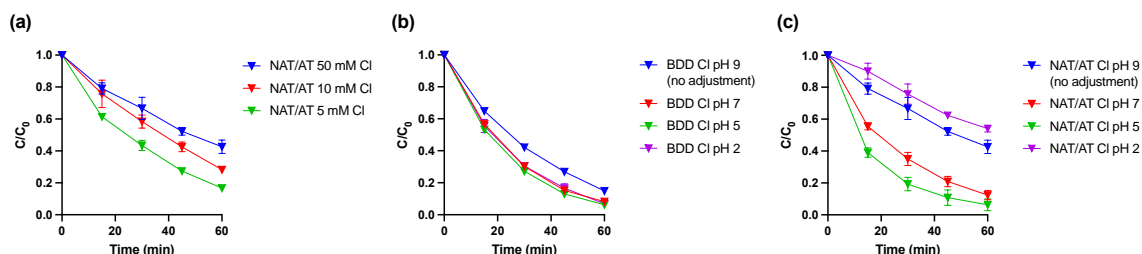


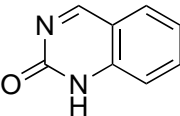
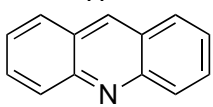
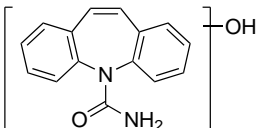
Figure 3.2 (a) FCZ degradation by NAT/AT under different chloride concentrations (50, 10, and 5 mM NaCl, 5 mM NaClO₄ was added to 5 mM NaCl to compensate for lower conductivity). Influence of pH on FCZ degradation by (b) BDD and (c) NAT/AT in 50 mM NaCl electrolytes. For degradation under pH 9 (no adjustment), no phosphate buffer was added.

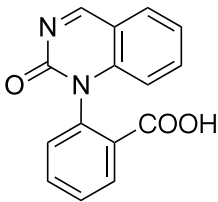
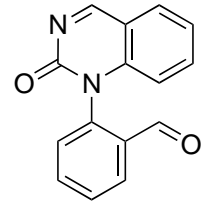
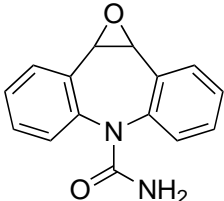
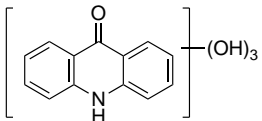
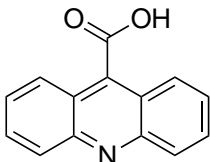
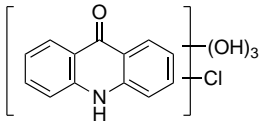
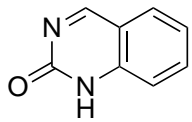
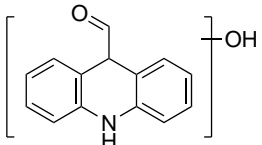
To explain the differences in FCZ degradation vs. pH, chlorine evolution was measured for each anode, and O₃ evolution was measured only on the NAT/AT anode. Chlorine evolution, due to the production of reactive chlorine species, intrinsically leads to an increase in solution pH because of the depletion of H⁺ at cathode comparing to OH⁻ at anode. During the chlorine evolution experiments, pH quickly rose to ~9 from circumneutral pH. On the other hand, it is also known that solution pH affects chlorine evolution kinetics.³⁷ With BDD, stable chlorine evolution rates as well as current efficiencies were recorded at all pH values from 2 to 9 (**Figure 3.S5a**). With NAT/AT, on the other hand, decreased chlorine evolution (CER) and lower current efficiencies were observed as the pH was decreased (**Figure 3.S5b**). Meanwhile, the aqueous O₃ concentrations followed an opposite trend in that during 15 min of electrolysis, the steady state [O₃] increased from ~0.5 mg/L at pH 9 to ~2 mg/L at pH 2 (**Figure 3.S6**). These results suggest that, at NAT/AT in the presence of Cl⁻, lower pH values favor the production of O₃ over chlorine evolution, which can explain the FCZ degradation trend in the pH range from 9 to 5. At pH 2, despite higher O₃ production, the slowest FCZ removal can be attributed to the different reactivities between deprotonated and protonated

species with O₃.³⁸ In many cases, reactions rate of the deprotonated species of a compound can be several orders of magnitude higher than that of its protonated species. FCZ has pKa values of 2.6, 2.9, and 11.0, where 2.6 and 2.9 correspond to the two nitrogens in the triazole rings.³⁹ At pH 2, a protonated nitrogen could have significantly lower or no reactivity with O₃, resulting in retarded removal. Though kinetic data is not available for FCZ, the deprotonated form of imidazole, with a similar structure to triazole, reacts with O₃ four orders of magnitude faster compared to its protonated form.³⁸

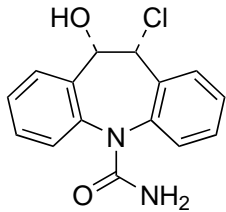
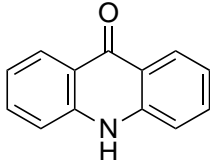
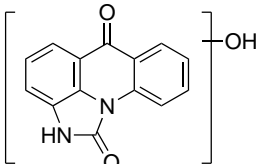
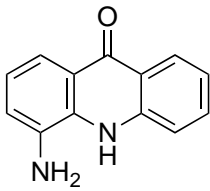
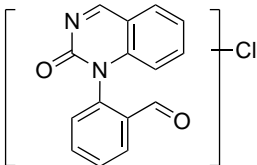
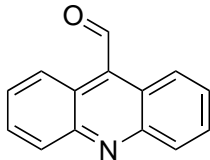
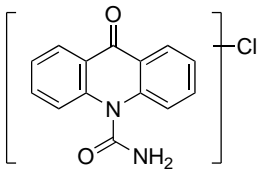
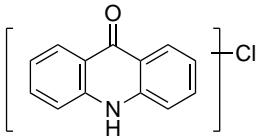
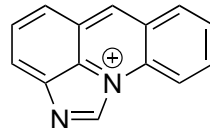
Transformation product formation, identification, and removal. LC-MS analysis showed that there were 23 distinct transformation products (TPs) observed during CBZ oxidation, ten of which have not been previously reported. Properties of the TPs as documented in **Table 3.1** include the corresponding retention times (RT), the measured *m/z* ratios, major fragment ions, mass error to theoretical *m/z* ratios, calculated chemical formulas, and proposed structures and their confidence levels. Reaction pathways for TP formation are proposed in **Figure 3.3** based on this information and further TP analysis (*vide infra*). The pathways presented, as will be shown later, may not be comprehensive, and formation of many TPs is possible via multiple pathways.

Table 3.1 Carbamazepine (CBZ) transformation products.

TP ^{a,b,c}	RT (min)	TP <i>m/z</i> (Name)	Major fragment ions <i>m/z</i>	Mass error (ppm)	Calculated formula	Proposed structure	Confidence level ^d	Refs
NaClO₄ Electrolytes								
TP147	3.11	147.0556	129.0451	1.4	C ₈ H ₇ N ₂ O		2b	this study
TP180	3.55	180.0819 (acridine)	-	3.3	C ₁₃ H ₁₀ N		1	40-42 std
TP253 a	4.02	253.0972	235.0853 207.0823 180.0814	2.0	C ₁₅ H ₁₃ N ₂ O ₂		3	42 Figure 3.S7

TP267	4.12	267.0768 (BaQM)	249.0671 221.0719	0.7	$C_{15}H_{11}N_2$ O_3		2a	40,43,44	
TP251	4.23	251.0824 (BQM)	208.0767 180.0816	1.2	$C_{15}H_{11}N_2$ O_2		2a	41,43,45, 46	
TP253 b	4.44	253.0972 (CBZ epoxide)	236.0717 210.0924 180.0818	2.0	$C_{15}H_{13}N_2$ O_2		1	41- 43,46-48 std	
NaCl Electrolytes									
TP244	1.58	244.0619	200.0712 182.0611	3.7	$C_{13}H_{10}N$ O_4		3	this study	
TP224	2.63	224.0716	196.0766 180.0833 167.0726	1.8	$C_{14}H_{10}N$ O_2		2a	40,41,43, 46,48 std	
TP278	3.00	278.0229	234.0323 216.0220	3.2	$C_{13}H_9NO$ $4Cl$		3	this study	
TP147	3.11	147.0556	129.0451	1.4	$C_8H_7N_2O$		2b	this study	
TP226	3.15	226.0869	208.0767 180.0814	0.4	$C_{14}H_{12}N$ O_2		3	42	

TP271	3.49	271.1083	210.0926	0.0	$C_{15}H_{15}N_2$ O_3		2a	41– 43,46–48
TP180	3.55	180.0813 (acridine)	-	0.0	$C_{13}H_{10}N$		1	40-42 std
TP181	3.67	181.0173	146.0467	2.2	$C_8H_6N_2O$ Cl		3	this study
TP253 a	3.97	253.0981	236.0711 210.0922 180.0817	1.6	$C_{15}H_{13}N_2$ O_2		3	42
TP267	4.12	267.0768 (BaQM)	249.0671 221.0719	0.7	$C_{15}H_{11}N_2$ O_3		2a	40,43,44
TP210	4.23	210.0918	180.0820	0.5	$C_{14}H_{12}N$ O		2a	42
TP251	4.23	251.0826 (BQM)	208.0767 180.0816	2.0	$C_{15}H_{11}N_2$ O_2		2a	41,43,45, 46
TP301	4.30	301.0380	221.0725 195.0681	0.0	$C_{15}H_{10}N_2$ O_3Cl		3	this study
TP253 b	4.37	253.0981 (CBZ epoxide)	236.0717 210.0924 180.0818	1.6	$C_{15}H_{13}N_2$ O_2		1	41– 43,46–48 std

TP289	4.40	289.0746	228.0583 193.0901 180.0823	0.7	$C_{15}H_{14}N_2$ O_2Cl		2b	49
TP196	4.48	196.0769 (acridone)	180.0815 167.0730	3.6	$C_{13}H_{10}N$ O		2a	40-42
TP253 c	4.51	253.0613	235.0508 179.0609	0.0	$C_{14}H_9N_2$ O_3		3	this study
TP211	4.58	211.0875	-	1.9	$C_{13}H_{11}N_2$ O		3	this study
TP285	4.75	285.0437	221.0720	2.1	$C_{15}H_{10}N_2$ O_2Cl		3	this study
TP208	5.17	208.0768	180.0811	2.9	$C_{14}H_{10}N$ O		2a	40,41,43, 46
TP273	5.23	273.0434	196.0769 180.0818 167.0738	1.1	$C_{14}H_{10}N_2$ O_2Cl		3	this study
TP230	5.23	230.0380	195.0681 180.0815 167.0735	3.0	$C_{13}H_9NO$ Cl		3	42
TP205	5.89	205.0769	178.0656 151.0550	1.5	$C_{14}H_9N_2$		3	this study

- a. TPs marked with underline have, to the best of our knowledge, not been reported before.
- b. TPs marked in green are not detected at BDD, and TPs marked in blue are not detected at NAT/AT, in respective electrolytes.
- c. Mass spectra of TPs containing Cl in their chemical formula are provided in **Figure 3.S8**.
- d. Confidence levels are assigned based on the level system proposed by Schymanski et al.⁵⁰ for emerging pollutant transformation product identification. The meaning of each level is: level 1 – confirmed structure by reference standard; level 2 – probable structure by 2a. literature matching of fragmentation patterns and 2b. diagnostic evidence where only one structure fits the experimental information; level 3 – tentative candidate where either the structure is tentative and/or substitution positions are uncertain. For level 3 TPs where structure rather than substitution position is uncertain, tentative structure is proposed based on fragmentation analysis when available (**Table 3.S2**).

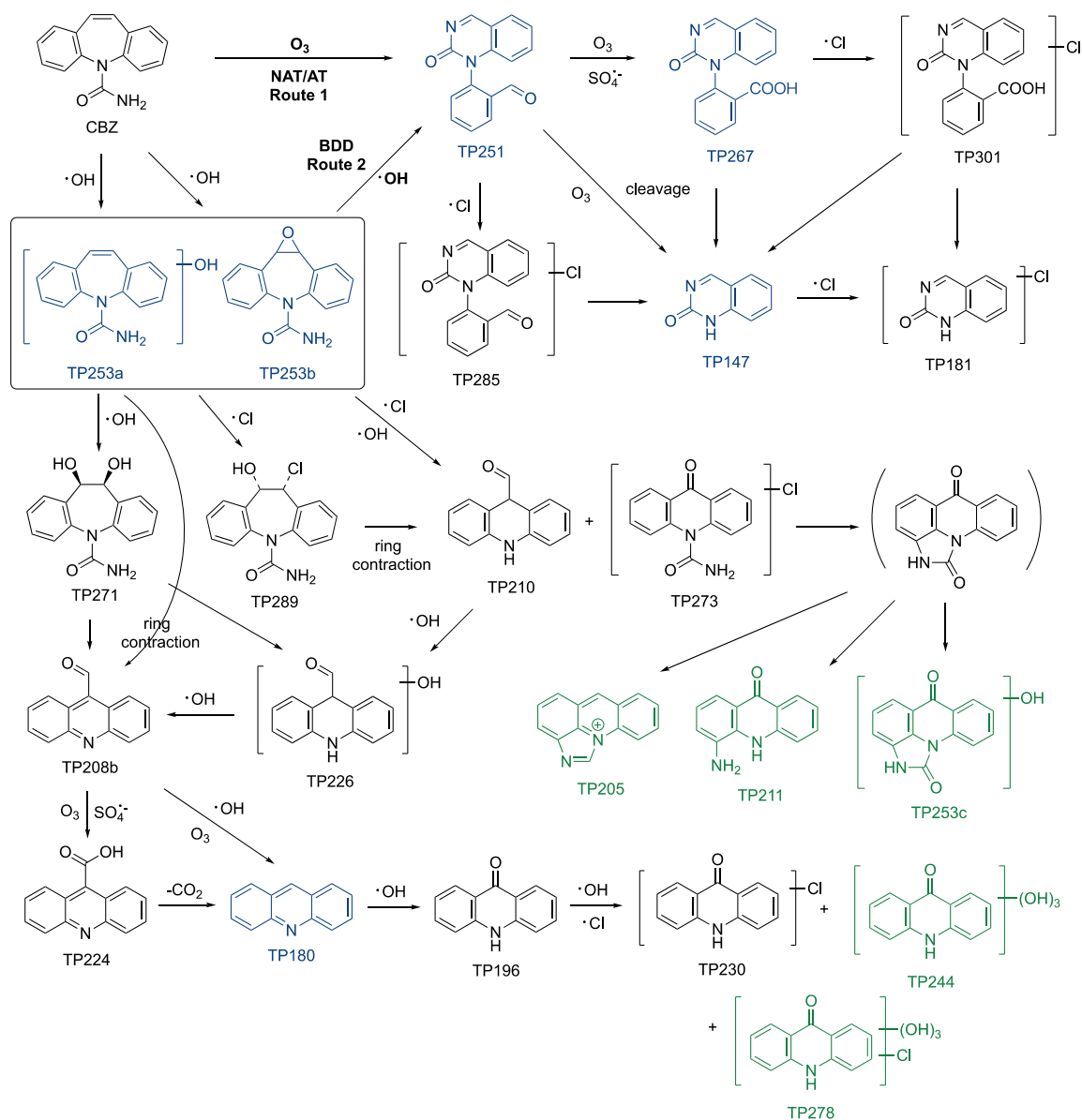


Figure 3.3 Proposed carbamazepine (CBZ) transformation pathways. Blue structures mark products detected during electrolysis in NaClO_4 electrolytes. Green structures mark products with higher confidence levels/higher uncertainties and thus more tentative structures and pathways.

CBZ in NaClO_4 electrolytes. In NaClO_4 electrolytes, 5 TPs (TP147, TP180, TP253a, TP267, and TP251) were detected using NAT/AT and 5 (TP180, TP253a, TP267, TP251, and

TP253b) using BDD (**Figure 3.3**, labeled blue). For NAT/AT, TP251 ($m/z = 251.0824$, $C_{15}H_{11}N_2O_2$) showed an MS response one order of magnitude higher than all the other TPs in $NaClO_4$ -based electrolytes (**Figure 3.4a**). This TP was identified as 1-(2-benzaldehyde)-4-hydro-(1H,3H)-quinazoline-2-one (BQM), which has been previously reported as a major CBZ ozonation product (**Figure 3.3**, route 1).^{43,45} Another identified product was TP267 ($m/z = 267.0768$, $C_{15}H_{11}N_2O_3$). While various structures have been proposed for the same m/z ratios in the literature, based on its fragmentation patterns, TP267 was identified as the carboxylic acid of TP251 (BaQM). The oxidation of BQM (TP251) to BaQM (TP267) has been reported before during ozonation.⁴³ Other pathways for BaQM formation were also seen during biological⁴⁰ and ferrate⁴⁴ oxidation of CBZ, where BQM was not detected. Similar to the oxidation of BQM to BaQM, an aldehyde-to-carboxylic-acid pathway has been reported in a variety of treatment options including ozonation,⁴⁵ UV/chlorine,⁴² UV/TiO₂ photocatalysis,⁴⁷ ferrate,⁴⁴ and biodegradation with white-rot fungus *Pleurotus ostreatus*.^{41,46} In our case, the abundance of TP267 increased significantly when SO_4^{2-} was added in the electrolyte solution (**Figure 3.S9a**), which implies that $SO_4^{\cdot-}$ is also capable of oxidizing aldehydes to carboxylic acids. Following TP251 and TP267, TP147 ($m/z = 147.0556$, $C_8H_7N_2O$) was formed via bond cleavage. Due to fast reaction between CBZ and O_3 , oxidation by $\cdot OH$ played a minor role in oxidation with NAT/AT. The hydroxylated product, TP253a ($m/z = 253.0972$, $C_{15}H_{13}N_2O_2$), was detected with the lowest response among all 5 TPs, with its maximum peak area three orders of magnitude less than that of TP251.

For BDD electro-oxidation, the TP with the highest response in the MS was also TP251, although the maximum peak area was one order of magnitude smaller compared to that for NAT/AT (**Figure 3.4b**), which can be explained by the longer treatment time. Another TP with $m/z = 253.0972$ (TP253b) was detected, which was not seen during NAT/AT electrolysis. This product is carbamazepine 10,11-epoxide (CBZ-EP) based on direct comparison to commercial standard. The peak area of CBZ-EP stayed relatively constant during 20 min of electrolysis (**Figure 3.S9b**). In the case of BDD-induced $\cdot OH$ -mediated oxidation, in comparison to the direct formation of TP251 (BQM) via ozonation, we propose that CBZ is first oxidized to its hydroxylated product (TP253a), which is in turn oxidized to BQM (**Figure 3.3**, route 2). The bond cleavage product TP147 was not detected during BDD

electrolysis in NaClO₄ electrolytes. Additionally, TP267 was detected at very low levels only in the presence of SO₄²⁻, which indicates that ·OH was less effective than SO₄⁻ for the oxidation of aldehydes to carboxylic acids.

Finally, electrolysis in NaClO₄ led to the formation of TP180 ($m/z = 180.0819$, C₁₃H₁₀N), which was confirmed using a reference standard to be acridine, a known mutagenic and carcinogenic compound.¹¹ TP180 is relatively stable. It forms in CBZ stock solutions and, in cases where the stock was kept for longer times, was actually detected without electrolysis. TP180 is also transformed slowly by ·OH. Comparing to the relatively fast removal by O₃ with NAT/AT, it was only slowly removed using BDD (Figure 3.S9b).

Removal of the TPs was slower in comparison to parent compound degradation. The 5 TPs detected using NAT/AT were formed and basically completely removed within 5 min of electrolysis (Figure 3.4a and 3.S9a). For BDD, the TP concentrations leveled off after 20 min, after which their concentrations started to decrease due to further oxidation (Figure 3.4b and 3.S9b). This result indicates that longer treatment times are required for further oxidative removal of the TPs where ·OH is the sole oxidant.

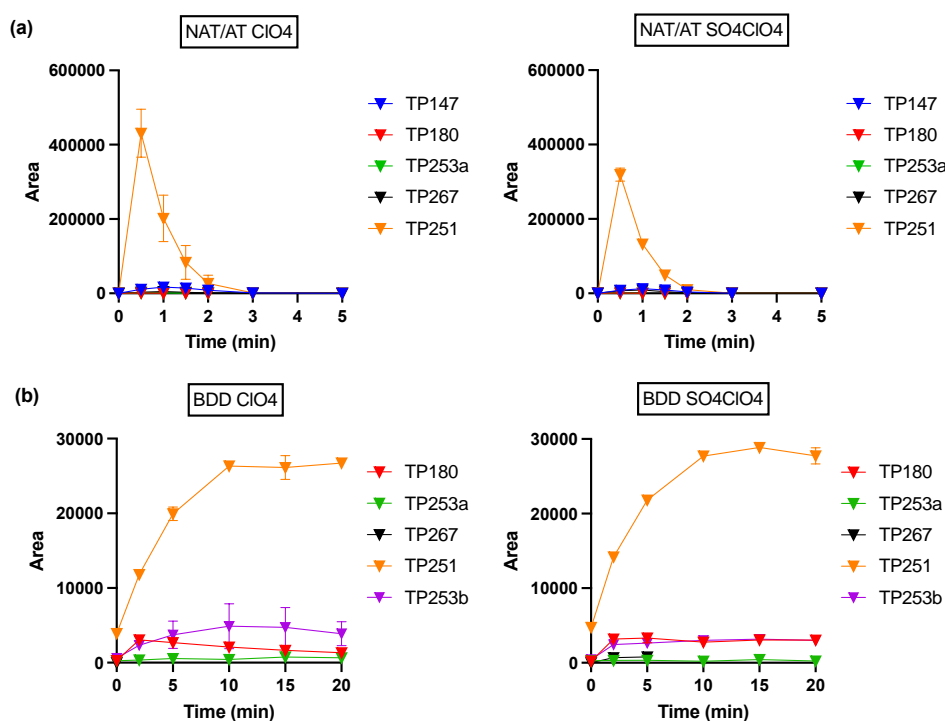


Figure 3.4 CBZ transformation product evolution in NaClO₄ electrolytes at (a) NAT/AT and (b) BDD.

CBZ in NaCl electrolytes. In NaCl electrolytes, more TPs were detected compared to those found during electrolysis in NaClO₄. During electrolysis in NaCl, 22 and 18 out of all 23 TPs were detected using NAT/AT and BDD anodes, respectively. For NAT/AT, TP251 was again the highest response TP with maximum peak intensity occurring at 0.5 min (**Figure 3.5a**). In this case, unlike that in NaClO₄, it was no longer the overwhelming peak in the MS. If we assign the peak area of TP251 at 0.5 min to be a response of 1.0, then 7 of the other TPs had maximum responses of >0.05. TP285 ($m/z = 285.0437$, C₁₅H₁₀N₂O₂Cl) had a response of ~0.74 and was identified as the chlorination by-product of TP251. TP253b (CBZ-EP), the epoxide product mediated by ·OH oxidation, was also detected at substantial levels in NaCl compared to that in NaClO₄. Another set of interesting TPs included TP208 ($m/z = 208.0768$, C₁₄H₁₀NO), TP224 ($m/z = 224.0716$, C₁₄H₁₀NO₂), TP180, and TP196 ($m/z = 196.0768$, C₁₃H₁₀NO). TP208 was determined to be 9-acridine-carboxaldehyde. Possible precursors for it include TP253a and TP253b (*vide infra*). The pathway TP253b → TP208 has been reported during ozonation,⁴³ ClO₂ oxidation,⁵¹ and biotransformation^{46,51} by ring contraction and loss of the carbamoyl group. Oxidation of the aldehyde group on TP208 gives the corresponding carboxylic acid product TP224 (9-acridinecarboxylic acid), which can undergo decarboxylation to give TP180, acridine. TP208 and TP224 represent another aldehyde-to-carboxylic-acid pair like TP251 and TP267. Hydroxylation and oxidation of TP180 then leads to the formation of TP196, acridone, which also had a relative response factor of >0.05. The oxidation of acridine to acridone has been confirmed in electrochemical oxidation³⁹ and represents a known biological detoxification process.⁴⁶ The sequence of pathways from TP208 to TP196 has been observed in biotransformation in WWTP biological processes⁴⁰ as well as with the white-rot fungus *Pleurotus ostreatus*.^{41,46} Direct formation of TP180 from TP208 by cleavage of the aldehyde group is also possible.^{46,51} In addition to the above 4 TPs, TP226 ($m/z = 226.0869$, C₁₄H₁₂NO₂) could be another hydroxylated precursor of TP208, and TP253c ($m/z = 253.0613$, C₁₄H₉N₂O₃) is proposed to form via an intramolecular cyclization at the carbamoyl group. Overall, since O₃ production is inhibited

in the presence of Cl^- , other oxidation pathways played more important roles in the formation of the other TPs.

Many additional TPs were observed using NAT/AT although with lower relative responses. In addition to TP285, which is the chlorinated by-product of TP251, TP301 ($m/z = 301.0380$, $\text{C}_{15}\text{H}_{10}\text{N}_2\text{O}_3\text{Cl}$), TP181 ($m/z = 181.0173$, $\text{C}_8\text{H}_6\text{N}_2\text{OCl}$), TP289 ($m/z = 289.0746$, $\text{C}_{15}\text{H}_{14}\text{N}_2\text{O}_2\text{Cl}$),⁴⁹ and TP230 ($m/z = 230.0380$, $\text{C}_{13}\text{H}_9\text{NOCl}$) were identified as the chlorinated by-products of TP267, TP147, TP253b, and TP196, respectively. TP271 ($m/z = 271.1088$, $\text{C}_{15}\text{H}_{15}\text{N}_2\text{O}_3$) was identified as 10,11-dihydro-10,11-*cis*-dihydroxy-carbamazepine (*cis*-diOH-CBZ). TP205 ($m/z = 205.0769$, $\text{C}_{14}\text{H}_9\text{N}_2$) and TP211 ($m/z = 211.0875$, $\text{C}_{13}\text{H}_{11}\text{N}_2\text{O}$) were two other products, besides TP253c, that may have formed after carbamoyl group intramolecular cyclization. This cyclization pathway has also been proposed in the treatment of CBZ by UV/chlorine and UV/ H_2O_2 .^{42,48,52} Finally, TP230 ($m/z = 230.0380$, $\text{C}_{13}\text{H}_9\text{NOCl}$), TP244 ($m/z = 244.0619$, $\text{C}_{13}\text{H}_{10}\text{NO}_4$), and TP278 ($m/z = 278.0229$, $\text{C}_{13}\text{H}_9\text{NO}_3\text{Cl}$) are proposed to be the singly and multiply hydroxylated and chlorinated product of TP196, acridone.

Formation patterns of several TPs were different when SO_4^{2-} was present in the electrolyte. Like TPs formed in NaClO_4 electrolytes, the relative response factor of TP267 was significantly higher (**Figure 3.S10a**) along with its corresponding chlorinated by-product, TP301 (**Figure 3.S10b**). Another carboxylic acid product, TP224, was also detected in higher abundance when SO_4^{2-} was added to the base electrolyte despite TP208 having a lower response (**Figure 3.S10c**). Meanwhile, lower response factors for several other TPs were observed. The more prominent ones include TP226, TP271, and TP253a (**Figure 3.S10d-e**). These collective observations indicate that, in the presence of SO_4^{2-} , oxidation was primarily promoted by $\cdot\text{OH}$ and $\text{SO}_4^{\cdot-}$ simultaneously along with subsequent chlorination. However, $\cdot\text{OH}$ played a smaller role in oxidation comparing to the cases in which SO_4^{2-} was absent. Since electron transfer is the preferred oxidation pathway by $\text{SO}_4^{\cdot-}$ as opposed to addition or H-abstraction, the hydroxylated products produced by $\cdot\text{OH}$ oxidation were formed in lower yields.

In the case of BDD electrolysis, the product with the highest response was TP208 with an intensity that peaked at 0.5 min (**Figure 3.5b**). TP208 was followed by TP253b and TP180

with relative response factors of ~ 0.59 and 0.36 , respectively. Like the reactions occurring in NaClO_4 electrolytes, the maximum MS peak area was also one order of magnitude smaller than that for NAT/AT. TP147 and TP267, as well as their chlorinated by-products TP181 and TP301, were not detected during BDD electrolysis at measurable levels in both solutions. Furthermore, TP251 appeared to be a less important TP, which suggests that other oxidation pathways predominated over route 2 in **Figure 3.3**. Overall, the same mixture of TPs was observed using BDD as those found with NAT/AT.

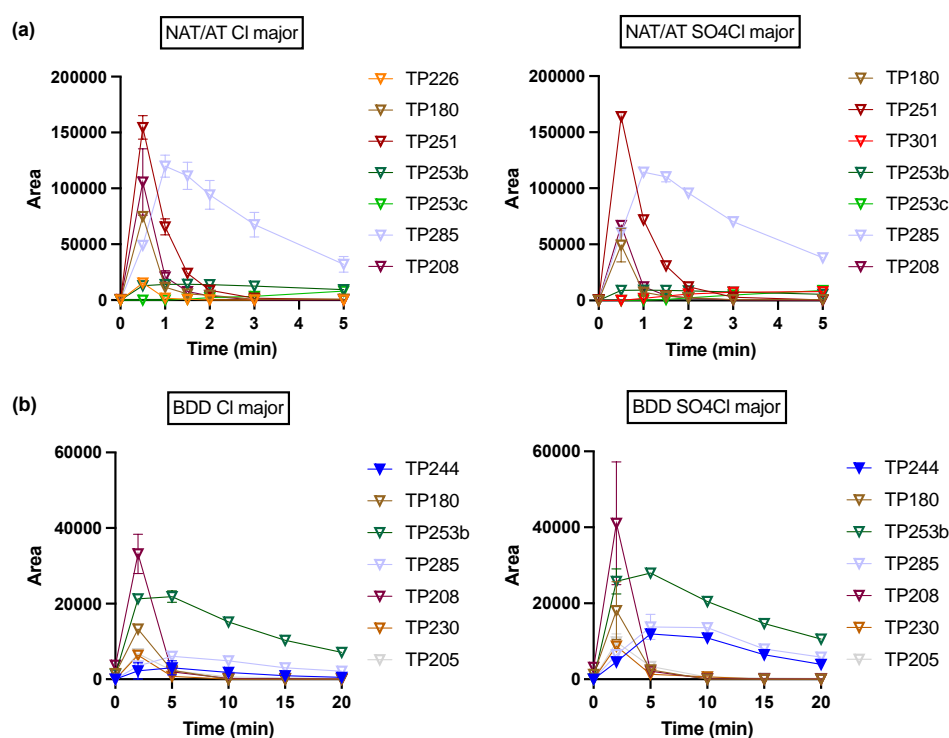


Figure 3.5 Major CBZ transformation product evolution in NaCl electrolytes at (a) NAT/AT and (b) BDD.

CBZ was completely degraded within 1 min of electrolysis using NAT/AT. Most of the 22 TPs detected during NAT/AT electrolysis peaked between 0.5 and 1 min and then were either removed completely or to a high degree after 5 min (**Figure 3.5a and 3.S11a**). For BDD, 100% CBZ removal occurred around 5 min, whereas most of the TPs peaked between 2 and 5 min and were then partially removed after 20 min of electrolysis (**Figure 3.5b and**

3.S11b). These results indicate the effectiveness of O₃ in eliminating the intermediate TPs in addition to the initial oxidation step of CBZ. Responses of all TPs in MS at the two electrodes in all four electrolyte combinations are summarized in **Table 3.S3**.

CBZ TP quantification and pathway elucidation. The more important TPs of CBZ were confirmed and quantified where commercial standards are available – TP180 (acridine), TP253b (carbamazepine 10,11-epoxide) and TP224 (9-acridinecarboxylic acid). TP180 and TP224 are also known to be toxic. More of all the 3 TPs was detected in NaCl than in NaClO₄ electrolytes. Peak concentrations of ~1.8, 2.0, and 0.054 μM were recorded for TP180, TP253b, and TP224, respectively (**Figure 3.S12**). In all electrolytes and in secondary effluent (discussed below), these 3 TPs did not constitute a major part (<15%) of the transformed CBZ in terms of mass balance. Mass balance is not closed here due to the variety of TPs detected and a lack of reference standards. However, identification over complete quantification of the TPs and of their removal trends can be more important for practical engineering purposes, since TP distributions can vary a lot depending on the wastewater composition, yet TP identification can help facilitate treatment efficiency evaluation and toxicity assessment in general.

Electrolysis using the TP253b and TP224 as parent compounds was also conducted to further elucidate and confirm the transformation pathways in **Figure 3.3** (more details in **Figure 3.S13-14**). In general, formation of many TPs are possible via multiple pathways.

FCZ. A lot less TPs (<10 total) have been reported for FCZ in literature compared to those for CBZ,^{12,25,53–56} ranging from 0 detected in constructed wetlands⁵⁶ to 6 under UV/chlorine.¹² In NAT/AT and BDD systems, only 1 TP, TP224 ($m/z = 224.0643$, C₁₀H₈F₂N₃O), was detected in the MS for FCZ degradation in NaClO₄ electrolytes. It formed from cleavage of the parent molecule (**Figure 3.6a**). This product has been reported previously as a degradation product during treatment with UV/chlorine and with H₂O₂ solutions.^{12,53} TP224 is predicted to have a higher toxicity than FCZ.¹² During NAT/AT electrolysis, TP224 peaked at 1.5 min and was completely removed after 5 min, while with BDD, its concentration leveled off at ~20 min (**Figure 3.6b**). The absence of TP224 in NaCl electrolytes suggests that it could be susceptible to attack by chlorine radical species. Given

the lack of detectable TPs, it appears that a fast total oxidation of the intermediate products takes place compared to the more persistent parent molecule FCZ.

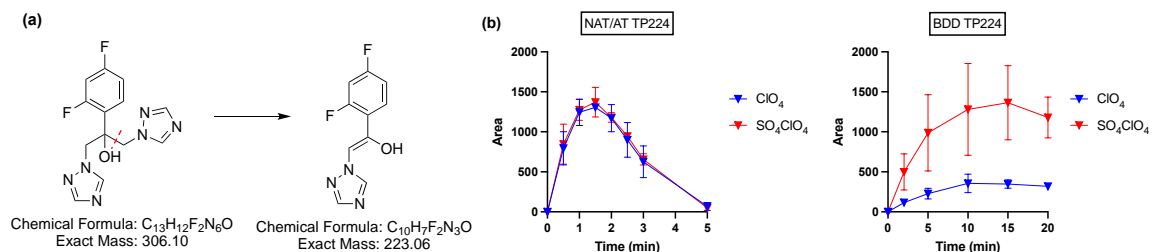


Figure 3.6 (a) Proposed formation pathway and (b) evolution of FCZ transformation product TP224 at NAT/AT and BDD.

Pharmaceutical removal in environmental waters. The oxidative degradation of CBZ and FCZ and formation of their transformation products were also carried out in actual latrine wastewater and in secondary effluent along with a mixture of common pharmaceutical compounds. Previously, Lee *et al.* characterized micropollutant elimination during ozonation into 5 categories based on their reaction rate constants with O_3 and $\cdot OH$.^{6,26} CBZ and FCZ fall into group Ia with the fastest kinetic rates and group IV with the slowest kinetic rates, respectively. In order to obtain a quantitative ranking of pharmaceutical degradation with NAT/AT, 5 other pharmaceuticals in the top 100 list¹ were selected from the different categories. They included atenolol (ATL, group Ib), gabapentin (GBP, group II), trimethoprim (TMP, group Ia), sulfamethoxazole (SMX, group Ia), and ibuprofen (IBP, group III). The physical chemical properties of the 7 target compounds including their pK_a values and rate constants with O_3 and $\cdot OH$ are summarized in [Table 3.S4](#). Individual degradation kinetics of ATL, GBP, and IBP at NAT/AT and their kinetic modeling predictions are shown in [Figure 3.S15](#).

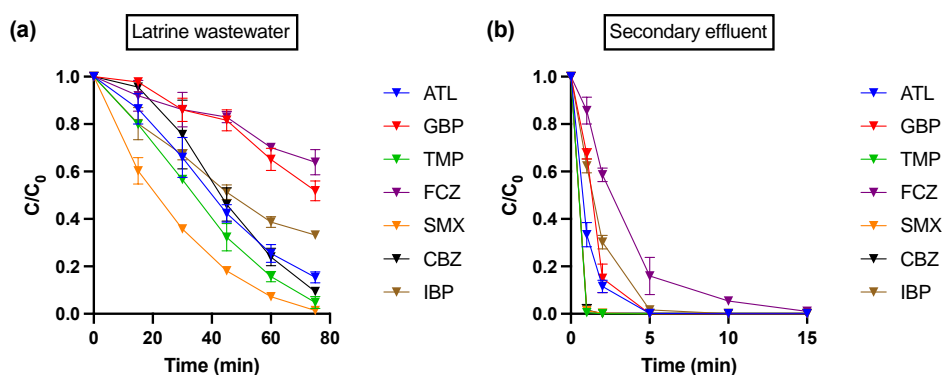


Figure 3.7 Removal of spiked pharmaceutical compounds ($2 \mu\text{M}$ each) during electrolysis of (a) latrine wastewater and (b) secondary effluent by NAT/AT.

The seven pharmaceuticals were spiked into the wastewaters at $2 \mu\text{M}$ each, which is higher than the typical concentrations detected in wastewater sources (ranging from 0 to several thousand ng/L), to investigate treatment with elevated concentrations.¹ The chemical compositions of the wastewaters are given in [Table 3.S5](#). In latrine wastewater, due to the presence of high background levels of COD (440 mg/L) and NH_4^+ (31 mM), and the resulting competitive consumption of oxidants, degradation was retarded comparing to that in pure electrolytes. In latrine wastewater, $>80\%$ removal of the spiked pharmaceutical compounds was achieved in 75 min electrolysis except for FCZ, GBP, and IBP ([Figure 3.7a](#)), indicating longer treatment times were required. In addition, a COD reduction of $\sim 300 \text{ mg/L}$ was attained simultaneously ([Figure 3.S16](#)). In domestic secondary wastewater treatment effluent, the pharmaceuticals were degraded faster in comparison to latrine wastewater due to low initial COD (80 mg/L) and NH_4^+ (0.3 mM) concentrations. Complete removal of all pharmaceuticals except for FCZ was achieved in 5 min of electrolysis, while the time required for FCZ removal was 15 min ([Figure 3.7b](#)), at which point the complete removal of COD was also obtained. 8 of the TPs of CBZ (TP147, TP271, TP180, TP253a, TP267, TP251, TP253b, and TP208) and TP224 of FCZ were detected. Accompanying parent compound degradation, complete removal of all 9 TPs for both CBZ and FCZ was also achieved in 15 min ([Figure 3.S17](#)). Compared to NAT/AT, BDD, while achieving similar COD reduction ([Figure 3.S16](#)), demonstrated better performance for pharmaceutical

degradation in latrine wastewater and worse performance in secondary effluent (**Figure 3.S18-19**). This result indicates the advantage of NAT/AT application in systems with lower chloride concentration. Potential improvement could also be achieved by including pretreatment units to lower COD and remove NH_4^+ and other interfering components from wastewaters before electrochemical treatment.

3.5 Conclusions

In summary, the NAT/AT anodes demonstrated promising performance in degrading a range of pharmaceutical compounds (with very different reactivities with O_3) as well as their transformation products. The NAT/AT-SS system, requiring lower cell voltage than BDD (**Table 3.S5**) under the same applied current density, could achieve similar or better removal with lower energy consumption. It thus potentially represents a more economical and efficient method for water treatment practices that is capable of large-scale implementation. Moreover, the secondary effluent used herein had similar chemical compositions to a biologically-treated hospital wastewater previously investigated,²² suggesting that electrolytic oxidation with NAT/AT could also provide a suitable treatment alternative for the control of pharmaceuticals in hospital wastewaters.

3.6 Acknowledgments

This research was supported by an investment grant made by the Bill and Melinda Gates Foundation (INV-003227). We are grateful to our program officers, Dr. Carl Hensman and Dr. Doulaye Kone, for their support and guidance.

3.7 References

- (1) Patel, M.; Kumar, R.; Kishor, K.; Mlsna, T.; Pittman, C. U.; Mohan, D. Pharmaceuticals of Emerging Concern in Aquatic Systems: Chemistry, Occurrence, Effects, and Removal Methods. *Chem. Rev.* **2019**, *119* (6), 3510–3673.
- (2) Ternes, T. A. Occurrence of Drugs in German Sewage Treatment Plants and Rivers | Dedicated to Professor Dr. Klaus Haberer on the Occasion of His 70th Birthday.1. *Water Res.* **1998**, *32* (11), 3245–3260.
- (3) Mompelat, S.; Le Bot, B.; Thomas, O. Occurrence and Fate of Pharmaceutical Products and By-Products, from Resource to Drinking Water. *Environ. Int.* **2009**, *35* (5), 803–814.

- (4) Jjemba, P. K. Excretion and Ecotoxicity of Pharmaceutical and Personal Care Products in the Environment. *Ecotoxicol. Environ. Saf.* **2006**, *63* (1), 113–130.
- (5) Ternes, T.; Joss, A. Human Pharmaceuticals, Hormones and Fragrances - The Challenge of Micropollutants in Urban Water Management. **2006**. <https://doi.org/10.2166/9781780402468>.
- (6) Lee, Y.; Gerrity, D.; Lee, M.; Bogeat, A. E.; Salhi, E.; Gamage, S.; Trenholm, R. A.; Wert, E. C.; Snyder, S. A.; von Gunten, U. Prediction of Micropollutant Elimination during Ozonation of Municipal Wastewater Effluents: Use of Kinetic and Water Specific Information. *Environ. Sci. Technol.* **2013**, *47* (11), 5872–5881.
- (7) Lian, L.; Yao, B.; Hou, S.; Fang, J.; Yan, S.; Song, W. Kinetic Study of Hydroxyl and Sulfate Radical-Mediated Oxidation of Pharmaceuticals in Wastewater Effluents. *Environ. Sci. Technol.* **2017**, *51* (5), 2954–2962.
- (8) Huber, M. M.; Canonica, S.; Park, G.-Y.; von Gunten, U. Oxidation of Pharmaceuticals during Ozonation and Advanced Oxidation Processes. *Environ. Sci. Technol.* **2003**, *37* (5), 1016–1024.
- (9) Benner, J.; Salhi, E.; Ternes, T.; von Gunten, U. Ozonation of Reverse Osmosis Concentrate: Kinetics and Efficiency of Beta Blocker Oxidation. *Water Res.* **2008**, *42* (12), 3003–3012.
- (10) Lee, Y.; von Gunten, U. Oxidative Transformation of Micropollutants during Municipal Wastewater Treatment: Comparison of Kinetic Aspects of Selective (Chlorine, Chlorine Dioxide, Ferrate VI, and Ozone) and Non-Selective Oxidants (Hydroxyl Radical). *Water Res.* **2010**, *44* (2), 555–566.
- (11) Chiron, S.; Minero, C.; Vione, D. Photodegradation Processes of the Antiepileptic Drug Carbamazepine, Relevant To Estuarine Waters. *Environ. Sci. Technol.* **2006**, *40* (19), 5977–5983.
- (12) Cai, W.-W.; Peng, T.; Yang, B.; Xu, C.; Liu, Y.-S.; Zhao, J.-L.; Gu, F.-L.; Ying, G.-G. Kinetics and Mechanism of Reactive Radical Mediated Fluconazole Degradation by the UV/Chlorine Process: Experimental and Theoretical Studies. *Chem. Eng. J.* **2020**, *402*, 126224.
- (13) Scholes, R. C.; Prasse, C.; Sedlak, D. L. The Role of Reactive Nitrogen Species in Sensitized Photolysis of Wastewater-Derived Trace Organic Contaminants. *Environ. Sci. Technol.* **2019**, *53* (11), 6483–6491.
- (14) Panizza, M.; Cerisola, G. Direct And Mediated Anodic Oxidation of Organic Pollutants. *Chem. Rev.* **2009**, *109* (12), 6541–6569.
- (15) Jasper, J. T.; Shafaat, O. S.; Hoffmann, M. R. Electrochemical Transformation of Trace Organic Contaminants in Latrine Wastewater. *Environ. Sci. Technol.* **2016**, *50* (18), 10198–10208.
- (16) Panizza, M.; Cerisola, G. Removal of Colour and COD from Wastewater Containing Acid Blue 22 by Electrochemical Oxidation. *J. Hazard. Mater.* **2008**, *153* (1), 83–88.
- (17) Zhuo, Q.; Deng, S.; Yang, B.; Huang, J.; Yu, G. Efficient Electrochemical Oxidation of Perfluorooctanoate Using a Ti/SnO₂-Sb-Bi Anode. *Environ. Sci. Technol.* **2011**, *45* (7), 2973–2979.
- (18) Wang, Y.-H.; Cheng, S.; Chan, K.-Y.; Li, X. Y. Electrolytic Generation of Ozone on Antimony- and Nickel-Doped Tin Oxide Electrode. *J. Electrochem. Soc.* **2005**, *152* (11), D197–D200.

- (19) Christensen, P. A.; Attidekou, P. S.; Egdell, R. G.; Maneelok, S.; Manning, D. A. C.; Palgrave, R. Identification of the Mechanism of Electrocatalytic Ozone Generation on Ni/Sb-SnO₂. *J. Phys. Chem. C* **2017**, *121* (2), 1188–1199.
- (20) Ciríaco, L.; Anjo, C.; Correia, J.; Pacheco, M. J.; Lopes, A. Electrochemical Degradation of Ibuprofen on Ti/Pt/PbO₂ and Si/BDD Electrodes. *Electrochim. Acta* **2009**, *54* (5), 1464–1472.
- (21) Murugananthan, M.; Latha, S. S.; Bhaskar Raju, G.; Yoshihara, S. Anodic Oxidation of Ketoprofen—An Anti-Inflammatory Drug Using Boron Doped Diamond and Platinum Electrodes. *J. Hazard. Mater.* **2010**, *180* (1), 753–758.
- (22) Lan, Y.; Coetsier, C.; Causserand, C.; Groenen Serrano, K. On the Role of Salts for the Treatment of Wastewaters Containing Pharmaceuticals by Electrochemical Oxidation Using a Boron Doped Diamond Anode. *Electrochim. Acta* **2017**, *231*, 309–318.
- (23) Zhang, Y.; Yang, Y.; Yang, S.; Quispe-Cardenas, E.; Hoffmann, M. R. Application of Heterojunction Ni–Sb–SnO₂ Anodes for Electrochemical Water Treatment. *ACS EST Eng.* **2021**, *1* (8), 1236–1245.
- (24) Mohapatra, D. P.; Brar, S. K.; Tyagi, R. D.; Picard, P.; Surampalli, R. Y. Analysis and Advanced Oxidation Treatment of a Persistent Pharmaceutical Compound in Wastewater and Wastewater Sludge-Carbamazepine. *Sci. Total Environ.* **2014**, *470–471*, 58–75.
- (25) Chen, Z.-F.; Ying, G.-G.; Jiang, Y.-X.; Yang, B.; Lai, H.-J.; Liu, Y.-S.; Pan, C.-G.; Peng, F.-Q. Photodegradation of the Azole Fungicide Fluconazole in Aqueous Solution under UV-254: Kinetics, Mechanistic Investigations and Toxicity Evaluation. *Water Res.* **2014**, *52*, 83–91.
- (26) Lee, Y.; Kovalova, L.; McArdell, C. S.; von Gunten, U. Prediction of Micropollutant Elimination during Ozonation of a Hospital Wastewater Effluent. *Water Res.* **2014**, *64*, 134–148.
- (27) Cid, C. A.; Jasper, J. T.; Hoffmann, M. R. Phosphate Recovery from Human Waste via the Formation of Hydroxyapatite during Electrochemical Wastewater Treatment. *ACS Sustainable Chem. Eng.* **2018**, *6* (3), 3135–3142.
- (28) Hu, Y.; Jing, Z.; Sudo, Y.; Niu, Q.; Du, J.; Wu, J.; Li, Y.-Y. Effect of Influent COD/SO₄²⁻ Ratios on UASB Treatment of a Synthetic Sulfate-Containing Wastewater. *Chemosphere* **2015**, *130*, 24–33.
- (29) Bader, H.; Hoigné, J. Determination of Ozone in Water by the Indigo Method. *Water Res.* **1981**, *15* (4), 449–456.
- (30) Ianni, J. C. *Kintecus*, Windows Version 6.80, 2020, www.kintecus.com.
- (31) Neta, P.; Huie, R. E.; Ross, A. B. Rate Constants for Reactions of Inorganic Radicals in Aqueous Solution. *J. Phys. Chem. Ref. Data* **1988**, *17* (3), 1027–1284.
- (32) Buxton, G. V.; Greenstock, C. L.; Helman, W. P.; Ross, A. B. Critical Review of Rate Constants for Reactions of Hydrated Electrons, Hydrogen Atoms and Hydroxyl Radicals ($\cdot\text{OH}/\cdot\text{O}^-$ in Aqueous Solution. *J. Phys. Chem. Ref. Data* **1988**, *17* (2), 513–886.
- (33) Huie, R. E.; Clifton, C. L.; Neta, P. Electron Transfer Reaction Rates and Equilibria of the Carbonate and Sulfate Radical Anions. *Int. J. Radiat. Appl. Instrum. Part C. Radiation Physics and Chemistry* **1991**, *38* (5), 477–481.

- (34) Fang, J.; Fu, Y.; Shang, C. The Roles of Reactive Species in Micropollutant Degradation in the UV/Free Chlorine System. *Environ. Sci. Technol.* **2014**, *48* (3), 1859–1868.
- (35) McMurry, J. E.; Fay, R. C. *General Chemistry: Atoms First*; Pearson Higher Ed: Upper Saddle River, NJ, 2010.
- (36) Lutze, H. V.; Bircher, S.; Rapp, I.; Kerlin, N.; Bakkour, R.; Geisler, M.; von Sonntag, C.; Schmidt, T. C. Degradation of Chlorotriazine Pesticides by Sulfate Radicals and the Influence of Organic Matter. *Environ. Sci. Technol.* **2015**, *49* (3), 1673–1680.
- (37) Consonni, V.; Trasatti, S.; Pollak, F.; O’Grady, W. E. Mechanism of Chlorine Evolution on Oxide Anodes Study of PH Effects. *J. Electroanal. Chem. Interfacial Electrochem.* **1987**, *228* (1), 393–406.
- (38) Hoigné, J.; Bader, H. Rate Constants of Reactions of Ozone with Organic and Inorganic Compounds in Water—II: Dissociating Organic Compounds. *Water Res.* **1983**, *17* (2), 185–194.
- (39) Corrêa, J. C. R.; Duarte Vianna-Soares, C.; Salgado, H. R. N. Development and Validation of Dissolution Test for Fluconazole Capsules by HPLC and Derivative UV Spectrophotometry. *Chromatogr. Res. Int.* **2012**, *2012*, 610427.
- (40) Kaiser, E.; Prasse, C.; Wagner, M.; Bröder, K.; Ternes, T. A. Transformation of Oxcarbazepine and Human Metabolites of Carbamazepine and Oxcarbazepine in Wastewater Treatment and Sand Filters. *Environ. Sci. Technol.* **2014**, *48* (17), 10208–10216.
- (41) Seiwert, B.; Golan-Rozen, N.; Weidauer, C.; Riemenschneider, C.; Chefetz, B.; Hadar, Y.; Reemtsma, T. Electrochemistry Combined with LC–HRMS: Elucidating Transformation Products of the Recalcitrant Pharmaceutical Compound Carbamazepine Generated by the White-Rot Fungus *Pleurotus Ostreatus*. *Environ. Sci. Technol.* **2015**, *49* (20), 12342–12350.
- (42) Pan, Y.; Cheng, S.; Yang, X.; Ren, J.; Fang, J.; Shang, C.; Song, W.; Lian, L.; Zhang, X. UV/Chlorine Treatment of Carbamazepine: Transformation Products and Their Formation Kinetics. *Water Res.* **2017**, *116*, 254–265.
- (43) Hübner, U.; Seiwert, B.; Reemtsma, T.; Jekel, M. Ozonation Products of Carbamazepine and Their Removal from Secondary Effluents by Soil Aquifer Treatment – Indications from Column Experiments. *Water Res.* **2014**, *49*, 34–43.
- (44) Hu, L.; Martin, H. M.; Arce-Bulted, O.; Sugihara, M. N.; Keating, K. A.; Strathmann, T. J. Oxidation of Carbamazepine by Mn(VII) and Fe(VI): Reaction Kinetics and Mechanism. *Environ. Sci. Technol.* **2009**, *43* (2), 509–515.
- (45) McDowell, D. C.; Huber, M. M.; Wagner, M.; von Gunten, U.; Ternes, T. A. Ozonation of Carbamazepine in Drinking Water: Identification and Kinetic Study of Major Oxidation Products. *Environ. Sci. Technol.* **2005**, *39* (20), 8014–8022.
- (46) Golan-Rozen, N.; Seiwert, B.; Riemenschneider, C.; Reemtsma, T.; Chefetz, B.; Hadar, Y. Transformation Pathways of the Recalcitrant Pharmaceutical Compound Carbamazepine by the White-Rot Fungus *Pleurotus Ostreatus*: Effects of Growth Conditions. *Environ. Sci. Technol.* **2015**, *49* (20), 12351–12362.
- (47) Martínez, C.; Canle L., M.; Fernández, M. I.; Santaballa, J. A.; Faria, J. Kinetics and Mechanism of Aqueous Degradation of Carbamazepine by Heterogeneous Photocatalysis Using Nanocrystalline TiO₂, ZnO and Multi-Walled Carbon

- Nanotubes–Anatase Composites. *Appl. Catal. B: Environmental* **2011**, *102* (3), 563–571.
- (48) Wang, W.-L.; Wu, Q.-Y.; Huang, N.; Wang, T.; Hu, H.-Y. Synergistic Effect between UV and Chlorine (UV/Chlorine) on the Degradation of Carbamazepine: Influence Factors and Radical Species. *Water Res.* **2016**, *98*, 190–198.
- (49) Soufan, M.; Deborde, M.; Delmont, A.; Legube, B. Aqueous Chlorination of Carbamazepine: Kinetic Study and Transformation Product Identification. *Water Res.* **2013**, *47* (14), 5076–5087.
- (50) Schymanski, E. L.; Jeon, J.; Gulde, R.; Fenner, K.; Ruff, M.; Singer, H. P.; Hollender, J. Identifying Small Molecules via High Resolution Mass Spectrometry: Communicating Confidence. *Environ. Sci. Technol.* **2014**, *48* (4), 2097–2098.
- (51) Kosjek, T.; Andersen, H. R.; Kompore, B.; Ledin, A.; Heath, E. Fate of Carbamazepine during Water Treatment. *Environ. Sci. Technol.* **2009**, *43* (16), 6256–6261.
- (52) Keen, O. S.; Baik, S.; Linden, K. G.; Aga, D. S.; Love, N. G. Enhanced Biodegradation of Carbamazepine after UV/H₂O₂ Advanced Oxidation. *Environ. Sci. Technol.* **2012**, *46* (11), 6222–6227.
- (53) Lotfy, H.; Monir, H. H.; Abd El-Aleem, A. E.-A.-B. Novel Spectrophotometric Methods for the Determination of Fluconazole in the Presence of its Oxidative Degradation Product. *J. Chil. Chem. Soc.* **2012**, *57* (4), 1447–1455.
- (54) Castro, G.; Casado, J.; Rodríguez, I.; Ramil, M.; Ferradás, A.; Cela, R. Time-of-Flight Mass Spectrometry Assessment of Fluconazole and Climbazole UV and UV/H₂O₂ Degradability: Kinetics Study and Transformation Products Elucidation. *Water Res.* **2016**, *88*, 681–690.
- (55) Yang, J.-F.; Yang, L.-M.; Zhang, S.-B.; Ou, L.-H.; Liu, C.-B.; Zheng, L.-Y.; Yang, Y.-F.; Ying, G.-G.; Luo, S.-L. Degradation of Azole Fungicide Fluconazole in Aqueous Solution by Thermally Activated Persulfate. *Chem. Eng. J.* **2017**, *321*, 113–122.
- (56) Sochacki, A.; Marsik, P.; Chen, Z.; Sisa, M.; Vymazal, J. Fate of Antifungal Drugs Climbazole and Fluconazole in Constructed Wetlands - Diastereoselective Transformation Indicates Process Conditions. *Chem. Eng. J.* **2021**, *421*, 127783.

3.8 Supporting Information

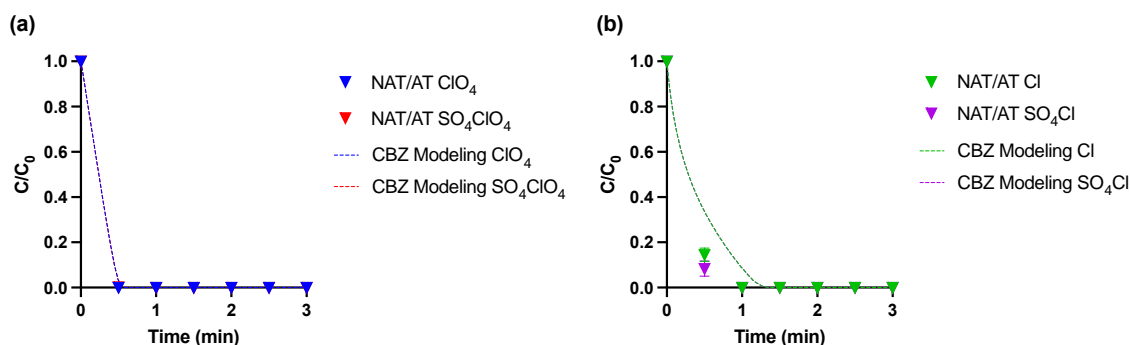


Figure 3.S1 Experimental results and kinetic modeling predictions (dashed lines) for CBZ degradation by NAT/AT in (a) ClO₄: 50 mM NaClO₄ and SO₄ClO₄: 5 mM Na₂SO₄ + 50 mM NaClO₄ and (b) Cl: 50 mM NaCl and SO₄Cl: 5 mM Na₂SO₄ + 50 mM NaCl electrolytes.

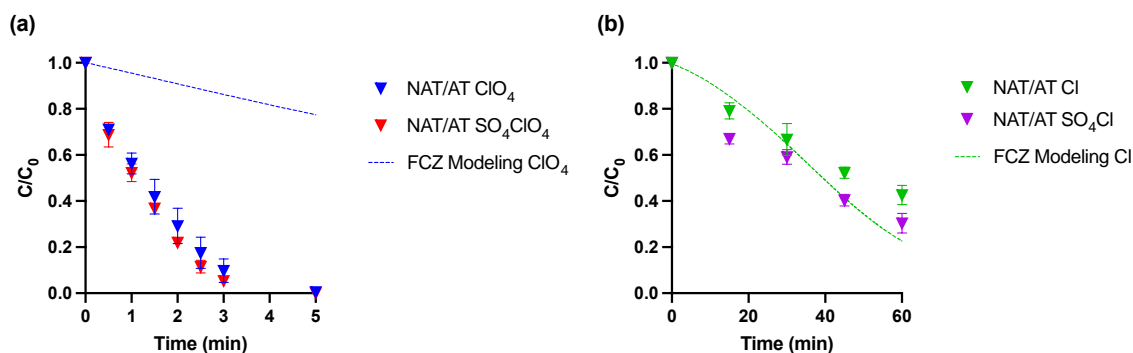


Figure 3.S2 Experimental results and kinetic modeling predictions (dashed lines) for FCZ degradation by NAT/AT in (a) ClO₄: 50 mM NaClO₄ and SO₄ClO₄: 5 mM Na₂SO₄ + 50 mM NaClO₄ and (b) Cl: 50 mM NaCl and SO₄Cl: 5 mM Na₂SO₄ + 50 mM NaCl electrolytes.

Modeling result in SO₄Cl (5 mM Na₂SO₄ + 50 mM NaCl) did not reflect the faster FCZ degradation in the presence of SO₄²⁻ as recorded in the experiments, suggesting that other pathways may potentially produce SO₄^{•-} in addition to the homogeneous reactions (reaction 60 through 78 in Table 3.S1). One possibility is that SO₄^{•-} was generated electrochemically like $\cdot\text{OH}$, O₃, and chlorine radicals. Taking an estimated zero-order rate constant of $\sim 1 \times 10^{-8} \text{ s}^{-1}$ for SO₄^{•-} production, the model was able to reproduce a similar enhanced degradation kinetics.

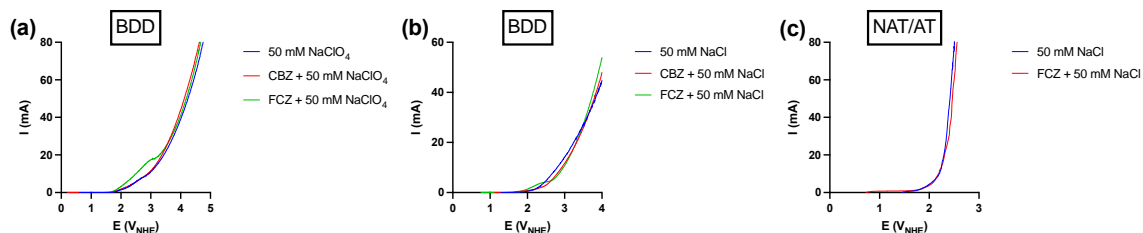


Figure 3.S3 Linear sweep voltammograms (LSV) of (a) BDD in 50 mM NaClO₄, (b) BDD in 50 mM NaCl, and (c) NAT/AT in 50 mM NaCl electrolytes in the absence and presence of 20 μM CBZ or FCZ.

Evidence for direct electron transfer (DET) at BDD is suggested given the peak around 3.0 V_{NHE} in the FCZ + 50 mM NaClO_4 voltammogram, which was absent in the 50 mM NaClO_4 control voltammogram. A similar but less pronounced peak around 2.5 V_{NHE} in the FCZ + 50 mM NaCl voltammogram suggested that DET also happens in the presence of chloride but probably with less intensity. In both cases, no additional features were observed for CBZ compared to the 50 mM NaClO_4 or NaCl control voltammograms. On the other hand, DET is not known to happen at NAT/AT, which is also confirmed by the absent of DET peaks in the NAT/AT voltammograms.

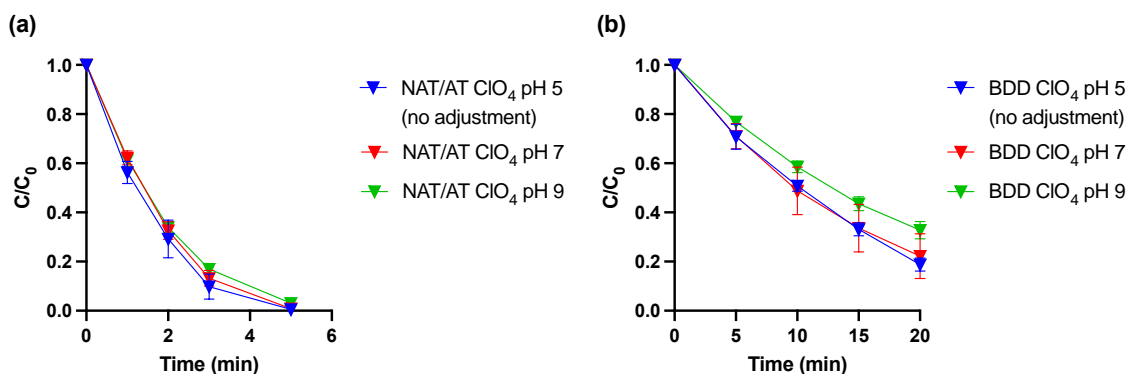


Figure 3.S4 FCZ degradation by (a) NAT/AT and (b) BDD in 50 mM NaClO_4 electrolytes with pH adjusted to 5, 7, and 9 in phosphate buffers. For degradation under pH 5 (no adjustment), no phosphate buffer was added.

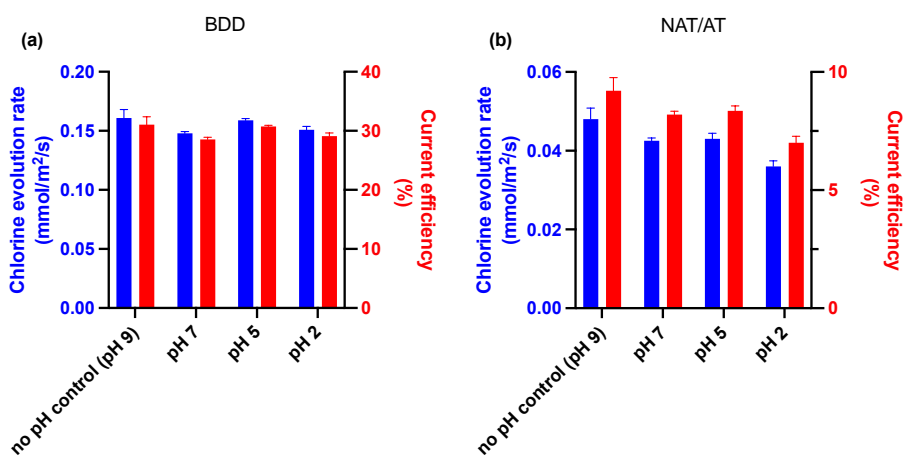


Figure 3.S5 Chlorine evolution rate and current efficiency measured in 50 mM NaCl electrolytes during electrolysis by (a) BDD and (b) NAT/AT.

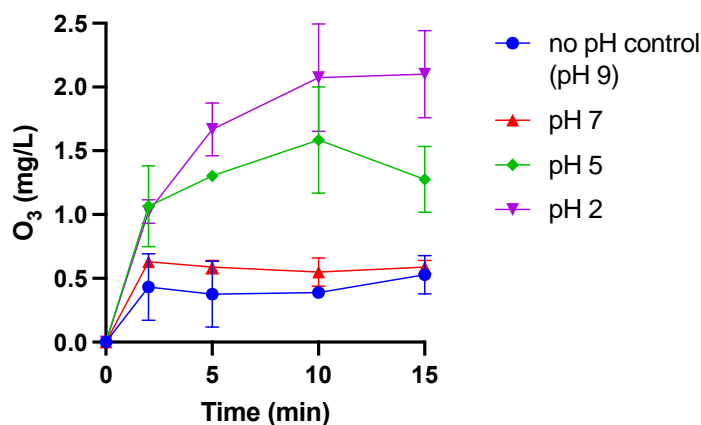


Figure 3.S6 Dissolved O_3 concentrations measured under different pHs in 50 mM NaCl electrolytes during electrolysis by NAT/AT.

The kinetic model showed that reaction between O_3 and OCl^- ($k_{O_3, OCl^-} = 120 \text{ M}^{-1}\text{s}^{-1}$ vs. $k_{O_3, HOCl} < 0.002 \text{ M}^{-1}\text{s}^{-1}$) did not play an important role in affecting $[O_3]$ under higher pH. At pH 9, reaction between O_3 and OH^- led to slight decrease in aqueous $[O_3]$. Most of the observed difference in $[O_3]$, however, should come from different O_3 production at NAT/AT.

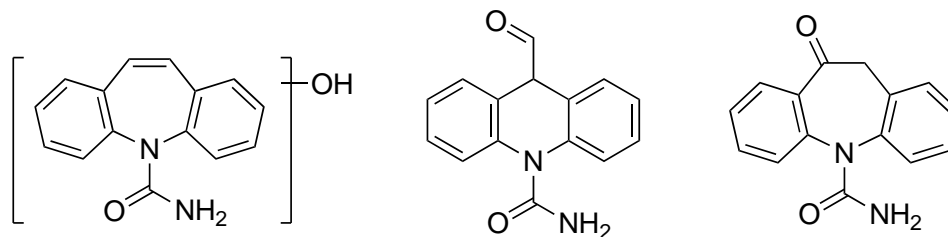
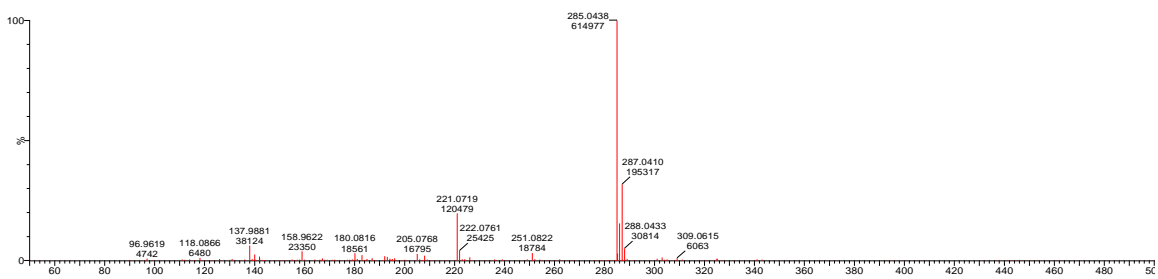
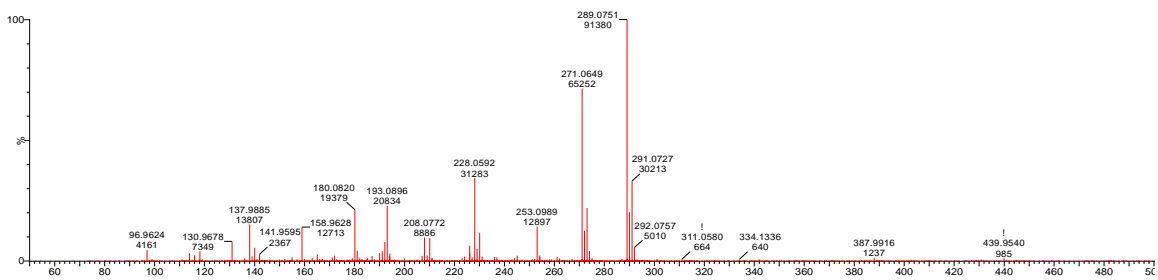
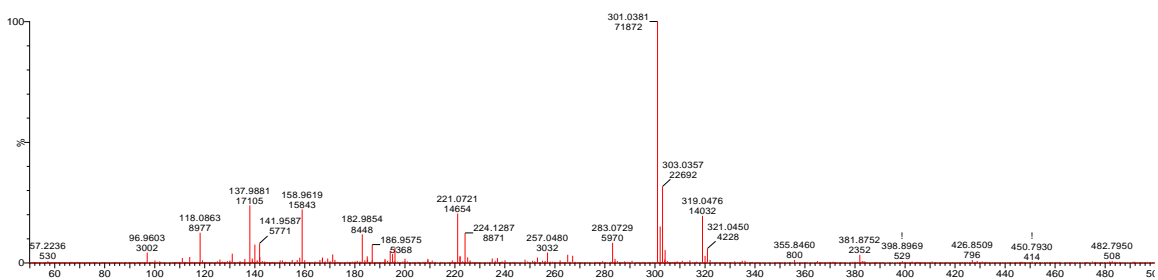
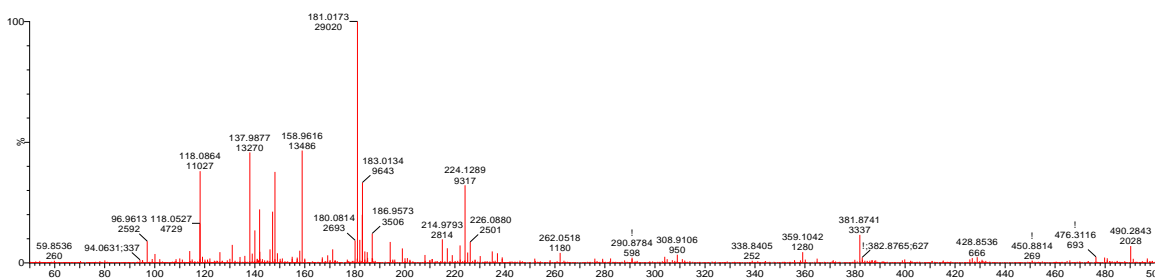
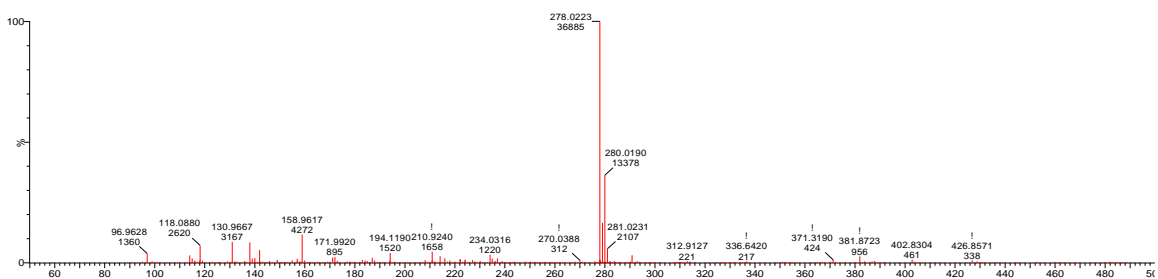


Figure 3.S7 Possible structures for TP253a.

Several structures for this hydroxy-CBZ TP have been proposed in literature. The structures shown have been proposed during ozonation,¹ heterogeneous photocatalysis,² UV/chlorine,^{3,4} chlorination,⁵ UV/ H_2O_2 ,⁶ photodegradation,⁷ and UV/ $S_2O_8^{2-}$.⁸ However, since a standard is not available, its exact structure cannot be determined.



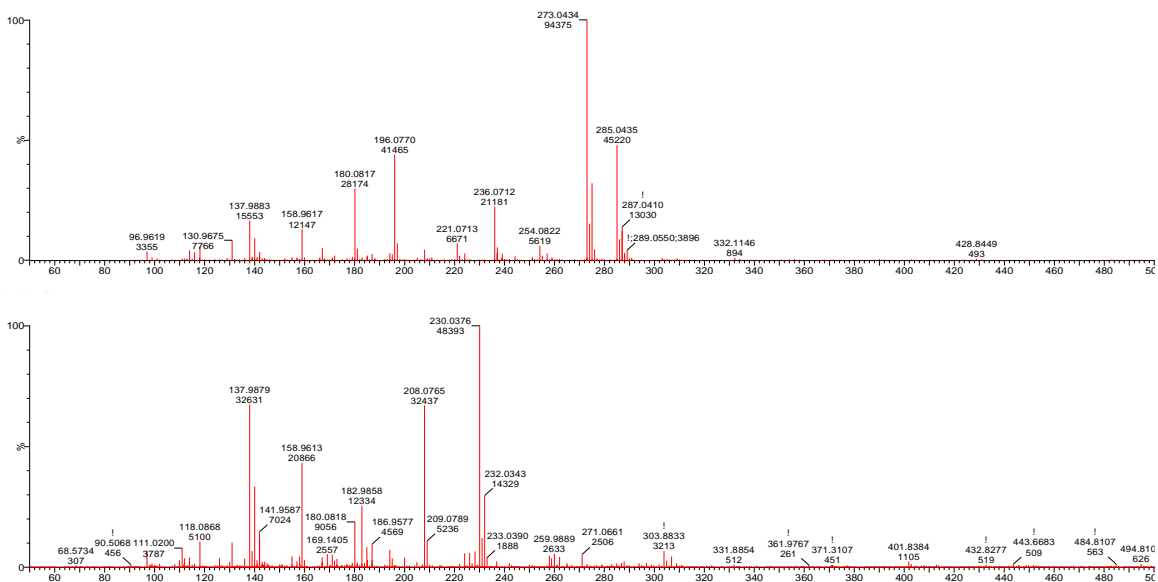


Figure 3.S8 Mass spectra of TP278, TP181, TP301, TP289, TP285, TP273, and TP230.

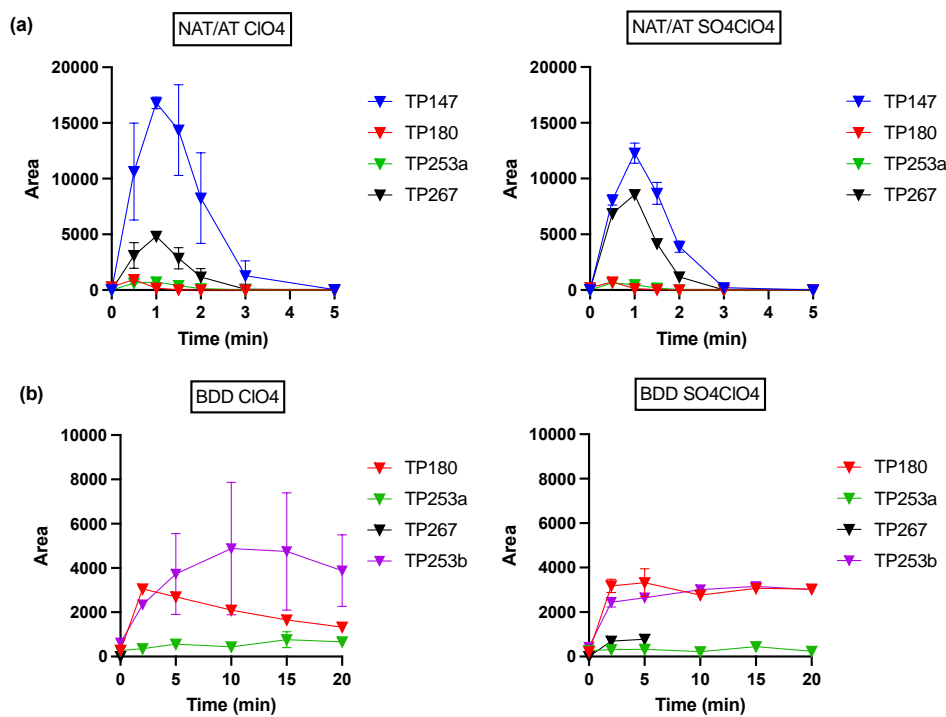


Figure 3.S9 A zoomed-in look at CBZ transformation product evolution (excluding TP251) in NaClO₄ electrolytes at (a) NAT/AT and (b) BDD.

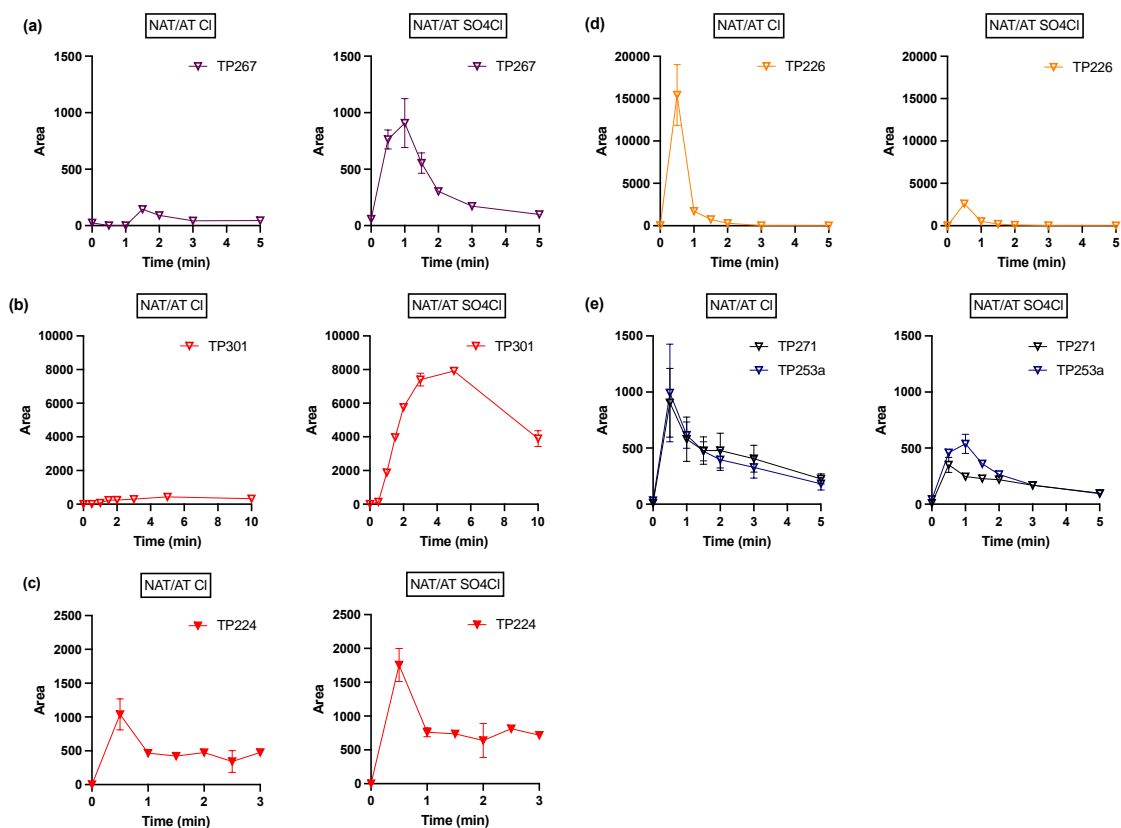


Figure 3.S10 Responses of (a) TP267, (b) TP301, (c) TP224, (d) TP226, and (e) TP271 and TP253a of CBZ at NAT/AT in the absence (left) and presence (right) of 5 mM Na₂SO₄ in 50 mM NaCl electrolytes.

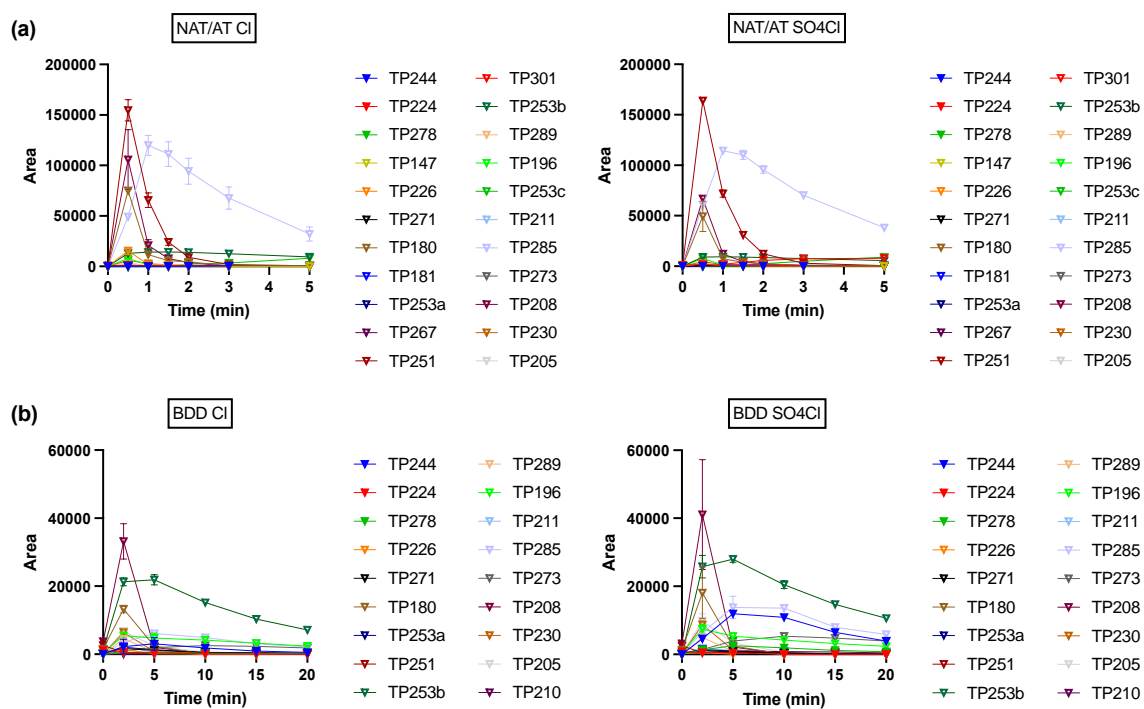


Figure 3.S11 CBZ transformation product evolution (all) in NaCl electrolytes at (a) NAT/AT and (b) BDD.

	Peak TP concentrations								SE ^a
	NAT/AT				BDD				
	ClO ₄	SO ₄ ClO ₄	Cl	SO ₄ Cl	ClO ₄	SO ₄ ClO ₄	Cl	SO ₄ Cl	SE
TP180, Acridine									
Area 1	1104	835	73777	60103	3075	2967	14091	12716	273
Area 2	764	599	76140	38880	3033	3762	12485	23449	231
Avg	934	717	74959	49492	3054	3365	13288	18083	252
Conc (μM)	0.022	0.017	1.75	1.16	0.071	0.071	0.31	0.42	0.0059
TP253b, Carbamazepine 10,11-epoxide									
Area 1	1094	863	14918	9497	2762	3039	22940	27339	155
Area 2	1036	903	13519	8812	7003	3265	20827	28606	116
Avg	1065	883	14219	9155	4883	3152	21884	27973	136
Conc (μM)	0.076	0.063	1.01	0.65	0.35	0.22	1.55	1.99	0.0096
TP224, 9-Acridinecarboxylic acid (estimated) ^b									
Area 1	n.d.	n.d.	1200	1583	n.d.	n.d.	627	457	n.d.
Area 2	n.d.	n.d.	877	1929	n.d.	n.d.	387	570	n.d.

Avg	n.d.	n.d.	1039	1756	n.d.	n.d.	507	514	n.d.
Conc (μM)	n.d.	n.d.	0.032	0.054	n.d.	n.d.	0.015	0.016	n.d.

- Treatment of secondary effluent by NAT/AT.
- Estimated concentration only since exact hydrate number of the standard is not available.

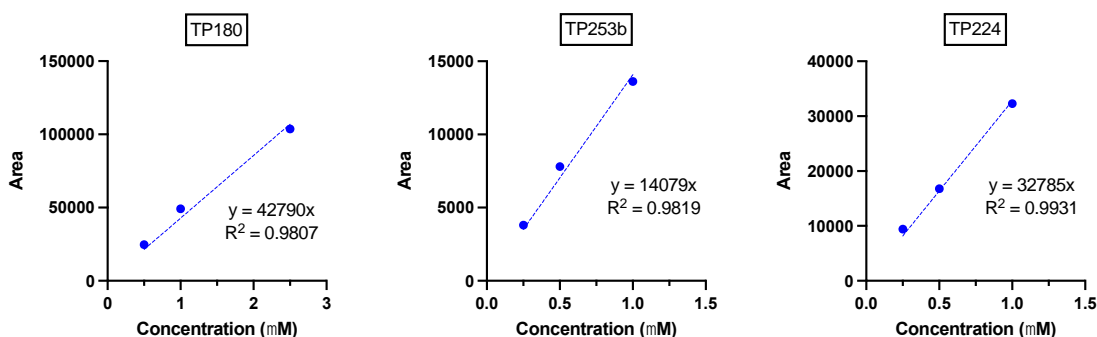


Figure 3.S12 Peak concentrations and calibration curves of TP180 (acridine), TP253b (carbamazepine 10,11-epoxide), and TP224 (9-acridinecarboxylic acid) at NAT/AT and BDD in different electrolytes.

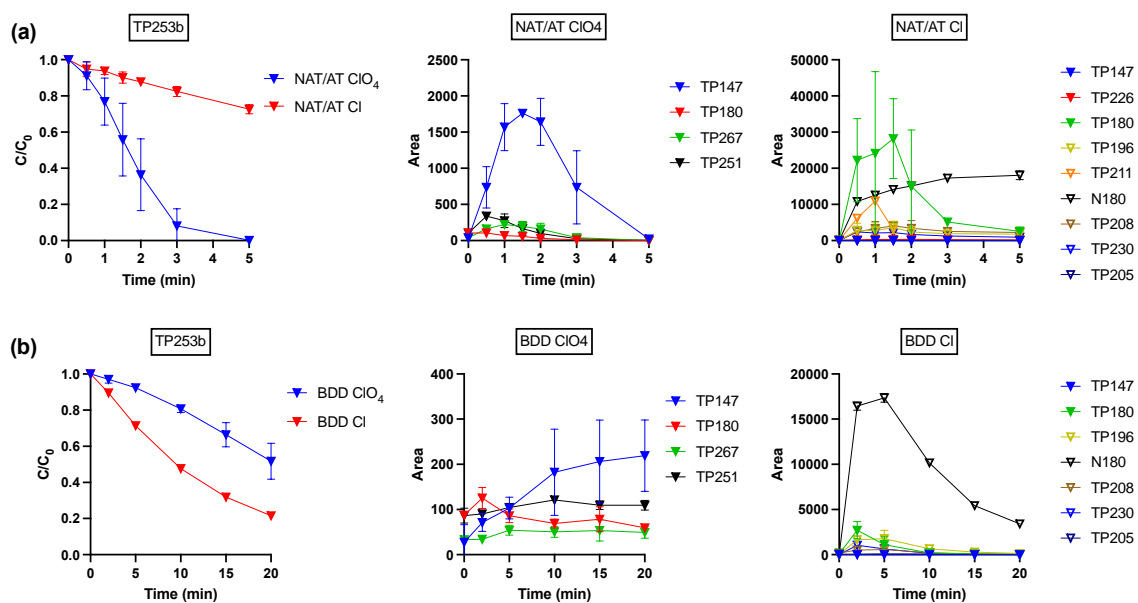


Figure 3.S13 Electrochemical oxidation and transformation product evolution of 20 μM TP253b (CBZ-EP) at (a) NAT/AT and (b) BDD in 50 mM NaClO_4 and NaCl electrolytes.

Oxidation of CBZ to form TP251 (BQM) via TP253b (CBZ-EP) and TP271 (diOH-CBZ) has been proposed in the biodegradation with white-rot fungus *Pleurotus ostreatus*.^{9,10} However, the intermediate TP271, which was commonly detected together with TP253b, was not detected in CBZ oxidation with both electrodes in NaClO₄ electrolytes. One possibility is that it was rapidly transformed.

To further investigate transformation pathways in the NAT/AT and BDD system, electrolysis of 20 μM TP253b (CBZ-EP) standard was conducted. It is obvious that O₃ greatly facilitated TP253b removal (Figure 3.S13a, left). While both TP251 and TP147 were detected in NaClO₄ electrolytes, their responses were very low comparing to those detected in CBZ degradation (Figure 3.4 and 3.S9), especially considering the elevated initial TP253b concentration. The same was true for the other two TPs, TP180 and TP267. Therefore, the above-proposed CBZ → TP253b → TP271 → TP251 pathway during biodegradation is likely not important to negligible in our system.

Similar observations can be made in NaCl electrolytes. While several CBZ TPs were detected during TP253b oxidation, their responses were very low in comparison (Figure 3.5 and 3.S11). However, the set of TPs (TP208, TP224, TP180, and TP196) in CBZ oxidation in NaCl electrolytes were all detected here as well, confirming the proposed TP253b → TP208 → TP224 → TP180 → TP196 sequence, even though it is not the only pathway. Other pathways likely contributed more significantly to the formation of these TPs during CBZ oxidation.

One other thing to note is that a new TP (N180, $m/z = 180.0802$, C₁₃H₁₀N) was detected. Its exact structure cannot be determined.

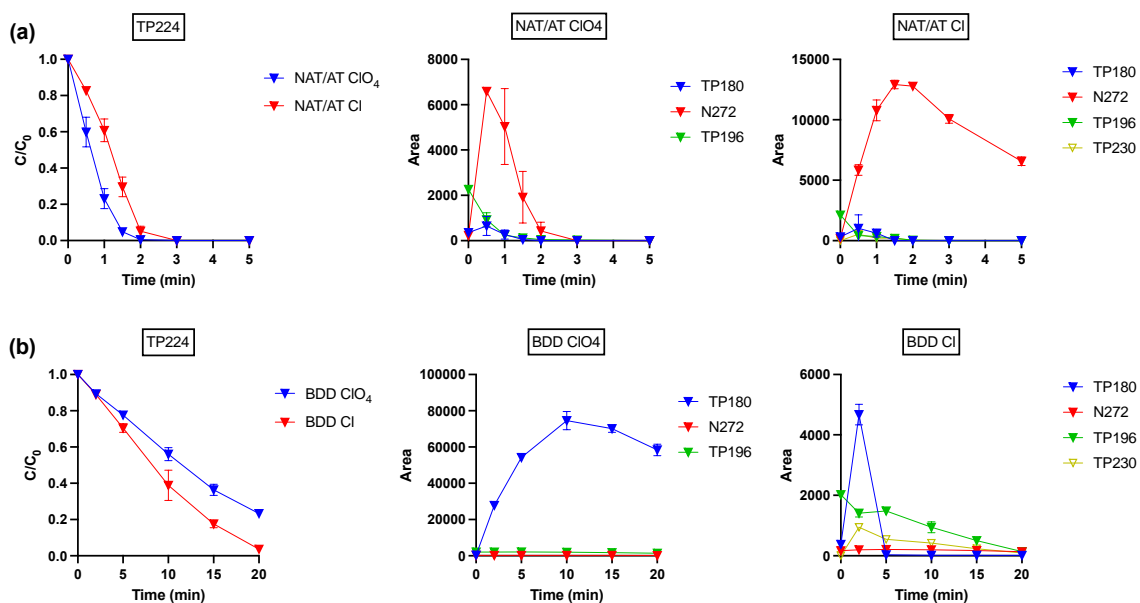


Figure 3.S14 Electrochemical oxidation and transformation product evolution of 20 μ M TP224 (9-acridinecarboxylic acid) at (a) NAT/AT and (b) BDD in 50 mM $NaClO_4$ and $NaCl$ electrolytes.

It was observed that O_3 also promoted TP224 removal (Figure 3.S14a, left). TP224 was only detected in $NaCl$ electrolytes during CBZ degradation. Focusing on the two figures on the right (NAT/AT and BDD Cl), we can see that formation of TP180 and TP196 from TP224 was confirmed. TP230, the chlorinated product of TP196, was also detected. Similar to the case for TP253b, responses of the detected TPs were very low comparing to those detected in CBZ degradation (Figure 3.5 and 3.S11), considering the elevated initial TP224 concentration. Other pathways likely contributed more significantly to the formation of these TPs during CBZ oxidation.

A new TP (N272, $m/z = 272.0558$, $C_{14}H_{10}NO_5$) was detected. It is proposed to be the trihydroxylated product of TP224.

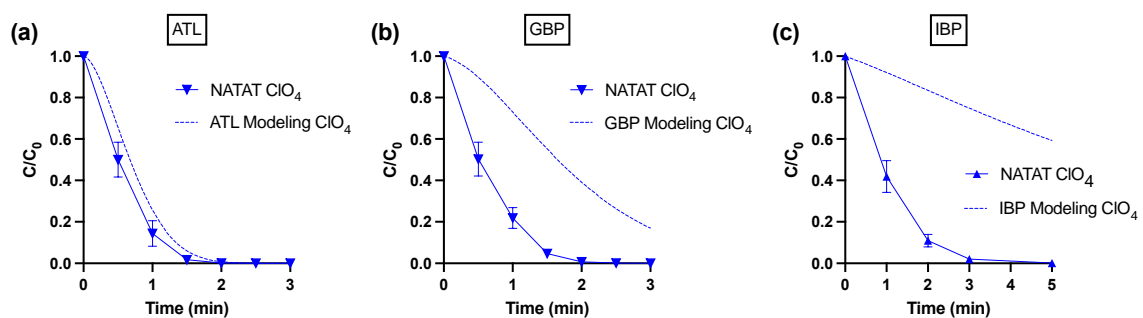


Figure 3.S15 Experimental results and kinetic modeling predictions (dashed lines) for (a) atenolol (ATL), (b) gabapentin (GBP), and (c) ibuprofen (IBP) degradation by NAT/AT in 50 mM NaClO_4 electrolytes.

Experimental degradation of both GBP (group II) and IBP (group III)^{11,12} was faster than model predictions, suggesting accelerated kinetics.¹³

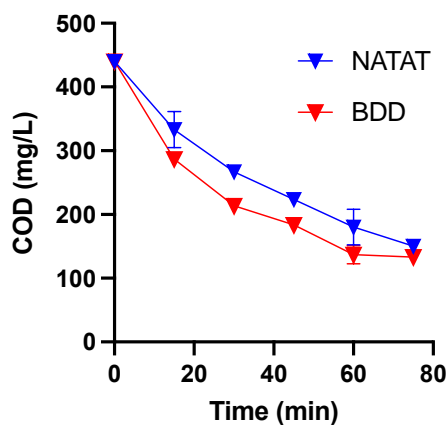


Figure 3.S16 COD removal during treatment of latrine wastewater spiked with pharmaceuticals.

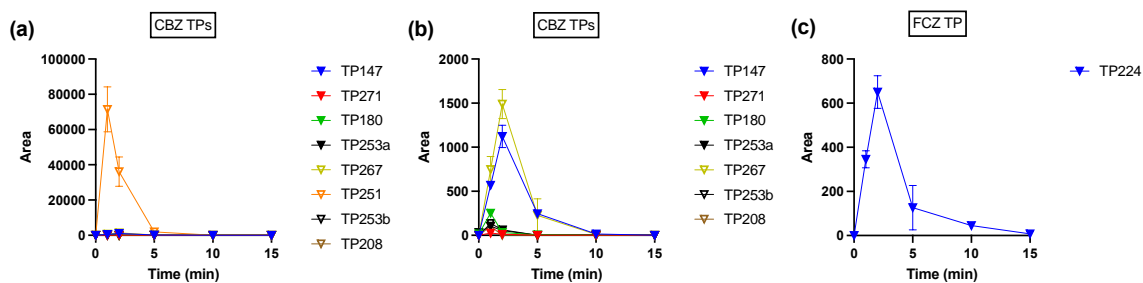


Figure 3.S17 Transformation product evolution for (a) CBZ, (b) a zoomed-in look for CBZ excluding TP251, and (c) FCZ during treatment of secondary effluent spiked with pharmaceuticals by NAT/AT.

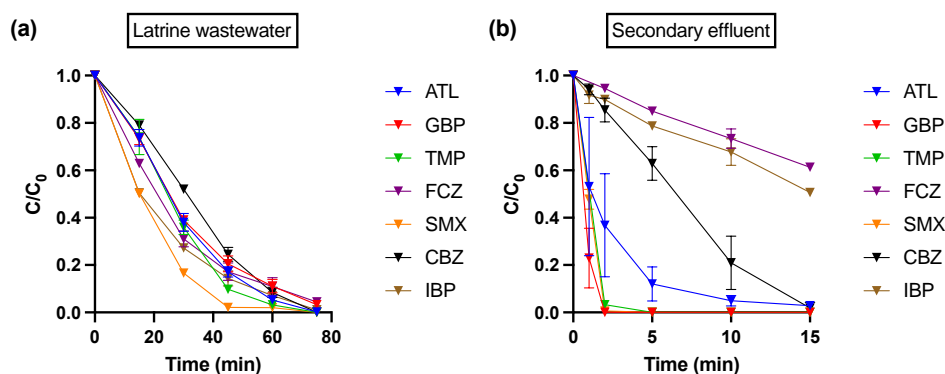


Figure 3.S18 Removal of spiked pharmaceutical compounds ($2 \mu\text{M}$ each) during electrolysis of (a) latrine wastewater and (b) secondary effluent by BDD.

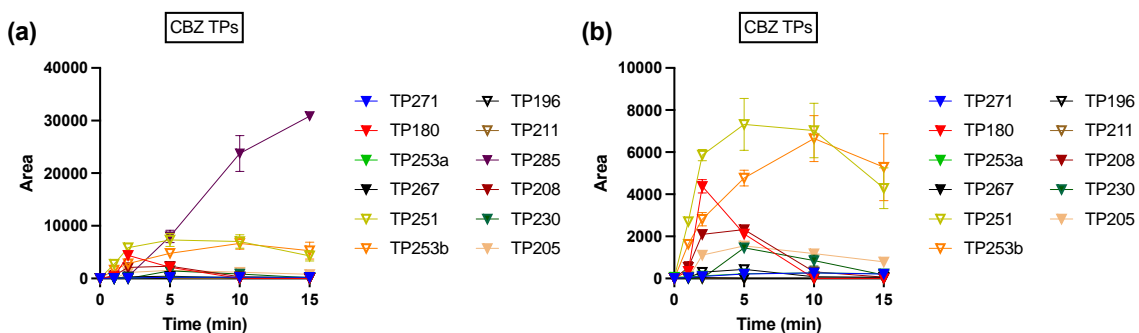


Figure 3.S19 Transformation product evolution for (a) CBZ, and (b) a zoomed-in look for CBZ excluding TP285 during treatment of secondary effluent spiked with pharmaceuticals by BDD. TP224 of FCZ was not detected.

Text 3.S1 Kinetic modeling.

Kinetic modeling was performed using the chemical kinetics software Kintecus 6.80.¹⁴ A total of 117 elementary reactions were included in the model. pH was set to 2 in all fitting scenarios. Rate constants were obtained from literature. NAT/AT electrode-specific rate constants were fitted in a previous paper.¹³ It is worth noting that the model can provide

valuable insights and predictions for pharmaceutical degradation but in a relative sense, since reactive species generation (especially O₃) varies depending on pH and other factors such as [Cl⁻]. In addition, in different solution matrices, reactive species are consumed to different degrees and sorption behaviors of organic compounds can also vary significantly.

Table 3.S1 Principle reactions in the kinetic model.

No.	Reaction	Rate constant	Reference
1	$H^+ + OH^- \rightarrow H_2O$	$1.00 \times 10^{11} M^{-1}s^{-1}$	15
2	$H_2O \rightarrow H^+ + OH^-$	$1.00 \times 10^{-3} s^{-1}$	15
3	$H^+ + HO_2^- \rightarrow H_2O_2$	$5.00 \times 10^{10} M^{-1}s^{-1}$	15
4	$H_2O_2 \rightarrow H^+ + HO_2^-$	$1.30 \times 10^{-1} s^{-1}$	15
5	$H^+ + Cl^- \rightarrow HCl$	$5.00 \times 10^{10} M^{-1}s^{-1}$	15
6	$HCl \rightarrow H^+ + Cl^-$	$8.60 \times 10^{16} s^{-1}$	15
7	$H^+ + OCl^- \rightarrow HOCl$	$5.00 \times 10^{10} M^{-1}s^{-1}$	15
8	$HOCl \rightarrow H^+ + OCl^-$	$1.40 \times 10^3 s^{-1}$	15
9	$H^+ + SO_4^{2-} \rightarrow HSO_4^-$	$5.00 \times 10^{10} M^{-1}s^{-1}$	Assumed
10	$HSO_4^- \rightarrow H^+ + SO_4^{2-}$	$6.00 \times 10^8 M^{-1}s^{-1}$	Calculated ^a
11	$H^+ + SO_5^{2-} \rightarrow HSO_5^-$	$5.00 \times 10^{10} M^{-1}s^{-1}$	15
12	$HSO_5^- \rightarrow H^+ + SO_5^{2-}$	$2.00 \times 10^1 M^{-1}s^{-1}$	15
13	$MO \rightarrow O_3$	$6.92/1.42 \times 10^{-7} s^{-1}$	13
14	$MO \rightarrow HO\cdot$	$1.69 \times 10^{-6} s^{-1}$	13
15	$MO + Cl^- \rightarrow Cl\cdot$	$1.50 \times 10^{-5} s^{-1}$	13
16	$MO + 2Cl^- \rightarrow Cl_2$	$8.05 \times 10^{-1} s^{-1}$	13
17	$MO + OCl^- \rightarrow OCl\cdot$	$3.89 \times 10^2 s^{-1}$	13
18	$HO\cdot + H_2O_2 \rightarrow HO_2\cdot + H_2O$	$2.70 \times 10^7 M^{-1}s^{-1}$	16
19	$HO\cdot + OH^- \rightarrow O\cdot^- + H_2O$	$1.20 \times 10^{10} M^{-1}s^{-1}$	17
20	$HO\cdot + HO\cdot \rightarrow H_2O_2$	$5.50 \times 10^9 M^{-1}s^{-1}$	16
21	$HO\cdot + Cl^- \rightarrow ClOH\cdot$	$4.30 \times 10^9 M^{-1}s^{-1}$	18

22	$\text{HO}\cdot \rightarrow \text{Products}$	$1.00 \times 10^7 \text{ s}^{-1}$	13
23	$\text{ClOH}\cdot^- \rightarrow \text{Cl}^- + \text{HO}\cdot$	$6.10 \times 10^9 \text{ s}^{-1}$	18
24	$\text{ClOH}\cdot^- + \text{H}^+ \rightarrow \text{Cl}\cdot + \text{H}_2\text{O}$	$2.10 \times 10^{10} \text{ M}^{-1}\text{s}^{-1}$	18
25	$\text{ClOH}\cdot^- + \text{Cl}^- \rightarrow \text{Cl}_2\cdot^- + \text{OH}^-$	$1.00 \times 10^4 \text{ M}^{-1}\text{s}^{-1}$	19
26	$\text{Cl}\cdot + \text{H}_2\text{O} \rightarrow \text{ClOH}\cdot^- + \text{H}^+$	$2.50 \times 10^5 \text{ M}^{-1}\text{s}^{-1}$	20
27	$\text{Cl}\cdot + \text{H}_2\text{O}_2 \rightarrow \text{HO}_2\cdot + \text{Cl}^- + \text{H}^+$	$2.00 \times 10^9 \text{ M}^{-1}\text{s}^{-1}$	21
28	$\text{Cl}\cdot + \text{OH}^- \rightarrow \text{ClOH}\cdot^-$	$1.80 \times 10^{10} \text{ M}^{-1}\text{s}^{-1}$	22
29	$\text{Cl}\cdot + \text{Cl}^- \rightarrow \text{Cl}_2\cdot^-$	$8.00 \times 10^9 \text{ M}^{-1}\text{s}^{-1}$	23
30	$\text{Cl}_2\cdot^- + \text{H}_2\text{O} \rightarrow \text{Cl}^- + \text{HClOH}$	$1.30 \times 10^3 \text{ M}^{-1}\text{s}^{-1}$	20
31	$\text{Cl}_2\cdot^- + \text{H}_2\text{O}_2 \rightarrow \text{HO}_2\cdot + 2\text{Cl}^- + \text{H}^+$	$1.40 \times 10^5 \text{ M}^{-1}\text{s}^{-1}$	24
32	$\text{Cl}_2\cdot^- + \text{OH}^- \rightarrow \text{ClOH}\cdot^- + \text{Cl}^-$	$4.50 \times 10^7 \text{ M}^{-1}\text{s}^{-1}$	19
33	$\text{Cl}_2\cdot^- \rightarrow \text{Cl}\cdot + \text{Cl}^-$	$6.00 \times 10^4 \text{ s}^{-1}$	23
34	$\text{HClOH} \rightarrow \text{Cl}\cdot + \text{H}_2\text{O}$	$1.00 \times 10^2 \text{ s}^{-1}$	20
35	$\text{HClOH} \rightarrow \text{ClOH}\cdot^- + \text{H}^+$	$1.00 \times 10^8 \text{ s}^{-1}$	20
36	$\text{HClOH} + \text{Cl}^- \rightarrow \text{Cl}_2\cdot^- + \text{H}_2\text{O}$	$5.00 \times 10^9 \text{ M}^{-1}\text{s}^{-1}$	20
37	$\text{Cl}\cdot + \text{Cl}\cdot \rightarrow \text{Cl}_2$	$8.80 \times 10^7 \text{ M}^{-1}\text{s}^{-1}$	25
38	$\text{Cl}\cdot + \text{Cl}_2\cdot^- \rightarrow \text{Cl}^- + \text{Cl}_2$	$2.10 \times 10^9 \text{ M}^{-1}\text{s}^{-1}$	21
39	$\text{Cl}_2\cdot^- + \text{HO}\cdot \rightarrow \text{HOCl} + \text{Cl}^-$	$1.00 \times 10^9 \text{ M}^{-1}\text{s}^{-1}$	26
40	$\text{Cl}_2\cdot^- + \text{Cl}_2\cdot^- \rightarrow 2\text{Cl}^- + \text{Cl}_2$	$9.00 \times 10^8 \text{ M}^{-1}\text{s}^{-1}$	21
41	$\text{Cl}_2 + \text{H}_2\text{O} \rightarrow \text{HOCl} + \text{Cl}^- + \text{H}^+$	$1.50 \times 10^1 \text{ M}^{-1}\text{s}^{-1}$	27
42	$\text{Cl}_2 + \text{H}_2\text{O}_2 \rightarrow \text{O}_2 + 2\text{HCl}$	$1.30 \times 10^4 \text{ M}^{-1}\text{s}^{-1}$	24
43	$\text{Cl}_2 + \text{O}_2\cdot^- \rightarrow \text{O}_2 + \text{Cl}_2\cdot^-$	$1.00 \times 10^9 \text{ M}^{-1}\text{s}^{-1}$	24
44	$\text{Cl}_2 + \text{HO}_2\cdot \rightarrow \text{O}_2 + \text{Cl}_2\cdot^- + \text{H}^+$	$1.00 \times 10^9 \text{ M}^{-1}\text{s}^{-1}$	28
45	$\text{Cl}_2 + \text{Cl}^- \rightarrow \text{Cl}_3^-$	$2.00 \times 10^4 \text{ M}^{-1}\text{s}^{-1}$	29
46	$\text{Cl}_3^- + \text{O}_2\cdot^- \rightarrow \text{Cl}_2\cdot^- + \text{Cl}^- + \text{O}_2$	$3.80 \times 10^9 \text{ M}^{-1}\text{s}^{-1}$	24

47	$\text{Cl}_3^- + \text{HO}_2^\cdot \rightarrow \text{Cl}_2^\cdot + \text{HCl} + \text{O}_2$	$1.00 \times 10^9 \text{ M}^{-1}\text{s}^{-1}$	28
48	$\text{Cl}_3^- \rightarrow \text{Cl}_2 + \text{Cl}^\cdot$	$1.10 \times 10^5 \text{ s}^{-1}$	29
49	$\text{HOCl} + \text{H}_2\text{O}_2 \rightarrow \text{HCl} + \text{H}_2\text{O} + \text{O}_2$	$1.10 \times 10^4 \text{ M}^{-1}\text{s}^{-1}$	30
50	$\text{HOCl} + \text{HO}^\cdot \rightarrow \text{OCl}^\cdot + \text{H}_2\text{O}$	$2.00 \times 10^9 \text{ M}^{-1}\text{s}^{-1}$	24
51	$\text{HOCl} + \text{O}_2^\cdot \rightarrow \text{Cl}^\cdot + \text{OH}^- + \text{O}_2$	$7.50 \times 10^6 \text{ M}^{-1}\text{s}^{-1}$	24
52	$\text{HOCl} + \text{HO}_2^\cdot \rightarrow \text{Cl}^\cdot + \text{H}_2\text{O} + \text{O}_2$	$7.50 \times 10^6 \text{ M}^{-1}\text{s}^{-1}$	24
53	$\text{HOCl} + \text{Cl}^\cdot \rightarrow \text{OCl}^\cdot + \text{Cl}^- + \text{H}^+$	$3.00 \times 10^9 \text{ M}^{-1}\text{s}^{-1}$	22
54	$\text{HOCl} + \text{Cl}^\cdot + \text{H}^+ \rightarrow \text{Cl}_2 + \text{H}_2\text{O}$	$1.82 \times 10^4 \text{ M}^{-2}\text{s}^{-1}$	27
55	$\text{OCl}^\cdot + \text{H}_2\text{O}_2 \rightarrow \text{Cl}^\cdot + \text{H}_2\text{O} + \text{O}_2$	$1.70 \times 10^5 \text{ M}^{-1}\text{s}^{-1}$	30
56	$\text{OCl}^\cdot + \text{HO}^\cdot \rightarrow \text{OCl}^\cdot + \text{OH}^-$	$8.80 \times 10^9 \text{ M}^{-1}\text{s}^{-1}$	24
57	$\text{OCl}^\cdot + \text{O}_2^\cdot + \text{H}_2\text{O} \rightarrow \text{Cl}^\cdot + 2\text{OH}^- + \text{O}_2$	$2.00 \times 10^8 \text{ M}^{-2}\text{s}^{-1}$	24
58	$\text{OCl}^\cdot + \text{Cl}^\cdot \rightarrow \text{OCl}^\cdot + \text{Cl}^- + \text{H}^+$	$8.20 \times 10^9 \text{ M}^{-1}\text{s}^{-1}$	22
59	$\text{OCl}^\cdot + \text{OCl}^\cdot \rightarrow \text{P}_3$	$7.50 \times 10^9 \text{ M}^{-1}\text{s}^{-1}$	31
60	$\text{HSO}_4^\cdot + \text{HO}^\cdot \rightarrow \text{SO}_4^\cdot + \text{H}_2\text{O}$	$6.90 \times 10^5 \text{ M}^{-1}\text{s}^{-1}$	16
61	$\text{HSO}_4^\cdot + \text{O}_3 \rightarrow \text{Products}$	$1.00 \times 10^{-4} \text{ M}^{-1}\text{s}^{-1}$	32
62	$\text{SO}_4^{2-} + \text{Cl}^\cdot \rightarrow \text{SO}_4^\cdot + \text{Cl}^-$	$2.50 \times 10^8 \text{ M}^{-1}\text{s}^{-1}$	33
63	$\text{SO}_4^\cdot + \text{H}_2\text{O} \rightarrow \text{HSO}_4^- + \text{HO}^\cdot$	$6.60 \times 10^2 \text{ M}^{-1}\text{s}^{-1}$	34
64	$\text{SO}_4^\cdot + \text{H}_2\text{O}_2 \rightarrow \text{HSO}_4^- + \text{HO}_2^\cdot$	$1.20 \times 10^7 \text{ M}^{-1}\text{s}^{-1}$	35
65	$\text{SO}_4^\cdot + \text{OH}^- \rightarrow \text{SO}_4^{2-} + \text{HO}^\cdot$	$1.40 \times 10^7 \text{ M}^{-1}\text{s}^{-1}$	34
66	$\text{SO}_4^\cdot + \text{HO}^\cdot \rightarrow \text{HSO}_5^\cdot$	$1.00 \times 10^{10} \text{ M}^{-1}\text{s}^{-1}$	36
67	$\text{SO}_4^\cdot + \text{HO}_2^\cdot \rightarrow \text{HSO}_4^- + \text{O}_2$	$3.50 \times 10^9 \text{ M}^{-1}\text{s}^{-1}$	37
68	$\text{SO}_4^\cdot + \text{SO}_4^\cdot \rightarrow \text{S}_2\text{O}_8^{2-}$	$7.60 \times 10^8 \text{ M}^{-1}\text{s}^{-1}$	37
69	$\text{SO}_4^\cdot + \text{HSO}_5^\cdot \rightarrow \text{HSO}_4^- + \text{SO}_5^\cdot$	$1.00 \times 10^6 \text{ M}^{-1}\text{s}^{-1}$	38
70	$\text{SO}_4^\cdot + \text{SO}_5^{2-} \rightarrow \text{SO}_4^{2-} + \text{SO}_5^\cdot$	$1.00 \times 10^8 \text{ M}^{-1}\text{s}^{-1}$	38
71	$\text{SO}_4^\cdot + \text{S}_2\text{O}_8^{2-} \rightarrow \text{SO}_4^{2-} + \text{S}_2\text{O}_8^\cdot$	$6.60 \times 10^5 \text{ M}^{-1}\text{s}^{-1}$	37
72	$\text{SO}_4^\cdot + \text{Cl}^- \rightarrow \text{SO}_4^{2-} + \text{Cl}^\cdot$	$4.70 \times 10^8 \text{ M}^{-1}\text{s}^{-1}$	33

73	$\text{HSO}_5^- + \text{HO}\cdot \rightarrow \text{SO}_5\cdot^- + \text{H}_2\text{O}$	$1.70 \times 10^7 \text{ M}^{-1}\text{s}^{-1}$	39
74	$\text{SO}_5^{2-} + \text{HO}\cdot \rightarrow \text{SO}_5\cdot^- + \text{OH}^-$	$2.10 \times 10^9 \text{ M}^{-1}\text{s}^{-1}$	39
75	$\text{SO}_5\cdot^- + \text{HO}_2\cdot \rightarrow \text{HSO}_5^- + \text{O}_2$	$5.50 \times 10^7 \text{ M}^{-1}\text{s}^{-1}$	40
76	$\text{SO}_5\cdot^- + \text{SO}_5\cdot^- \rightarrow 2\text{SO}_4\cdot^- + \text{O}_2$	$2.10 \times 10^8 \text{ M}^{-1}\text{s}^{-1}$	38
77	$\text{SO}_5\cdot^- + \text{SO}_5\cdot^- \rightarrow \text{S}_2\text{O}_8^{2-} + \text{O}_2$	$2.20 \times 10^8 \text{ M}^{-1}\text{s}^{-1}$	38
78	$\text{S}_2\text{O}_8^{2-} + \text{HO}\cdot \rightarrow \text{S}_2\text{O}_8\cdot^- + \text{OH}^-$	$1.40 \times 10^7 \text{ M}^{-1}\text{s}^{-1}$	41
79	$\text{O}_3 + \text{H}_2\text{O}_2 \rightarrow \text{O}_2 + \text{HO}\cdot + \text{HO}_2\cdot$	$6.50 \times 10^{-3} \text{ M}^{-1}\text{s}^{-1}$	42
80	$\text{O}_3 + \text{OH}^- \rightarrow \text{O}_2 + \text{HO}_2^-$	$7.00 \times 10^1 \text{ M}^{-1}\text{s}^{-1}$	43
81	$\text{O}_3 + \text{HO}\cdot \rightarrow \text{O}_2 + \text{HO}_2\cdot$	$1.10 \times 10^8 \text{ M}^{-1}\text{s}^{-1}$	43
82	$\text{O}_3 + \text{O}_2\cdot^- \rightarrow \text{O}_3\cdot^- + \text{O}_2$	$1.60 \times 10^9 \text{ M}^{-1}\text{s}^{-1}$	44
83	$\text{O}_3 + \text{HO}_2^- \rightarrow \text{O}_2 + \text{HO}\cdot + \text{O}_2\cdot^-$	$2.80 \times 10^6 \text{ M}^{-1}\text{s}^{-1}$	42
84	$\text{O}_3 + \text{Cl}^- \rightarrow \text{O}_2 + \text{OCl}^-$	$3.00 \times 10^{-3} \text{ M}^{-1}\text{s}^{-1}$	32
85	$\text{O}_3 + \text{HOCl} \rightarrow \text{Products}$	$2.00 \times 10^{-3} \text{ M}^{-1}\text{s}^{-1}$	32
86	$\text{O}_3 + \text{OCl}^- \rightarrow \text{Products}$	$1.20 \times 10^2 \text{ M}^{-1}\text{s}^{-1}$	32
87	$\text{O}_3 + \text{ClO}_3^- \rightarrow \text{Products}$	$1.00 \times 10^{-4} \text{ M}^{-1}\text{s}^{-1}$	32
88	$\text{O}_3 + \text{ClO}_4^- \rightarrow \text{Products}$	$2.00 \times 10^{-5} \text{ M}^{-1}\text{s}^{-1}$	32
89	$\text{O}_3 + \text{Cl}_2\cdot^- \rightarrow \text{Products}$	$9.00 \times 10^7 \text{ M}^{-1}\text{s}^{-1}$	45
90	$\text{O}_3 \rightarrow \text{Products}$	$7.04/3.28 \times 10^{-3} \text{ s}^{-1}$	13
91	$\text{O}_3\cdot^- + \text{H}^+ \rightarrow \text{HO}_3\cdot$	$5.20 \times 10^{10} \text{ M}^{-1}\text{s}^{-1}$	44
92	$\text{O}_3\cdot^- + \text{HO}\cdot \rightarrow \text{HO}_2\cdot + \text{O}_2\cdot^-$	$8.50 \times 10^9 \text{ M}^{-1}\text{s}^{-1}$	46
93	$\text{O}_3\cdot^- + \text{O}\cdot^- \rightarrow 2\text{O}_2\cdot^-$	$7.00 \times 10^8 \text{ M}^{-1}\text{s}^{-1}$	47
94	$\text{O}_3\cdot^- \rightarrow \text{O}_2 + \text{O}\cdot^-$	$3.30 \times 10^3 \text{ s}^{-1}$	48
95	$\text{O}_2\cdot^- + \text{H}_2\text{O}_2 \rightarrow \text{O}_2 + \text{HO}\cdot + \text{OH}^-$	$1.30 \times 10^{-1} \text{ M}^{-1}\text{s}^{-1}$	49
96	$\text{O}_2\cdot^- + \text{H}^+ \rightarrow \text{HO}_2\cdot$	$7.20 \times 10^{10} \text{ M}^{-1}\text{s}^{-1}$	50
97	$\text{O}_2\cdot^- + \text{HO}\cdot \rightarrow \text{O}_2 + \text{OH}^-$	$7.00 \times 10^9 \text{ M}^{-1}\text{s}^{-1}$	49
98	$\text{O}_2\cdot^- + \text{O}\cdot^- + \text{H}_2\text{O} \rightarrow \text{O}_2 + 2\text{OH}^-$	$6.00 \times 10^8 \text{ M}^{-2}\text{s}^{-1}$	47
99	$\text{O}_2\cdot^- + \text{HO}_2\cdot \rightarrow \text{HO}_2^- + \text{O}_2$	$9.70 \times 10^7 \text{ M}^{-1}\text{s}^{-1}$	49

100	$O_2\cdot^- + Cl_2\cdot^- \rightarrow O_2 + 2Cl\cdot$	$2.00 \times 10^9 M^{-1}s^{-1}$	24
101	$O_2\cdot^- + Cl\cdot \rightarrow \text{Products}$	$1.40 \times 10^{-2} M^{-1}s^{-1}$	51
102	$O_2\cdot^- + HOCl \rightarrow O_2 + Cl\cdot + HO\cdot$	$7.50 \times 10^6 M^{-1}s^{-1}$	51
103	$O\cdot + O_2 \rightarrow O_3\cdot^-$	$3.60 \times 10^9 M^{-1}s^{-1}$	16
104	$O\cdot + H_2O \rightarrow HO\cdot + OH\cdot$	$1.70 \times 10^6 M^{-1}s^{-1}$	16
105	$O\cdot + HO\cdot \rightarrow HO_2\cdot$	$2.00 \times 10^{10} M^{-1}s^{-1}$	16
106	$O\cdot + HO_2\cdot \rightarrow OH\cdot + O_2\cdot^-$	$4.00 \times 10^8 M^{-1}s^{-1}$	16
107	$O\cdot + OCl\cdot \rightarrow OCl\cdot + OH\cdot$	$2.30 \times 10^8 M^{-1}s^{-1}$	16
108	$HO_2\cdot + H_2O + O_2\cdot^- \rightarrow O_2 + H_2O_2 + OH\cdot$	$9.70 \times 10^7 M^{-2}s^{-1}$	51
109	$HO_2\cdot + H_2O_2 \rightarrow O_2 + H_2O + HO\cdot$	$3.00 \times 10^0 M^{-1}s^{-1}$	49
110	$HO_2\cdot + HO\cdot \rightarrow O_2 + H_2O$	$6.60 \times 10^9 M^{-1}s^{-1}$	49
111	$HO_2\cdot + HO_2\cdot \rightarrow O_2 + H_2O_2$	$8.30 \times 10^5 M^{-1}s^{-1}$	49
112	$HO_2\cdot + Cl_2\cdot^- \rightarrow O_2 + 2Cl\cdot + H^+$	$3.00 \times 10^9 M^{-1}s^{-1}$	24
113	$HO_2\cdot + Cl_2 \rightarrow Cl_2\cdot^- + O_2 + H^+$	$1.00 \times 10^9 M^{-1}s^{-1}$	28
114	$HO_2\cdot \rightarrow H^+ + O_2\cdot^-$	$7.90 \times 10^5 s^{-1}$	15
115	$HO_2\cdot + HO\cdot \rightarrow HO_2\cdot + OH\cdot$	$7.50 \times 10^9 M^{-1}s^{-1}$	16
116	$HO_3\cdot \rightarrow HO\cdot + O_2$	$1.10 \times 10^5 s^{-1}$	44
117	$HO_3\cdot \rightarrow O_3\cdot^- + H^+$	$3.70 \times 10^4 s^{-1}$	44

- a. Calculated using the HSO_4^- acid dissociation constant $K_a = 1.2 \times 10^{-2} M$ ($pK_a = 1.92$)⁵²

Table 3.S2 Fragmentation analyses of TP244, 278, 253a, 267, 253c, and 205 of CBZ.

TPs	Formula	Fragment m/z	Fragment elemental composition	Analysis
TP244	$C_{13}H_{10}NO_4$	200.0712	$C_{12}H_{10}NO_2$	- CO_2
		182.0611	$C_{12}H_8NO$	- CO_2 - H_2O
TP278	$C_{13}H_9NO_4Cl$	234.0323	$C_{12}H_9NO_2Cl$	- CO_2
		216.0220	$C_{12}H_7NOCl$	- CO_2 - H_2O
TP253a	$C_{15}H_{13}N_2O_2$	236.0711	$C_{15}H_{10}NO_2$	- NH_3
		210.0922	$C_{14}H_{12}NO$	- CHON

		180.0817	C ₁₃ H ₁₀ N	- NH ₃ - 2CO
TP267	C ₁₅ H ₁₁ N ₂ O ₃	249.0671	C ₁₅ H ₉ N ₂ O ₂	- H ₂ O
		221.0719	C ₁₄ H ₉ N ₂ O	- H ₂ O - CO
TP253c	C ₁₄ H ₉ N ₂ O ₃	235.0508	C ₁₄ H ₇ N ₂ O ₂	- H ₂ O
		179.0609	C ₁₂ H ₇ N ₂	- H ₂ O - 2CO
TP205	C ₁₄ H ₉ N ₂	178.0656	C ₁₃ H ₈ N	- CHN
		151.0550	C ₁₂ H ₇	- 2CHN

Table 3.S3 Sorted carbamazepine (CBZ) transformation product response^a at NAT/AT and BDD.

NaClO ₄ Electrolytes							
TPs	NAT/AT ClO ₄	TPs	NAT/AT SO ₄ ClO ₄	TPs	BDD ClO ₄	TPs	BDD SO ₄ ClO ₄
TP251	0.90382989	TP251	0.96226418	TP251	0.98952151	TP251	0.99620415
TP147	0.03610589	TP147	0.03701393	TP253b	0.18088225	TP180	0.1227268
TP267	0.01011511	TP267	0.02578316	TP180	0.14145966	TP253b	0.10876842
TP180	0.00196006	TP180	0.00216116	TP253a	0.02828460	TP267	0.02676076
TP253a	0.00167781	TP253a	0.0019577	TP267	0.01201729	TP253a	0.01528693

NaCl Electrolytes							
TPs	NAT/AT Cl	TPs	NAT/AT SO ₄ Cl	TPs	BDD Cl	TPs	BDD SO ₄ Cl
TP251	0.95408979	TP251	0.99613983	TP208	0.90001086	TP208	0.78266212
TP285	0.73981642	TP285	0.6952044	TP253b	0.59386958	TP253b	0.53289073
TP208	0.65311634	TP208	0.4061866	TP180	0.3606068	TP180	0.34448106
TP180	0.46270393	TP180	0.30062261	TP205	0.18332926	TP285	0.28327174
TP226	0.09525558	TP253	0.05691551	TP230	0.17303048	TP244	0.22690124
TP253b	0.08776798	TP253c	0.05457997	TP285	0.16501126	TP205	0.18694277
TP253c	0.05010463	TP301	0.0481018	TP196	0.14764308	TP230	0.16624438
TP196	0.04887316	TP196	0.04570856	TP289	0.12194361	TP196	0.14185019
TP230	0.03736705	TP230	0.02646237	TP244	0.08163044	TP273	0.10105349
TP205	0.02609243	TP205	0.0177823	TP251	0.06925561	TP289	0.09438581
TP289	0.0134358	TP226	0.01577173	TP273	0.06841434	TP278	0.04815972
TP211	0.01318202	TP224	0.01087495	TP211	0.06335314	TP251	0.04692144
TP224	0.00792113	TP211	0.01051145	TP253a	0.05441125	TP211	0.03343367
TP253a	0.00612342	TP289	0.00872597	TP271	0.04591712	TP253a	0.02721367
TP271	0.0055833	TP181	0.00800583	TP226	0.03709734	TP271	0.02276537

<u>TP244</u>	0.00449258	<u>TP278</u>	0.00581835	TP224	0.02863036	TP210	0.01748838
TP301	0.0026327	TP267	0.00551236	TP210	0.01774811	TP224	0.01503086
<u>TP273</u>	0.00210493	TP253a	0.00327097	<u>TP278</u>	0.01287688	TP226	0.0089728
TP181	0.00146913	<u>TP273</u>	0.0021928				
TP147	0.00144135	TP271	0.00212902				
<u>TP278</u>	0.0013882	TP147	0.00083521				
TP267	0.00090123	<u>TP244</u>	0.00081129				

- Take the peak area of the TP with highest maximum response in MS to be 1.0, the table summarized responses of other TPs relative to the max.
- Tps marked with underline have, to the best of our knowledge, not been reported before.
- Tps marked in green are not detected at BDD, and Tps marked in blue are not detected at NAT/AT, in respective electrolytes.

Table 3.S4 Target pharmaceutical compound properties.

	pKa	log K _{ow}	k _{O₃} (M ⁻¹ s ⁻¹) ^a	Ref	k _{OH} (M ⁻¹ s ⁻¹)	Ref
Carbamazepine (CBZ)	-	2.3-2.77	3.0 × 10 ⁵	53	8.8 × 10 ⁹	53
Fluconazole (FCZ)	2.6, 2.9, 11.0	0.25-0.5	2.0	11	4.4 × 10 ⁹	11
Sulfamethoxazole (SMX)	5.7	0.89	5.7 × 10 ⁵	54	5.5 × 10 ⁹	53
Trimethoprim (TMP)	3.2, 7.1	0.91	2.7 × 10 ⁵	54	6.9 × 10 ⁹	54
Atenolol (ATL)	9.6	0.16	1.7 × 10 ³	55	8.0 × 10 ⁹	55
Gabapentin (GBP)	3.7	-1.1	2.2 × 10 ²	11	9.1 × 10 ⁹	11
Ibuprofen (IBP)	4.9	3.97	9.6	53	7.4 × 10 ⁹	53

- Rate constants with O₃ at pH 7.

Table 3.S5 Composition of latrine wastewater and secondary effluent.

Property	Latrine wastewater	Secondary effluent ^a
pH	8.3	7.5
Conductivity (mS cm ⁻¹)	16.5	1.2
Cell voltage (E _{WE} – E _{Ce} , V)	4.0 V (NAT/AT), 5.9 V (BDD)	5.4 V (NAT/AT), 7.5 V (BDD)
COD (mg O ₂ L ⁻¹)	440	~80
[NH ₄ ⁺] (mM)	31	0.3
[Cl ⁻] (mM)	72	4.1

[Na ⁺] (mM)	81	6.0
[K ⁺] (mM)	-	0.4
[Mg ²⁺] (mM)	-	0.7

- a. Composition of the secondary effluent was similar to a biologically-treated hospital wastewater used by Lan *et al.*⁵⁶ (pH 7.84, conductivity 1.2 mS/cm, COD 86 mg/L, [Cl⁻] 2.0 mM, [Na⁺] 7.0 mM, [K⁺] 0.9 mM, [Mg²⁺] 0.4 mM).

References

- (1) Hübner, U.; Seiwert, B.; Reemtsma, T.; Jekel, M. Ozonation Products of Carbamazepine and Their Removal from Secondary Effluents by Soil Aquifer Treatment – Indications from Column Experiments. *Water Res.* **2014**, *49*, 34–43.
- (2) Martínez, C.; Canle L., M.; Fernández, M. I.; Santaballa, J. A.; Faria, J. Kinetics and Mechanism of Aqueous Degradation of Carbamazepine by Heterogeneous Photocatalysis Using Nanocrystalline TiO₂, ZnO and Multi-Walled Carbon Nanotubes–Anatase Composites. *Appl. Catal. B: Environmental* **2011**, *102* (3), 563–571.
- (3) Pan, Y.; Cheng, S.; Yang, X.; Ren, J.; Fang, J.; Shang, C.; Song, W.; Lian, L.; Zhang, X. UV/Chlorine Treatment of Carbamazepine: Transformation Products and Their Formation Kinetics. *Water Res.* **2017**, *116*, 254–265.
- (4) Wang, W.-L.; Wu, Q.-Y.; Huang, N.; Wang, T.; Hu, H.-Y. Synergistic Effect between UV and Chlorine (UV/Chlorine) on the Degradation of Carbamazepine: Influence Factors and Radical Species. *Water Res.* **2016**, *98*, 190–198.
- (5) Soufan, M.; Deborde, M.; Delmont, A.; Legube, B. Aqueous Chlorination of Carbamazepine: Kinetic Study and Transformation Product Identification. *Water Res.* **2013**, *47* (14), 5076–5087.
- (6) Keen, O. S.; Baik, S.; Linden, K. G.; Aga, D. S.; Love, N. G. Enhanced Biodegradation of Carbamazepine after UV/H₂O₂ Advanced Oxidation. *Environ. Sci. Technol.* **2012**, *46* (11), 6222–6227.
- (7) Chiron, S.; Minero, C.; Vione, D. Photodegradation Processes of the Antiepileptic Drug Carbamazepine, Relevant To Estuarine Waters. *Environ. Sci. Technol.* **2006**, *40* (19), 5977–5983.
- (8) Wu, Y.; Yang, Y.; Liu, Y.; Zhang, L.; Feng, L. Modelling Study on the Effects of Chloride on the Degradation of Bezafibrate and Carbamazepine in Sulfate Radical-Based Advanced Oxidation Processes: Conversion of Reactive Radicals. *Chem. Eng. J.* **2019**, *358*, 1332–1341.
- (9) Seiwert, B.; Golan-Rozen, N.; Weidauer, C.; Riemenschneider, C.; Chefetz, B.; Hadar, Y.; Reemtsma, T. Electrochemistry Combined with LC–HRMS: Elucidating Transformation Products of the Recalcitrant Pharmaceutical Compound Carbamazepine Generated by the White-Rot Fungus *Pleurotus Ostreatus*. *Environ. Sci. Technol.* **2015**, *49* (20), 12342–12350.
- (10) Golan-Rozen, N.; Seiwert, B.; Riemenschneider, C.; Reemtsma, T.; Chefetz, B.; Hadar, Y. Transformation Pathways of the Recalcitrant Pharmaceutical Compound

- Carbamazepine by the White-Rot Fungus *Pleurotus Ostreatus*: Effects of Growth Conditions. *Environ. Sci. Technol.* **2015**, *49* (20), 12351–12362.
- (11) Lee, Y.; Kovalova, L.; McArdell, C. S.; von Gunten, U. Prediction of Micropollutant Elimination during Ozonation of a Hospital Wastewater Effluent. *Water Res.* **2014**, *64*, 134–148.
- (12) Lee, Y.; Gerrity, D.; Lee, M.; Bogeat, A. E.; Salhi, E.; Gamage, S.; Trenholm, R. A.; Wert, E. C.; Snyder, S. A.; von Gunten, U. Prediction of Micropollutant Elimination during Ozonation of Municipal Wastewater Effluents: Use of Kinetic and Water Specific Information. *Environ. Sci. Technol.* **2013**, *47* (11), 5872–5881.
- (13) Zhang, Y.; Yang, Y.; Yang, S.; Quispe-Cardenas, E.; Hoffmann, M. R. Application of Heterojunction Ni–Sb–SnO₂ Anodes for Electrochemical Water Treatment. *ACS EST Eng.* **2021**, *1* (8), 1236–1245.
- (14) Ianni, J. C. *Kintecus*, Windows Version 6.80, 2020, www.kintecus.com.
- (15) Yang, Y.; Pignatello, J. J.; Ma, J.; Mitch, W. A. Comparison of Halide Impacts on the Efficiency of Contaminant Degradation by Sulfate and Hydroxyl Radical-Based Advanced Oxidation Processes (AOPs). *Environ. Sci. Technol.* **2014**, *48* (4), 2344–2351.
- (16) Buxton, G. V.; Greenstock, C. L.; Helman, W. P.; Ross, A. B. Critical Review of Rate Constants for Reactions of Hydrated Electrons, Hydrogen Atoms and Hydroxyl Radicals ($\cdot\text{OH}/\cdot\text{O}^-$ in Aqueous Solution. *J. Phys. Chem. Ref. Data* **1988**, *17* (2), 513–886.
- (17) V. Buxton, G. Pulse Radiolysis of Aqueous Solutions. Rate of Reaction of OH with OH⁻. *Transactions of the Faraday Society* **1970**, *66* (0), 1656–1660.
- (18) G. Jayson, G.; J. Parsons, B.; J. Swallow, A. Some Simple, Highly Reactive, Inorganic Chlorine Derivatives in Aqueous Solution. Their Formation Using Pulses of Radiation and Their Role in the Mechanism of the Fricke Dosimeter. *J. Chem. Soc., Faraday Trans. 1: Physical Chemistry in Condensed Phases* **1973**, *69* (0), 1597–1607.
- (19) Grigor'ev, A. E.; Makarov, I. E.; Pikaev, A. K. Formation of Cl₂⁻ in the bulk of solution during radiolysis of concentrated aqueous solutions of chlorides. *Khimiya Vysokikh Ehnergij* **1987**, *21* (2), 123–126.
- (20) McElroy, W. John. A Laser Photolysis Study of the Reaction of Sulfate(1-) with Chloride and the Subsequent Decay of Chlorine(1-) in Aqueous Solution. *J. Phys. Chem.* **1990**, *94* (6), 2435–2441.
- (21) Yu, X.-Y.; Barker, J. R. Hydrogen Peroxide Photolysis in Acidic Aqueous Solutions Containing Chloride Ions. II. Quantum Yield of HO•(Aq) Radicals. *J. Phys. Chem. A* **2003**, *107* (9), 1325–1332.
- (22) Klänig, U. K.; Wolff, T. Laser Flash Photolysis of HClO, ClO⁻, HBrO, and BrO⁻ in Aqueous Solution. Reactions of Cl- and Br-Atoms. *Berichte der Bunsengesellschaft für physikalische Chemie* **1985**, *89* (3), 243–245.
- (23) Nagarajan, V.; Fessenden, R. W. Flash Photolysis of Transient Radicals. 1. X₂⁻ with X = Cl, Br, I, and SCN. *J. Phys. Chem.* **1985**, *89* (11), 2330–2335.
- (24) Matthew, B. M.; Anastasio, C. A Chemical Probe Technique for the Determination of Reactive Halogen Species in Aqueous Solution: Part 1? Bromide Solutions. *Atmospheric Chem. Phys. Discussions* **2006**, *6* (1), 899–940.

- (25) Wu, D.; Wong, D.; Di Bartolo, B. Evolution of Cl⁻² in Aqueous NaCl Solutions. *J. Photochem.* **1980**, *14* (4), 303–310.
- (26) Wagner, I.; Karthäuser, J.; Strehlow, H. On the Decay of the Dichloride Anion Cl⁻² in Aqueous Solution. *Berichte der Bunsengesellschaft für physikalische Chemie* **1986**, *90* (10), 861–867.
- (27) Wang, T. X.; Margerum, D. W. Kinetics of Reversible Chlorine Hydrolysis: Temperature Dependence and General-Acid/Base-Assisted Mechanisms. *Inorg. Chem.* **1994**, *33* (6), 1050–1055.
- (28) Bjergbakke, E.; Navaratnam, S.; Parsons, B. J.; Swallow, A. J. Reaction between Hydroperoxy Radicals and Chlorine in Aqueous Solution. *J. Am. Chem. Soc.* **1981**, *103* (19), 5926–5928.
- (29) Ershov, B. G. Kinetics, Mechanism and Intermediates of Some Radiation-Induced Reactions in Aqueous Solutions. *Russ. Chem. Rev.* **2004**, *73* (1), 101–113.
- (30) Connick, R. E. The Interaction of Hydrogen Peroxide and Hypochlorous Acid in Acidic Solutions Containing Chloride Ion. *J. Am. Chem. Soc.* **1947**, *69* (6), 1509–1514.
- (31) V. Buxton, G.; S. Subhani, M. Radiation Chemistry and Photochemistry of Oxychlorine Ions. Part 1.—Radiolysis of Aqueous Solutions of Hypochlorite and Chlorite Ions. *J. Chem. Soc., Faraday Trans. 1: Physical Chemistry in Condensed Phases* **1972**, *68* (0), 947–957.
- (32) Hoigné, J.; Bader, H.; Haag, W. R.; Staehelin, J. Rate Constants of Reactions of Ozone with Organic and Inorganic Compounds in Water—III. Inorganic Compounds and Radicals. *Water Res.* **1985**, *19* (8), 993–1004.
- (33) Huie, R. E.; Clifton, C. L.; Neta, P. Electron Transfer Reaction Rates and Equilibria of the Carbonate and Sulfate Radical Anions. *Int. J. Radiat. Appl. Instrum. Part C. Radiation Physics and Chemistry* **1991**, *38* (5), 477–481.
- (34) Herrmann, H.; Reese, A.; Zellner, R. Time-Resolved UV/VIS Diode Array Absorption Spectroscopy of SO_x⁻ (X=3, 4, 5) Radical Anions in Aqueous Solution. *J. Mol. Struct.* **1995**, *348*, 183–186.
- (35) Wine, P. H.; Tang, Y.; Thorn, R. P.; Wells, J. R.; Davis, D. D. Kinetics of Aqueous Phase Reactions of the SO₄⁻ Radical with Potential Importance in Cloud Chemistry. *J. Geophys. Res. Atmos.* **1989**, *94* (D1), 1085–1094.
- (36) Klaning, U. K.; Sehested, K.; Appelman, E. H. Laser Flash Photolysis and Pulse Radiolysis of Aqueous Solutions of the Fluoroxysulfate Ion, SO₄F⁻. *Inorg. Chem.* **1991**, *30* (18), 3582–3584.
- (37) Jiang, P.-Y.; Katsumura, Y.; Nagaishi, R.; Domae, M.; Ishikawa, K.; Ishigure, K.; Yoshida, Y. Pulse Radiolysis Study of Concentrated Sulfuric Acid Solutions. Formation Mechanism, Yield and Reactivity of Sulfate Radicals. *J. Chem. Soc., Faraday Trans.* **1992**, *88* (12), 1653–1658.
- (38) Das, T. N. Reactivity and Role of SO₅^{•-} Radical in Aqueous Medium Chain Oxidation of Sulfite to Sulfate and Atmospheric Sulfuric Acid Generation. *J. Phys. Chem. A* **2001**, *105* (40), 9142–9155.
- (39) Maruthamuthu, P.; Neta, P. Radiolytic Chain Decomposition of Peroxomonophosphoric and Peroxomonosulfuric Acids. *J. Phys. Chem.* **1977**, *81* (10), 937–940.

- (40) Yermakov, A. N.; Zhitomirsky, B. M.; Poskrebyshev, G. A.; Stoliarov, S. I. Kinetic Study of SO₅⁻ and HO₂ Radicals Reactivity in Aqueous Phase Bisulfite Oxidation. *J. Phys. Chem.* **1995**, *99* (10), 3120–3127.
- (41) Buxton, G. V.; Salmon, G. A.; Wood, N. D. A Pulse Radiolysis Study of the Chemistry of Oxysulphur Radicals in Aqueous Solution. In *Physico-Chemical Behaviour of Atmospheric Pollutants: Air Pollution Research Reports*; Restelli, G., Angeletti, G., Eds.; Springer Netherlands: Dordrecht, 1990; pp 245–250.
- (42) Staehelin, Johannes.; Hoigne, Juerg. Decomposition of Ozone in Water: Rate of Initiation by Hydroxide Ions and Hydrogen Peroxide. *Environ. Sci. Technol.* **1982**, *16* (10), 676–681.
- (43) Lesko, T. M.; Colussi, A. J.; Hoffmann, M. R. Hydrogen Isotope Effects and Mechanism of Aqueous Ozone and Peroxone Decompositions. *J. Am. Chem. Soc.* **2004**, *126* (13), 4432–4436.
- (44) Buehler, R. E.; Staehelin, J.; Hoigne, J. Ozone Decomposition in Water Studied by Pulse Radiolysis. 1. Perhydroxyl (HO₂)/Hyperoxide (O₂⁻) and HO₃/O₃⁻ as Intermediates. *J. Phys. Chem.* **1984**, *88* (12), 2560–2564.
- (45) Bielski, B. H. J. A Pulse Radiolysis Study of the Reaction of Ozone with Cl⁻2 in Aqueous Solutions. *Radiat. Phys. Chem.* **1993**, *41* (3), 527–530.
- (46) Sehested, K.; Holcman, J.; Bjergbakke, E.; Hart, E. J. Formation of Ozone in the Reaction of Hydroxyl with O₃⁻ and the Decay of the Ozonide Ion Radical at PH 10-13. *J. Phys. Chem.* **1984**, *88* (2), 269–273.
- (47) Sehested, K.; Holcman, J.; Bjergbakke, E.; Hart, E. J. Ultraviolet Spectrum and Decay of the Ozonide Ion Radical, O₃⁻, in Strong Alkaline Solution. *J. Phys. Chem.* **1982**, *86* (11), 2066–2069.
- (48) Gall, B. L.; Dorfman, L. M. Pulse Radiolysis Studies. XV. Reactivity of the Oxide Radical Ion and of the Ozonide Ion in Aqueous Solution. *J. Am. Chem. Soc.* **1969**, *91* (9), 2199–2204.
- (49) Crittenden, J. C.; Hu, S.; Hand, D. W.; Green, S. A. A Kinetic Model for H₂O₂/UV Process in a Completely Mixed Batch Reactor. *Water Res.* **1999**, *33* (10), 2315–2328.
- (50) Field, R. J.; Noyes, R. M.; Postlethwaite, D. Photoreduction of Hydrogen Peroxide by Hydrogen. *J. Phys. Chem.* **1976**, *80* (3), 223–229.
- (51) Bielski, B. H. J.; Cabelli, D. E.; Arudi, R. L.; Ross, A. B. Reactivity of HO₂/O⁻2 Radicals in Aqueous Solution. *J. Phys. Chem. Ref. Data* **1985**, *14* (4), 1041–1100.
- (52) McMurry, J. E.; Fay, R. C. *General Chemistry: Atoms First*; Pearson Higher Ed: Upper Saddle River, NJ, 2010.
- (53) Huber, M. M.; Canonica, S.; Park, G.-Y.; von Gunten, U. Oxidation of Pharmaceuticals during Ozonation and Advanced Oxidation Processes. *Environ. Sci. Technol.* **2003**, *37* (5), 1016–1024.
- (54) Dodd, M. C.; Buffle, M.-O.; von Gunten, U. Oxidation of Antibacterial Molecules by Aqueous Ozone: Moiety-Specific Reaction Kinetics and Application to Ozone-Based Wastewater Treatment. *Environ. Sci. Technol.* **2006**, *40* (6), 1969–1977.
- (55) Benner, J.; Salhi, E.; Ternes, T.; von Gunten, U. Ozonation of Reverse Osmosis Concentrate: Kinetics and Efficiency of Beta Blocker Oxidation. *Water Res.* **2008**, *42* (12), 3003–3012.

- (56) Lan, Y.; Coetsier, C.; Causserand, C.; Groenen Serrano, K. On the Role of Salts for the Treatment of Wastewaters Containing Pharmaceuticals by Electrochemical Oxidation Using a Boron Doped Diamond Anode. *Electrochim. Acta* **2017**, *231*, 309–318.

3.9 Additional Notes

In both chapter 2 and 3, neither the experimental nor the kinetic modeling section took into account specific effects from the carbonate system (bicarbonate and carbonate), which can act as another sink for the oxidant species, especially $\cdot\text{OH}$. However, the model included a general-sink reaction (No. 20 and 22 in chapter 2 and 3, respectively) for $\cdot\text{OH}$ with an assumed rate constant of $1.00 \times 10^7 \text{ s}^{-1}$. Taking the rate constants between $\cdot\text{OH}$ and $\text{HCO}_3^-/\text{CO}_3^{2-}$ ($k_{\cdot\text{OH},\text{HCO}_3^-} = 8.5 \times 10^6 \text{ M}^{-1}\text{s}^{-1}$, $k_{\cdot\text{OH},\text{CO}_3^{2-}} = 3.9 \times 10^8 \text{ M}^{-1}\text{s}^{-1}$),¹⁶ the rate of consumption of $\cdot\text{OH}$ from the carbonate system is not important under typical water and wastewater carbonate concentrations. A similar analysis can be made for O_3 ($k_{\text{O}_3,\text{HCO}_3^-} \ll 0.01 \text{ M}^{-1}\text{s}^{-1}$, $k_{\text{O}_3,\text{CO}_3^{2-}} < 0.01 \text{ M}^{-1}\text{s}^{-1}$).³² Still, incorporating the carbonate-related reactions into the kinetic model could make it more comprehensive and more applicable in water matrices with higher bicarbonate/carbonate concentrations.

Also in chapter 2 and 3, for treatment of spiked pharmaceuticals in wastewaters, all pharmaceuticals were assumed to be completely dissolved, which may not be accurate in many cases. Investigation into the sorption behaviors of different compounds would give us a better understanding of their degradation in different waste streams.

Chapter 4

NOVEL SYNTHESIS PATHWAYS FOR HIGHLY OXIDATIVE IRON
SPECIES: GENERATION, STABILITY, AND TREATMENT
APPLICATIONS OF FERRATE(IV/V/VI)

McBeath, S. T.; Zhang, Y.; Hoffmann, M. R. Novel Synthesis Pathways for Highly Oxidative Iron Species: Generation, Stability, and Treatment Applications of Ferrate(IV/V/VI). *Environ. Sci. Technol.* **2023**. <https://doi.org/10.1021/acs.est.2c09237>.

4.1 Abstract

Difficulties arise related to the economy-of-scale and practicability in applying conventional water treatment technologies to small and remote systems. A promising oxidation technology better suited for these applications is that of electro-oxidation (EO), whereby contaminants are degraded via direct, advanced and/or electrosynthesized oxidant mediated reactions. One species of oxidants of particular interest are ferrates (Fe(VI)/(V)/(IV)), where only recently has their circumneutral synthesis been demonstrated, using high oxygen overpotential (HOP) electrodes, namely boron-doped diamond (BDD). In this study, the generation of ferrates using various HOP electrodes (BDD, NAT/Ni-Sb-SnO₂ and AT/Sb-SnO₂) was investigated. Ferrate synthesis was pursued in a current density range of 5-15 mA cm⁻² and initial Fe³⁺ concentrations of 10-15 mM. Faradaic efficiencies ranged 11-23 %, depending on operating conditions, with BDD and NAT significantly outperforming AT electrodes. Speciation tests revealed that NAT synthesizes both ferrate(IV/V) and ferrate(VI), while the BDD and AT electrodes synthesized only ferrate(IV/V) species. A number of organic scavenger probes were used to test the relative reactivity, including nitrobenzene, carbamazepine and fluconazole, whereby ferrate(IV/V) was significantly more oxidative than ferrate(VI). Finally, the ferrate(VI) synthesis mechanism by NAT electrolysis was elucidated, where co-production of ozone was found to be a key phenomenon for Fe³⁺ oxidation to ferrate(VI).

Keywords: Electro-oxidation, electro-synthesis, ferrate, ozone, boron-doped diamond, nickel-doped antimony tin oxide

4.2 Introduction

The prospect of electrochemical technologies in water treatment processes has been growing due to their favorability in various niche applications, when compared to traditional technologies. In general, electrochemical technologies are suitable in non-conventional water treatment applications, in part due to their favorable economy-of-scale and relative simplicity. Electrochemical oxidation (electro-oxidation, EO), for example, is a promising alternative technology for small and decentralized system applications, as it can eliminate the chemical supply chain associated with conventional oxidation/disinfection options by generating chemicals on-site and on-demand.

Conventional EO processes, employing efficient nonactive electrode materials, typically proceed via two reaction pathways: (1) direct electron transfer (DET) at the electrode surface, and (2) hydroxyl radical ($\bullet\text{OH}$) mediated oxidation. The latter reaction pathway is possible during EO when using high oxygen overpotential (HOP) electrode materials, such as boron-doped diamond (BDD) and other mixed metal oxides (MMO), which possess a greatly increased potential range (reduction and oxidation) of water stability (e.g., BDD: $-1.25 - 2.3 V_{\text{SHE}}^1$). Although the primary mechanism for pollutant degradation during EO processes has been attributed to $\bullet\text{OH}$ mediated oxidation², the reaction is limited at the electrode surface where reactive oxygen species are generated³. A third EO reaction mechanism exists however, whereby the electrosynthesis of residual chemical oxidants proceeds via ion oxidation at the electrode surface, resulting in pollutant degradation in the bulk water solution (e.g., not limited to the electrode surface). Some examples of electro-generated oxidant species include persulfate ($E^0 = 1.96 V_{\text{SHE}}^4$), peroxodiphosphate ($E^0 = 2.07 V_{\text{SHE}}^5$) and various reactive chlorine species^{6,7}, when sulfate, phosphate and chloride are present in the water matrix, respectively.

An additional group of powerful oxidants that has yet to receive the same attention, as it relates to circumneutral electrosynthesis for water treatment applications, is the generation of high oxidation state iron species known as ferrates. Ferrates are particularly well-suited

for water treatment applications⁸⁻¹⁰, as they are not known to form recalcitrant oxidation by-products like chlorinated disinfection by-products¹¹ and their reduced products are non-toxic hydrolysis Fe^{3+} species, which have also been reported to effectively function as coagulant chemicals¹²⁻¹⁴. Most commonly in water treatment practices, potassium ferrate (K_2FeO_4) is used to form aqueous ferrate(VI) ($\text{Fe(VI)/Fe}^{\text{VI}}\text{O}_4^{2-}$), which is characteristically purple and has a high redox potential ($E^0 = 2.2 \text{ V}_{\text{SHE}}$). However, lesser reported high oxidation state iron species also exist, namely ferrate(V) ($\text{Fe(V)/Fe}^{\text{V}}\text{O}_3^{3-}$) and ferrate(IV) ($\text{Fe(IV)/Fe}^{\text{IV}}\text{O}_4^{4-}$)^{15,16}. Some studies have found that Fe(V) and Fe(IV) ferrate species yield degradation rates as much as 2-5 orders of magnitude greater than Fe(VI) for various organic pollutants, such as organosulfur and phenolic compounds, in high pH conditions^{16,17}. In general, much is still unknown about the various ferrate species and their reactivity and stability in circumneutral aqueous conditions.

While ferrates are conventionally synthesized using a wet chemical method by oxidation of Fe^{3+} in highly alkaline conditions^{15,18-20}, electrochemical^{21,22} and thermal chemical²² methods also exist under challenging and unstable conditions. More recently, evidence of circumneutral ferrate electrosynthesis has been reported through the use of BDD electrodes and $\text{Fe}^{2+}/\text{Fe}^{3+}$ precursors for water treatment applications²³⁻²⁹. In these studies, however, no iron speciation was performed and ferrate was assumed to be in its most stable Fe(VI) form. Although BDD has been the preferred material for the circumneutral generation of ferrate to date, due to its aforementioned electrocatalytic properties, it also has several limitations. In addition to prohibitive costs³⁰, BDD electrodes require slow growth rates to yield high quality films, they are limited to substrates that are compatible with its growth conditions and are generally size-limited due to the chemical vapor deposition method by which they are synthesized³¹. Another group of promising materials are substoichiometric alternatives to platinum group metal oxides, known as Magnéli phase titanium oxides ($\text{Ti}_n\text{O}_{2n-1}$, $4 \leq n \leq 10$)^{32,33}, which also possess many favorable electrocatalytic properties for water treatment and ferrate synthesis. However, similar to BDD, their applications are somewhat limited due to a challenging production process requiring the reduction of TiO_2 in high temperature conditions and pure H_2 ³⁴. Another material considered as an HOP material is antimony-doped tin(IV) oxide (AT/Sb- SnO_2), which has a comparatively facile and

inexpensive preparation method by dip or brush coating and subsequent annealing (400-600°C)³⁵. Additionally, several metal precursors can be added to the coating solution to generate metal-doped AT electrodes. Of particular interest, nickel-doped AT electrodes (NAT/Ni-Sb-SnO₂) has been observed to coproduce O₃ in addition to •OH³⁶, and facilitate enhanced degradation of a number of organic pollutants when compared to AT electrodes^{37,38}. The fabrication method of both AT and NAT electrodes can facilitate the fabrication of high-surface-area flow-through electrodes^{31,39}, which can enhance mass transport and faradaic efficiency, and therefore the electrochemical generation of ferrate.

In this study, the circumneutral electrosynthesis of ferrates was investigated using a heterojunction NAT and AT electrodes. To date, the circumneutral electrosynthesis of ferrates has yet to be yielded with any electrode other than BDD. In this study we highlight the successful generation of ferrates, including the first report of the circumneutral electrosynthesis of powerful intermediate state ferrate(IV) and ferrate(V) species, using these MMO and BDD materials. Moreover, an in-depth mechanistic study yields the a novel reaction pathway to Fe(VI) from Fe(III), via electrolysis and ozone. The study also includes oxidation kinetics, oxidant stability and speciation, as well as application for water treatment purposes, presenting a potentially powerful alternative to conventional and costly BDD electrodes and wet chemical synthesis processes for conventional ferrate(VI) generation.

4.3 Materials and Methods

Electrode preparation. Three types of electrodes were used, including: (1) a single layer AT coated electrode on a Ti substrate, (2) a double-layer coated electrode consisting of a NAT top layer and an AT bottom layer, on a Ti substrate, and (3) a monocrystalline BDD electrode. The MMO electrodes were prepared using clean Ti plates (2 x 3 cm), which were etched using a 1:4 HF:HNO₃ solution for 1 min. The AT precursor solution was prepared using 360 mM SnCl₄·5H₂O (98%, Aldrich) and 40 mM SbCl₃ (>99.0%, Aldrich). The NAT precursor solution was prepared using 360 mM SnCl₄·5H₂O, 15 mM SbCl₃, and 4 mM Ni(OCOCH₃)₂·4H₂O (98%, Aldrich). The respective metal oxide coatings were deposited on the Ti plates using a dip-coater (MTI Corporation Bridgman Crystal Growth Furnace), which included repeated intervals of dipping the substrate into the aqueous metal oxide

precursor solution(s) for 20 s, drying at room temperature, followed by a calcination step by annealing at 600°C for 10 min. This was repeated until a desired mass loading was achieved (AT electrode: 1.3 mg cm⁻², NAT electrode: 1.3 mg cm⁻² AT and 1.3 mg cm⁻² NAT), whereby a final annealing step at 600°C was performed for 1.5 h. The BDD electrode was commercially purchased from NeoCoat®. It was prepared by a chemical vapor deposition process and has a thin-film (2-3 μm) monocrystalline layer on a 1 mm silicon substrate.

Experimental methods and procedures. All experiments were performed using an undivided electrolysis cell (50 mL). All electrolyte solutions were continuously stirred with a magnetic stirrer at a rate of 400 rpm. The anode (AT, NAT and BDD) and cathode (stainless steel) were 6 cm² for all experiments, separated by a 5 mm inter-electrode gap. All tests were performed in a three-electrode configuration, using an Ag/AgCl reference electrode (BASI Inc.) and Biologic VSP-300 potentiostat. The base water matrix used for all experiments was a phosphate buffer (pH = 7.0, 0.1 M), composed of MilliQ water, NaH₂PO₄ and Na₂HPO₄ (Millipore Sigma). The desired initial Fe³⁺ concentration was attained by addition of FeCl₃ (Sigma-Aldrich). Current densities of 5, 10 and 15 mA cm⁻² were investigated, to operate in a potential range avoiding excess oxygen evolution, while maximizing hydroxyl radical, DET and ozone formation, depending on each respective electrode. Samples for ferrate, probe or pollutant analysis were extracted from the electrochemical cell at a maximum volume of 0.5 mL throughout 60 or 90 min experiments. After electrolysis, ferrate solutions were centrifuged for 2 minutes at 5000 rcf and subsequently filtered using a 0.45 μm glass fiber syringe filter (Tisch), to remove any non-aqueous iron species (e.g., Fe²⁺/Fe³⁺ oxides and hydroxides).

Linear sweep voltammetry (LSV) and cyclic voltammetry (CV) experiments were also conducted under a scan rate of 50 mV s⁻¹ in relevant electrolytes for electrode material characterization as well as oxidation mechanism and ferrate speciation analysis.

Analytical methods. Ferrate concentration was measured with an indirect spectrophotometric method, using an ABTS (2,2'-azino-bis(3-ethylbenzothiazoline-6-sulfonic acid)) reagent (Sigma-Aldrich). In the presence of excess ABTS, ferrate(VI) oxidizes ABTS with a 1:1 M ratio, producing a light-absorbing radical cation (ABTS^{•+}) with

a visible UV-absorption maxima at 415 nm⁴⁰⁻⁴². Ferrate standards and samples were analyzed using a UV-Vis spectrophotometer (Thermo Scientific Nanodrop 2000c) and a 1 cm quartz cuvette. Ferrate standards were prepared using potassium ferrate (99%) (Element 26) in a concentration range of 0-10 mM. Ferrate(VI) was also directly analyzed using direct UV-Vis spectrophotometry at 530 nm in 1 cm and 5 cm quartz cuvettes, in a concentration range of 0-2 mM with co-occurring Fe³⁺ (dosed with FeCl₃), to simulate water matrix conditions during electrolysis experiments and to understand the effects on UV-absorbance and ferrate(VI) stability. Raman spectroscopy (Renishaw inVia Qontor) and Fourier transform infrared spectroscopy (FTIR) (Thermo Scientific Nicolet iS50) were also pursued for a limited number of test (operating methods are detailed in the Supporting Information). Free chlorine concentrations were also monitored using the DPD (*N,N*-diethyl-*p*-phenylenediamine) reagent (Hach DPD method 1012) and a DR 300 colorimeter.

Oxidant probe species and micropollutants, namely nitrobenzene (NB), carbamazepine (CBZ) and fluconazole (FCZ) (Sigma-Aldrich) were quantified using high performance liquid chromatography (HPLC), equipped with a ZORBAX Eclipse XDB-C18 column (Agilent, 2.1 x 50 mm, 3.5 μm particles) and a UV detector at 254, 285 and 205 nm, respectively. The mobile phase, flowing at 0.5 mL min⁻¹, was a composition of water with 0.1% formic acid and acetonitrile (ACN) under the gradient: 0 min, 10% ACN; 2 min, 10% ACN; 6 min, 95% ACN; 8 min, 95% ACN; 9 min, 10% ACN; 12 min, 10% ACN. An injection volume of 20 μL was used with a total runtime of 12 minutes for each sample.

4.4 Results and Discussion

Electrode performance. Nonactive electrodes are characterized by their high oxygen evolution reaction (OER) overpotential⁴³. The NAT and AT electrodes have previously been shown to have oxygen evolution potential at ~2.4 V_{RHE}³⁸. BDD demonstrates even higher OER potential at ~2.7 V_{RHE}⁴⁴ (see [Figure 4.S1](#) in the Supporting Information). One primary mechanism of oxidation, with respect to all three electrode materials (e.g., BDD, NAT and AT), is mediated through the generation of •OH, which was previously demonstrated by Zhang *et al.* through radical scavenging studies involving nitrobenzene and benzoic acid³⁸ and widely reported for BDD electro-oxidation². Moreover, when Cl⁻ is present in the water

matrix, all three electrodes are observed to generate reactive chlorines species (RCS). The NAT electrode is unique in its O_3 production capacity. Equilibrium aqueous O_3 concentration can reach as high as $\sim 4.7 \text{ mg L}^{-1}$ in the absence of chloride, and goes down with higher chloride concentration³⁸. The BDD electrode is the only material of the three that is shown to facilitate direct electron transfer (DET) mediated oxidation. Specifically, DET is known to contribute to FCZ degradation during BDD electrolysis⁴⁵.

Ferrate generation. Ferrate generation experiments were first performed using an initial $FeCl_3$ concentration of 10 mM and a current density of 10 mA cm^{-2} , with the NAT, AT and BDD electrodes. Control experiments were run in parallel with 30 mM NaCl, yielding an equivalent Cl^- concentration, to understand the oxidative effect of co-generated reactive chlorine species (RCS) during ferrate experiments. Additional control experiments were conducted to determine whether phosphate active species could also be generated, whereby electrolysis was performed in the presence of the base PBS water matrix and subsequently analyzed for any oxidative species.

For all anode materials, evidence of ferrate generation was observed using the ABTS quantification method^{40,41} (see Supporting Information [Figure 4.S2-S12](#) for all ABTS absorbance data). While the circumneutral generation of ferrate has been recently reported using BDD²⁴, this is the first evidence of ferrate generation using both NAT and AT electrodes. Faradaic efficiencies of 22.5, 21.3 and 12.0% were yielded for the BDD, NAT and AT electrodes, respectively (see [Figure 4.1b](#)).

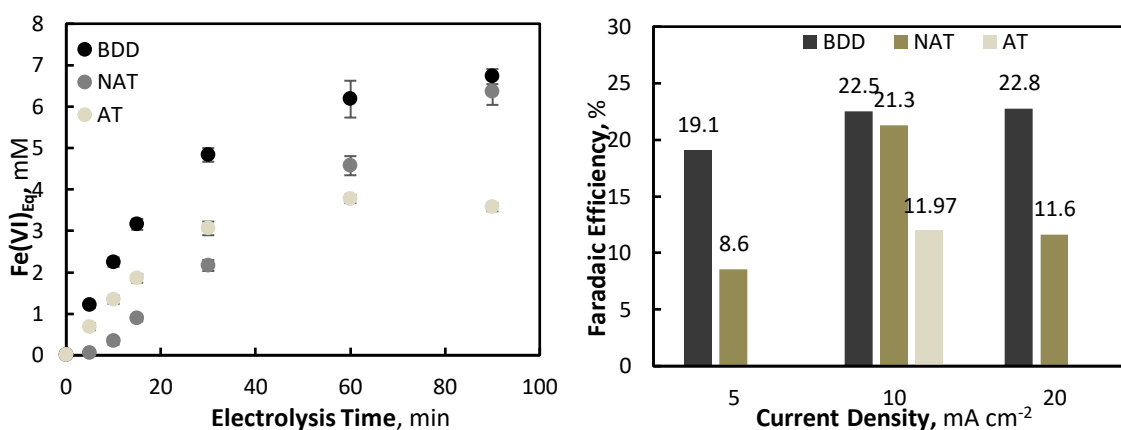


Figure 4.1 (A) Ferrate(IV/V/VI) generation using BDD, NAT and AT electrodes with a $\text{Fe}^{3+}_0 = 10 \text{ mM}$ and 10 mA cm^{-2} . $\text{Fe(VI)}_{\text{Eq}}$ = Equivalent oxidative capacity of Fe(VI) with ABTS (1:1 molar ratio). (B) Faradaic efficiency of ferrate (IV/V/VI) generation at 5, 10 and 15 mA cm^{-2} and with a $\text{Fe}^{3+}_0 = 10 \text{ mM}$.

Qualitatively, the final ferrate solutions were significantly different (see [Figure 4.2](#) inset). While the NAT electrode produced a purplish/pink solution that is characteristic of ferrate(VI)⁹, both the BDD and AT electrodes produced a yellowish/white solution (see [Figure 4.2](#)), indicating that ferrate(VI) was not produced. The electro-synthesis of oxidative iron species was also observed to increase with both current density (20 mA cm^{-2}) and initial Fe^{3+} concentration (15 mM) (see Supporting Information [Figure 4.S13](#) for all ABTS absorbance data). During NAT experiments, ferrate yields of 12.8, 63.5 and 69.4% were achieved during 5, 10 and 20 mA cm^{-2} operations. However, the Faradaic efficiency was maximized during 10 mA cm^{-2} electrolysis at 21.3%. Similarly, during BDD electrolysis, the greatest Faradaic efficiency was yielded during 10 mA cm^{-2} (see [Figure 4.1b](#)), with yields of 28.5, 67.2 and 135.8% during 5, 10 and 20 mA cm^{-2} operations. Average cell potentials of 3.5, 3.9 and 4.7 V were yielded during NAT electro-synthesis, while BDD potentials recorded were 4.7, 5.6 and 6.9 V during 5, 10 and 20 mA cm^{-2} operations, respectively. At 20 mA cm^{-2} BDD operations, as well as for all current density conditions using an initial FeCl_3 concentration of 15 mM, ABTS results suggested ferrate(VI) yields exceeded 100%, indicating errors associated with the ABTS method for ferrate quantification.

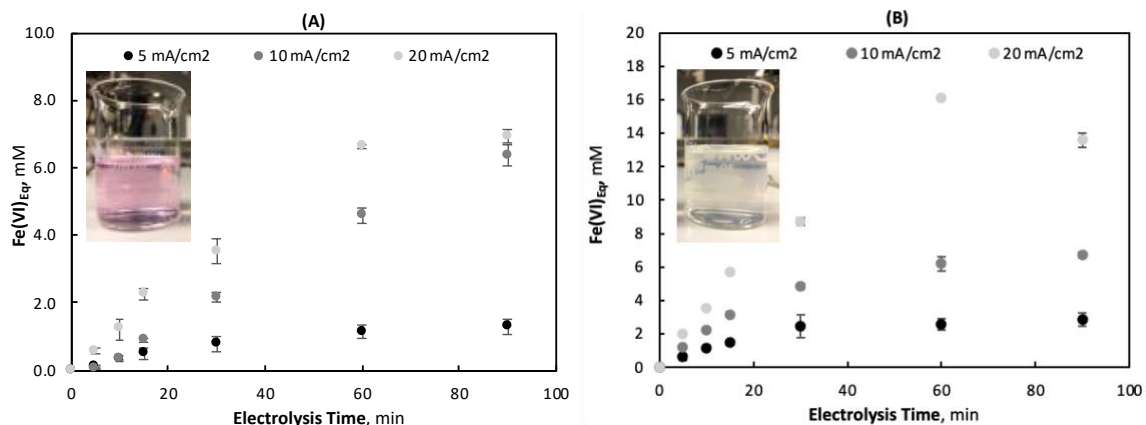


Figure 4.2 Ferrate(IV/V/VI) generation with a $\text{Fe}^{3+}_0 = 10 \text{ mM}$ at 5, 10 and 20 mA cm^{-2} using (A) NAT electrode, and (B) BDD electrode. Inset figures are final ferrate solutions after 90 min of electrolysis. $\text{Fe(VI)}_{\text{Eq}}$ = Equivalent oxidative capacity of Fe(VI) with ABTS (1:1 molar ratio).

In theory, ferrate(VI) can facilitate the exchange of 3 mols of electrons for every 1 mol of ferrate(VI) through its subsequent conversion to Fe(V), Fe(IV) and Fe(III). In phosphate buffer, however, it has previously been found that ferrate(VI) has a 1:1.18 ratio with ABTS to form ABTS^{*+} in circumneutral pH, whereby the subsequent oxidative effect of Fe(V) and Fe(IV) are muted through rapid auto-decomposition⁴⁶. Under the same conditions, roughly 9% of Fe(V) was found to react with ABTS to form Fe(IV), whereby 93% of that Fe(IV) subsequently reacting with ABTS to form ABTS^{*+} ⁴⁶. Achieving ferrate yields greater than 100% using the ABTS method (which assumes a 1:1 reaction stoichiometry) for BDD electrosynthesis experiments suggests that Fe(V), or some combination of Fe(V) and Fe(IV), is formed, resulting in a 1:1-2 molar reaction ratio. The ABTS technique, and the resulting molar reaction ratio has been previously used to identify the role of intermediate ferrate species (e.g., Fe(IV/V)) in water treatment processes⁴⁷.

The generation and use of Fe(IV) and Fe(V) species, particularly for water treatment processes, has been a recent topic of much research interest and has primarily been reported through the activation of ferrate(VI)⁴⁷. The activation of ferrate(VI), to exploit the high oxidation capabilities of Fe(IV/V), has been investigated using a number of strategies including the use of acid⁴⁸, UV⁴⁹, and metal cations like Fe(III)⁵⁰, amongst many other organic and inorganic activators⁴⁷. Of particular relevance, the role of Fe(III) in Fe(IV/V) generation is notable, due to its efficacy towards Fe(IV) generation and its co-occurrence during ferrate electrosynthesis.

Ferrate speciation. Several difficulties arise when conducting a speciation study on ferrate(IV/V/VI), particularly for direct detection and quantification of low concentration aqueous solutions. Both Raman spectroscopy and Fourier transform infrared (FTIR) spectroscopy were used to analyze the ferrate solutions obtained during BDD and NAT electrolysis, but no differentiating peaks were observed (see Supporting Information for

Raman and FTIR spectra graphs, [Figure 4.S14 and 4.S15](#), respectively). Moreover, high-valent iron-oxo complexes can exist in various forms and the exact structures are still largely unknown⁴⁷. For example, the synthesis of ferrate(IV), by hydroxyl radical mediated oxidation of Fe(III), in phosphate, pyrophosphate and carbonate solutions has been reported. The resulting ferrate(IV) species include one or more hydroxide, pyrophosphate or carbonate ligands (L_m). However, the exact $Fe^{IV}-L_m$ structure and number of ligands attached to the central iron atom are not known^{51,52}. It should also be noted that phosphate has previously been observed to function as a Fe(IV/V) ligand (e.g., Fe^V-L_m and $Fe^{IV}-L_m$)⁴⁷, which may play a crucial role in ferrate speciation in this study, due to the presence of phosphate in the base PBS water matrix. The stability of ferrate species has also been observed to vary depending exact structure and the ligand(s) coordinated to the iron atom⁵².

Direct colorimetry can also be used to identify ferrate(VI) in solution^{53,54}, at a much lower molar absorption coefficient than that of ABTS, therefore higher concentrations and/or longer UV pathlengths are required. Using a 5 cm quartz cuvette, both the BDD and NAT electrogenerated ferrates were analyzed (see [Figure 4.3](#)). The UV absorbance spectra confirmed the qualitative observations, whereby the solution produced with the NAT electrode showed evidence of ferrate(VI) with an absorbance maximum at 526 nm⁴⁰. This peak is slightly higher than that of ferrate(VI) observed with the chemical standard (using K_2FeO_4) and the peak shapes are notably different, as seen in [Figure 4.S35](#) with a maximum at 524 nm. When Fe(III) was added to the K_2FeO_4 mixture, however, the same absorbance maximum was achieved (see [Figure 4.S35](#)). Moreover, while the NAT-produced ferrate(VI) solution was more pink (compared to a purple color traditionally associated with a high concentration of ferrate(VI)), it was similar to the color yielded using K_2FeO_4 and Fe(III). These results indicate that the lighter color observed during NAT electrolysis is due to either the PBS and/or co-occurring Fe(III) cations in solution. A secondary shoulder between 275 and 310 nm was observed for both the BDD and NAT derived ferrates, which is also characteristic of ferrate(VI) UV-spectra⁴⁰. No absorbance maxima was observed for the BDD solution, including at 530 nm (e.g., ferrate(VI) absorbance peak in the presence of Fe^{3+}), conclusively indicating the absence of ferrate(VI). Cyclic voltammetry provided further

direct evidence of two different iron species in the BDD and NAT solutions, as seen by the different reduction peaks in [Figure 4.3](#).

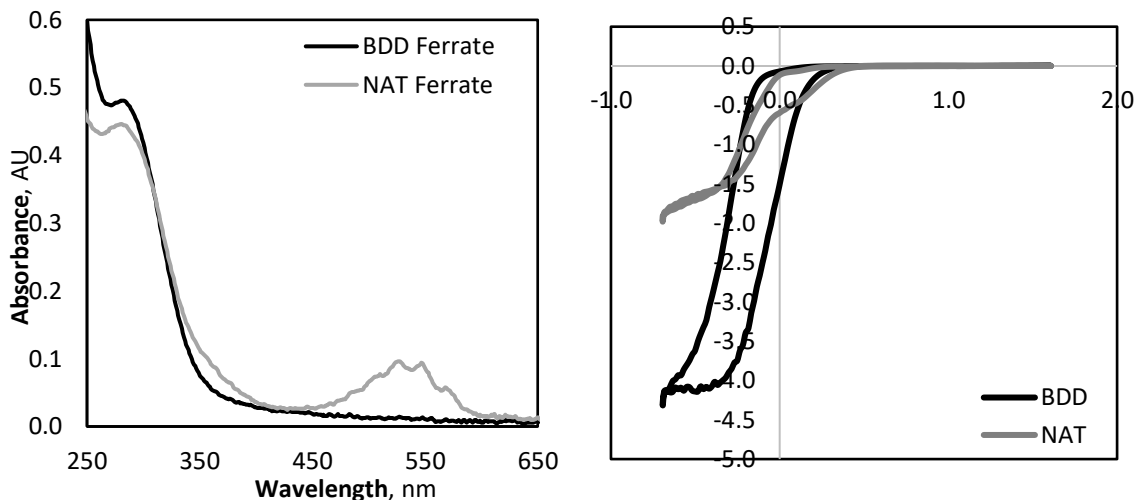


Figure 4.3 UV-spectra (left) and cyclic voltammograms (right) of final BDD and NAT ferrate solutions after 90 min of electrolysis at 10 mA cm^{-2} and an initial FeCl_3 concentration of 10 mM (CV condition: scan rate 50 mV s^{-1} , 0.0 V vs. Eoc to -1.3 V vs. ref.).

To further understand ferrate speciation between the BDD and NAT derived solutions, the use of selective organic probes was pursued. The recalcitrance of nitrobenzene (NB) to ferrate(VI) oxidation has previously been reported^{15,55,56}. Using an initial concentration of 0.1 mM , no detectable NB degradation was observed to occur as a result of the NAT produced ferrate(VI), when compared to the control study containing RCS produced during electrolysis of the NaCl control solution (see Supporting Information [Figure 4.S16-S17](#)). During parallel experiments using the BDD-derived solution, NB degradation was observed to increase in the presence of ferrate(IV/V), when compared to the control solution containing only RCS, with pseudo first-order reaction rate constants of 0.0055 and 0.0047 min^{-1} , respectively (see Supporting Information [Figure 4.S18](#)).

Carbamazepine (CBZ) was also selected as a suitable probe, particularly in the water matrix post-electrolysis which contains a high concentration of RCS, due to its relative persistence in highly chlorinated waters^{57,58}. With all electrodes (NAT, AT and BDD),

minimal CBZ degradation was observed during control (NaCl) experiments. Ferrate(VI), produced using the NAT electrode, facilitated the slow degradation of CBZ over ~15 minutes of mixing, yielding a second-order reaction rate constant of $1.4 \text{ M}^{-1} \text{ s}^{-1}$. The degradation rate of CBZ with ferrate(VI) has been previously observed to be highly dependent on pH, with k_2 constants ranging from 0.1 to $70 \text{ M}^{-1} \text{ s}^{-1}$ between pH conditions of 8 to 6 respectively^{59,60}, which is in agreement with the present study. Significantly faster CBZ oxidation was observed using the BDD generated ferrate(IV/V), whereby 83% of CBZ degradation took place in the first 20 seconds of mixing, yielding an apparent first-order reaction rate constant of 0.08 s^{-1} . This reaction rate is similar to that which has been observed for CBZ degradation with permanganate/Mn(VII)/ MnO_4^- ⁶⁰, an analogous highly oxidative manganese species also used for aqueous micropollutant degradation⁶¹⁻⁶⁴. The pseudo first order reaction rate constant of permanganate with CBZ was found to increase with the initial permanganate concentration, whereby a $k' \sim 0.045 \text{ s}^{-1}$ was yielded with an initial permanganate concentration of $160 \text{ }\mu\text{M}$. Although in general, ferrate(VI) is more highly oxidative than the permanganate ion, the latter was reported to degrade CBZ more readily due to its high reactivity with olefin groups^{65,66}. At present, no previous studies have been published investigating the used of ferrate(V) or ferrate(IV) on the degradation of CBZ, but is observed to perform similarly to permanganate. CBZ degradation was also observed using the ferrate(IV/V) generated using the AT electrode. Similar to the BDD derived ferrate solution, rapid degradation was observed in the first 20 seconds (see Supporting Information [Figure 4.S22](#)), with an absolute CBZ removal much less than BDD due to the significantly lower initial concentration of ferrate(IV/V).

Fluconazole (FCZ) was used as a probe, as it is recalcitrant to both chlorine and chlorine radicals (Cl_2^{\bullet}). Similar to CBZ, no FCZ degradation was observed during control experiments with both the NAT and BDD produced ferrate solutions. Moreover, ferrate(VI) synthesized using the NAT electrode, did not yield any detectable oxidation of FCZ. A small amount of FCZ degradation was observed using the ferrate(IV/V), produced with the BDD electrode, once again highlighting the greater oxidation potential of these iron species compared to ferrate(VI). In agreement with previous researchers, the BDD produced ferrate(IV/V) consistently yielded greater degradation rates when compared to ferrate(VI)

for all organic micropollutant tested^{16,17}. A complete set of the CBZ and FCZ degradation data can be found in the Supporting Information document ([Figure 4.S19-S24](#)).

To better understand the ferrate speciation during NAT electrolysis, a combination of ABTS and direct UV-spectrophotometer analysis was conducted in parallel at 415 nm and 530 nm, to evaluate the relative ferrate(IV/V) and ferrate(VI) synthesis, respectively. The absorbance related to the generation of ferrate(VI) increased over the initial 10 minutes of electrolysis, thereafter it stabilized for the remainder of the experiment. The ABTS absorbance, which reflects oxidation by ferrate(IV), ferrate (V) and ferrate(VI), continued to increase significantly throughout the entirety of the electrolysis (see [Figure 4.4](#)). These results indicate that only a small fraction of the initial Fe^{3+} is converted to ferrate(VI); 1.65 mM (± 0.2 mM) under these conditions (10 mA cm^{-2} and $[\text{Fe}^{3+}]_0 = 15 \text{ mM}$) in a fast reaction within 10 minutes of starting electrolysis, and remained constant thereafter. Although ferrate(VI) generation reaches a plateau, the formation of ferrate(IV/V) continues to be facilitated throughout the 90 minutes of electrolysis.

Each of the techniques used in this study, however, is indirect analysis for ferrate speciation. In future studies, it would be important to incorporate direct analysis, particularly the use of Mössbauer spectroscopy. In order to use Mössbauer spectroscopy, reactor design and current efficiency limitations of the current setup would need to be improved, as a higher concentration of ferrates in a solid sample would be required⁴⁷.

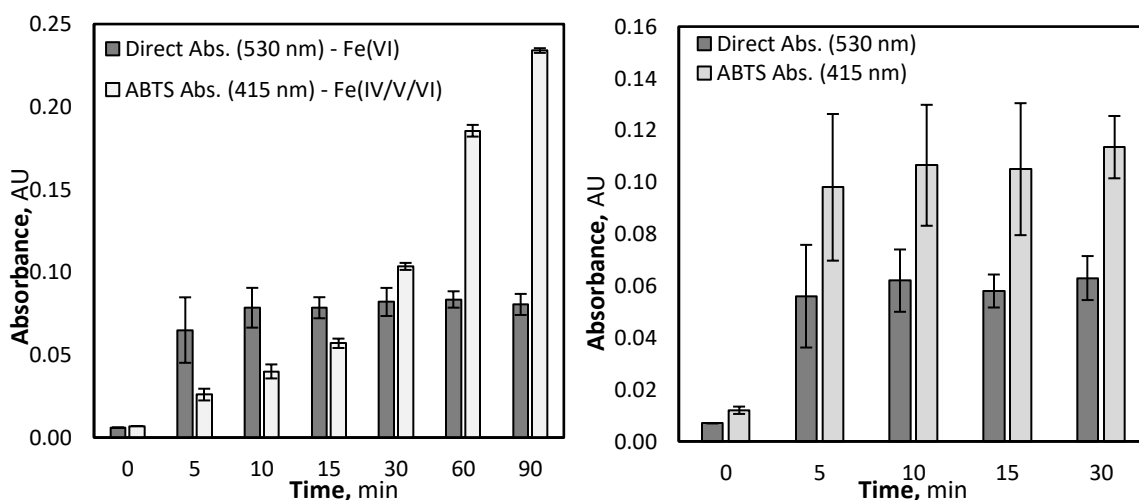


Figure 4.4 ABTS (415 nm) and direct (530 nm) UV-vis spectrophotometric results from NAT electrolysis at 10 mA cm⁻² and FeCl₃ of 15 mM (left), and O₃ oxidation with an initial FeCl₃ of 15 mM (right).

Ferrate stability. A long term stability study was performed on both the ferrate(VI) (e.g., NAT produced ferrate) and ferrate(IV/V) (e.g., BDD produced ferrates), to understand their relative self-decomposition in ambient temperature (20°C) and light conditions. Similar to the previously described ferrate generation and speciation tests, all stability tests were performed in parallel with control experiments using NaCl solutions and monitoring the degradation of co-generated RCS. Using the same initial FeCl₃ (15 mM) concentration with both the NAT and BDD electrodes, after 60 minutes of electrolysis, initial Fe(VI)_{Eq} concentrations of 3.9 and 13.6 mM were achieved after centrifugation and filtration, respectively. The ABTS absorbances were subsequently monitored for the ferrate and RCS control solutions over 70 days.

The oxidant species stability of all solutions (e.g., ferrate and control) degraded similarly, however some outlier ABTS absorbances were observed between days 3-11 for the BDD ferrate(IV/V). Unlike the remainder of the stability data, these outliers included large variations in ferrate(IV/V) concentrations and no conclusive evidence had been gathered to explain these outliers. One possible explanation may be related to the decomposition of Fe(V) to Fe(IV) and/or Fe(III), during sampling by oxidation with non-aqueous iron hydr(oxides) (e.g., reduced ferrate products). All ABTS stability data is included in the Supporting Information ([Figure 4.S25-S28](#)).

When accounting for the effect of RCS, zero-order degradation was observed for both the NAT produced ferrate(VI) and BDD produced ferrate(IV/V). Excluding the previously describe unaccountable outlier samples, high coefficients of determination were yielded for both ferrate solutions, with degradation rate constants of 0.0691 and 0.234 mM day⁻¹ for ferrate(VI) and ferrate(IV/V), respectively. However, when degradation rates were normalized for initial ferrate concentrations differences, both solutions were observed to degrade at a very similar rate (see [Figure 4.5](#)).

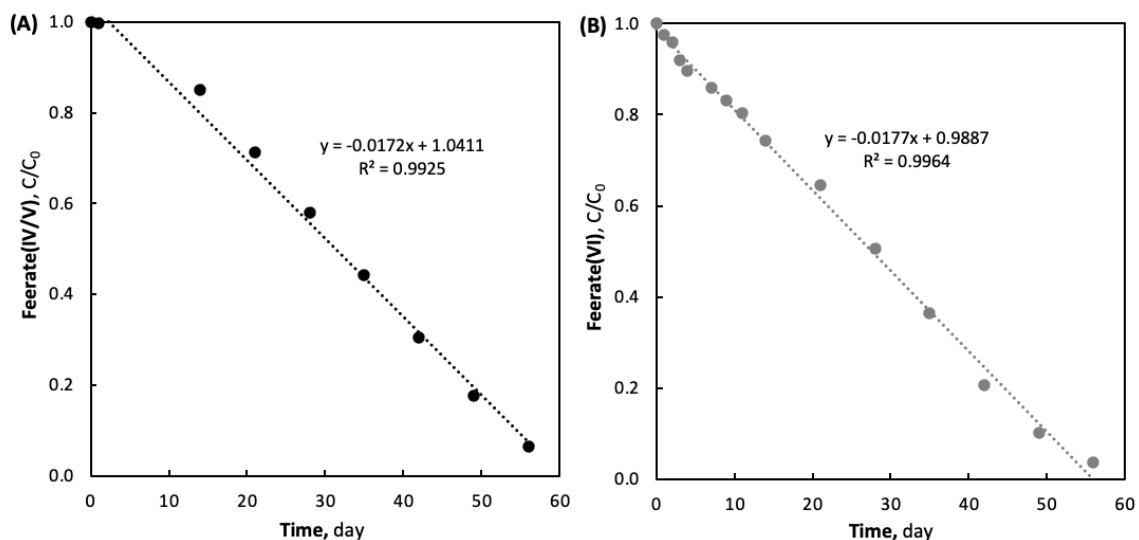


Figure 4.5 Normalized ferrate degradation with (A) BDD derived ferrate(IV/V) ($\text{Fe(VI)}_{\text{Eq}} = 13.6 \text{ mM}$), and (B) NAT derived ferrate(VI) ($\text{Fe(VI)} = 3.9 \text{ mM}$).

CVs were also run each week throughout the duration of the stability tests, with a particular interest in determining whether multiple peaks would develop/regress in the BDD solution, to provide insights towards Fe(V) and Fe(IV) species. Only a single reduction peak at $\sim -0.3 \text{ V}_{\text{RHE}}$ is visible in the ferrate(IV/V) CVs throughout the six weeks of the degradation study (see [Figure 4.3](#)). Interestingly, two reduction peaks are visible for the NAT produced ferrate(VI) throughout the stability test, which may be associated with the reduction of Fe(VI) and subsequent reduction of Fe(IV/V). All CVs for both the NAT and BDD produced ferrates can be found in the Supporting Information ([Figure 4.S29](#) and [4.S30](#)).

Ferrate generation mechanism. There are few differences between the predominant oxidation mechanisms, as it relates to BDD, NAT and AT electro-oxidation. In the former, DET can be facilitated as a secondary pathway to the predominant $\bullet\text{OH}$ mediated oxidation. In the case of NAT electro-oxidation, appreciable amounts of O_3 are generated, but is also secondary to the predominant $\bullet\text{OH}$ mediated oxidation pathway³⁸. Although DET is exclusive to the BDD, it cannot be assumed to be the responsible mechanism for the electrosynthesis of ferrate(IV/V), as the AT electrode, which solely proceeds via $\bullet\text{OH}$

mediated electro-oxidation, also produces the same ferrate species as that of BDD.

Therefore, it was hypothesized that O_3 play a crucial role in facilitating the synthesis of ferrate(VI).

Three tests were performed to understand the role of O_3 for the generation of ferrate(VI). Firstly, after electrolysis and ferrate(IV/V) generation using the BDD electrode, O_3 was purged into the solution and mixed over 30 minutes. In the second experiment, O_3 was directly purged into the electrochemical cell during BDD electrolysis. The third experiment was similar to the first, however the ferrate(IV/V) solution generation after BDD electrolysis was centrifuged and filtered, to remove any reduced ferrate or hydrolyzed Fe^{3+} . In all experiments, ferrates were analyzed using the colorimetric ABTS and direct method, as well as through qualitative observations on the resulting solutions' color.

For the first two experiments, ferrate(VI) was observed to form. In the first process, where O_3 was purged into a mixing solution of ferrate(IV/V) post BDD electrolysis, the solution began to immediately turn from a yellowish/white color (see inset of [Figure 4.2b](#)) to the characteristic purple/pink solution that was yielded during NAT electrosynthesis experiments (see [Figure 4.6](#)). As the solution turned pink over the 30 minutes of O_3 purging and mixing, indicating the generation of ferrate(VI), the ABTS absorbance decreased significantly, which is consistent with the ABTS data yielded during ferrate generation experiments with the NAT electrode. Parallel control experiments were also conducted to account for $ABTS^{++}$ formation due to O_3 oxidation. ABTS absorbance data for both ferrate and control experiments can be found in the Supplement Materials ([Figure 4.S31, 4.S33 and 4.S34](#)).

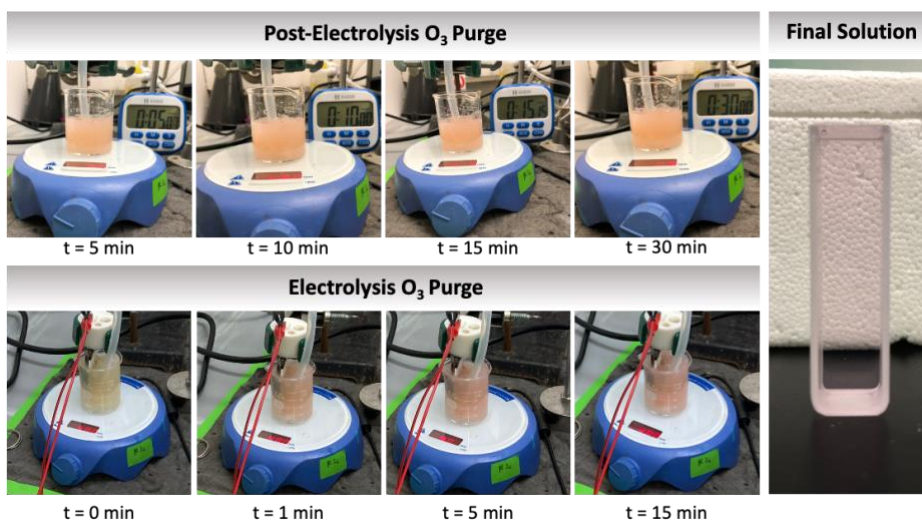


Figure 4.6 Ferrate(IV/V) oxidation experiments with O_3 post and during electrolysis to form ferrate(VI).

A similar trend was observed when O_3 was purged during electrolysis, whereby a pink/purple solution was yielded within minutes of applying current (see [Figure 4.6](#)). The ABTS data suggested appreciable amounts of Fe(IV/V) was still being generated, however, as the absorbance was significantly greater than that yielded during NAT electrolysis, but still greatly below the absorbances observed during the standard BDD ferrate generation experiments (i.e., without purging O_3). These results highlight the relatively high current efficiency for BDD-iron reactions and reveal a potentially high efficiency reaction path for ferrate(VI) electro-generation in concurrence with O_3 oxidation.

Lastly, during the third experiment where O_3 was purged into a centrifuged and filtered solution of ferrate(IV/V) post BDD electrolysis, no evidence of ferrate(VI) generation was observed. These results suggested that ferrate(VI) synthesis was predominantly facilitated by the oxidation of Fe^{3+} by ozone, rather than ferrate(IV/V) species by ozone. To further confirm these findings, ozone was purged directly into a Fe^{3+} solution ($[FeCl_3]_0 = 15 \text{ mM}$) and the ABTS and direct UV-absorbance was measured to quantify the ferrate(IV/V) and ferrate(VI) generation, respectively. Control experiments were conducted with the ozonation a Cl⁻ containing solution ($[NaCl]_0 = 45 \text{ mM}$) and the base phosphate buffer solution, to account for the effect of ABTS oxidation by RCS and/or ozone (control experiment data can be found

in the Supporting Information **Figure 4.S33**). Over 30 minutes of purging and mixing, ferrate(VI) was observed to be generated, demonstrating the first evidence of an ozone synthesis pathway. Based on the control experiments, as well as previous research that found ozone to have a small reaction rate coefficient with Cl^- to form RCS^{67} , the primary mechanism for ferrate(VI) generation was determined to be by ozone oxidation. ABTS and direct UV-absorbance increased proportionately over the time of ozone purging, as seen in **Figure 4.4**. Although the purge-rate for ozone during these tests (0.011 L min^{-1}) were much greater than that which occurs during NAT electrolysis ($<1.8\text{E-}06 \text{ L min}^{-1}$ at 10 mA cm^{-2}), more ferrate(VI) is produced during the latter process, suggesting some electrocatalytic effects of the NAT material, and/or to the co-production of hydroxyl radicals and ferrate(IV/V) during electrolysis. This effect is currently out of the scope of this project, however.

This study demonstrates that MMO materials, particularly NAT and AT electrodes, are capable of generating high oxidation state iron species ferrate(VI) and ferrate(IV/V). Moreover, this work provides the first extensive evidence of ferrate(IV/V) electrochemical generation in circumneutral pH conditions, using the BDD, NAT and AT electrodes. These intermediate state ferrate species were shown to be more highly oxidative against persistent organic pollutants, which are recalcitrant towards ferrate(VI) oxidation. Finally, a key mechanism for ferrate(VI) electrosynthesis using the NAT electrode was proposed, which was identified to be attributed to co-occurring ozone oxidation of Fe^{3+} , demonstrating two novel reaction pathways for ferrate(VI) generation.

4.5 Acknowledgments

This research was supported by the Resnick Sustainability Institute (RSI) Impact Grant. The authors would also like to thank Heng Dong for help with the Raman spectroscopy work, and Carl K. McBeath for the graphical abstract illustration.

4.6 References

- (1) Kraft, A. Doped Diamond: A Compact Review on a New, Versatile Electrode Material. *Int. J. Electrochem. Sci.* **2007**, *2*, 355–385.
- (2) McBeath, S. T.; Wilkinson, D. P.; Graham, N. J. D. Application of Boron-Doped

- Diamond Electrodes for the Anodic Oxidation of Pesticide Micropollutants in a Water Treatment Process: A Critical Review. *Environ. Sci. Water Res. Technol.* **2019**, *5*, 2090–2107.
- (3) Zhu, X.; Tong, M.; Shi, S.; Zhao, H.; Ni, J. Essential Explanation of the Strong Mineralization Performance of Boron-Doped Diamond Electrodes. *Environ. Sci. Technol.* **2008**, *42* (13), 4914–4920.
 - (4) de Freitas Araújo, K. C.; da Silva, D. R.; dos Santos, E. V.; Varela, H.; Martínez-Huitle, C. A. Investigation of Persulfate Production on BDD Anode by Understanding the Impact of Water Concentration. *J. Electroanal. Chem.* **2020**, *860*, 113927.
 - (5) Sánchez, A.; Llanos, J.; Sáez, C.; Cañizares, P.; Rodrigo, M. A. On the Applications of Peroxodiphosphate Produced by BDD-Electrolyses. *Chem. Eng. J.* **2013**, *233*, 8–13.
 - (6) Mostafa, E.; Reinsberg, P.; Garcia-Segura, S.; Baltruschat, H. Chlorine Species Evolution during Electrochlorination on Boron-Doped Diamond Anodes: In-Situ Electrogeneration of Cl₂, Cl₂O and ClO₂. *Electrochim. Acta* **2018**, *281*, 831–840.
 - (7) Dong, H.; Yu, W.; Hoffmann, M. R. Mixed Metal Oxide Electrodes and the Chlorine Evolution Reaction. *J. Phys. Chem. C* **2021**.
 - (8) Jiang, J.-Q. Advances in the Development and Application of Ferrate(VI) for Water and Wastewater Treatment. *J. Chem. Technol. Biotechnol.* **2013**, *89* (2), 165–177.
 - (9) Sharma, V. K.; Chen, L.; Zboril, R. Review on High Valent FeVI (Ferrate): A Sustainable Green Oxidant in Organic Chemistry and Transformation of Pharmaceuticals. *ACS Sustain. Chem. Eng.* **2016**, *4* (1), 18–34.
 - (10) Sharma, V. K. Potassium Ferrate(VI): An Environmentally Friendly Oxidant. *Adv. Environ. Res.* **2002**, *6* (2), 143–156.
 - (11) Murugananthan, M.; Latha, S. S.; Bhaskar Raju, G.; Yoshihara, S. Role of Electrolyte on Anodic Mineralization of Atenolol at Boron Doped Diamond and Pt Electrodes. *Sep. Purif. Technol.* **2011**, *79* (1), 56–62.
 - (12) Jiang, J.-Q.; Stanford, C.; Petri, M. Practical Application of Ferrate(VI) for Water and Wastewater Treatment – Site Study’s Approach. *Water-Energy Nexus* **2018**, *1* (1), 42–46.
 - (13) Tien, K. T.; Graham, N.; Jiang, J. Q. Evaluating the Coagulation Performance of Ferrate: A Preliminary Study. In *ACS Symposium Series*; 2008.
 - (14) Jiang, J. Q.; Lloyd, B. Progress in the Development and Use of Ferrate(VI) Salt as an Oxidant and Coagulant for Water and Wastewater Treatment. *Water Res.* **2002**, *36* (6), 1397–1408.
 - (15) Sharma, V. K. Ferrate(VI) and Ferrate(V) Oxidation of Organic Compounds: Kinetics and Mechanism. *Coord. Chem. Rev.* **2013**, *257* (2), 495–510.
 - (16) Sharma, V. K. Oxidation of Inorganic Compounds by Ferrate (VI) and Ferrate(V): One-Electron and Two-Electron Transfer Steps. *Environ. Sci. Technol.* **2010**, *44* (13), 5148–5152.
 - (17) Sharma, V. K. Oxidation of Inorganic Contaminants by Ferrates (VI, V, and IV)– Kinetics and Mechanisms: A Review. *J. Environ. Manage.* **2011**, *92* (4), 1051–1073.
 - (18) Li, C.; Li, X. Z.; Graham, N. J. D. A Study of the Preparation and Reactivity of Potassium Ferrate. *Chemosphere* **2005**, *61* (4), 537–543.
 - (19) Schreyer, J. M.; Thompson, G. W.; Ockerman, L. T. Inorganic Syntheses (Volume

- IV). In *Inorganic Syntheses*; Bilar Jr., J. C., Ed.; McGraw-Hill Book Company, Inc.: York, PA, 1953; Vol. 4, pp 164–168.
- (20) Thompson, G. W.; Ockerman, L. T.; Schreyer, J. M. Preparation and Purification of Potassium Ferrate. VI. *J. Am. Chem. Soc.* **1951**, *73* (3), 1379–1381.
- (21) Sun, X.; Zu, K.; Liang, H.; Sun, L.; Zhang, L.; Wang, C.; Sharma, V. K. Electrochemical Synthesis of Ferrate(VI) Using Sponge Iron Anode and Oxidative Transformations of Antibiotic and Pesticide. *J. Hazard. Mater.* **2018**, *344*, 1155–1164.
- (22) Mácová, Z.; Bouzek, K.; Híveš, J.; Sharma, V. K.; Terryn, R. J.; Baum, J. C. Research Progress in the Electrochemical Synthesis of Ferrate(VI). *Electrochim. Acta* **2009**, *54* (10), 2673–2683.
- (23) McBeath, S. T.; Graham, N. J. D. Simultaneous Electrochemical Oxidation and Ferrate Generation for the Treatment of Atrazine: A Novel Process for Water Treatment Applications. *J. Hazard. Mater.* **2021**, *411*, 125167.
- (24) McBeath, S. T.; Wilkinson, D. P.; Graham, N. J. D. Exploiting Water Contaminants: In-Situ Electrochemical Generation of Ferrates Using Ambient Raw Water Iron (Fe²⁺). *J. Environ. Chem. Eng.* **2020**, *8* (4), 103834.
- (25) McBeath, S. T.; Graham, N. J. D. Degradation of Perfluorooctane Sulfonate via In-Situ Electro-Generated Ferrate and Permanganate Oxidants in NOM-Rich Source Waters. *Environ. Sci. Water Res. Technol.* **2021**.
- (26) McBeath, S. T.; English, J. T.; Wilkinson, D. P.; Graham, N. J. D. Circumneutral Electrosynthesis of Ferrate Oxidant: An Emerging Technology for Small, Remote and Decentralised Water Treatment Applications. *Curr. Opin. Electrochem.* **2021**, *27*, 100680.
- (27) Mora, A. S.; McBeath, S. T.; Cid, C. A.; Hoffmann, M. R.; Graham, N. J. D. Diamond Electrode Facilitated Electrosynthesis of Water and Wastewater Treatment Oxidants. *Curr. Opin. Electrochem.* **2022**, *32*, 100899.
- (28) Cataldo-Hernández, M. A.; Bonakdarpour, A.; English, J. T.; Mohseni, M.; Wilkinson, D. P. A Membrane-Based Electrochemical Flow Reactor for Generation of Ferrates at near Neutral PH Conditions. *React. Chem. Eng.* **2019**, *4* (6), 1116–1125.
- (29) Cataldo-Hernández, M. A.; Govindarajan, R.; Bonakdarpour, A.; Mohseni, M.; Wilkinson, D. P. Electrosynthesis of Ferrate in a Batch Reactor at Neutral Conditions for Drinking Water Applications. *Can. J. Chem. Eng.* **2018**, *9999*, 1–8.
- (30) Chaplin, B. P. The Prospect of Electrochemical Technologies Advancing Worldwide Water Treatment. *Acc. Chem. Res.* **2019**, *52* (3), 596–604.
- (31) Chaplin, B. P. The Prospect of Electrochemical Technologies Advancing Worldwide Water Treatment. *Acc. Chem. Res.* **2019**, *52* (3), 596–604.
- (32) Comninellis, C. K Jüttner; U Galla; H Schmieder. *Electrochim. Acta* **1994**, *39* (11–12), 1857–1862.
- (33) Bejan, D.; Guinea, E.; Bunce, N. J. On the Nature of the Hydroxyl Radicals Produced at Boron-Doped Diamond and Ebonex[®] Anodes. *Electrochim. Acta* **2012**, *69*, 275–281.
- (34) Nayak, S.; Chaplin, B. P. Fabrication and Characterization of Porous, Conductive, Monolithic Ti₄O₇ Electrodes. *Electrochim. Acta* **2018**, *263*, 299–310.
- (35) Jarzebski, Z. M.; Marton, J. P. Physical Properties of SnO₂ Materials: I. Preparation

- and Defect Structure. *J. Electrochem. Soc.* **1976**.
- (36) Christensen, P. A.; Attidekou, P. S.; Egdell, R. G.; Maneelok, S.; Manning, D. A. C.; Palgrave, R. Identification of the Mechanism of Electrocatalytic Ozone Generation on Ni/Sb-SnO₂. *J. Phys. Chem. C* **2017**, *121* (2), 1188–1199.
- (37) Yang, S. Y.; Kim, D.; Park, H. Shift of the Reactive Species in the Sb-SnO₂-Electrocatalyzed Inactivation of E. Coli and Degradation of Phenol: Effects of Nickel Doping and Electrolytes. *Environ. Sci. Technol.* **2014**, *48* (5), 2877–2884.
- (38) Zhang, Y.; Yang, Y.; Yang, S.; Quispe-Cardenas, E.; Hoffmann, M. R. Application of Heterojunction Ni–Sb–SnO₂ Anodes for Electrochemical Water Treatment. *ACS EST Eng.* **2021**, *1* (8), 1236–1245.
- (39) Zhang, C.; Jiang, Y.; Li, Y.; Hu, Z.; Zhou, L.; Zhou, M. Three-Dimensional Electrochemical Process for Wastewater Treatment: A General Review. *Chem. Eng. J.* **2013**, *228*, 455.
- (40) Luo, Z.; Strouse, M.; Jiang, J. Q.; Sharma, V. K. Methodologies for the Analytical Determination of Ferrate(VI): A Review. *J. Environ. Sci. Heal. - Part A* **2011**, *46* (5), 453–460.
- (41) Lee, Y.; Yoon, J.; Von Gunten, U. Spectrophotometric Determination of Ferrate (Fe(VI)) in Water by ABTS. *Water Res.* **2005**, *39* (10), 1946–1953.
- (42) Golovko, D. A.; Sharma, V. K.; Suprunovich, V. I.; Pavlova, O. V.; Golovko, I. D.; Bouzek, K.; Zboril, R. A Simple Potentiometric Titration Method to Determine Concentration of Ferrate(VI) in Strong Alkaline Solutions. *Anal. Lett.* **2011**, *44* (7), 1333–1340.
- (43) Panizza, M.; Cerisola, G. Direct and Mediated Anodic Oxidation of Organic Pollutants. *Chem. Rev.* **2009**, *109* (12), 6541–6569.
- (44) Trellu, C.; Chaplin, B. P.; Coetsier, C.; Esmilaire, R.; Cerneaux, S.; Causserand, C.; Cretin, M. Electro-Oxidation of Organic Pollutants by Reactive Electrochemical Membranes. *Chemosphere* **2018**, *208*, 159–175.
- (45) Zhang, Y.; Guo, L.; Hoffmann, M. R. Ozone- and Hydroxyl Radical-Mediated Oxidation of Pharmaceutical Compounds Using Ni-Doped Sb-SnO₂ Anodes: Degradation Kinetics and Transformation Products. *ACS EST Eng.* **2023**.
- (46) Huang, Z. S.; Wang, L.; Liu, Y. L.; Jiang, J.; Xue, M.; Xu, C. B.; Zhen, Y. F.; Wang, Y. C.; Ma, J. Impact of Phosphate on Ferrate Oxidation of Organic Compounds: An Underestimated Oxidant. *Environ. Sci. Technol.* **2018**, *52* (23), 13897–13907.
- (47) Sharma, V. K.; Feng, M.; Dionysiou, D. D.; Zhou, H. C.; Jinadatha, C.; Manoli, K.; Smith, M. F.; Luque, R.; Ma, X.; Huang, C. H. Reactive High-Valent Iron Intermediates in Enhancing Treatment of Water by Ferrate. *Environ. Sci. Technol.* **2022**, *56* (1), 30–47.
- (48) Manoli, K.; Nakhla, G.; Ray, A. K.; Sharma, V. K. Enhanced Oxidative Transformation of Organic Contaminants by Activation of Ferrate(VI): Possible Involvement of FeV/FeIV Species. *Chem. Eng. J.* **2017**, *307*, 513–517.
- (49) Yang, T.; Mai, J.; Cheng, H.; Zhu, M.; Wu, S.; Tang, L.; Liang, P.; Jia, J.; Ma, J. UVA-LED-Assisted Activation of the Ferrate(VI) Process for Enhanced Micropollutant Degradation: Important Role of Ferrate(IV) and Ferrate(V). *Environ. Sci. Technol.* **2022**, *56* (2), 1221–1232.
- (50) Zhang, X.; Feng, M.; Luo, C.; Nesnas, N.; Huang, C. H.; Sharma, V. K. Effect of

- Metal Ions on Oxidation of Micropollutants by Ferrate(VI): Enhancing Role of FeIVSpecies. *Environ. Sci. Technol.* **2021**, *55* (1), 623–633.
- (51) Melton, J. D.; Bielski, B. H. J. Studies of the Kinetic, Spectral and Chemical Properties of Fe(IV) Pyrophosphate by Pulse Radiolysis. *Int. J. Radiat. Appl. Instrumentation. Part* **1990**, *36* (6), 725–733.
- (52) Bielski, B. H. J. Generation of Iron(IV) and Iron(V) Complexes in Aqueous Solutions. *Methods Enzymol.* **1990**, *186*, 108–113.
- (53) Cataldo-Hernández, M. A.; May, A.; Bonakdarpour, A.; Mohseni, M.; Wilkinson, D. P. Analytical Quantification of Electrochemical Ferrates for Drinking Water Treatments. *Can. J. Chem.* **2017**, *95*, 105–112.
- (54) Luo, Z.; Strouse, M.; Jiang, J. Q.; Sharma, V. K. Methodologies for the Analytical Determination of Ferrate(VI): A Review. *J. Environ. Sci. Heal. - Part A Toxic/Hazardous Subst. Environ. Eng.* **2011**, *46* (5), 453–460.
- (55) Sun, S.; Liu, Y.; Ma, J.; Pang, S.; Huang, Z.; Gu, J.; Gao, Y.; Xue, M.; Yuan, Y.; Jiang, J. Transformation of Substituted Anilines by Ferrate(VI): Kinetics, Pathways, and Effect of Dissolved Organic Matter. *Chem. Eng. J.* **2018**, *332* (May 2017), 245–252.
- (56) Lacina, P.; Goold, S. Use of the Ferrates (FeIV-VI) in Combination with Hydrogen Peroxide for Rapid and Effective Remediation of Water - Laboratory and Pilot Study. *Water Sci. Technol.* **2015**, *72* (10), 1869–1878.
- (57) Gibs, J.; Stackelberg, P. E.; Furlong, E. T.; Meyer, M.; Zaugg, S. D.; Lippincott, R. L. Persistence of Pharmaceuticals and Other Organic Compounds in Chlorinated Drinking Water as a Function of Time. *Sci. Total Environ.* **2007**, *373* (1), 240–249.
- (58) Lee, Y.; von Gunten, U. Oxidative Transformation of Micropollutants during Municipal Wastewater Treatment: Comparison of Kinetic Aspects of Selective (Chlorine, Chlorine Dioxide, FerrateVI, and Ozone) and Non-Selective Oxidants (Hydroxyl Radical). *Water Res.* **2010**, *44* (2), 555–566.
- (59) Lee, Y.; Zimmermann, S. G.; Kieu, A. T.; Von Gunten, U. Ferrate (Fe(VI)) Application for Municipal Wastewater Treatment: A Novel Process for Simultaneous Micropollutant Oxidation and Phosphate Removal. *Environ. Sci. Technol.* **2009**, *43* (10), 3831–3838.
- (60) Hu, L.; Martin, H. M.; Arce-Bulted, O.; Sugihara, M. N.; Keating, K. A.; Strathmann, T. J. Oxidation of Carbamazepine by Mn(VII) and Fe(VI): Reaction Kinetics and Mechanism. *Environ. Sci. Technol.* **2009**, *43* (4), 509.
- (61) McBeath, S. T.; Graham, N. J. D. In-Situ Electrochemical Generation of Permanganate for the Treatment of Atrazine. *Sep. Purif. Technol.* **2021**, *260*, 118252.
- (62) McBeath, S. T.; Wilkinson, D. P.; Graham, N. J. D. Advanced Electrochemical Oxidation for the Simultaneous Removal of Manganese and Generation of Permanganate Oxidant. *Environ. Sci. Water Res. Technol.* **2020**.
- (63) Hu, L.; Stemig, A. M.; Wammer, K. H.; Strathmann, T. J. Oxidation of Antibiotics during Water Treatment with Potassium Permanganate: Reaction Pathways and Deactivation. *Environ. Sci. Technol.* **2011**, *45* (8), 3635–3642.
- (64) Hu, L.; Martin, H. M.; Strathmann, T. J. Oxidation Kinetics of Antibiotics during Water Treatment with Potassium Permanganate. *Environ. Sci. Technol.* **2010**, *44* (16), 6416–6422.

- (65) Yan, Y. E.; Schwartz, F. W. Kinetics and Mechanism for TCE Oxidation by Permanganate. *Environ. Sci. Technol.* **2000**, *34*, 2535–2541.
- (66) Waldemer, R. H.; Tratnyek, P. G. Kinetics of Contaminant Degradation by Permanganate. *Environ. Sci. Technol.* **2006**, *40* (3), 1055–1061.
- (67) Hoigné, J.; Bader, H.; Haag, W. R.; Staehelin, J. Rate Constants of Reactions of Ozone with Organic and Inorganic Compounds in Water-III. Inorganic Compounds and Radicals. *Water Res.* **1985**, *19* (8), 993–1004.

4.7 Supporting Information

4.S.1 Electrode Characterization

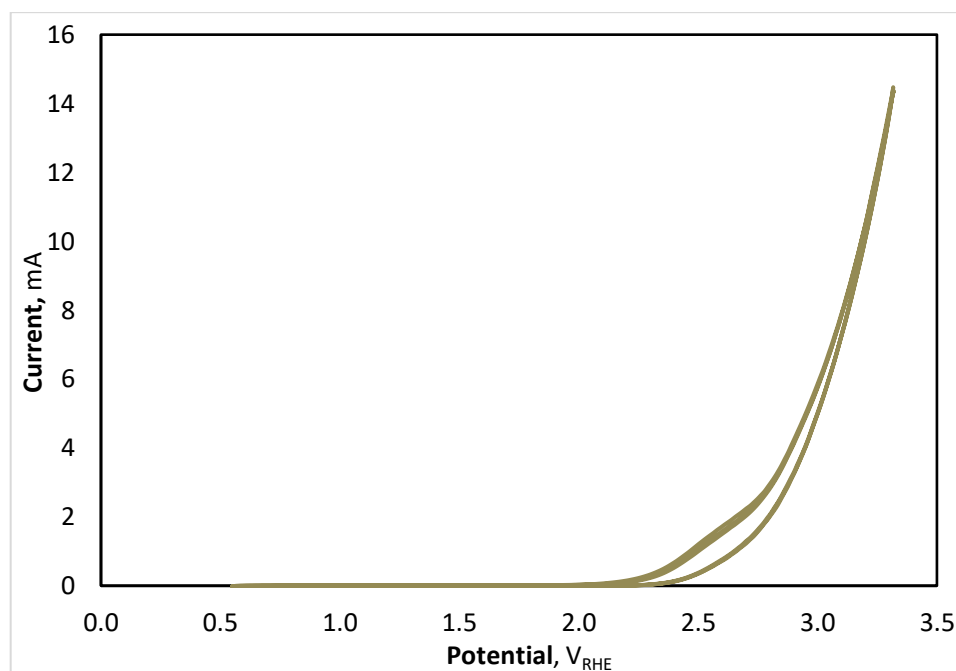


Figure 4.S1 Cyclic voltammograms of BDD with OER potential at $\sim 2.7 V_{RHE}$. CV condition: scan rate 50 mV s^{-1} , 0.0 V vs. Eoc to $+3.0 \text{ V vs. ref.}$

4.S.2 Ferrate Generation

The ABTS indirect ferrate quantification method was chosen due its sensitivity in determining low concentrations of Fe(VI). In a 50 mL Erlenmeyer flask, 5 mL of acetate buffer (pH=4.1), 1 mL of ABTS reagent (1 g/L) and 9 mL of MilliQ water is added. New ABTS reagent solutions were made prior to each electrolysis experiment and stored in the refrigerator at 4°C to avoid degradation due to increased temperature and light exposure. A 0.5 mL ferrate sample was added to the Erlenmeyer flask, followed by 9.5 mL of phosphate

buffer, to reach a final volume of 25 mL. This ABTS solution was then analyzed using the spectrophotometer at 415 nm, a visible maxima for ABTS^{•+}. Ferrate concentrations were determined from experimental measurements as follows:

$$[Fe(VI)] = \frac{\Delta A_{415} V_f}{\epsilon l V_s} \quad (1)$$

Where ΔA_{415} , V_f , ϵ , l and V_s represent the UV-absorbance at 415 nm, the final sample volume, the absorption coefficient as determined by the standards, the cell path length, and the volume of the ferrate sample.

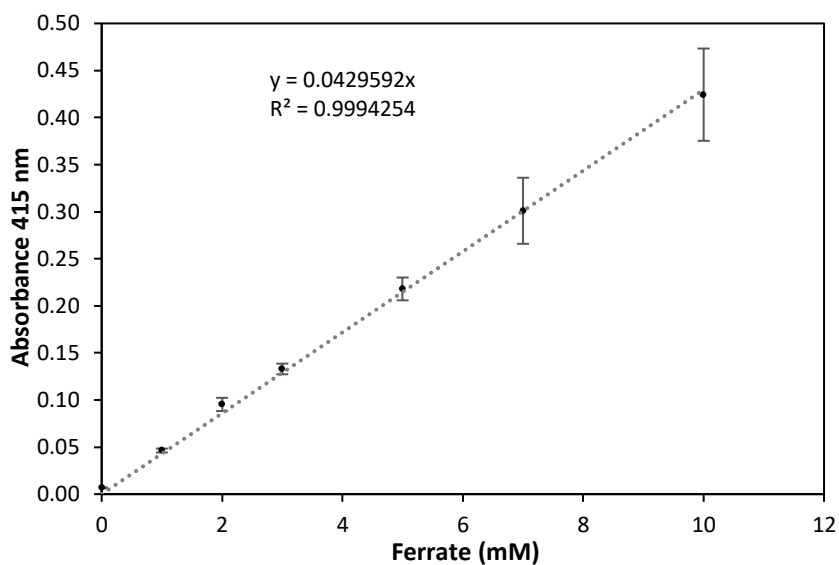


Figure 4.S2 Ferrate(VI) ABTS calibration curves using K_2SO_4 (Element 26) in phosphate buffer (pH = 7.0), yielding a molar absorption coefficient of $0.043 \text{ mM}^{-1} \text{ cm}^{-1}$.

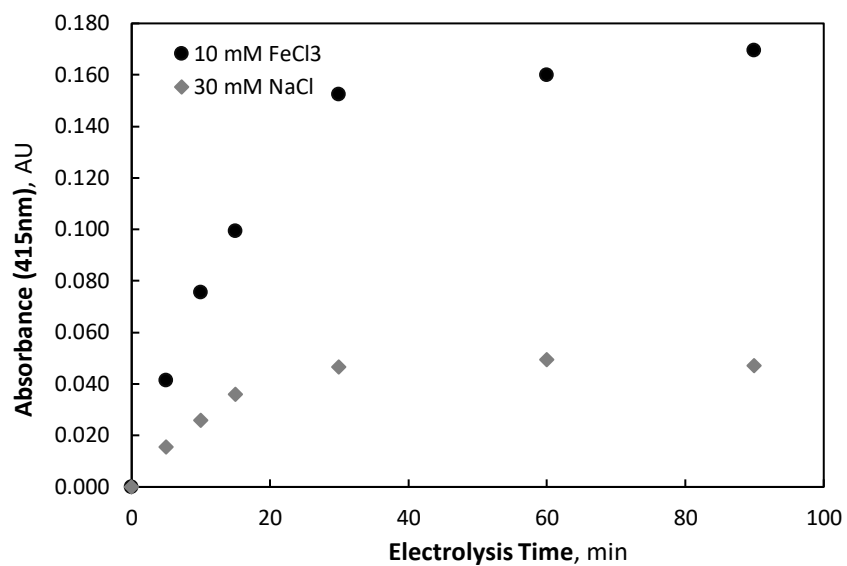


Figure 4.S3 ABTS absorbance during BDD ferrate (5 mA cm^{-2} , 10 mM FeCl_3) and control (5 mA cm^{-2} , 30 mM NaCl) experiments.

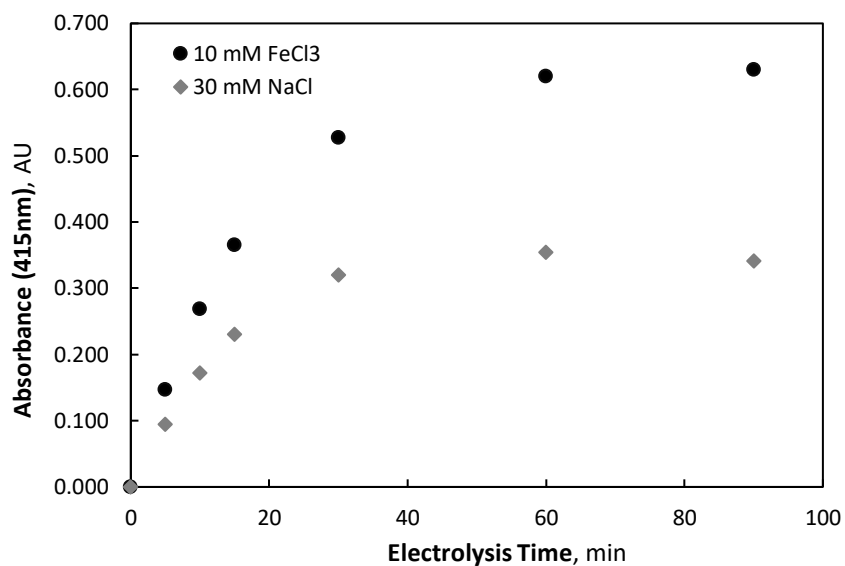


Figure 4.S4 ABTS absorbance during BDD ferrate (10 mA cm^{-2} , 10 mM FeCl_3) and control (10 mA cm^{-2} , 30 mM NaCl) experiments.

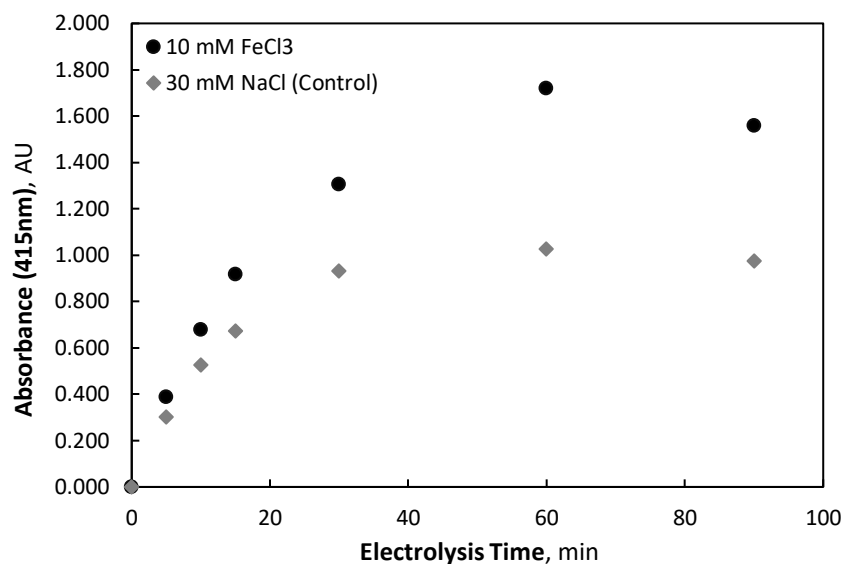


Figure 4.S5 ABTS absorbance during BDD ferrate (20 mA cm^{-2} , 10 mM FeCl_3) and control (20 mA cm^{-2} , 30 mM NaCl) experiments.

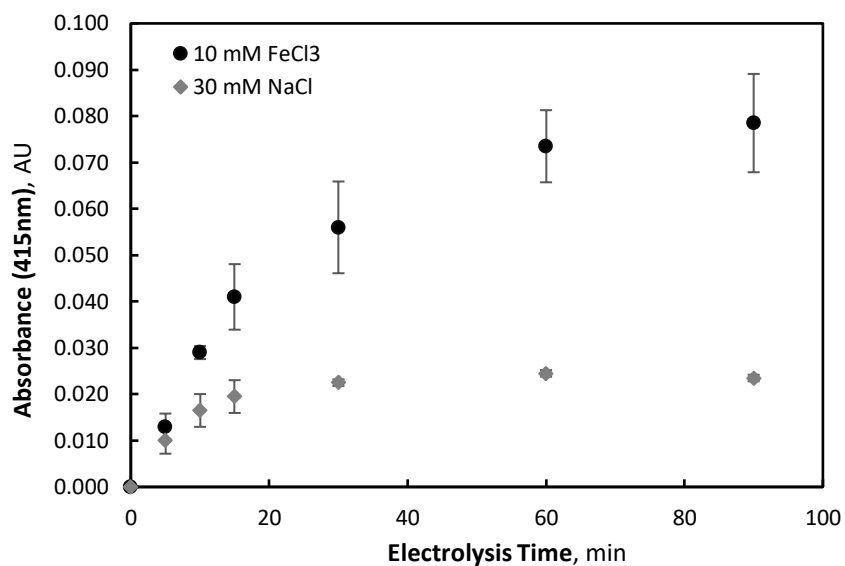


Figure 4.S6 ABTS absorbance during NAT ferrate (5 mA cm^{-2} , 10 mM FeCl_3) and control (5 mA cm^{-2} , 30 mM NaCl) experiments.

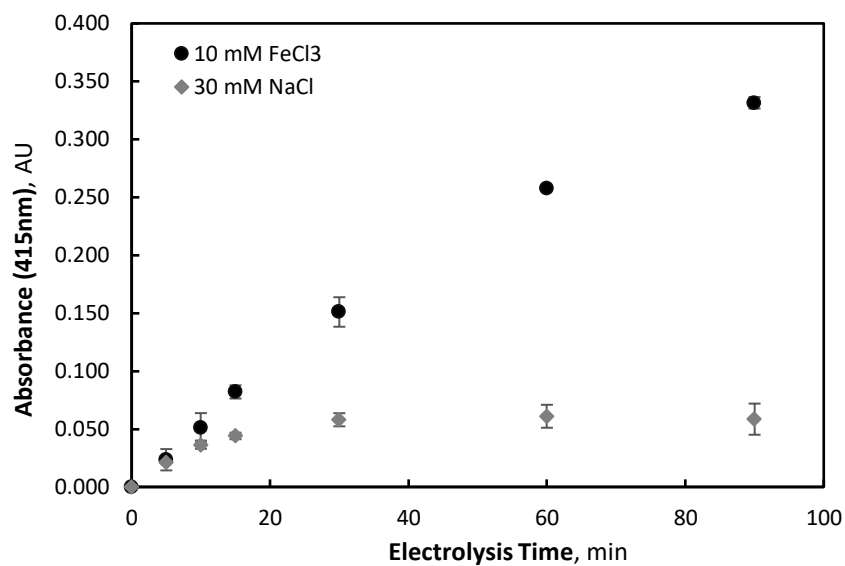


Figure 4.S7 ABTS absorbance during NAT ferrate (10 mA cm², 10 mM FeCl₃) and control (10 mA cm², 30 mM NaCl) experiments.

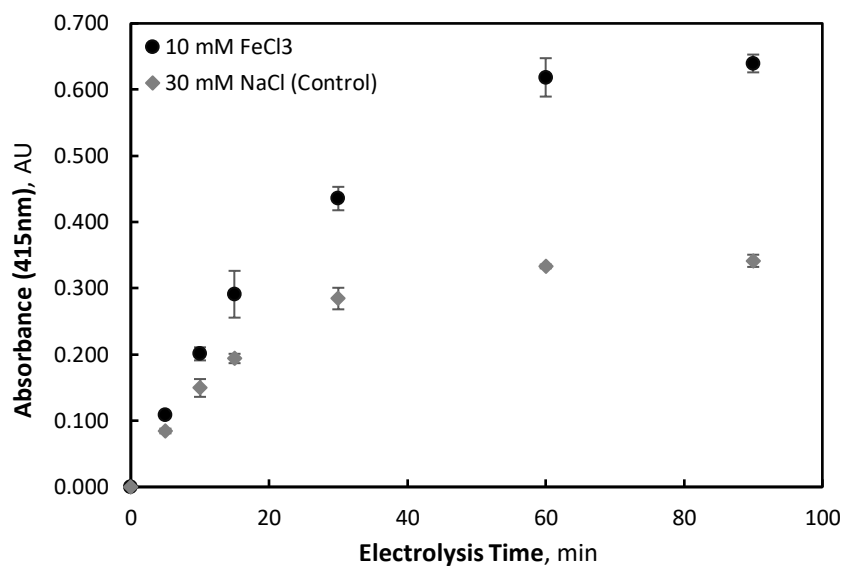


Figure 4.S8 ABTS absorbance during NAT ferrate (20 mA cm², 10 mM FeCl₃) and control (20 mA cm², 30 mM NaCl) experiments.

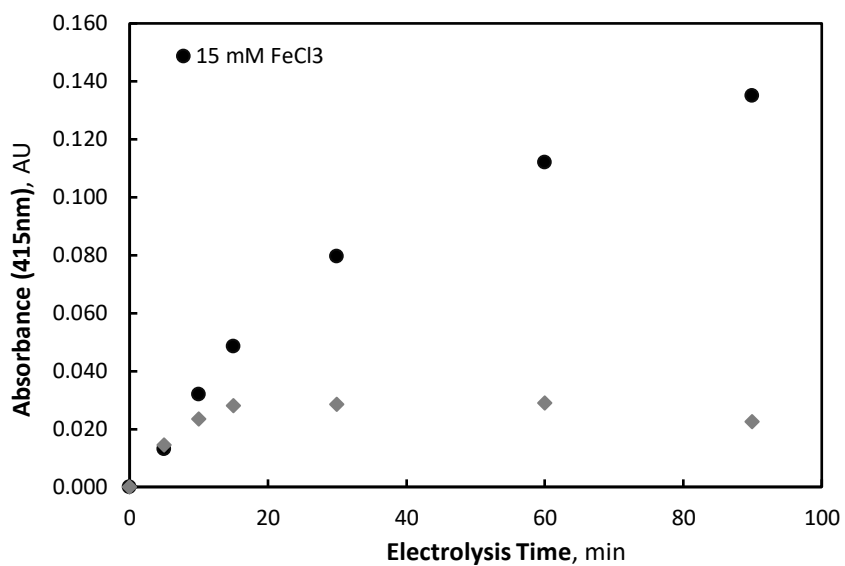


Figure 4.S9 ABTS absorbance during NAT ferrate (5 mA cm^2 , 15 mM FeCl_3) and control (5 mA cm^2 , 45 mM NaCl) experiments.

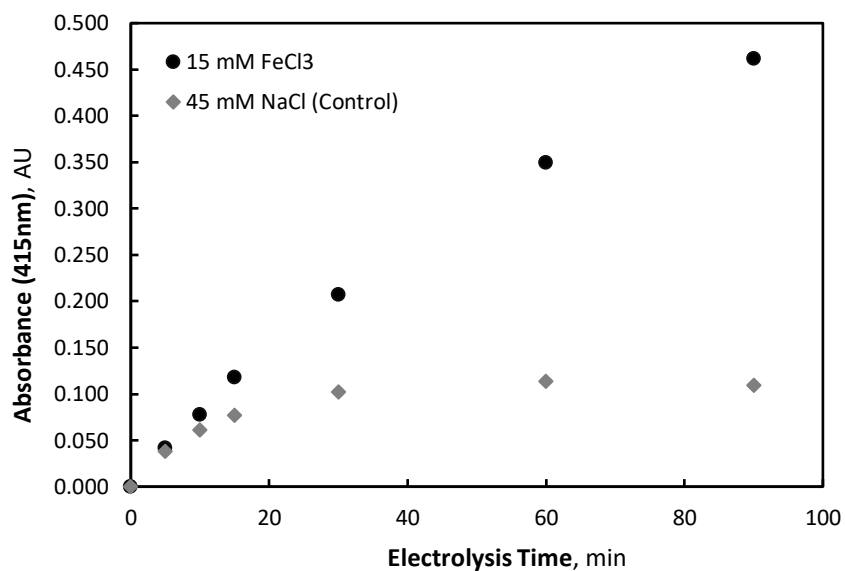


Figure 4.S10 ABTS absorbance during NAT ferrate (10 mA cm^2 , 15 mM FeCl_3) and control (10 mA cm^2 , 45 mM NaCl) experiments.

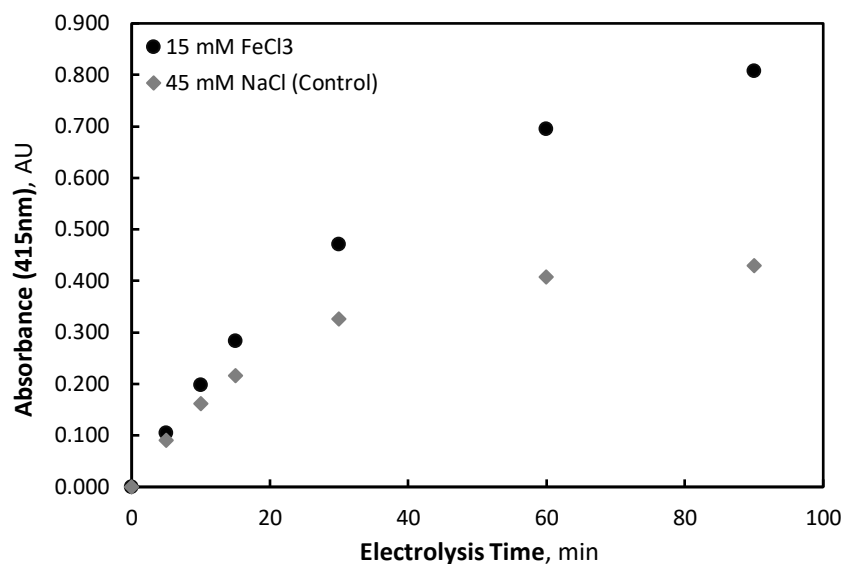


Figure 4.S11 ABTS absorbance during NAT ferrate (20 mA cm², 15 mM FeCl₃) and control (20 mA cm², 45 mM NaCl) experiments.

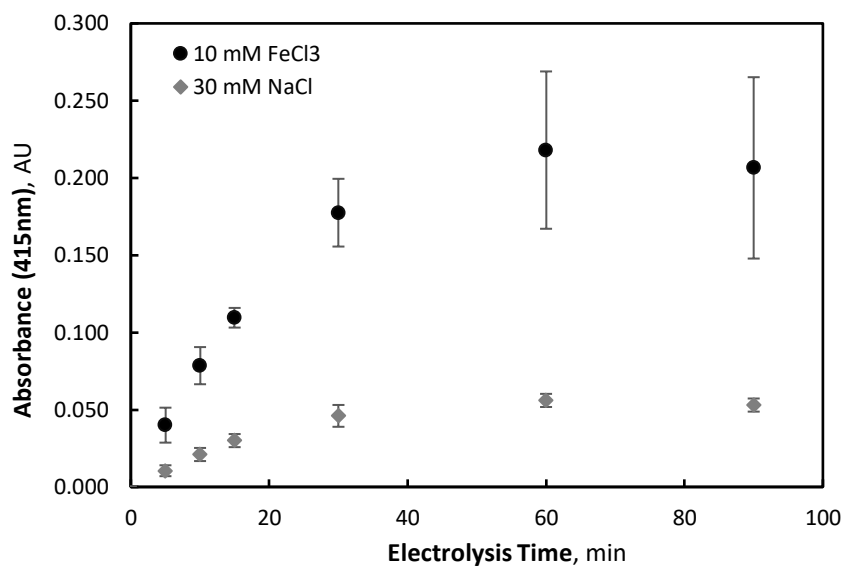


Figure 4.S12 ABTS absorbance during AT ferrate (10 mA cm², 10 mM FeCl₃) and control (10 mA cm², 30 mM NaCl) experiments.

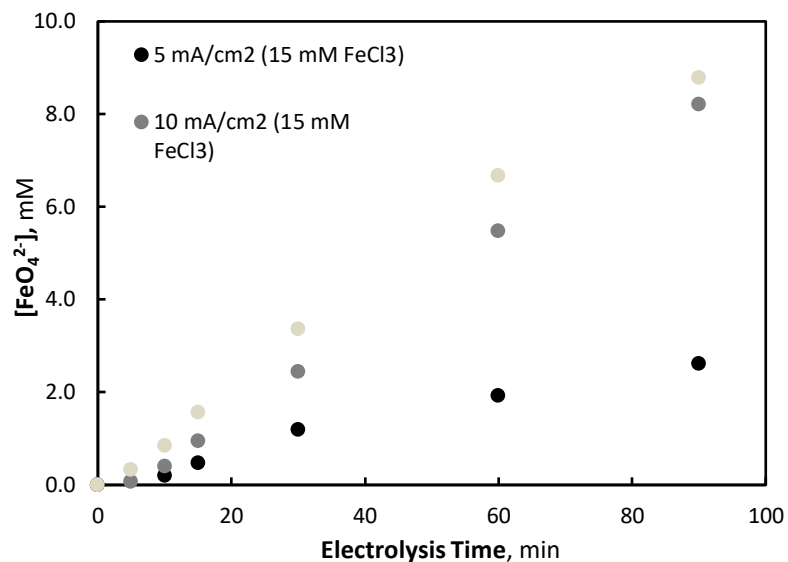
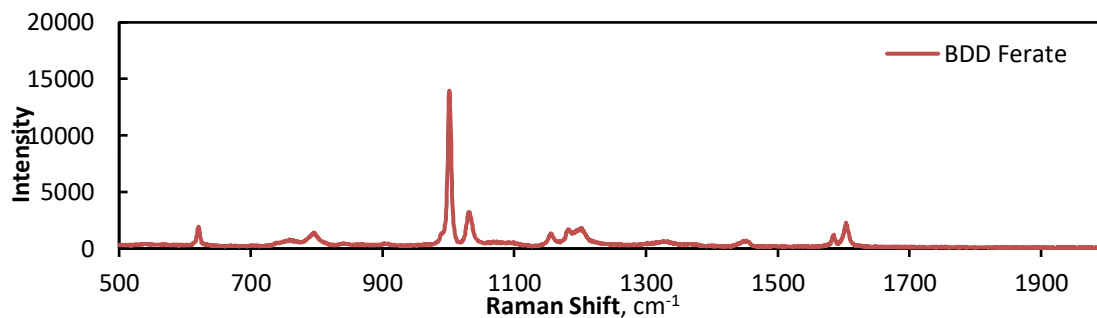


Figure 4.S13 Ferrate(VI) generation using an NAT electrodes with a $\text{Fe}^{3+}_0 = 15 \text{ mM}$ and current densities of at 5, 10 and 20 mA cm^{-2} .

4.S.3 Ferrate Speciation

The BDD and NAT produced ferrate(IV/V/VI) solutions were analyzed using Raman spectroscopy (Renishaw inVia Qontor) to determine whether the different ferrate species (e.g., Fe(IV), Fe(V) and/or Fe(VI)) could be identified. Raman micro-spectroscopy was performed using a 514 nm laser as the exciting light. Calibration was done using a silicon wafer with a Raman band centered at 520.5 cm^{-1} .



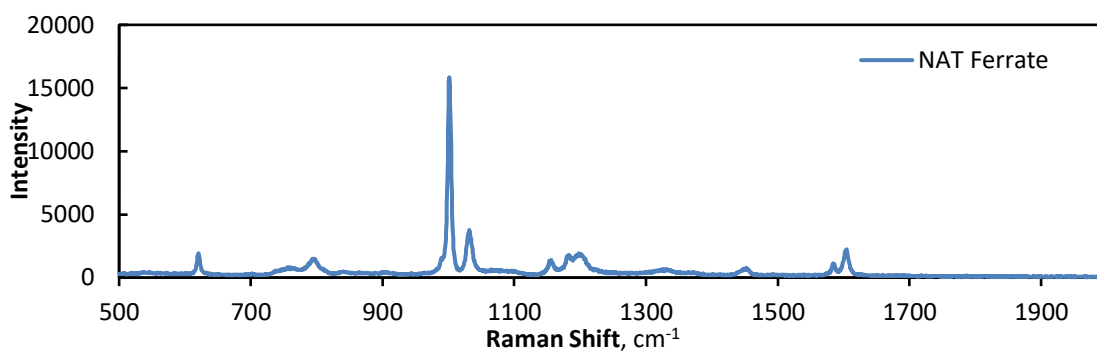


Figure 4.S14 Raman spectra graph of final BDD and NAT ferrate solutions after 90 min of electrolysis at 10 mA cm⁻² and an initial FeCl₃ concentration of 10 mM.

The BDD and NAT produced ferrate(IV/V/VI) solutions were also analyzed using FTIR spectroscopy (Thermo Scientific Nicolet iS50) to determine whether the different ferrate species (e.g., Fe(IV), Fe(V) and/or Fe(VI)) could be identified.

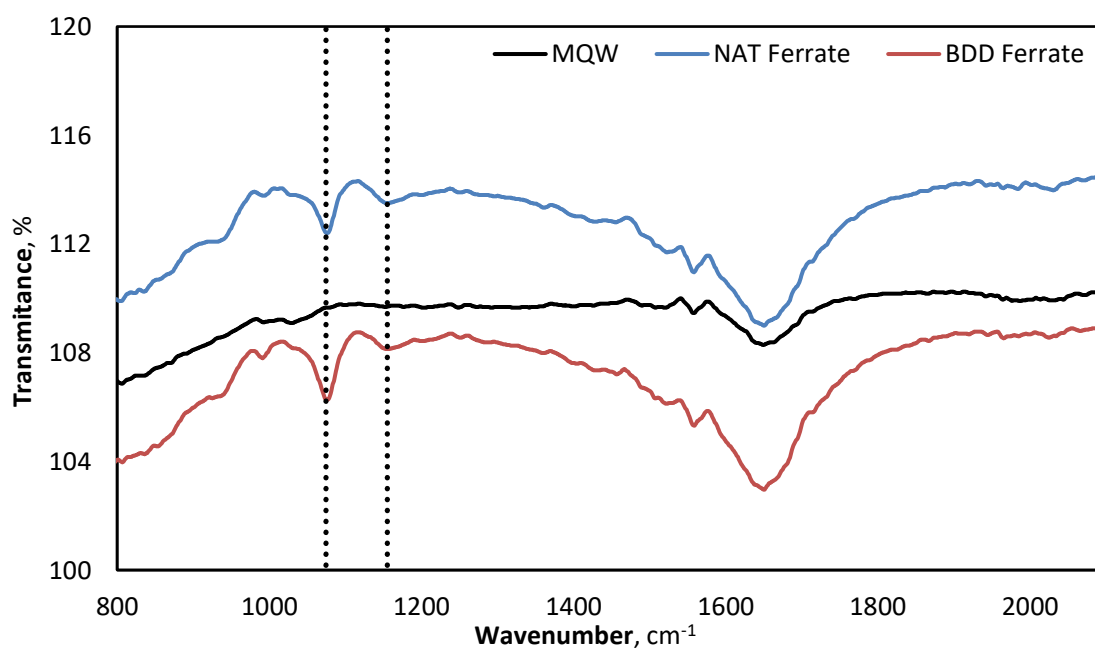


Figure 4.S15 FTIR spectra graph of final BDD and NAT ferrate solutions after 90 min of electrolysis at 10 mA cm⁻² and an initial FeCl₃ concentration of 10 mM.

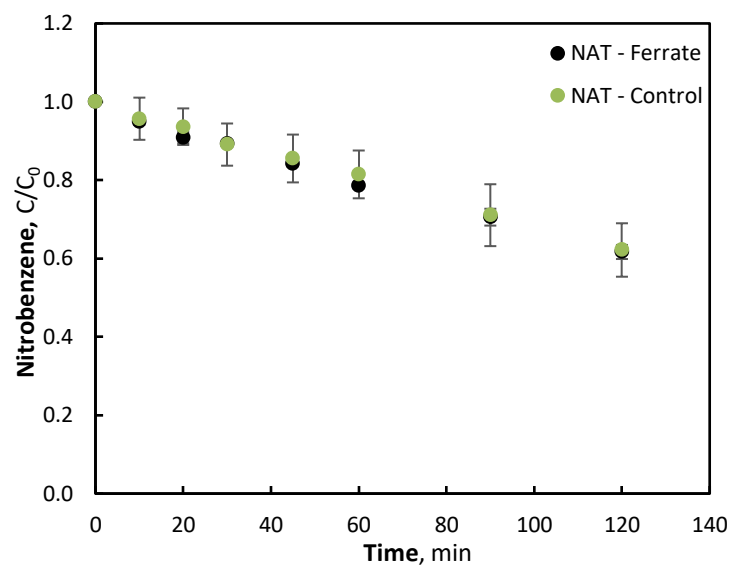


Figure 4.S16 Nitrobenzene degradation using NAT derived ferrate(VI) and NaCl control solutions ($NB_0 = 0.1 \text{ mM}$, $Fe(VI) = 1.52 \text{ mM}$).

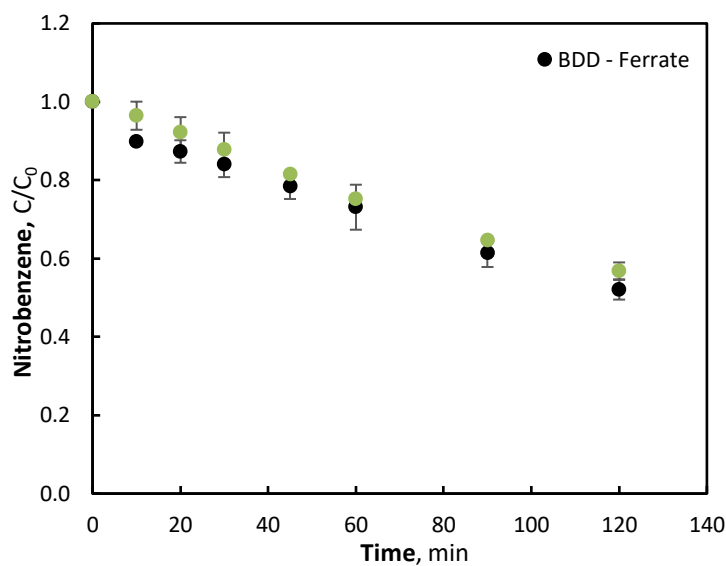


Figure 4.S17 Nitrobenzene degradation using BDD derived ferrate(IV/V) and NaCl control solutions ($NB_0 = 0.1 \text{ mM}$, $Fe(VI)_{Eq} = 3.83 \text{ mM}$).

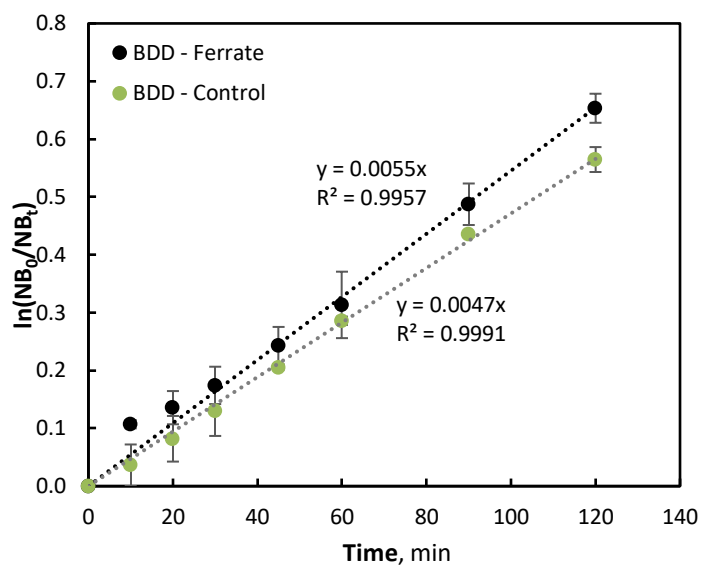


Figure 4.S18 Nitrobenzene degradation using BDD derived ferrate(IV/V) and NaCl control solutions ($NB_0 = 0.1 \text{ mM}$, $Fe(VI)_{Eq} = 3.83 \text{ mM}$).

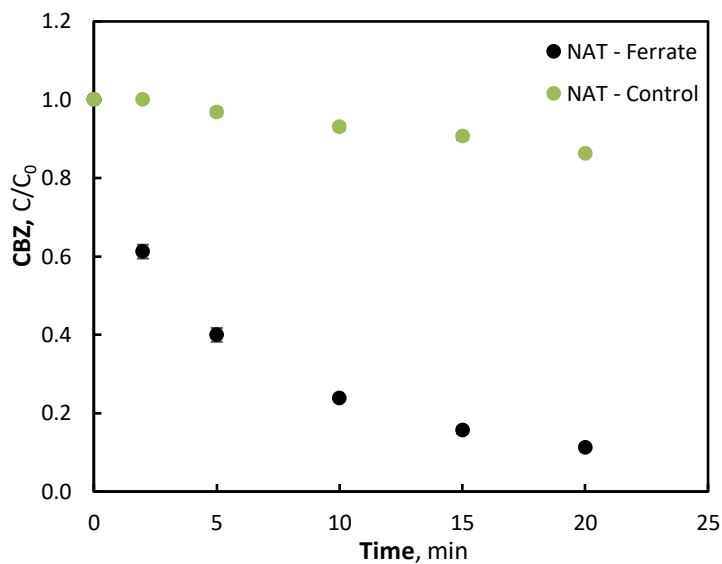


Figure 4.S19 CBZ degradation using NAT derived ferrate(VI) and NaCl control solutions ($CBZ_0 = 10 \text{ }\mu\text{M}$).

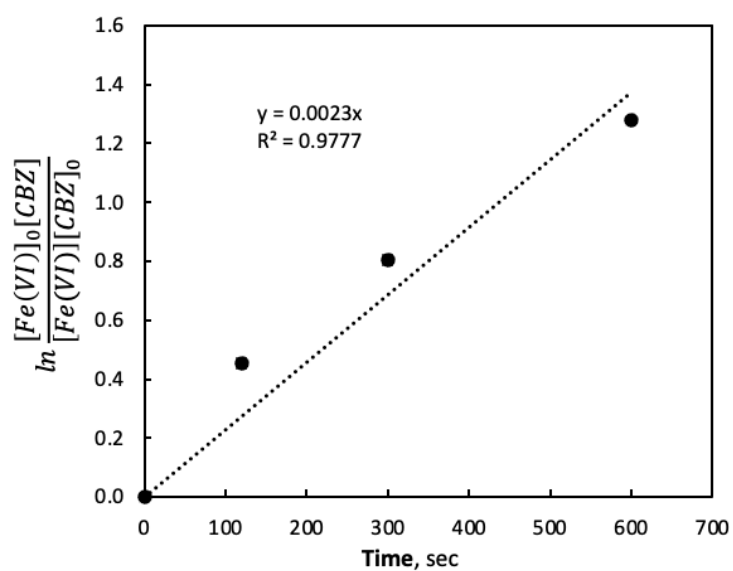


Figure 4.S20 Second-order reaction rate determination of CBZ and NAT derived ferrate(VI) ($\text{CBZ}_0 = 10 \mu\text{M}$, $\text{Fe(VI)}_0 = 1.66 \text{ mM}$).

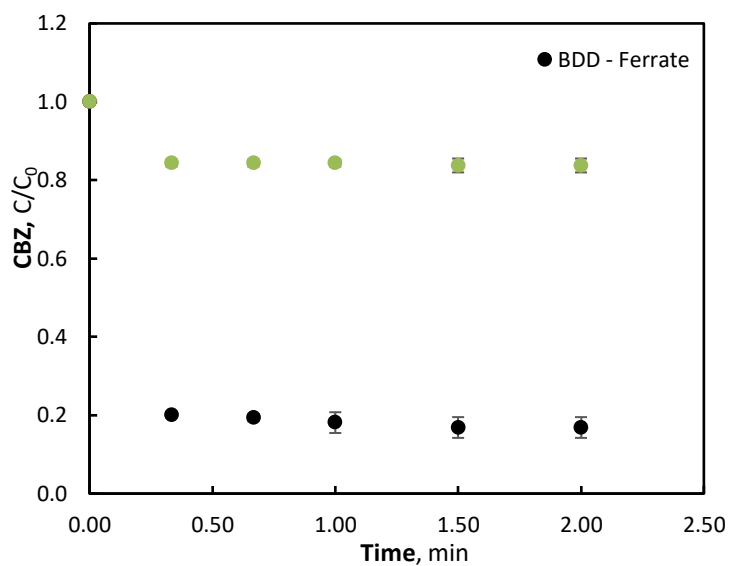


Figure 4.S21 CBZ degradation using BDD derived ferrate(IV/V) and NaCl control solutions ($\text{CBZ}_0 = 10 \mu\text{M}$).

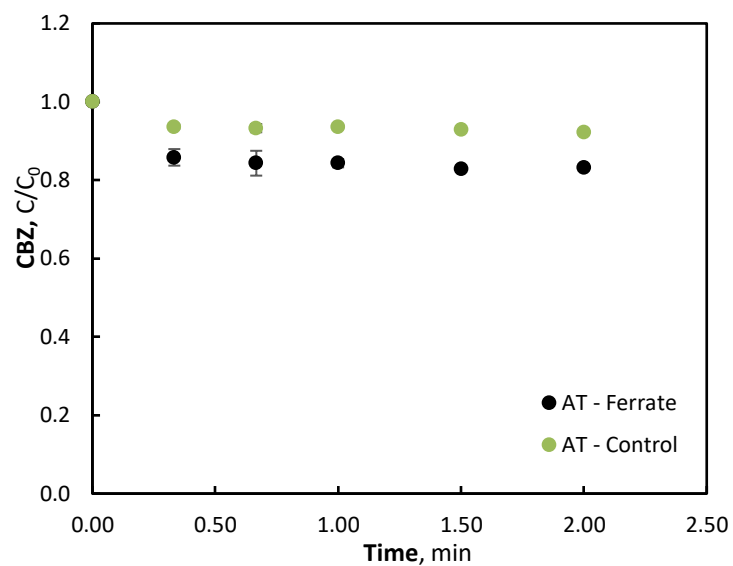


Figure 4.S22 CBZ degradation using AT derived ferrate(IV/V) and NaCl control solutions ($CBZ_0 = 10 \mu M$).

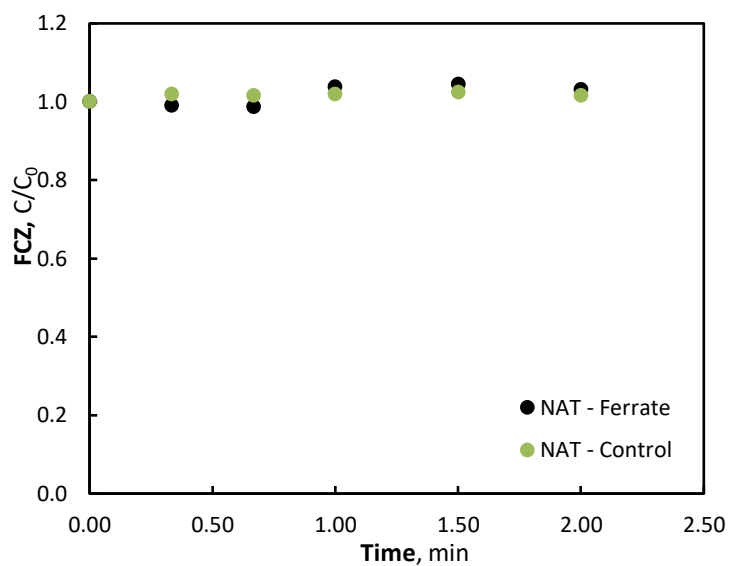


Figure 4.S23 FCZ degradation using NAT derived ferrate(VI) and NaCl control solutions ($FCZ_0 = 10 \mu M$).

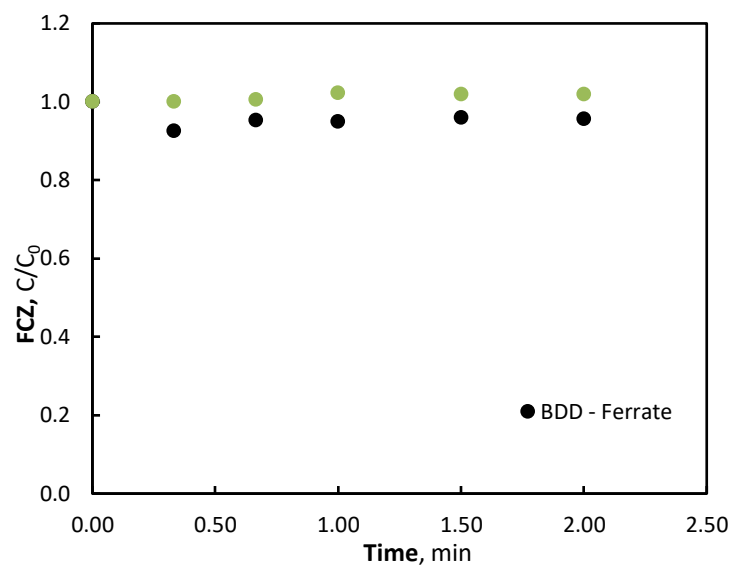


Figure 4.S24 FCZ degradation using BDD derived ferrate(IV/V) and NaCl control solutions ($FCZ_0 = 10 \mu M$).

4.S.4 Ferrate Stability

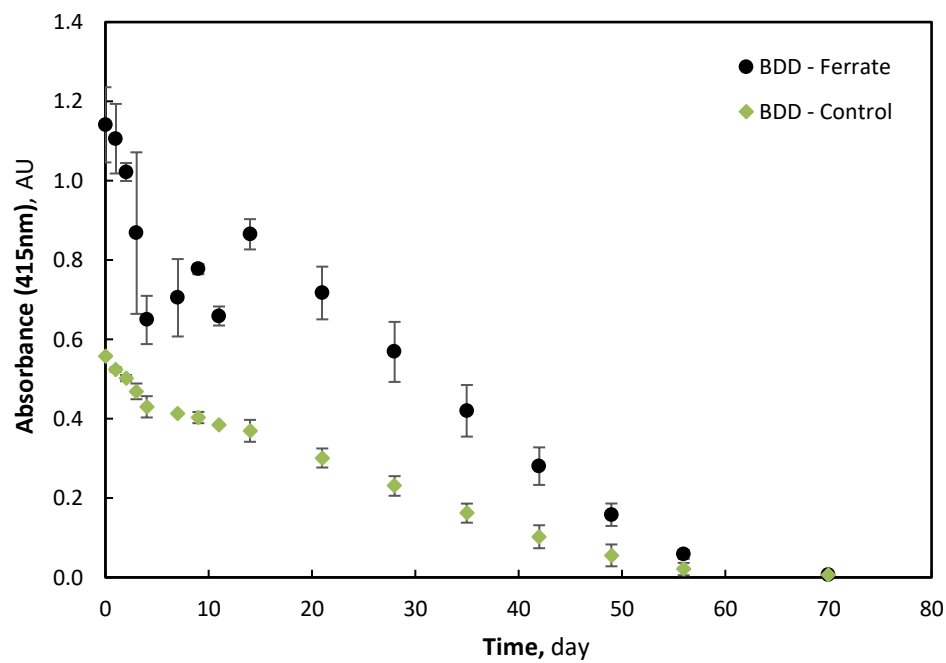


Figure 4.S25 ABTS absorbance data for ferrate(IV/V) degradation long term study ($Fe(VI)_{Eq} = 13.6 \text{ mM}$).

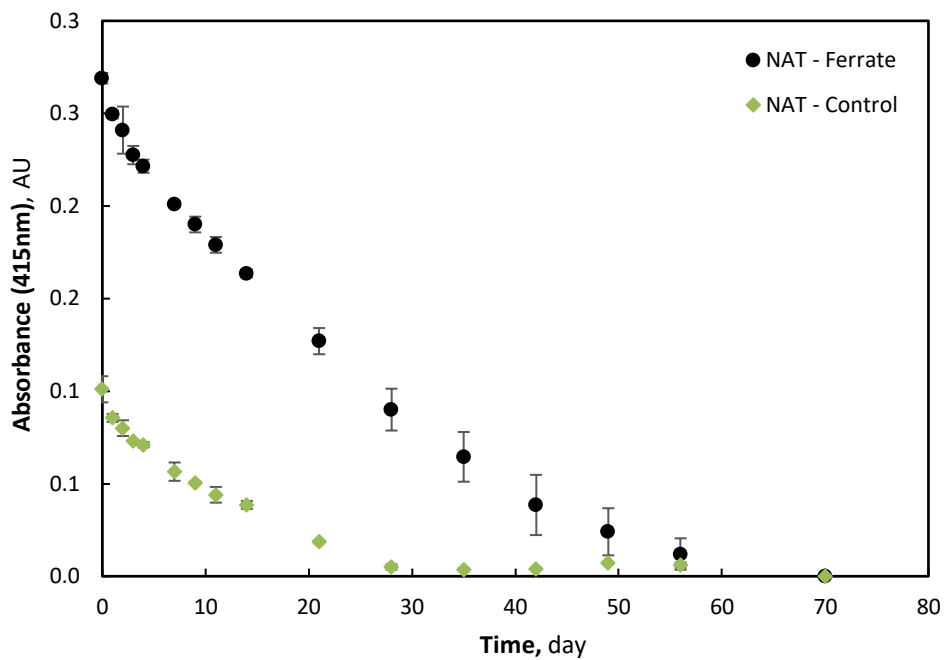


Figure 4.S26 ABTS absorbance data for ferrate(VI) degradation long term study ($\text{Fe(VI)} = 3.9 \text{ mM}$).

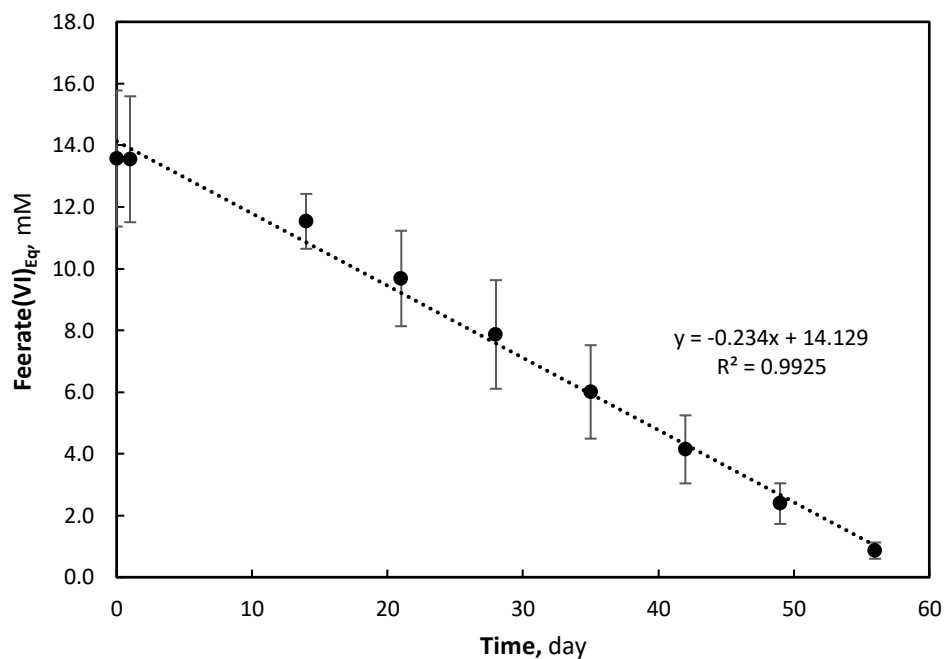


Figure 4.S27 $\text{Fe(VI)}_{\text{Eq}}$ data for ferrate(IV/V) degradation long term study ($\text{Fe(VI)}_{\text{Eq}} = 13.6 \text{ mM}$). $\text{Fe(VI)}_{\text{Eq}}$ = Equivalent oxidative capacity of Fe(VI) with ABTS (1:1 molar ratio).

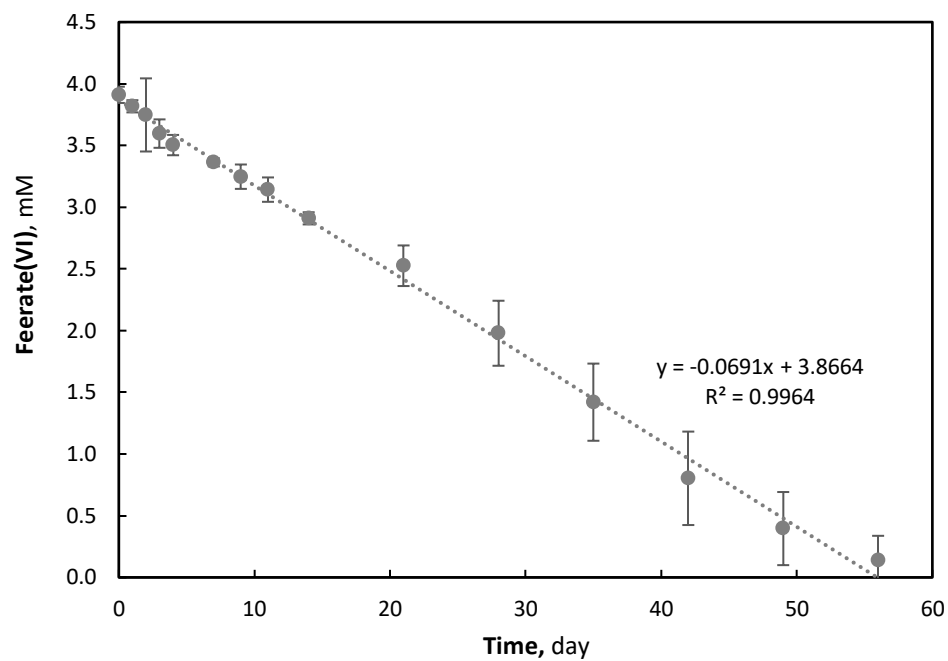


Figure 4.S28 Fe(VI) data for ferrate(VI) degradation long term study (Fe(VI) = 3.9 mM).

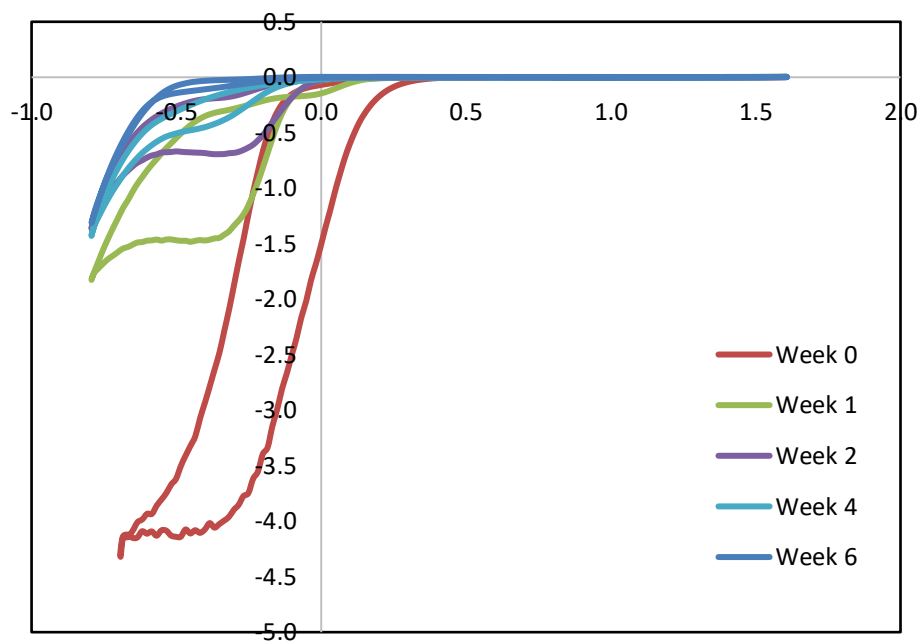


Figure 4.S29 Cyclic voltammograms of BDD derived ferrate(IV/V) solution over 6 week stability test. CV condition: scan rate 50 mV s^{-1} , 0.0 V vs. Eoc to -1.3 V vs. ref.

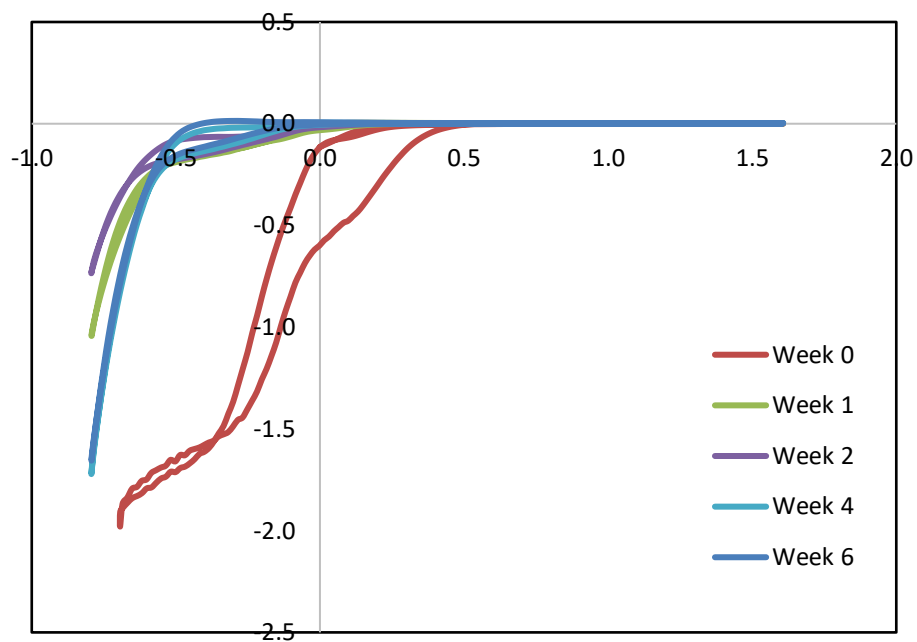


Figure 4.S30 Cyclic voltammograms of NAT derived ferrate(VI) solution over 6 week stability test. CV condition: scan rate 50 mV s^{-1} , 0.0 V vs. Eoc to -1.3 V vs. ref.

4.S.5 Ferrate Generation Mechanism

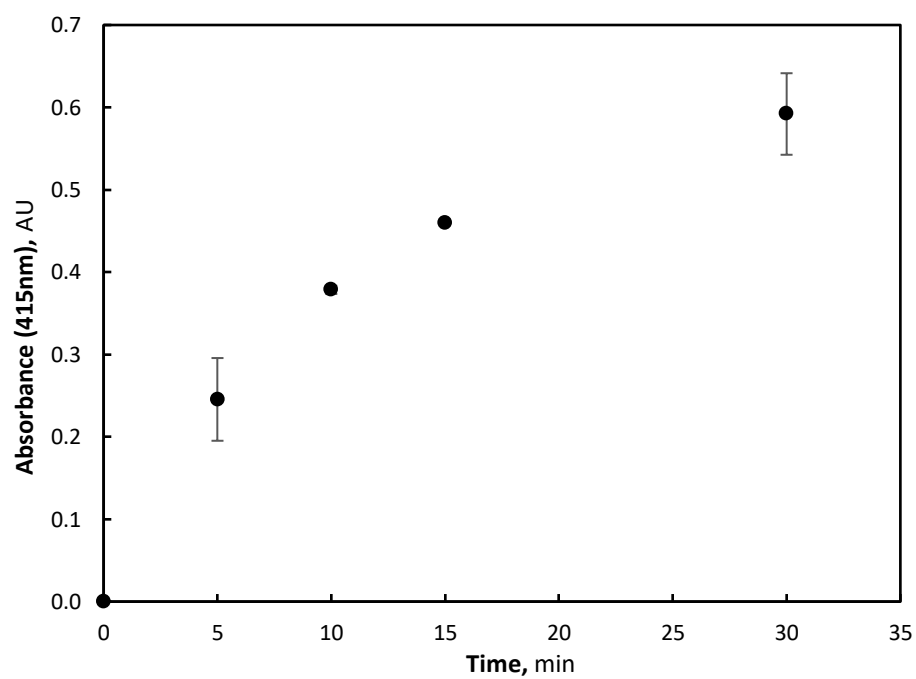


Figure 4.S31 ABTS absorbance during BDD electrolysis and O₃ purging (10 mA cm², 15 mM FeCl₃).

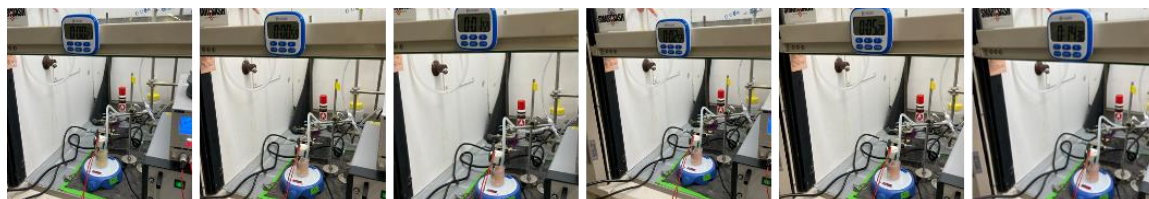


Figure 4.S32 Ferrate(IV/V) oxidation experiments with O₃ during electrolysis to form ferrate(VI) (full set of photos).

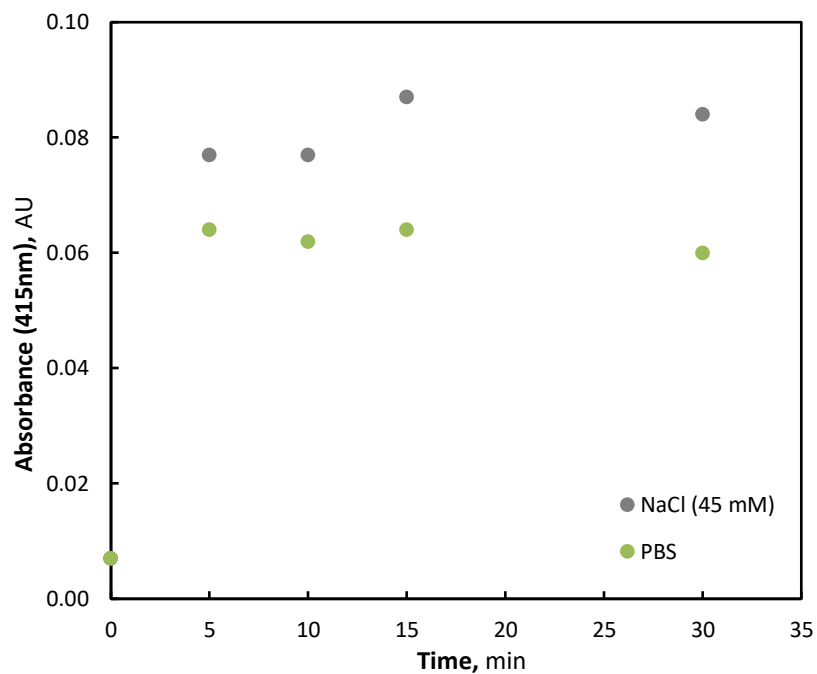


Figure 4.S33 ABTS absorbance of control ozonation of NaCl and PBS solution.

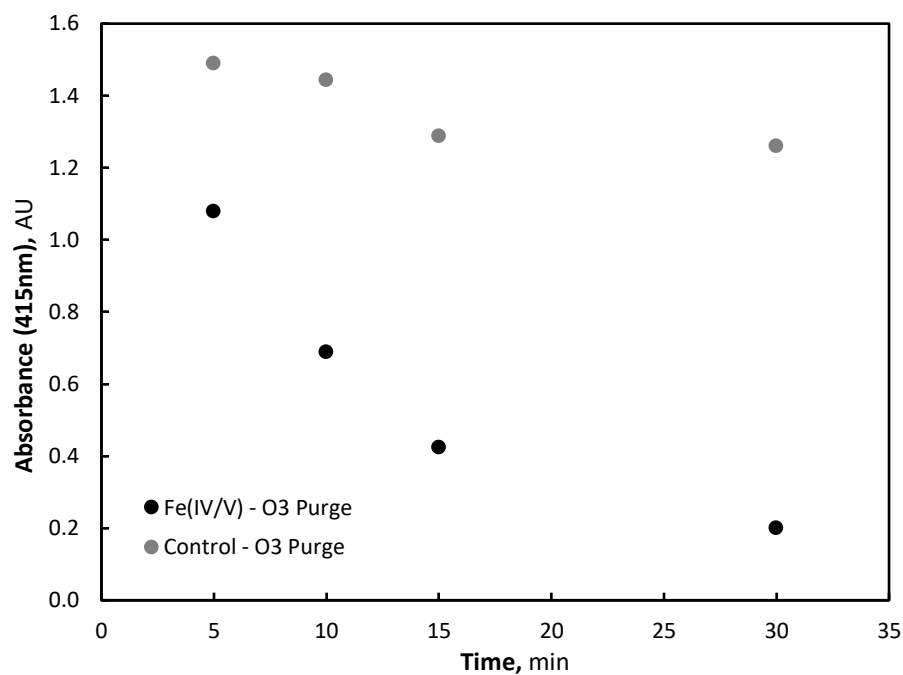


Figure 4.S34 ABTS absorbance during O₃ purging on ferrate(IV/V) solution produced with BDD electrolysis (10 mA cm², 15 mM FeCl₃) and control (10 mA cm², 45 mM NaCl).

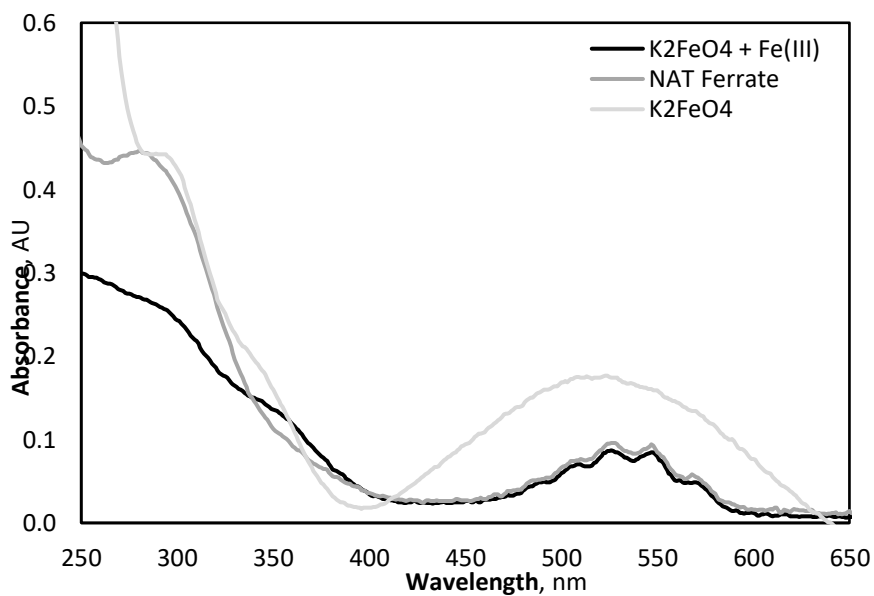


Figure 4.S35 UV-absorption spectra of ferrate(VI) from K₂FeO₄, K₂FeO₄ and Fe(III) (dosed using FeCl₃) and NAT-generated ferrate(VI).

MODULAR METAL-ORGANIC FRAMEWORKS
FUNCTIONALIZATION FACILITATING NITROGEN RECOVERY
FROM FRESH URINE

Guo, L.; Zhang, Y.; Osella, S.; Webb, S. M.; Yang, X.; Goddard, W. A.; Hoffmann, M. R. Modular Metal-Organic Frameworks Functionalization Facilitating Nitrogen Recovery from Fresh Urine. To be submitted.

5.1 Abstract

Urine contains a high concentration of nitrogen and is a valuable and sustainable resource for nitrogen recovery. While ammonia/ammonium are much easier substances to be separated and captured from water, they only dominate in *stored* urine, and the recovery relies heavily on the complete hydrolysis of urea which is time and spatial consuming. Moreover, a substantial loss of nitrogen is inevitable during urine storage, therefore compromising total nitrogen recovery. In this work, we developed a novel nitrogen recovery process targeting fresh urine that is more suitable for on-site treatment with high efficiency and is more time and spatial friendly. To achieve this, we leveraged the modularity of metal-organic frameworks (MOFs), designed and synthesized three functionalized MOFs with various modification methods to facilitate the process of nitrogen recovery from *fresh* urine. Specifically, we synthesized urease-incorporated MOF-808, **MOF-808-U**, for rapid urea hydrolysis, oxalate-decorated MOF-808, **MOF-808-OA**, for efficient ammonium capture, and Cu(II)-bonded MOF-808, **MOF-808-Cu**, for real-time ammonium monitoring. By further integrating these functionalized MOFs into our newly developed treatment process, we were able to achieve an average of 75% total nitrogen reduction and 45% nitrogen recovery in five cycles from synthetic fresh urine with each cycle taking 30 min. Ammonium nitrate was the major nitrogen recovery product, and urea was also found captured and recovered by MOF-808-OA due to the non-specific van der Waals interaction, which further boosted the total nitrogen recovery efficiency. In summary, the nitrogen recovery process

developed in this work provides a sustainable and efficient nutrient management that is suitable for decentralized toilet wastewater treatment system.

5.2 Introduction

Nitrogen recovery from urine is an important practice to promote the water-food-energy nexus. Human urine contributes to up to 80% of total nitrogen in domestic sewage¹ that can lead to eutrophication when left untreated. Approximately \$2.2 billion per annum is lost due to damage caused by eutrophication,^{2,3} and \$0.5/gpd per annum is spent on treatment methods for total nitrogen control in municipal wastewater treatment plants.⁴ Also, this abundant nitrogen in urine represents a valuable resource for fertilizers that can boost global agriculture production if managed wisely. It is projected that around 300 million tons nitrogen in fertilizer would be required for global food agriculture by 2030,⁵ whereas nitrogen excreted from urine alone can make up around 30 million tons,^{6,7} which can potentially feed hundreds of millions of people in the world.⁸⁻¹⁰ For comparison, nitrogen available from urine accounts for ~20% of ammonia generated from the energy-extensive Haber–Bosch process,¹¹ which is also responsible for roughly 60 million tons of global anthropogenic CO₂ emissions per annum.^{11,12} Therefore, nitrogen recovery from urine is now recognized as a critical step in the water-food-energy nexus towards a more sustainable economy.¹³

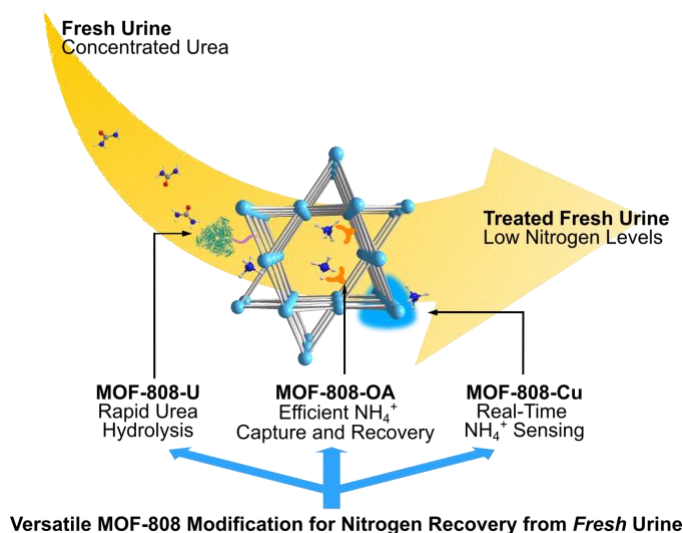
Nitrogen from urine can be captured either in the form of ammonia/ammonium in *stored* urine or urea in *fresh* urine. Urea is difficult to be separated from *fresh* urine because it is nonionic and yet has high water solubility. Current urea recovery processes mainly rely on volume reduction,^{14,15} membrane treatment,^{16,17} and precipitation,¹⁸ all of which require substantial external input of energy or chemicals. By contrast, ammonia/ammonium are easier targets for capture and recovery as ammonia is volatile, and ammonium can be readily separated based on electrostatics interactions. Common ammonia/ammonium recovery methods include ion exchange,¹⁹⁻²² gas stripping,²³⁻²⁶ electrochemical treatment,^{24,27-29} and precipitation.^{23,30-32} However, ammonia/ammonium recovery from stored urine heavily relies on the complete hydrolysis of urea which can take up to days depending on the specific environment.^{31,33,34} This further requires large areas for urine storage, efforts for urine

collection and transportation, and sophisticated urine stabilization prior to the nitrogen recovery treatment³⁵ – all leading to higher capital costs and maintenance expenses.^{7,36} Additionally, a substantial amount of ammonia-nitrogen is lost during the long-term urine storage,⁷ which significantly decreases the overall nitrogen recovery of the treatment process.

To tackle the challenges in current urine nitrogen recovery techniques, we report here an integrated decentralized treatment platform for nitrogen recovery from *fresh* urine that can circumvent the long-term spatial urine storage and minimize nitrogen lost during this process (Scheme 1). We expect that by accelerating urea's hydrolysis rate artificially in *fresh* urine and capturing the hydrolysis product *in situ*, we can achieve greater yield of nitrogen from *fresh* urine. Furthermore, on-site ammonium-nitrogen monitoring can provide real-time information on nitrogen levels in the treated effluent, reflecting the recovery efficiency during operation. No urine storage is required in this case; therefore the treatment process is more applicable for point-of-use wastewater treatment.

In order to fulfill the multiple tasks in the proposed *fresh* urine treatment, we (i) selected a highly water stable and porous zirconium metal-organic framework, MOF-808, (ii) leveraged the high modularity of this material, and (iii) designed and synthesized an array of functional MOF-808 specifically for the purpose of *fresh* urine nitrogen recovery. MOF-808 is a class of zirconium MOF with high thermal and water stability, porosity, and physicochemical properties tunability. It has been studied extensively in a diverse array of water treatment applications, including target molecule sensing, desalination, pollutant removal, and both catalytic oxidation, and reduction.^{37–42} As the first example of employing MOF-808 in toilet wastewater treatment, we first designed a MOF-urease composite, called **MOF-808-U**, to create an artificial urease-enriched environment to significantly accelerate urea hydrolysis to facilitate nitrogen removal from fresh urine. We further developed a series of dicarboxylate-functionalized MOF-based adsorbents (called **MOF-808-OA**) as efficient and regenerable adsorbents for ammonium ion capture, and we carried out Molecular Dynamics calculations to provide atomic level information on the pore engineering-ammonium capture relationships. Lastly, we designed a Cu(II)-incorporated MOF-808, designated as **MOF-808-Cu**, to provide continuously visual color response towards ammonium to serve as an online system-monitoring component. MOF-808-U, MOF-808-

OA, and MOF-808-Cu were then effectively integrated into a fresh urine treatment process, and we were able to achieve 75% nitrogen removal and 45% recovery efficiency in as short as 30 min. This treatment process serves as a promising alternative for urine treatment and has the potential for use as a sustainable, decentralized wastewater treatment coupled with extraction of an important fertilizer for onsite use.



Scheme 5.1 Newly developed nitrogen recovery from *fresh* urine facilitated with functionalized MOFs.

5.3 Results

Urea hydrolysis with MOF-808-U. Urea hydrolysis is ubiquitous in nature and is naturally catalyzed by urease generated by the microbes in a slow and uncontrollable manner.⁴³ As a result, the rate of ureolysis has been reported to be quite variable in different studies, indicating that it is highly dependent on the local environment. For example, Udert *et al.* reported that 960 g urea-N d⁻¹ could be hydrolyzed in NoMix pipes and 180 g urea-N d⁻¹ in collection tanks.⁴³ A study by Liu *et al.* indicated complete urea hydrolysis could take up to 2 to over 6.5 days.³³ A more recent study focusing on urine collection on a building-scale by Jagtap *et al.* demonstrated that complete urea hydrolysis could be achieved in 8 h.³⁴ This variable nature of urea hydrolysis inevitably results in unpredictable processing time and efficiency from batch to batch, creating uncertainty in a centralized facility.

Consequently, large-scale urine storage is necessary to be incorporated with onsite urine treatment for complete urea conversion prior to nitrogen recovery. This increases capital costs and makes it challenging for decentralized treatment systems (e.g., single family houses).

In order to significantly boost urea hydrolysis in fresh urine to compensate the natural processes, we developed an artificial urease-enriched environment with the assistance of MOF-808. Jackbean urease was immobilized onto the MOF-808 backbone via strong covalent bonds, providing a MOF-urease composite that can serve as a highly efficient, stable, and more sustainable catalyst for urine hydrolysis. Optimizing from the previously reported procedure and incorporating N-hydroxysuccinimide to increase the stability of the intermediate ester in aqueous solutions,^{44,45} we successfully grafted urease onto the MOF backbone by forming amide bonds between the amino residues on urease and the terminal carboxylate groups on MOF-808 (**Figure 5.1a**). This MOF-urease composite is designated as **MOF-808-U**, for which we determined the loading capacity to be 1.7 g urease/g MOF-808. Successful immobilization of urease was confirmed by FT-IR spectra, where both the amide I (1714 cm^{-1}) and amide II bands (1654 cm^{-1}) from free urease were observed in the spectrum of MOF-808-U (**Figure 5.S1**).⁴⁶ The crystalline structure of the MOF was well-maintained during the modification process as confirmed by powder X-ray diffraction (PXRD) measurements (**Figure 5.1b**), and the morphology of the crystallites remained unaltered as evidenced by SEM images (**Figure 5.S8 and 5.S9**), demonstrating that MOF-808 provides a robust backbone for materials engineering purposes.

Catalytic activity of the immobilized urease was assayed first, leading to Michaelis–Menten saturation curves plotted for both MOF-808-U and free urease in **Figure 5.1c**. MOF-808-U possessed a very similar Michaelis–Menten constant ($K_m(\text{MOF-808-U}) = 25.15\text{ mM}$) compared to that of free urease ($K_m(\text{free urease}) = 24.80\text{ mM}$), indicating that the affinity of MOF-808-U towards urea is almost comparable to that of the free enzyme. We observed a decrease of k_{cat} for MOF-808-U (**Table 5.S1**), as commonly observed for enzyme immobilization.^{47–50} Most importantly, stability of the immobilized urease was significantly enhanced in MOF-808-U (**Figure 1d**). While free urease almost completely denatured after being stored in an aqueous solution for one day, MOF-808-U still possessed 40% of its

original activity after one day, and maintained around 20% activity after six days. This unprecedented prolonged stability of MOF-808-U likely originates from the multipoint strong covalent attachment of urease onto the MOF backbone that maintains the intrinsic structural integrity of the enzyme.^{51,52} This suggests that MOF-808-U is more suitable to fit into daily consumables to provide reliable and controllable performance.

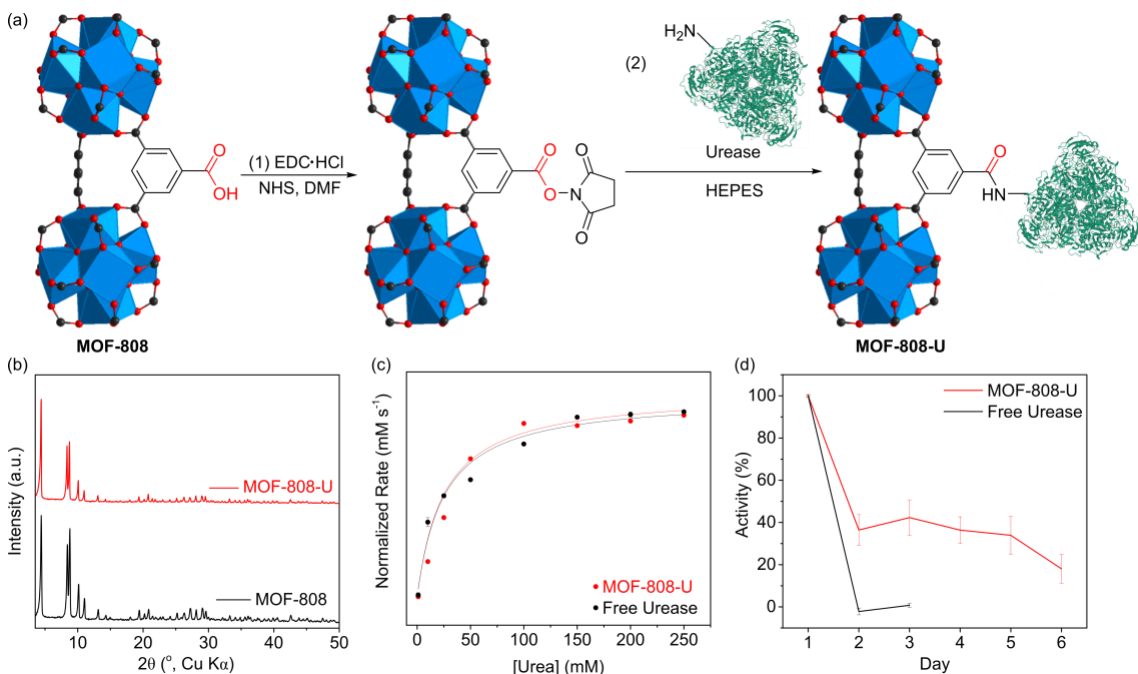


Figure 5.1 (a) Synthesis scheme for MOF-808-U. Urease structure from pdb 4H9M. (b) PXRD patterns of MOF-808-U and pristine MOF-808. Almost identical PXRD patterns indicates that the crystallinity of MOF structure was well-maintained during the incorporation of urease. (c) Michaelis–Menten kinetic measurement of MOF-808-U and free urease. MOF-808-U exhibited near-identical enzymatic activity as that of free urease. (d) Stability tests of MOF-808-U and free urease, where MOF-808-U demonstrated its stability (up to 6 days) compared to free urease.

Ammonium capture with MOF-808-OA. One major driving force for ammonium capture in common adsorbents is electrostatic interaction, exemplified by negatively charged functionalization of the sorbents.^{19,53} In order to introduce ammonium binding affinity to the

MOF-808 backbone, we selected a series of dicarboxylic acid compounds, namely oxalic acid (OA), malonic acid (MA), and succinic acid (SA), as anionic functional groups in this work. For each compound, one carboxylate stitches strongly to the Zr_6O_8 cluster via bidentate chelating,⁵⁴ whereas the other remains dangling inside the pore to serve as the ammonium adsorptive site (**Figure 5.2a**). Successful incorporation of MA and SA was confirmed and quantified with 1H NMR spectra of the digested samples (**Figure 5.S6 and 5.S7**), whereas the incorporated OA was determined via colorimetric assay of the digested MOF-808-OA.⁵⁵ FT-IR spectra further confirmed the successful introduction of the dicarboxylic acids. The absorbance corresponding to the carbonyl stretching from formate in pristine MOF-808 shifted from 1704 cm^{-1} to 1697 cm^{-1} , 1699 cm^{-1} , and 1703 cm^{-1} in MOF-808-OA, MOF-808-MA, and MOF-808-SA, respectively, which follows the trend in molecular compounds (**Figure 5.S2**).⁵⁶ At the same time, the MOF-808 backbone remained intact with its crystallinity confirmed by the almost identical PXRD pattern (**Figure 5.2b**) and morphology (**Figure 5.S10-12**) with pristine MOF-808. These results again corroborate MOF-808 as a robust and versatile material for varying functionalization.

With the materials in hand, we examined ammonium uptake performance of the four MOF-808-based adsorbents. The ammonium adsorption isotherms were fitted best with the Langmuir-Freundlich model for all materials (**Figure 5.2c**). While all adsorbents exhibited a decent level of ammonium capture, MOF-808-OA exhibited the highest ammonium capture capacity ($Q_e = 113\text{ mg g}^{-1}$ using the Langmuir-Freundlich model), followed by MOF-808-MA, MOF-808-SA, and pristine MOF-808. Time-course adsorption measurements were further carried out. Ammonium capture by all materials was kinetically efficient (**Figure 5.2d**). MOF-808-OA again outperformed the others, reaching equilibrium capacity within 1 min.

The favorable properties of MOF-808-OA indicated that functionalities on MOF-808 play a major role in their ammonium binding affinity. To better understand how the above pore engineering influenced the ammonium uptake behavior, we carried out molecular dynamics (MD) simulations on all four MOF materials (for details see Section 8 of the SI). After a 20 ns MD production run in the NVT ensemble for each system, in which the ammonium ions were added accordingly to the experimental concentrations, we observed a

strong interaction between the anionic carboxyl oxygen atoms of the different acids (OA, MA and SA) and the ammonium ions, which has been analyzed by the radial distribution function (RDF) (**Figure 5.2e**). From this plot we estimated an average distance of 0.285 nm between the ammonium ions and the carboxylic oxygens. Integrating the RDF leads to 1.24, 3.33 and 2.74 oxygen atoms per ammonium ion (**Figure 5.S18**). This result supports the formation of an ionic complex in which no water is involved, reflecting not only the different amount of acids present in the modified MOF-808, but also the decreasing pore size due to the increasing chain lengths of the MA and SA acids (**Table 5.S4**), which in turn allows ammonium ions to get closer to more oxygen atoms. In comparison, the pristine MOF-808 presented a much longer average distance of 0.445 nm between the ammonium and the hydrogen of the formate group, corresponding to having two hydrogen atoms close to the ammonium ions. This suggests that a layer of water is present between the ions, weakening the interaction.

To quantify the strength of these N^+-O^- interactions, we carried out two-phase thermodynamic (2PT) analysis to compute the adsorption free energy difference between the ions in water compared to the cases when they were adsorbed in the MOF. Our calculations indicate that MOF-808-OA presents the strongest adsorption free energy (-4537 kcal/mol), followed by MOF-808-MA (-4303 kcal/mol) and MOF-808-SA (-3109 kcal/mol). These results have the same trend as found from experimental adsorption data. As comparison, the pristine MOF-808 showed an adsorption free energy of only -2172 kcal/mol, confirming the added benefit of the incorporation of carboxylic acid in the MOF structure for ammonium adsorption. These MD calculations also supported the experimental finding that the best candidate is MOF-808-OA, as found experimentally, which we then used as the ammonium adsorbent for the remainder of our studies.

The regeneration of MOF-808-OA, an important property for sustainability in nitrogen recovery, was evaluated further. We used $NaNO_3$ solution to treat ammonium-saturated MOF-808-OA, during which sodium ions were exchanged with ammonium to regenerate MOF-808-OA carrying sodium ions. This provided ammonium nitrate in solution as the nitrogen recovery product. MOF-808-OA could be reused for at least 10 cycles while retaining the ammonium capture capacity. Moreover, quantification of ammonium before

and after adsorption and during recovery indicated that near complete recovery of ammonium was achieved (Figure 5.2g). These results thus demonstrated the potential of utilizing MOF-808-OA for sustainable nitrogen recovery in water treatment.

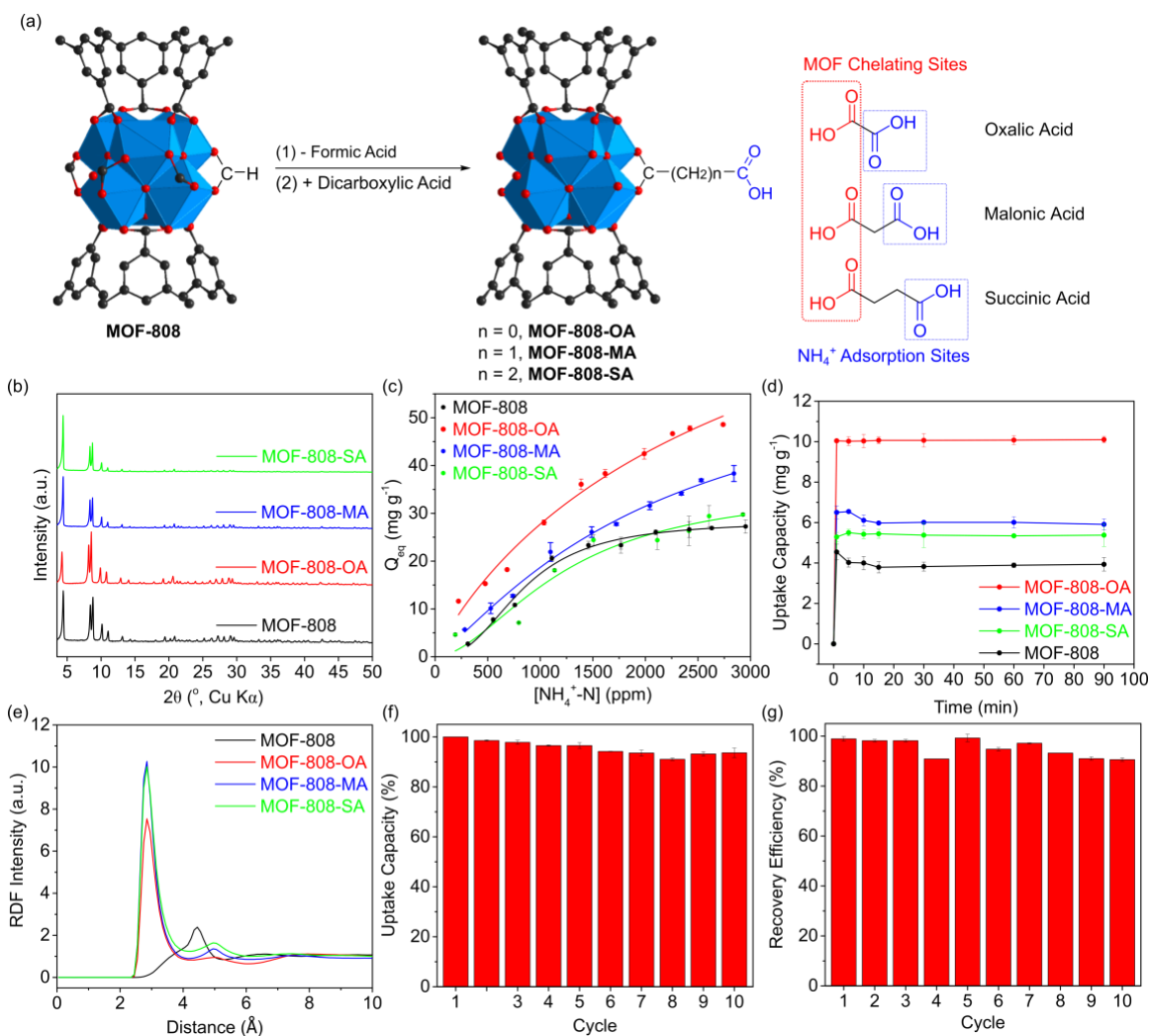


Figure 5.2 (a) Synthesis scheme of MOF-808-based ammonium adsorbents. (b) PXRD patterns, (c) ammonium uptake isotherms, and (d) ammonium capture kinetics experiments of MOF-808, MOF-808-OA, MOF-808-MA, and MOF-808-SA. While all four MOF materials shared identical structure, modification of interior pore environment has a direct and significant impact on their ammonium capture performances. (e) Cumulative RDF analysis for the nitrogen-oxygen distance for all the studied MOF systems. (f) Ammonium uptake capacity and (g) recovery efficiency of MOF-808-OA with 10 cycles of regeneration,

where sodium nitrate solution was used as the regeneration reagent and ammonium nitrate as the recovery product.

Real-time ammonium sensing with MOF-808-Cu. Online monitoring of nutrient levels in pre- and post-treated water is essential to water management processes to ensure the desired treatment. As for the ammonium ion, the commonly used Berthelot method requires several reaction steps and reagents (e.g., basic conditions, hypochlorite, and phenol) followed by a UV colorimetric determination of the concentration,^{57,58} which complicates decentralized point-of-use applications. The emergence of innovative nanomaterials has opened up new avenues for ammonium-based sensors.^{59,60} While most of current ammonium sensing systems afford nanomolar detection limits and a working range up to millimolar, they are not suitable for the direct use in toilet wastewater treatment because of the ultrahigh ammonium levels in urine. Therefore, a sensitive, accurate, and feasible point-of-use ammonium sensor with high detection limit is required for use in onsite toilet wastewater treatment systems. Towards this end, we developed another MOF-808-based functionalized material to serve as the online water quality indicator.

Inspired by the well-known Cu(II)-ammonia complex that possesses a distinguishing dark blue color, we selected Cu(II) to be incorporated onto the MOF-808 backbone for colorimetric sensing of ammonium. MOF-808-Cu was easily synthesized by impregnating MOF-808 with a CuSO₄ methanolic solution. Strong absorbance within the range of 1200-900 cm⁻¹ in the FT-IR spectrum of MOF-808-Cu is assigned to the vibration of Zr-O-Cu bonds as well as the coordinated sulfate on the Cu (**Figure 5.S3**).⁶¹⁻⁶³ Loading of Cu was quantified as 4.75% w/w by ICP-MS and the Zr-to-Cu atomic ratio was determined to be 4.72:1. The highly crystalline structure of the pristine MOF-808 was again well-maintained upon incorporation of Cu, as well as after binding of ammonia during sensing (**Figure 5.3a**). SEM-EDS mapping further indicated that Cu was homogeneously distributed throughout the MOF backbone (**Figure 5.3b and 5.S13**). This further modification of MOF-808 indicates that MOF-808 is a robust candidate for multivariate functionalizations for use in environmental engineering applications.

We evaluated MOF-808-Cu's response to ammonium ion. Upon exposure to ammonium, the solids immediately changed color from pale green to blue. This colorimetric response was observed in the UV-Vis diffuse reflectance spectra (Figure 5.S18), which showed a significant blue shift of the UV-Vis absorbance maximum from 757 nm to 667 nm. Furthermore, the obvious color change could be readily quantified using a digital camera (e.g., a smartphone camera) (insert of Figure 5.3c). By decomposing the image into red (R), green (G) or blue (B) channels from the image of Figure 5.3c, a linear curve within the range of 200-4000 ppm could be constructed from the data points obtained from the R and G channels, where R channels afforded the highest accuracy and linearity (Figure 5.3c and 5.S19-21). Notably, MOF-808-Cu can also be reused for at least five cycles with mild heat treatment to regenerate Cu (II) coordination sites while readings of the R channel remained mostly constant (Figure 5.3d). As such, MOF-808-Cu can be used in fresh urine treatment systems as a color sensor to realize real-time water quality monitoring.

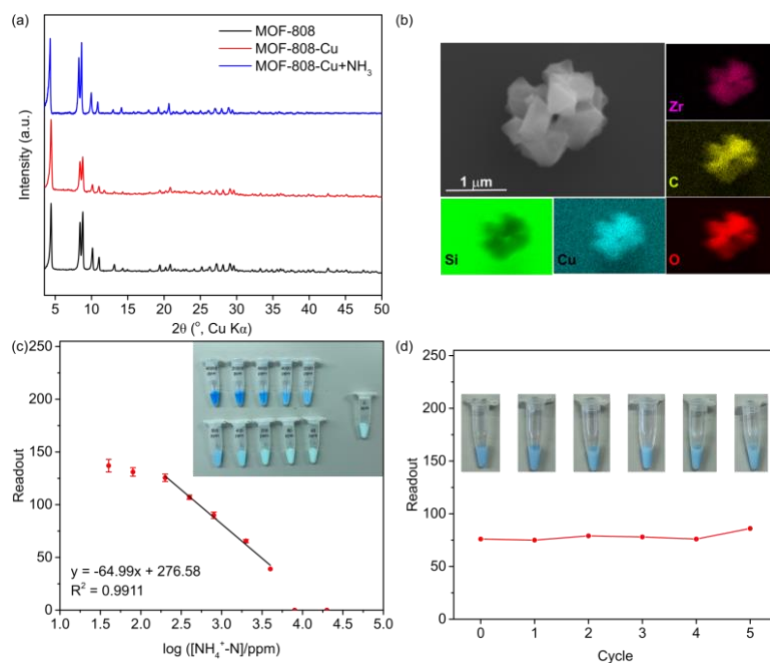


Figure 5.3 (a) PXRD patterns of pristine MOF-808, MOF-808-Cu, and MOF-808-Cu exposed with [NH₄⁺-N] of 2000 ppm. (b) SEM-EDS images of MOF-808-Cu. (c) Linear relationship between the readout of the R channel of an image of MOF-808-Cu suspension and [NH₄⁺-N]. Inset: an image of MOF-808-Cu suspended in a series of solutions with

different $[\text{NH}_4^+\text{-N}]$ levels. Concentrations from top left to bottom right are: 40000, 20000, 8000, 4000, 2000, 800, 400, 200, 80, and 40 ppm. Single vial on the right was MOF-808-Cu suspended in water. (d) Readout of the R channel of MOF-808-Cu after 5 cycles of regeneration. Inset: an image of regenerated MOF-808-Cu suspended in a solution of 2000 ppm $[\text{NH}_4^+\text{-N}]$.

Nitrogen recovery from *fresh* urine. Integrating all three functionalized MOF materials, we developed a prototype system specifically for nitrogen recovery from fresh urine (**Figure 5.4a**). The working prototype utilizes two major steps that can work in parallel:

- (1) 30 min of nitrogen conversion and
- (2) 30 min of nitrogen removal and recovery.

First, fresh urine was incubated with MOF-808-U for 30 min to hydrolyze the majority, if not all, of the urea. Hydrolyzed effluent was then mixed with MOF-808-OA for 15 min to ensure that the adsorption of ammonium reached equilibrium given the fast rate of the adsorption of ammonium. Saturated MOF-808-OA was regenerated with NaNO_3 with a 15 min mixing, yielding ammonium exchanged with sodium in the regeneration solution and the adsorptive sites free and ready for the next runs. During nitrogen capture and recovery, MOF-808-U could accommodate more incoming fresh urine for the next cycle to ensure a continuous operation of the treatment train. Therefore, theoretically, the current setup allows for the treatment of fresh urine every 30 min when functioning consecutively.

As a proof of concept, we performed five cycles of treatment with synthetic fresh urine (prepared following a previously reported recipe).⁶⁴ Given the high concentration of nitrogen in the initial influent ($[\text{Urea-N}] = 7000$ ppm), a high loaded level of MOF-808-U and MOF-808-OA (200 g/L) was required for sufficient nitrogen removal. The concentrations of urea and ammonium were measured after each treatment to determine the overall nitrogen removal and recovery efficiency. As shown in **Figure 5.4b**, the first three cycles of the treatment resulted in ~80% total nitrogen removal, which meets the ISO30500 standard for 70% total nitrogen reduction.⁶⁵ A slight drop of total nitrogen reduction efficiency was observed in the fourth and the fifth cycle, but the majority of nitrogen (67% and 62%) could still be removed with a 30 min treatment. Total nitrogen recovery efficiency, however,

followed the opposite trend – relatively low for the first two cycles and increased to 48%-64% for the later cycles. This phenomenon was due to near-complete urea hydrolysis during the first three cycles (Figure 5.4c), which resulted in high ammonium ion formation coupled with evaporative losses of ammonia resulting in a reduced adsorption of ammonium.⁶⁶ During the subsequent two cycles, the loss of ammonia was reduced as the hydrolysis product was readily captured by MOF-808-OA, resulting in a total recovery efficiency reaching to the total removal efficiency. Overall, the current treatment process yielded an average of 75% total nitrogen reduction and an average of 45% nitrogen recovery in five cycles. Furthermore, MOF-808-Cu, the *in situ* chromophoric probe gave the anticipated color changes that could be visually observed with (Figure 5.4c). While the blue color (top) indicated significant ammonium was generated by MOF-808-U, the change of color to green (bottom) demonstrated substantial removal of ammonium by MOF-808-OA. Such color changes could be observed for all five cycles, indicating that urea hydrolysis, ammonium capture, as well as regeneration of MOF-808-OA were carried out successfully for each cycle. Based on the above results, it is clear that all three MOF materials performed as predicted and have the potential for sustainable nitrogen capture and subsequent elution from fresh urine.

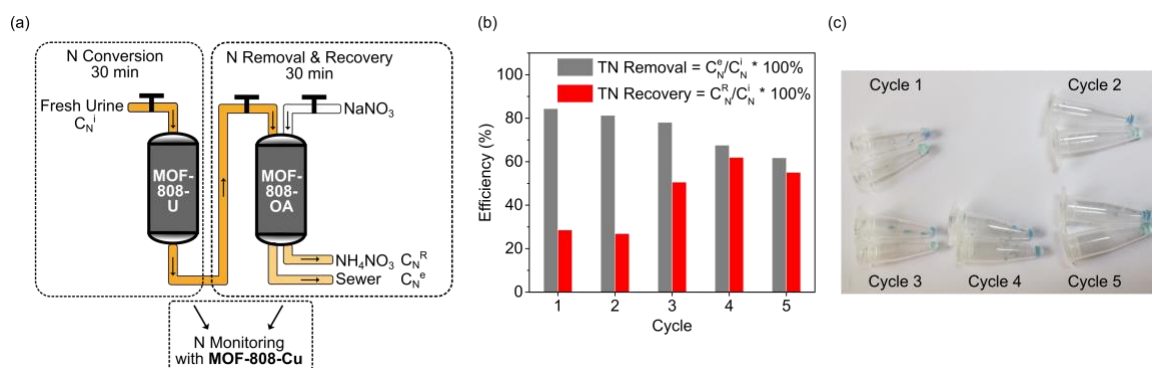


Figure 5.4 (a) Schematic diagram of fresh urine treatment integrating the functionalized MOF materials designed in this work. (b) Total nitrogen removal and recovery efficiency of five cycles of entire treatment. (c) MOF-808-Cu suspended in the treated solution after MOF-808-U (top) and MOF-808-OA (bottom) in each of the five cycles, demonstrating efficiency of each treatment steps (urea conversion, ammonium capture, and regeneration of ammonium adsorbent).

5.4 Discussion

In summary, we developed an integrated system that, to our knowledge, **for the first time achieved simultaneous nitrogen removal and recovery from *fresh* urine**. Efficient nitrogen reduction was achieved in the effluent, which significantly reduced the burden for downstream treatment (e.g., biological and electrochemical treatment in onsite systems) to remove nutrients and minimize the risk of further eutrophication. Efficient nitrogen recovery further provides valuable byproducts for use as potential fertilizers for agricultural applications. Materials developed in this work can be readily synthesized at large scale and are highly durable for regeneration and reuse, therefore providing a promising basis for future implementation and commercialization. Taken together, the *fresh* urine treatment system described herein has the potential to transform decentralized urine treatment approaches and to contribute to the water-food-energy nexus concerns in rural and developing communities.

The MOFs used in this study showcase their ultrahigh versatility as modular materials to be functionalized towards specific environmental applications. This work renders itself as the first example of employing MOFs for complicated toilet wastewater treatment and fulfilling multi-tasks. We incorporated three distinctly different functions, including the capacity for the **rapid but stable enzymatic hydrolysis of urine**, the **efficient and reusable sorptive capture of ammonium**, and the *in situ* **sensing of ammonium with a MOF platform**. Together with other reports of MOFs used for removal or sensing of target pollutants in water, we anticipate that MOFs will be used as robust and versatile substrates that will have use for improving water quality and the sustainable recycling of nitrogen and phosphorus nutrients.

5.5 References

- (1) Jimenez, J.; Bott, C.; Love, N.; Bratby, J. Source Separation of Urine as an Alternative Solution to Nutrient Management in Biological Nutrient Removal Treatment Plants. *Water Environ. Res.* **2015**, *87* (12), 2120–2129.
- (2) Dodds, W. K.; Bouska, W. W.; Eitzmann, J. L.; Pilger, T. J.; Pitts, K. L.; Riley, A. J.; Schloesser, J. T.; Thornbrugh, D. J. Eutrophication of U.S. Freshwaters: Analysis of Potential Economic Damages. *Environ. Sci. Technol.* **2009**, *43* (1), 12–19.

- (3) Kapsalis, V. C.; Kalavrouziotis, I. K. Eutrophication—A Worldwide Water Quality Issue. In *Chemical Lake Restoration: Technologies, Innovations and Economic Perspectives*; Zamparas, M. G., Kyriakopoulos, G. L., Eds.; Springer International Publishing: Cham, 2021; pp 1–21.
- (4) U.S. Environmental Protection Agency. A Compilation of Cost Data Associated with the Impacts and Control of Nutrient Pollution. **2015**.
- (5) Liu, J.; Ma, K.; Ciais, P.; Polasky, S. Reducing Human Nitrogen Use for Food Production. *Sci. Rep.* **2016**, *6* (1), 30104.
- (6) Rose, C.; Parker, A.; Jefferson, B.; Cartmell, E. The Characterization of Feces and Urine: A Review of the Literature to Inform Advanced Treatment Technology. *Crit. Rev. Environ. Sci. Technol.* **2015**, *45* (17), 1827–1879.
- (7) Larsen, T. A.; Riechmann, M. E.; Udert, K. M. State of the Art of Urine Treatment Technologies: A Critical Review. *Water Res. X* **2021**, 100114.
- (8) *World Population Prospects - Population Division - United Nations*. <https://population.un.org/wpp/> (accessed 2022-07-06).
- (9) Whalen, J. M.; Matlin, S. A.; Holme, T. A.; Stewart, J. J.; Mahaffy, P. G. Transforming the Science of Transformation toward Sustainability: The Case of Ammonia and Reactive Nitrogen. **2022**.
- (10) Erisman, J. W.; Sutton, M. A.; Galloway, J.; Klimont, Z.; Winiwarter, W. How a Century of Ammonia Synthesis Changed the World. *Nat. Geosci.* **2008**, *1* (10), 636–639.
- (11) Smith, C.; Hill, A. K.; Torrente-Murciano, L. Current and Future Role of Haber–Bosch Ammonia in a Carbon-Free Energy Landscape. *Energy Environ. Sci.* **2020**, *13* (2), 331–344.
- (12) Nørskov, J.; Chen, J.; Miranda, R.; Fitzsimmons, T.; Stack, R. *Sustainable Ammonia Synthesis – Exploring the Scientific Challenges Associated with Discovering Alternative, Sustainable Processes for Ammonia Production*; US DOE Office of Science, 2016.
- (13) Lin, S.; Hatzell, M.; Liu, R.; Wells, G.; Xie, X. Mining Resources from Water. *Resour. Conserv. Recycl.* **2021**, *175*, 105853.
- (14) Senecal, J.; Vinnerås, B. Urea Stabilisation and Concentration for Urine-Diverting Dry Toilets: Urine Dehydration in Ash. *Sci. Total Environ.* **2017**, *586*, 650–657.
- (15) Marepula, H.; Courtney, C. E.; Randall, D. G. Urea Recovery from Stabilized Urine Using a Novel Ethanol Evaporation and Recrystallization Process. *Chem. Eng. J. Adv.* **2021**, *8*, 100174.
- (16) Ray, H.; Perreault, F.; Boyer, T. H. Urea Recovery from Fresh Human Urine by Forward Osmosis and Membrane Distillation (FO–MD). *Environ. Sci. Water Res. Technol.* **2019**, *5* (11), 1993–2003.
- (17) Xu, L.; Ding, R.; Mao, Y.; Peng, S.; Li, Z.; Zong, Y.; Wu, D. Selective Recovery of Phosphorus and Urea from Fresh Human Urine Using a Liquid Membrane Chamber Integrated Flow-Electrode Electrochemical System. *Water Res.* **2021**, *202*, 117423.
- (18) Behrendt, J.; Arevalo, E.; Gulyas, H.; Niederste-Hollenberg, J.; Niemlec, A.; Zhou, J.; Otterpohl, R. Production of Value Added Products from Separately Collected Urine. *Water Sci. Technol. J. Int. Assoc. Water Pollut. Res.* **2002**, *46* (6–7), 341–346.

- (19) Huang, J.; Kankanamge, N. R.; Chow, C.; Welsh, D. T.; Li, T.; Teasdale, P. R. Removing Ammonium from Water and Wastewater Using Cost-Effective Adsorbents: A Review. *J. Environ. Sci.* **2018**, *63*, 174–197.
- (20) Clark, B.; Tarpeh, W. A. Selective Recovery of Ammonia Nitrogen from Wastewaters with Transition Metal-Loaded Polymeric Cation Exchange Adsorbents. *Chem. – Eur. J.* **2020**, *26* (44), 10099–10112.
- (21) Tarpeh, W. A.; Udert, K. M.; Nelson, K. L. Comparing Ion Exchange Adsorbents for Nitrogen Recovery from Source-Separated Urine. *Environ. Sci. Technol.* **2017**, *51* (4), 2373–2381.
- (22) Manto, M. J.; Xie, P.; Keller, M. A.; Liano, W. E.; Pu, T.; Wang, C. Recovery of Ammonium from Aqueous Solutions Using ZSM-5. *Chemosphere* **2018**, *198*, 501–509.
- (23) Xu, K.; Zhang, C.; Li, J.; Cheng, X.; Wang, C. Removal and Recovery of N, P and K from Urine via Ammonia Stripping and Precipitations of Struvite and Struvite-K. *Water Sci. Technol.* **2016**, *75* (1), 155–164.
- (24) Christiaens, M. E. R.; Gildemyn, S.; Matassa, S.; Ysebaert, T.; De Vrieze, J.; Rabaey, K. Electrochemical Ammonia Recovery from Source-Separated Urine for Microbial Protein Production. *Environ. Sci. Technol.* **2017**, *51* (22), 13143–13150.
- (25) Jagtap, N.; Boyer, T. H. Integrated, Multi-Process Approach to Total Nutrient Recovery from Stored Urine. *Environ. Sci. Water Res. Technol.* **2018**, *4* (10), 1639–1650.
- (26) Christiaens, M. E. R.; Udert, K. M.; Arends, J. B. A.; Huysman, S.; Vanhaecke, L.; McAdam, E.; Rabaey, K. Membrane Stripping Enables Effective Electrochemical Ammonia Recovery from Urine While Retaining Microorganisms and Micropollutants. *Water Res.* **2019**, *150*, 349–357.
- (27) Kuntke, P.; Śmiech, K. M.; Bruning, H.; Zeeman, G.; Saakes, M.; Sleutels, T. H. J. A.; Hamelers, H. V. M.; Buisman, C. J. N. Ammonium Recovery and Energy Production from Urine by a Microbial Fuel Cell. *Water Res.* **2012**, *46* (8), 2627–2636.
- (28) Kuntke, P.; Rodrigues, M.; Sleutels, T.; Saakes, M.; Hamelers, H. V. M.; Buisman, C. J. N. Energy-Efficient Ammonia Recovery in an Up-Scaled Hydrogen Gas Recycling Electrochemical System. *ACS Sustain. Chem. Eng.* **2018**, *6* (6), 7638–7644.
- (29) Tarpeh, W. A.; Barazesh, J. M.; Cath, T. Y.; Nelson, K. L. Electrochemical Stripping to Recover Nitrogen from Source-Separated Urine. *Environ. Sci. Technol.* **2018**, *52* (3), 1453–1460.
- (30) Wei, S. P.; van Rossum, F.; van de Pol, G. J.; Winkler, M.-K. H. Recovery of Phosphorus and Nitrogen from Human Urine by Struvite Precipitation, Air Stripping and Acid Scrubbing: A Pilot Study. *Chemosphere* **2018**, *212*, 1030–1037.
- (31) Kabdaşlı, I.; Tünay, O.; İşlek, Ç.; Erdinç, E.; Hüskalar, S.; Tatlı, M. B. Nitrogen Recovery by Urea Hydrolysis and Struvite Precipitation from Anthropogenic Urine. *Water Sci. Technol.* **2006**, *53* (12), 305–312.
- (32) Tan, X.; Yu, R.; Yang, G.; Wei, F.; Long, L.; Shen, F.; Wu, J.; Zhang, Y. Phosphate Recovery and Simultaneous Nitrogen Removal from Urine by Electrochemically Induced Struvite Precipitation. *Environ. Sci. Pollut. Res.* **2021**, *28* (5), 5625–5636.
- (33) Liu, Z.; Zhao, Q.; Wang, K.; Lee, D.; Qiu, W.; Wang, J. Urea Hydrolysis and Recovery of Nitrogen and Phosphorous as MAP from Stale Human Urine. *J. Environ. Sci.* **2008**, *20* (8), 1018–1024.

- (34) Jagtap, N. S.; Boyer, T. H. Urine Collection in a Multi-Story Building and Opportunities for Onsite Recovery of Nutrients and Non-Potable Water. *J. Environ. Chem. Eng.* **2020**, *8* (4), 103964.
- (35) Yang, W.; Li, J.; Yang, X. Features and Applications of Urine Stabilization Methods: A Review. *Front. Sustain.* **2021**, *2*.
- (36) Maurer, M.; Pronk, W.; Larsen, T. A. Treatment Processes for Source-Separated Urine. *Water Res.* **2006**, *40* (17), 3151–3166.
- (37) Furukawa, H.; Gándara, F.; Zhang, Y.-B.; Jiang, J.; Queen, W. L.; Hudson, M. R.; Yaghi, O. M. Water Adsorption in Porous Metal–Organic Frameworks and Related Materials. *J. Am. Chem. Soc.* **2014**, *136* (11), 4369–4381.
- (38) Li, Z.-Q.; Yang, J.-C.; Sui, K.-W.; Yin, N. Facile Synthesis of Metal-Organic Framework MOF-808 for Arsenic Removal. *Mater. Lett.* **2015**, *160*, 412–414.
- (39) Zheng, H.-Q.; Liu, C.-Y.; Zeng, X.-Y.; Chen, J.; Lü, J.; Lin, R.-G.; Cao, R.; Lin, Z.-J.; Su, J.-W. MOF-808: A Metal–Organic Framework with Intrinsic Peroxidase-Like Catalytic Activity at Neutral PH for Colorimetric Biosensing. *Inorg. Chem.* **2018**, *57* (15), 9096–9104.
- (40) Chen, X.; Chen, D.; Li, N.; Xu, Q.; Li, H.; He, J.; Lu, J. Modified-MOF-808-Loaded Polyacrylonitrile Membrane for Highly Efficient, Simultaneous Emulsion Separation and Heavy Metal Ion Removal. *ACS Appl. Mater. Interfaces* **2020**, *12* (35), 39227–39235.
- (41) Ji, C.; Yu, H.; Lu, J.; Ren, Y.; Lv, L.; Zhang, W. High-Efficiency and Sustainable Desalination Using Thermo-Regenerable MOF-808-EDTA: Temperature-Regulated Proton Transfer. *ACS Appl. Mater. Interfaces* **2021**, *13* (20), 23833–23842.
- (42) Plonka, A. M.; Grissom, T. G.; Musaev, D. G.; Balboa, A.; Gordon, W. O.; Collins-Wildman, D. L.; Ghose, S. K.; Tian, Y.; Ebrahim, A. M.; Mitchell, M. B.; Hill, C. L.; Morris, J. R.; Frenkel, A. I. Effect of Carbon Dioxide on the Degradation of Chemical Warfare Agent Simulant in the Presence of Zr Metal Organic Framework MOF-808. *Chem. Mater.* **2019**, *31* (23), 9904–9914.
- (43) Udert, K. M.; Larsen, T. A.; Biebow, M.; Gujer, W. Urea Hydrolysis and Precipitation Dynamics in a Urine-Collecting System. *Water Res.* **2003**, *37* (11), 2571–2582.
- (44) Guo, L.; Jia, S.; Diercks, C. S.; Yang, X.; Alshimri, S. A.; Yaghi, O. M. Amidation, Esterification, and Thioesterification of a Carboxyl-Functionalized Covalent Organic Framework. *Angew. Chem. Int. Ed.* **2020**, *59* (5), 2023–2027.
- (45) Mattson, G.; Conklin, E.; Desai, S.; Nielander, G.; Savage, M. D.; Morgensen, S. A Practical Approach to Crosslinking. *Mol. Biol. Rep.* **1993**, *17* (3), 167–183.
- (46) Liang, W.; Xu, H.; Carraro, F.; Maddigan, N. K.; Li, Q.; Bell, S. G.; Huang, D. M.; Tarzia, A.; Solomon, M. B.; Amenitsch, H.; Vaccari, L.; Sumbly, C. J.; Falcaro, P.; Doonan, C. J. Enhanced Activity of Enzymes Encapsulated in Hydrophilic Metal–Organic Frameworks. *J. Am. Chem. Soc.* **2019**, *141* (6), 2348–2355.
- (47) Rodrigues, R. C.; Ortiz, C.; Berenguer-Murcia, Á.; Torres, R.; Fernández-Lafuente, R. Modifying Enzyme Activity and Selectivity by Immobilization. *Chem. Soc. Rev.* **2013**, *42* (15), 6290–6307.
- (48) Liese, A.; Hilterhaus, L. Evaluation of Immobilized Enzymes for Industrial Applications. *Chem. Soc. Rev.* **2013**, *42* (15), 6236–6249.

- (49) Bolivar, J. M.; Nidetzky, B. On the Relationship between Structure and Catalytic Effectiveness in Solid Surface-Immobilized Enzymes: Advances in Methodology and the Quest for a Single-Molecule Perspective. *Biochim. Biophys. Acta BBA - Proteins Proteomics* **2020**, *1868* (2), 140333.
- (50) Liang, W.; Wied, P.; Carraro, F.; Sumbly, C. J.; Nidetzky, B.; Tsung, C.-K.; Falcaro, P.; Doonan, C. J. Metal–Organic Framework-Based Enzyme Biocomposites. *Chem. Rev.* **2021**, *121* (3), 1077–1129.
- (51) *Potential of Different Enzyme Immobilization Strategies to Improve Enzyme Performance - Garcia-Galan - 2011 - Advanced Synthesis & Catalysis - Wiley Online Library*. <https://onlinelibrary.wiley.com/doi/full/10.1002/adsc.201100534> (accessed 2022-07-09).
- (52) Mateo, C.; Palomo, J. M.; Fernandez-Lorente, G.; Guisan, J. M.; Fernandez-Lafuente, R. Improvement of Enzyme Activity, Stability and Selectivity via Immobilization Techniques. *Enzyme Microb. Technol.* **2007**, *40* (6), 1451–1463.
- (53) Han, B.; Butterly, C.; Zhang, W.; He, J.; Chen, D. Adsorbent Materials for Ammonium and Ammonia Removal: A Review. *J. Clean. Prod.* **2021**, *283*, 124611.
- (54) Lyu, H.; Chen, O. I.-F.; Hanikel, N.; Hossain, M. I.; Flaig, R. W.; Pei, X.; Amin, A.; Doherty, M. D.; Impastato, R. K.; Glover, T. G.; Moore, D. R.; Yaghi, O. M. Carbon Dioxide Capture Chemistry of Amino Acid Functionalized Metal–Organic Frameworks in Humid Flue Gas. *J. Am. Chem. Soc.* **2022**, *144* (5), 2387–2396.
- (55) Bergerman, J.; Elliot, J. S. Method for Direct Colorimetric Determination of Oxalic Acid. *Anal. Chem.* **1955**, *27* (6), 1014–1015.
- (56) Craver, C. D. *The Coblentz Society Desk Book of Infrared Spectra*; National Standard Reference Data System, 1977. <https://apps.dtic.mil/sti/citations/ADD095421> (accessed 2022-04-01).
- (57) Weatherburn, M. W. Phenol-Hypochlorite Reaction for Determination of Ammonia. *Anal. Chem.* **1967**, *39* (8), 971–974.
- (58) US EPA, O. *EPA Method 350.1: Determination of Ammonia Nitrogen by Semi-Automated Colorimetry*. <https://www.epa.gov/esam/epa-method-3501-determination-ammonia-nitrogen-semi-automated-colorimetry> (accessed 2022-07-12).
- (59) Mahmud, M. A. P.; Ejeian, F.; Azadi, S.; Myers, M.; Pejčić, B.; Abbassi, R.; Razmjou, A.; Asadnia, M. Recent Progress in Sensing Nitrate, Nitrite, Phosphate, and Ammonium in Aquatic Environment. *Chemosphere* **2020**, *259*, 127492.
- (60) Zhu, Y.; Chen, J.; Yuan, D.; Yang, Z.; Shi, X.; Li, H.; Jin, H.; Ran, L. Development of Analytical Methods for Ammonium Determination in Seawater over the Last Two Decades. *TrAC Trends Anal. Chem.* **2019**, *119*, 115627.
- (61) Otake, K.; Cui, Y.; Buru, C. T.; Li, Z.; Hupp, J. T.; Farha, O. K. Single-Atom-Based Vanadium Oxide Catalysts Supported on Metal–Organic Frameworks: Selective Alcohol Oxidation and Structure–Activity Relationship. *J. Am. Chem. Soc.* **2018**, *140* (28), 8652–8656.
- (62) Zhang, J.; Peh, S. B.; Wang, J.; Du, Y.; Xi, S.; Dong, J.; Karmakar, A.; Ying, Y.; Wang, Y.; Zhao, D. Hybrid MOF-808-Tb Nanospheres for Highly Sensitive and Selective Detection of Acetone Vapor and Fe³⁺ in Aqueous Solution. *Chem. Commun.* **2019**, *55* (32), 4727–4730.

- (63) Jiang, J.; Gándara, F.; Zhang, Y.-B.; Na, K.; Yaghi, O. M.; Klemperer, W. G. Superacidity in Sulfated Metal–Organic Framework-808. *J. Am. Chem. Soc.* **2014**, *136* (37), 12844–12847.
- (64) Zhang, R.; Sun, P.; Boyer, T. H.; Zhao, L.; Huang, C.-H. Degradation of Pharmaceuticals and Metabolite in Synthetic Human Urine by UV, UV/H₂O₂, and UV/PDS. *Environ. Sci. Technol.* **2015**, *49* (5), 3056–3066.
- (65) 14:00-17:00. *ISO* *30500:2018*. *ISO*. <https://www.iso.org/cms/render/live/en/sites/isoorg/contents/data/standard/07/25/72523.html> (accessed 2022-05-31).
- (66) Siegrist, H.; Laureni, M.; Udert, K. M. Transfer into the Gas Phase: Ammonia Stripping. *Source Sep. Decentralization Wastewater Manag.* **2013**, 337–350.

5.6 Supporting Information

5.S1 General Information

Chemical reagents were purchased from Sigma-Aldrich, Fisher Scientific, and TCI America. Unless otherwise noted, all commercial reagents were used without further purification.

Powder X-ray diffraction data for unit cell determination were collected using a Panalytical X'Pert Pro and a Rigaku SmartLab. FT-IR spectra were obtained from a Nicolet™ iS50 FTIR Spectrometer. Digested MOF samples were prepared by dissolving 5 mg powder in 20 μ L of HF solution and 480 μ L of (CD₃)₂SO, followed by 5 min of sonication (and heating, if needed) to ensure all the solids were fully dissolved. Final clear solutions were used for ¹H NMR measurement. Solution ¹H NMR spectra were acquired on a Bruker DRX500 NMR spectrometer. Samples for SEM study were prepared by dropcasting the MOF-methanol suspension onto a silicon wafer. SEM/EDS analysis was carried out on a ZEISS 1550VP Field Emission SEM - Oxford EDS - HKL EBSD system. During the SEM measurement, the accelerating voltage was 5 kV and the working distance was kept at 6 mm. For the SEM/EDS measurement of MOF-808-Cu, the accelerating voltage was 15 kV and the working distance was kept at 6 mm. UV–vis diffuse reflectance measurement was carried out on Cary 5000.

Concentration of ammonium was determined by the colorimetric assay adapted from the Berthelot method.^{1,2} 50 μ L of sample was added to a mixture (pH 11.0) of 6.95 mL of Milli-Q water, 0.5 mL of phenol (3%) solution, and 2 mL of Na₂HPO₄ solution, and 0.25 mL of

nitroprusside solution (0.50 g/L). After complete mixing, 250 μ L of NaClO (2.5%) solution was added, and the final solution was put in a 80°C water bath for 10 min, followed by cooling with water to room temperature. Full spectrum was collected with a NanoDrop 2000 spectrometer and absorbance at 628 nm was used to quantify the amount of ammonium in solutions.

Concentration of urea was determined by the colorimetric assay adapted from a previous report.³ Sample solution (1 mL) was first mixed with a potassium phosphate buffer (50 mM, pH 7.2, 1 mL), and p-dimethylaminobenzaldehyde solution (0.1 M in 10:1 ethanol and concentrated HCl (v/v), 0.5 mL) was then added. Mixture was mixed at room temperature for 30 min and UV-Vis spectra was taken with a NanoDrop 2000 spectrometer. Absorbance at 435 nm was recorded to determine urea concentrations.

5.S2 Synthesis Procedures

MOF-808: Microcrystalline MOF-808 was synthesized and activated following the previous procedure.⁴ Organic component of MOF-808 was quantified with ¹H NMR spectrum of the digested sample and the chemical formula of synthesized MOF-808 was determined as $Zr_6O_7.2(OH)_{0.8}(C_9H_3O_6)_2(HCOO)_{2.8}$.

MOF-808-U: Urease was covalently immobilized onto MOF-808 backbone *via* the carbodiimide coupling reaction and the condition was optimized from the reported procedure.⁵ MOF-808 (10 mg) was immersed in an anhydrous DMF solution (1 mL) containing EDC·HCl (9.6 mg), DMAP (1.5 mg), and NHS (5.8 mg). The suspension was completely mixed at 37°C for 30 min, and the solids were separated and washed with DMF and H₂O. The amine-active-NHS ester intermediate was then immersed in urease solution (1 mL, 20000 ppm in 50 mM HEPES solution, pH 7.0), and the mixture was allowed to rotate at a revolver at 10 rpm at room temperature overnight for complete coupling. Solids were then separated and washed with 50 mM HEPES solution. Supernatant in the second step of coupling was collected and added into cold acetone (4 times of the volume), fully mixed, and stored in a -20°C freezer overnight. On the next day, the precipitated protein was centrifuged, separated, and dried under vacuum, and quantified with Pierce BCA protein colorimetric assay. The immobilization yield of urease onto MOF-808 was determined as 1.7g/g.

MOF-808-no FA: MOF-808-no FA was synthesized as an intermediate for incorporation of the dicarboxylate. Activated MOF-808 was suspended in a HCl solution and heated at 80°C for 2 days. Over a period of 24 hours, MOF powders were separated and the supernatant was decanted and replaced with fresh HCl solution. The solids were washed with water and were carried onto the following post-synthetic modification.

MOF-808-OA: MOF-808-no FA was added into a sodium oxalate (OA) aqueous solution and stirred at room temperature for 2 days. Over a period of 24 hours, MOF powders were separated and the supernatant was decanted and replaced with fresh sodium oxalate solution. The solids were washed with water and anhydrous acetone and dried under vacuum. Successful incorporation of oxalate was confirmed and quantified by a reported colorimetric assay procedure,⁶ and chemical formula was determined as $Zr_6O_7(OH)(C_9H_3O_6)_2(O_2CCO_2Na)_3$.

MOF-808-MA: MOF-808-no FA was added into a malonic acid (MA) aqueous solution for 2 days. Over a period of 24 hours, MOF powders were separated and the supernatant was decanted and replaced with fresh malonic acid solution. The solids were washed with water and anhydrous acetone and dried under vacuum. Successful incorporation of malonic acid was confirmed and quantified with the ¹H NMR spectrum of the digested sample, and chemical formula was determined as $Zr_6O_{4.2}(OH)_{3.8}(C_9H_3O_6)_2(MA)_{5.8}$.

MOF-808-SA: MOF-808-no FA was added into a succinic acid (SA) aqueous solution for 2 days. Over a period of 24 hours, MOF powders were separated and the supernatant was decanted and replaced with fresh succinic acid solution. The solids were washed with water and anhydrous acetone and dried under vacuum. Successful incorporation of succinic acid was confirmed and quantified with the ¹H NMR spectrum of the digested sample, and chemical formula was determined as $Zr_6O_{4.7}(OH)_{3.3}(C_9H_3O_6)_2(SA)_{5.3}$.

MOF-808-Cu: MOF-808 was added into a CuSO₄ methanolic solution. The suspension was rotated at 10 rpm at room temperature overnight for complete mixing. Solids were separated by centrifuge, washed with MeOH, and dried under vacuum.

5.S3 FT-IR Spectra

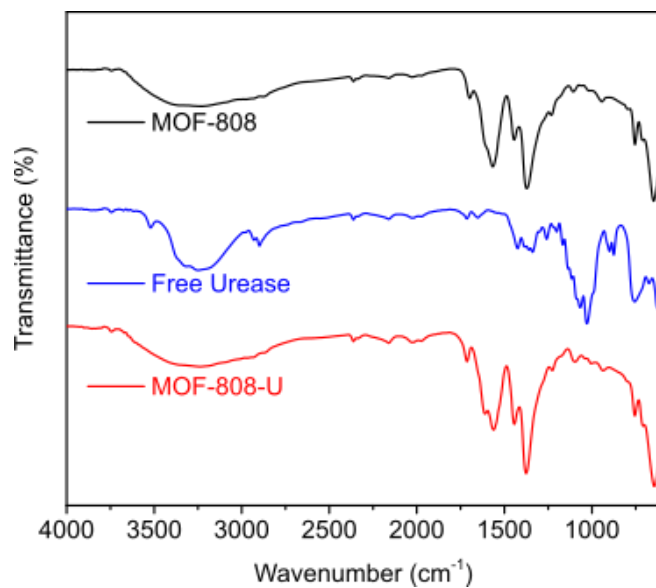


Figure 5.S1 FT-IR spectra of MOF-808, free urease, and MOF-808-U.

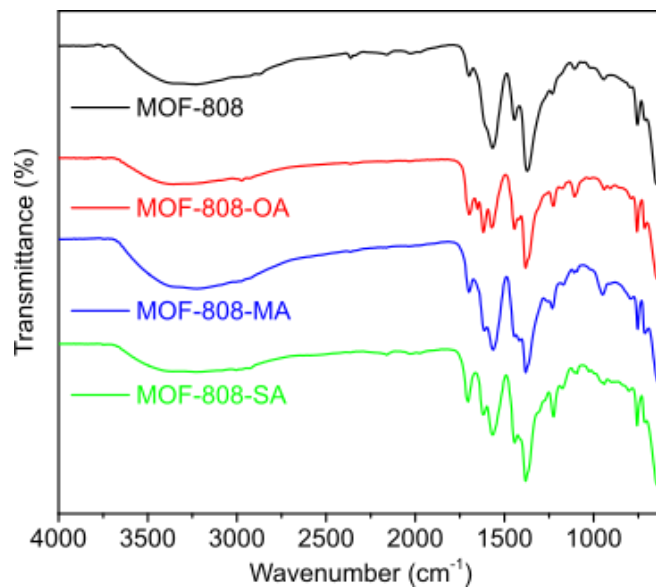


Figure 5.S2. FT-IR spectra of MOF-808 and the dicarboxylate functionalized derivatives.

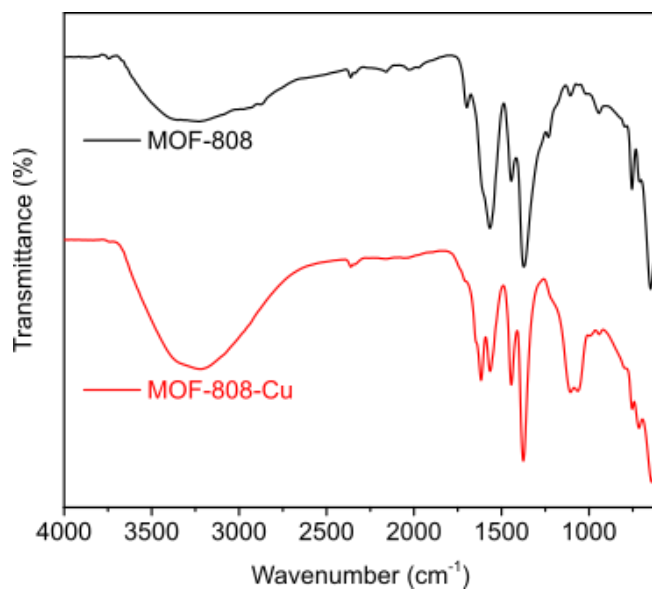


Figure 5.S3 FT-IR spectra of MOF-808 and MOF-808-Cu.

5.S4 ^1H NMR Spectra of Digested MOF Samples

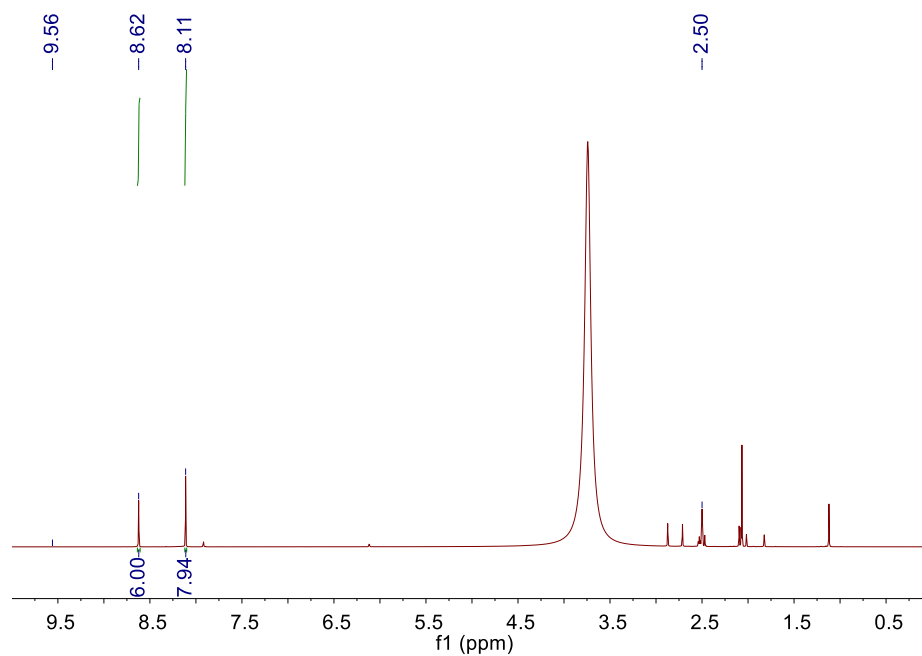


Figure 5.S4 ^1H NMR spectrum of digested MOF-808. Peak with the chemical shift of 8.08 ppm is assigned to formic acid (FA). Ratio of BTC and FA was determined as 2:2.82.

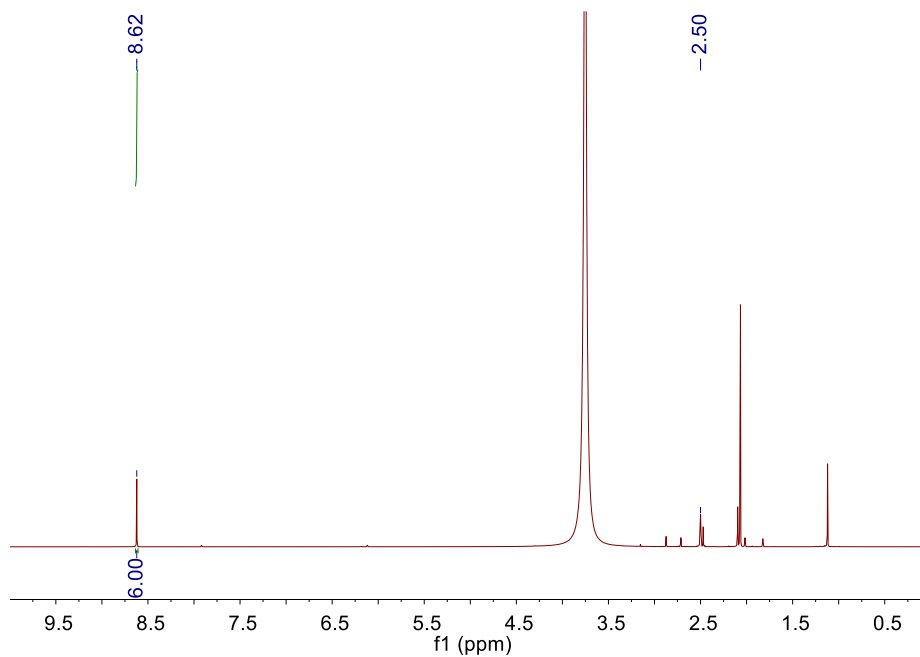


Figure 5.S5 ^1H NMR spectrum of digested MOF-808-OA.

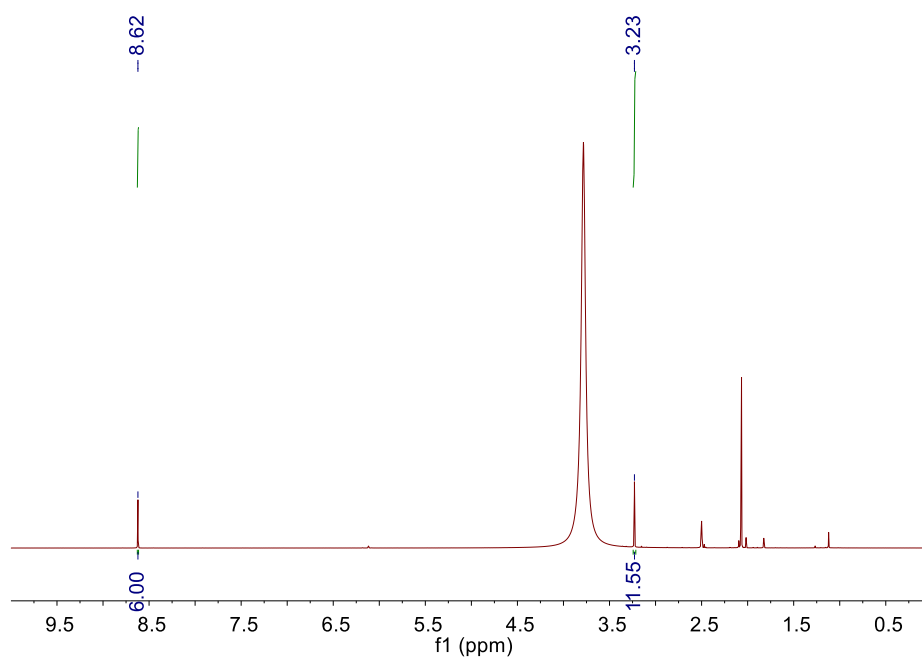


Figure 5.S6 ^1H NMR spectrum of digested MOF-808-MA. Peak with the chemical shift of 3.23 ppm is assigned to malonic acid (MA). Ratio of BTC and MA was determined as 2:5.78.

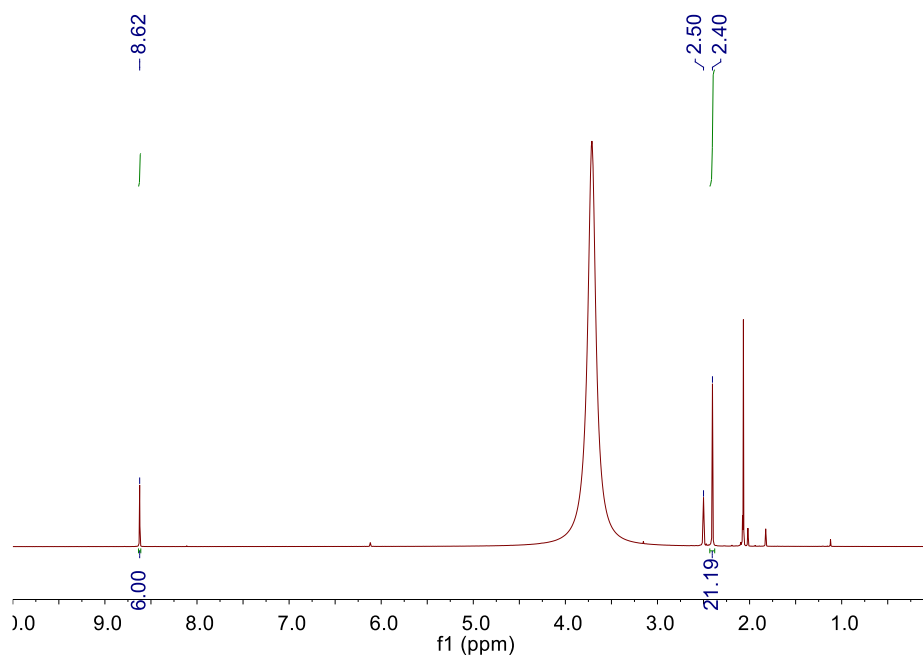


Figure 5.S7 ^1H NMR spectrum of digested MOF-808-SA. Peak with the chemical shift of 2.40 ppm is assigned to succinic acid (SA). Ratio of BTC and SA was determined as 2:5.30.

5.S5 SEM Images

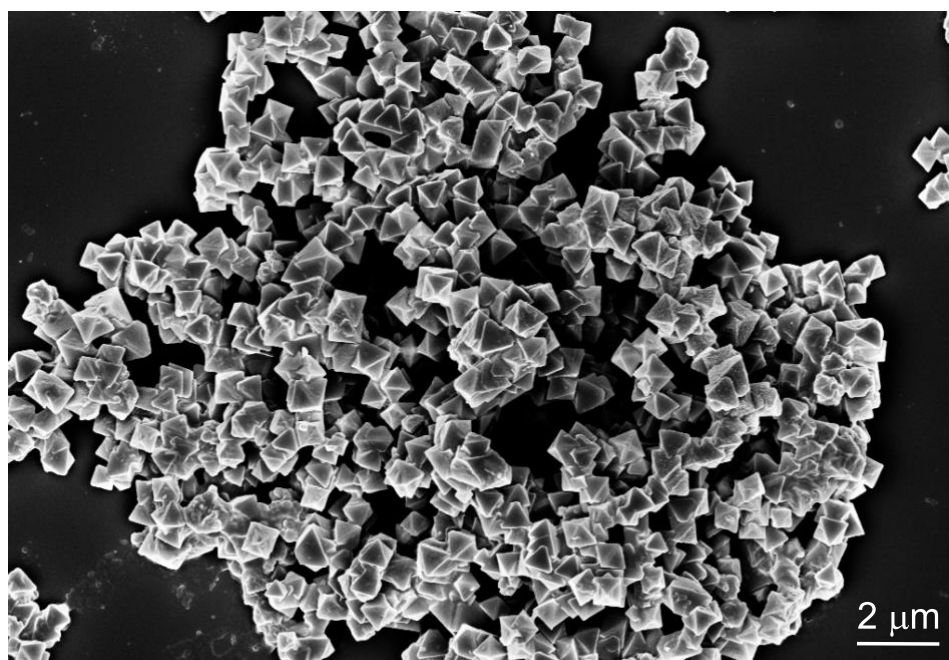


Figure 5.S8 SEM image of MOF-808.

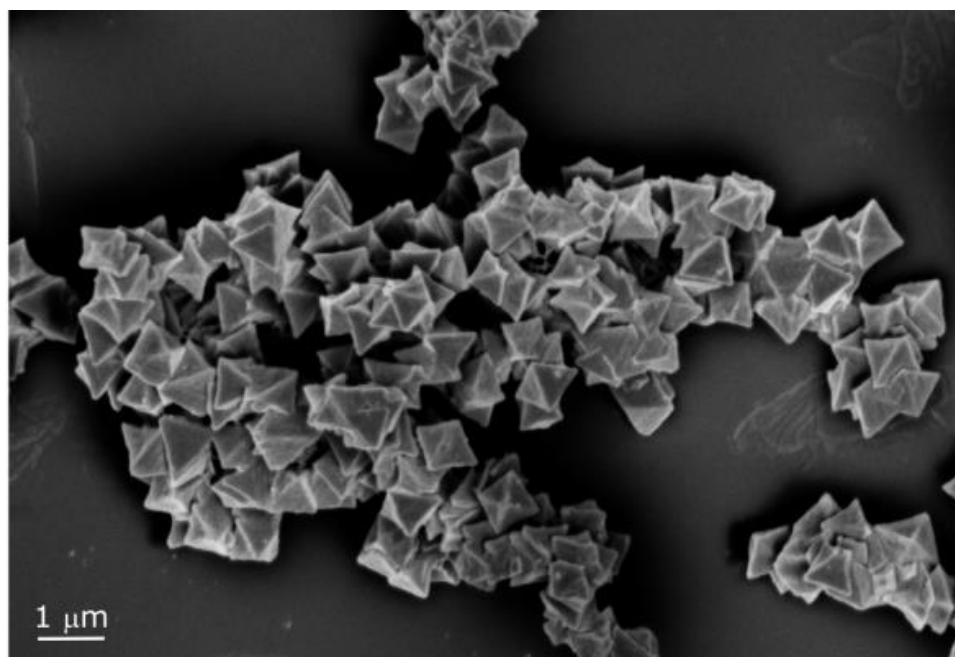


Figure 5.S9 SEM image of MOF-808-U.

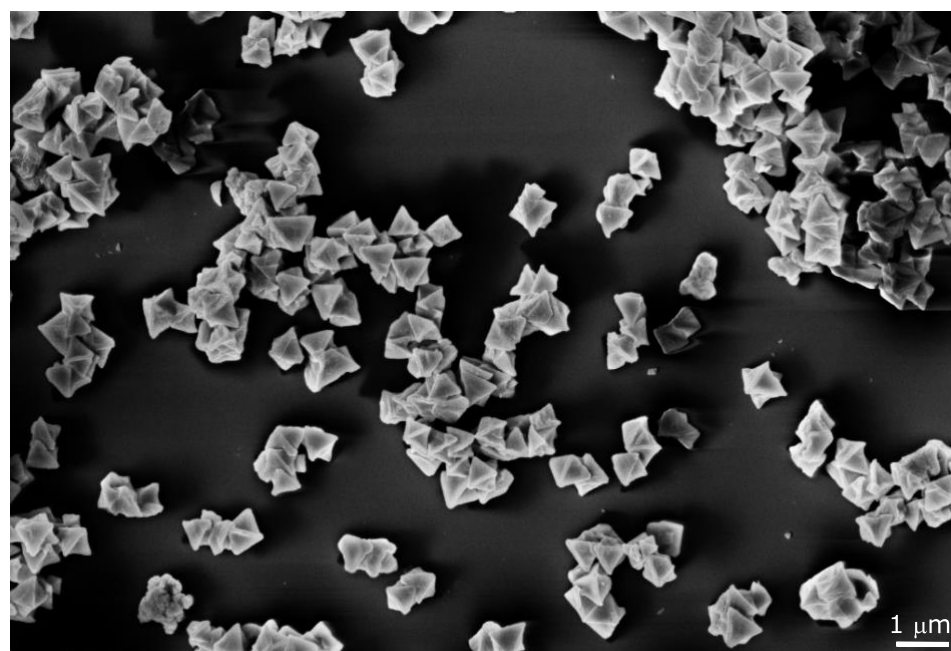


Figure 5.S10 SEM image of MOF-808-OA.

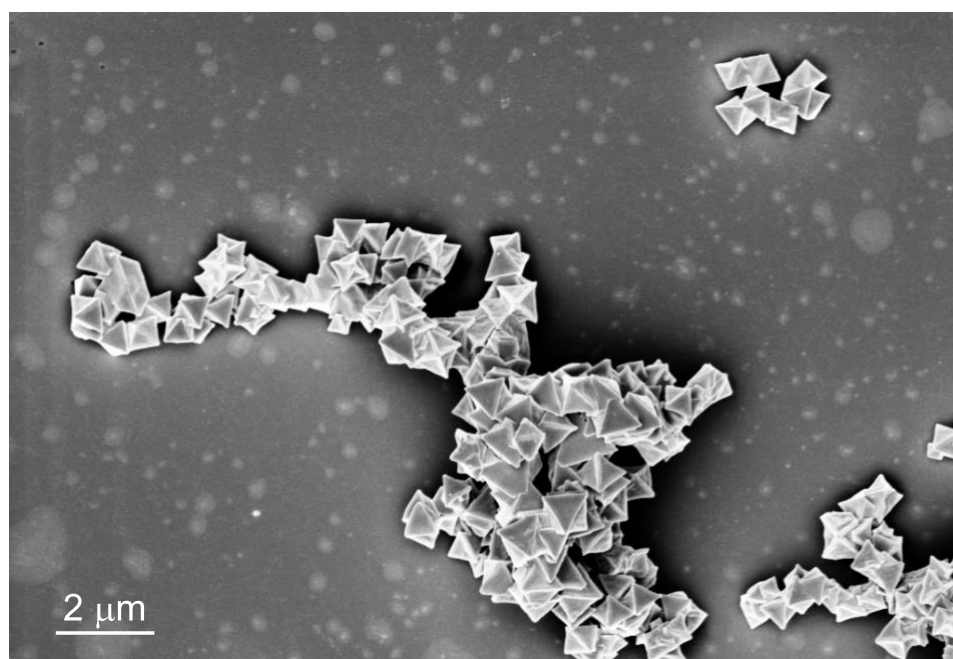


Figure 5.S11 SEM image of MOF-808-MA.

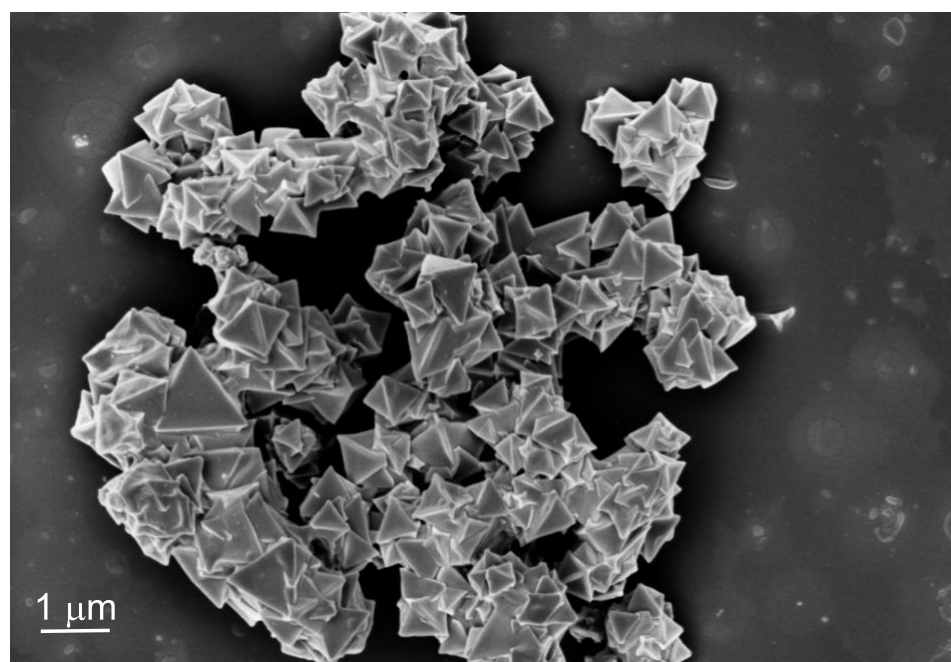


Figure 5.S12 SEM image of MOF-808-SA.

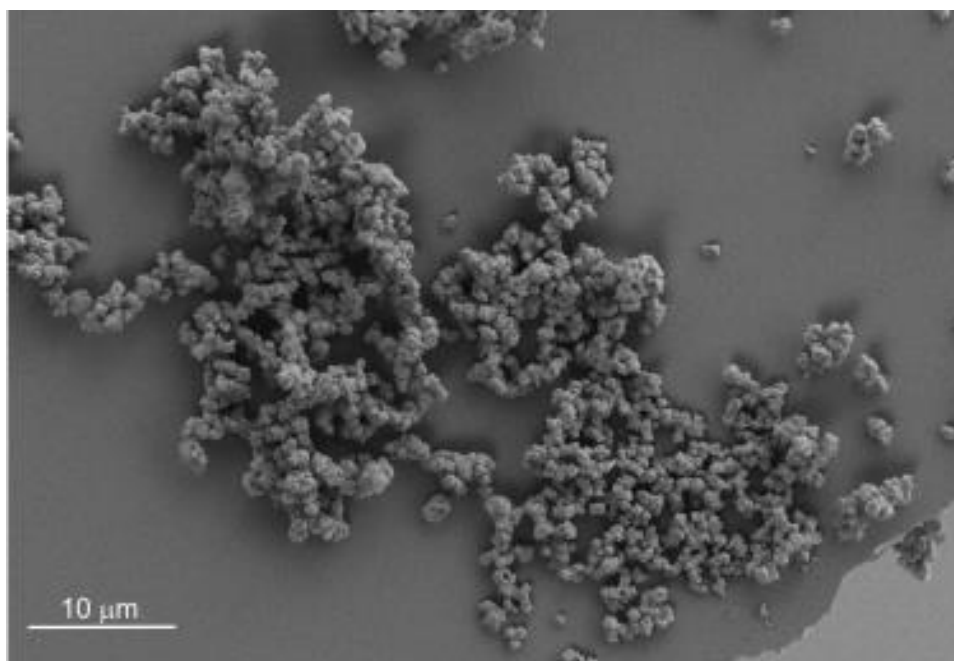


Figure 5.S13 SEM image of MOF-808-Cu.

5.S6 Characterization of MOF-808-U

Michaelis–Menten kinetics experiments

As-synthesized MOF-808-U (10 mg) was added to urea solutions of various concentrations. Upon complete mixing, the suspensions were further rotated at 10 rpm at room temperature for 10 min. Mixtures were centrifuged, and the ammonium concentration of the supernatant was determined to evaluate the hydrolysis efficiency. For free urease, the procedures were similar except that 50 μL of the urease solution (20000 ppm in 10 mM HEPES, pH 7.0) was used as the enzyme source, and ammonium concentration was determined after 1 min of reaction.

Table 5.S1 Enzymatic kinetic parameters determined from the Michaelis–Menten plot.

	K_m (mM)	k_{cat} (mM s ⁻¹ g ⁻¹)
MOF-808-U	25.15	0.1825
Free Urease	24.80	0.3565

Stability tests

MOF-808-U (10 mg) was added to a urea solution (250 mM, 1 mL). Suspension was left at a rotator (10 rpm) for 24 h, and urea concentration was measured to calculate the amount of consumed substrate. Free urea solution was then added to the separated MOF-808-U for the measurement of the immobilized urease's activity on the following day. To determine the stability of free urease in the solution (10 mM HEPES, pH 7.0), a stock solution was firstly made (20000 ppm) and kept at room temperature. For each day's measurement, 50 μ L of urease solution was taken from the stock solution and added to a urea solution. The mixture was left at a rotator for 24 h before urea concentration was determined.

5.S7 Characterization of MOF-808-Based Adsorbents

Ammonium adsorption isotherms measurements

Aqueous solutions of ammonium bicarbonate (NH_4HCO_3) of different concentrations were prepared by dissolving the salt of proper amount in Milli-Q water. NH_4HCO_3 was selected for the isotherm measurement as the pH of the solutions was well-maintained in a wide range of concentrations of the solute (pH: 8.20 ± 0.04).

MOF powders were added into different concentration ammonium solutions with a final suspension concentration of 10 g/L. The mixtures were left at a rotate revolver at 10 rpm at room temperature overnight to ensure adsorption equilibrium was reached. Suspensions were centrifuged, and the supernatant was directly used for the quantification of ammonium.

Q_{eq} , ammonium capture capacity was calculated using the following equation:

$$Q_{eq} = \frac{(C_i - C_e) \times V}{m}$$

where V is the volume of the solution (mL), m is the mass of adsorbents (mg), and C_i and C_e are initial and final concentrations of solution, respectively.

Three adsorption isotherm models, namely, Langmuir, Freundlich, and Langmuir–Freundlich models were applied to fit the experimental data. Fitting parameters of three models for MOF-808, MOF-808-SA, MOF-808-MA, and MOF-808-OA were summarized in the following table (Table 5.S2). The Langmuir–Freundlich model yielded the best fit for all adsorbents.

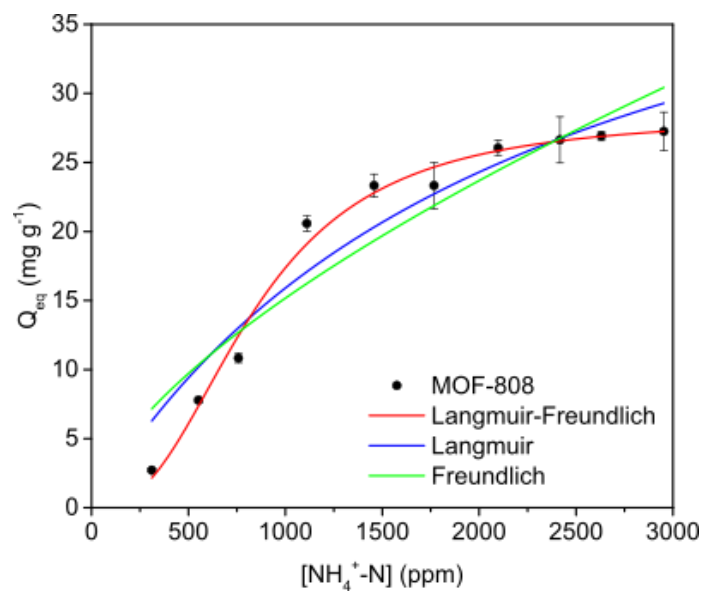


Figure 5.S14 Comparison of Langmuir, Freundlich, and Langmuir–Freundlich models of MOF-808 for fitting the experimental uptake data.

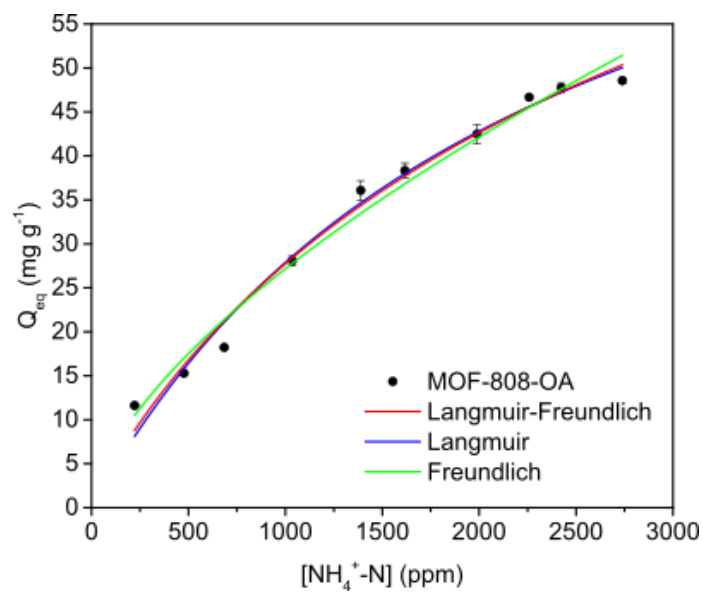


Figure 5.S15 Comparison of Langmuir, Freundlich, and Langmuir–Freundlich models of MOF-808-OA for fitting the experimental uptake data.

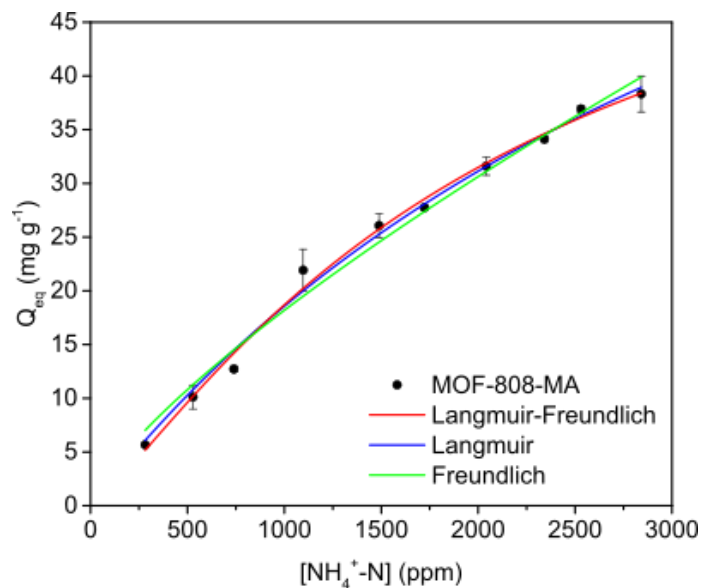


Figure 5.S16 Comparison of Langmuir, Freundlich, and Langmuir–Freundlich models of MOF-808-MA for fitting the experimental uptake data.

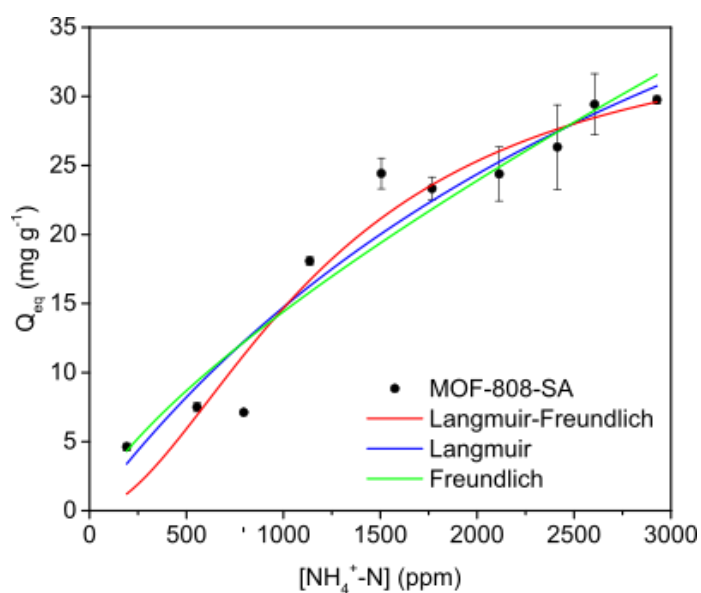


Figure 5.S17 Comparison of Langmuir, Freundlich, and Langmuir–Freundlich models of MOF-808-SA for fitting the experimental uptake data.

Table 5.S2 Fitting parameters of three different models for MOF-808-based adsorbents.

Langmuir, $Q_{eq} = \frac{Q_{sat}K_L C_e}{1+K_L C_e}$				
	Q_{sat} (mg g ⁻¹)	K_L (L mg ⁻¹)		R^2
MOF-808	51.47106	4.7151*10 ⁻⁴		0.92128
MOF-808-SA	70.63362	2.63402*10 ⁻⁴		0.92361
MOF-808-MA	96.24274	2.39109*10 ⁻⁴		0.99152
MOF-808-OA	92.17529	4.33557*10 ⁻⁴		0.98305
Freundlich, $Q_{eq} = K_F C_e^{\frac{1}{n}}$				
	K_F (L ^{1/n} mg ^{-1/n})	n		R^2
MOF-808	0.17906	1.55601		0.87519
MOF-808-SA	0.09316	1.37022		0.91011
MOF-808-MA	0.10093	1.32989		0.98358
MOF-808-OA	0.34153	1.57846		0.97915
Langmuir- Freundlich, $Q_{eq} = \frac{Q_{sat}(K_{LF}C_e)^{\frac{1}{n}}}{1+(K_{LF}C_e)^{\frac{1}{n}}}$				
	Q_{sat} (mg g ⁻¹)	K_{LF} (L ^{1/n} mg ^{-1/n})	n	R^2
MOF-808	28.35427	4.02817*10 ⁻⁸	0.39507	0.98696
MOF-808-SA	35.71255	2.66543*10 ⁻⁶	0.55382	0.92753
MOF-808-MA	65.28451	9.03994*10 ⁻⁵	0.82257	0.99253
MOF-808-OA	112.58567	2.88443*10 ⁻⁴	1.11177	0.98545

Adsorption kinetics experiment

MOF-based adsorbents were added into a 50 mM ammonium bicarbonate solution with a loading of 50 g/L. The mixtures were rotated at 10 rpm at room temperature for 90 min, during which aliquots were taken at intervals. MOF powders were separated and ammonium levels in the resulting solutions were analyzed with the colorimetric assay.

Regeneration of MOF-808-OA and ammonium recovery

Exhausted MOF-808-OA was mixed with NaNO₃ solution (1 M, 10 g/L) and left at a rotate revolver at 10 rpm overnight. Suspension was centrifuged and concentration of ammonium in the supernatant was measurement. Nitrogen recovery efficiency was calculated using the following equation:

$$\text{Recovery Efficiency} = \frac{C_r \times V_r}{m} \times 100\%$$

where C_r is the ammonium concentration in the regeneration reagent after the treatment, V is the volume of the regeneration reagent, and m is the mass of adsorbed nitrogen.

5.S8 Computation Studies on Adsorption of Ammonium onto MOF-808-Based Adsorbents

System preparation

A unit cell with dimension 3.5 nm x 3.5 nm x 3.5 nm was created to accommodate 96 Zr MOF-808 clusters. The pristine MOF-808 structure⁷ was modified to incorporate oxalic acid, malonic acid, and succinic acid for MOF-808-OA, MOF-808-MA, and MOF-808-SA, respectively. To simulate the actual experimental conditions, all the hydrogen (H) atoms of the carboxylic acid groups that serve as ammonium adsorption sites were removed. The amount of acids present in the unit cell reflect the experimental measured amount of 3 acids per pore for OA, 6 for MA and 6 for SA, respectively. The unit cell was then solvated with water molecules, described with the SPC method. In order to reproduce the experimental condition of the highest absorption concentration (around 2700 ppm), different number of ammonium ions were added to the solvated system. In particular, 73, 66, 54 and 38 ammonium cations per cell were added for MOF-808-OA, MOF-808-MA, MOF-808-SA and MPOF-808, respectively. In order to assure neutrality of the whole system, a balanced number of bicarbonate and hydronium ions were added.

Molecular dynamic simulations

All the four different systems followed the following protocol to obtain the molecular dynamics production simulations. First, a 500 steps of step descendent minimization followed by 500 steps of conjugate gradient minimization were performed. Afterwards, the system was heated to 298 K in the NVT ensemble for 10 ps, followed by a 2 ns equilibration in the NPT ensemble. Finally, a 15 ns long NVT production dynamics was run and the geometrical analyses preformed. LAMMPS software⁸ with the UFF force field was used for the entire simulations,⁹ in which the default atom type and charge were used. A timestep of 0.5 fs was used for all systems and the coordinates and velocity were saved every ns.

The same MD protocol was used to obtain the production dynamics for the ions when solvated in water but without the MOF. The same amount of ions as described before (73,

66, 54 and 38 ammonium cations and bicarbonates ions per cell, for the four systems) were considered.

Two-phase thermodynamic (2PT) simulations

The last frame of the production MD simulation was used as input to run three 20 ps long NVT MD simulations at room temperature, which were subsequently used for the 2PT analysis,⁸ for each system. The same software, forcefield and parameters as the MD protocol described before were considered. A timestep of 0.5 fs was used for all systems and the coordinates and velocity were saved every fs.

We refer to the previous reports for a detailed description of the 2PT method and theory.¹⁰⁻¹² Briefly, from the classical MD simulation the program calculates the velocity autocorrelation function of each saved time step, and from them the density of states (DOS) are computed. Finally, from the DOS different thermodynamic properties are computed and among them, the free energy is considered to assess the strength of the ionic interactions in the systems. Thus, from the three 20 ps MD for each system, we compute the free energy and the average values is reported. The program allows to subdivide the whole system into groups, and the ammonium ions were considered as a separate group from the rest.

The same MD protocol and 2PT analysis were used also for the ions immersed in water, without the presence of the MOF, but in the same concentration, in order to have a reference point for each system studied. The final difference in free energy is obtained by subtracting the energy of the ions in water and in the MOF.

Radial distribution function and cumulative distribution function analyses

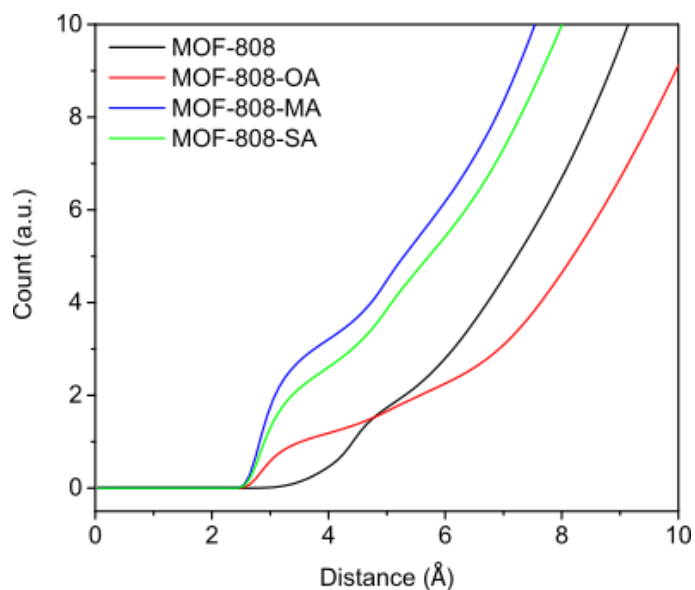


Figure 5.S18 Cumulative distribution function (CDF) analyses of four MOF systems. For MOF-808-OA, MOF-808-MA, and MOF-808-SA, RDF intensity of carboxylate oxygen and ammonium nitrogen was integrated, whereas for MOF-808, RDF intensity of formate hydrogen and ammonium nitrogen was integrated.

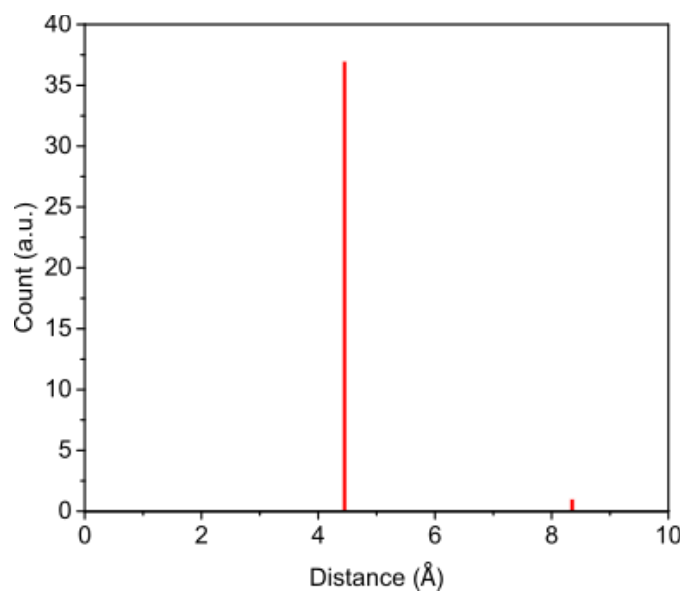


Figure 5.S19 Histogram of the RDF analysis for each ammonium-H pair present in the MOF-808 system.

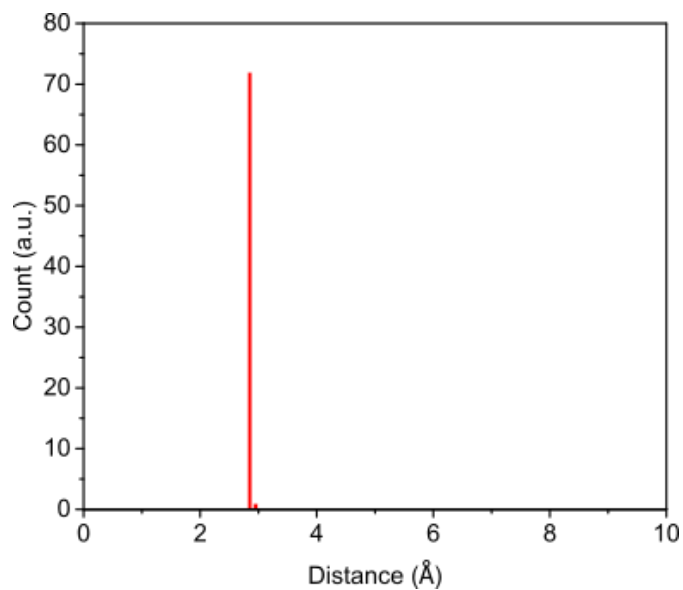


Figure 5.S20 Histogram of the RDF analysis for each ammonium-oxygen pair present in the MOF-808-OA system.

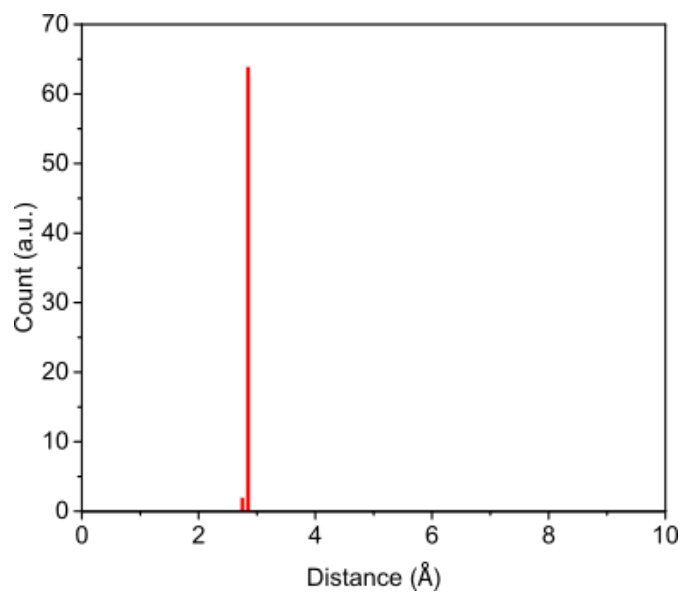


Figure 5.S21 Histogram of the RDF analysis for each ammonium-oxygen pair present in the MOF-808-MA system.

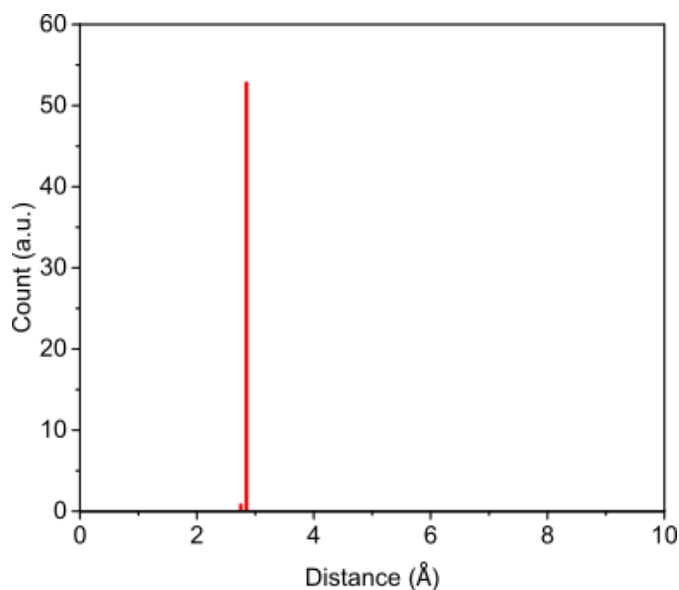


Figure 5.S22 Histogram of the RDF analysis for each ammonium-oxygen pair present in the MOF-808-SA system.

2PT free energy analysis

The adsorption free energy for ammonium uptake by MOF systems Q was calculated with the following equation:

$$Q_{\text{adsorption}} = E_{\text{MOF-ammonium}} - E_{\text{ammonium(aq)}}$$

Free energy values are reported in Table 5.S3.

Table 5.S3 Adsorption free energies of all MOF systems.

Free Energy (kcal/mol)	MOF-808	MOF-808-OA	MOF-808-MA	MOF-808-SA
$E_{\text{MOF-ammonium}}$	-1138	-2181	-2246	-1527
$E_{\text{ammonium(aq)}}$	1034	2356	2057	1582
$Q_{\text{adsorption}}$	-2172	-4537	-4303	-3109

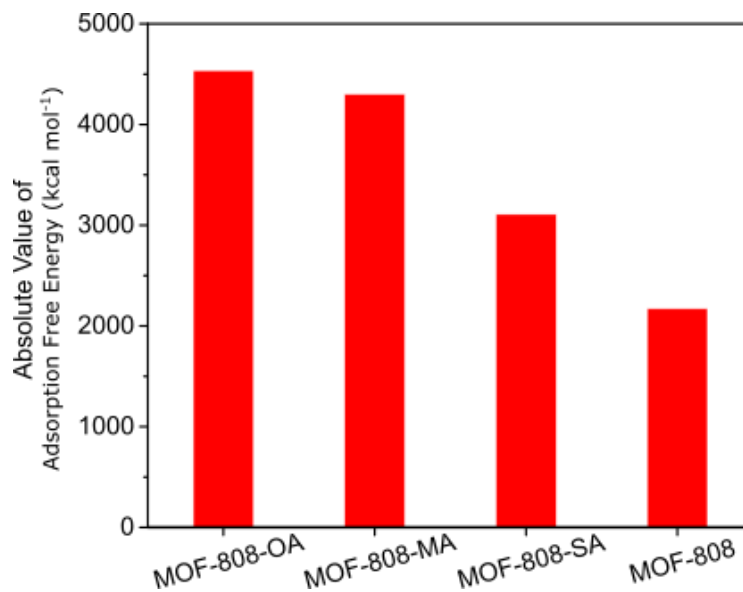


Figure 5.S23 Histogram of the adsorption free energy (absolute value) of all MOF systems.

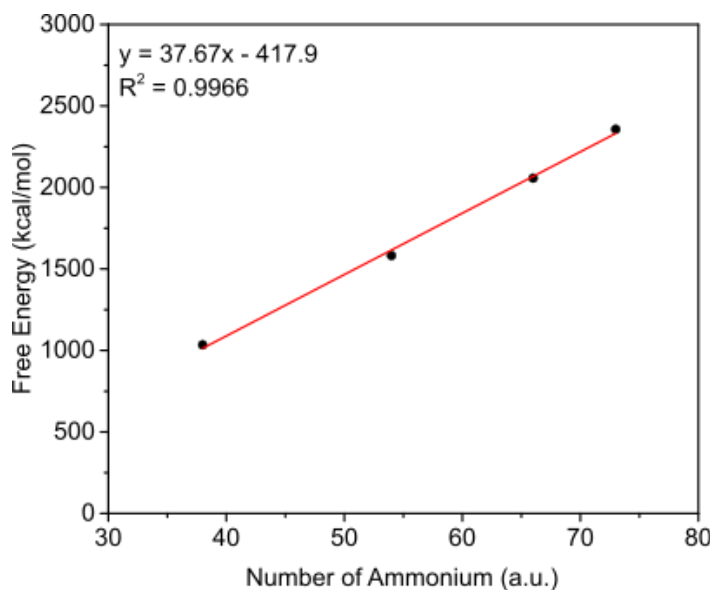


Figure 5.S24 Free energy of different amount of ammonium ions in water solution. High linearity of the curve indicates the high validity of the 2PT analysis.

Pore size analysis

MD simulations using the same protocol as described above, but at 77K were performed on the four different acid modified and solvated MOF systems, in order to assess the pore

size distribution. After the 15 ns MD production run, the last frame of the simulation was extracted and used as input for the void analysis. The Free Volume Calculator tool of the Maestro software¹³ was used, considering a probe radius of 0.15 nm and a grid spacing of 0.025 nm. The results of the analysis are reported in Table 5.S4.

Table 5.S4 Pore size analysis of all MOF systems.

System	MOF-808	MOF-808-OA	MOF-808-MA	MOF-808-SA
Free volume (%)	52.08	44.56	32.67	28.95
Mean void size (nm ³)	0.331	0.244	0.112	0.0978
Radius (nm)	1.84-1.91	1.74-1.81	1.56-1.62	1.49-1.55

5.S9 Detection of Ammonium with MOF-808-Cu

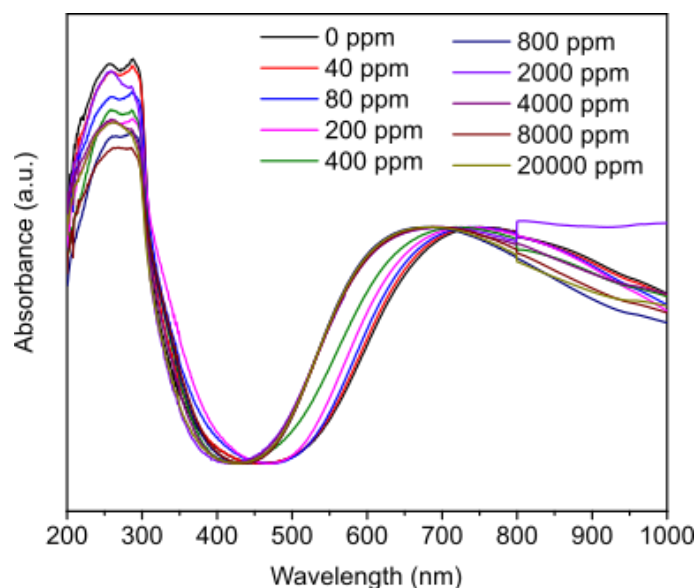


Figure 5.S25 UV-vis diffuse reflectance spectra for MOF-808-Cu after exposing to ammonium hydroxide solutions of different concentrations.

Colorimetric response of MOF-808-Cu with ammonium

MOF-808-Cu was suspended in ammonium hydroxide solutions (40 g/L) and an immediate color change was detected from pale green to blue. RGB channels were extracted

from the digital images of the samples taken with an iPhone SE2 using an online application Color Picker (<https://imagecolorpicker.com/en>).

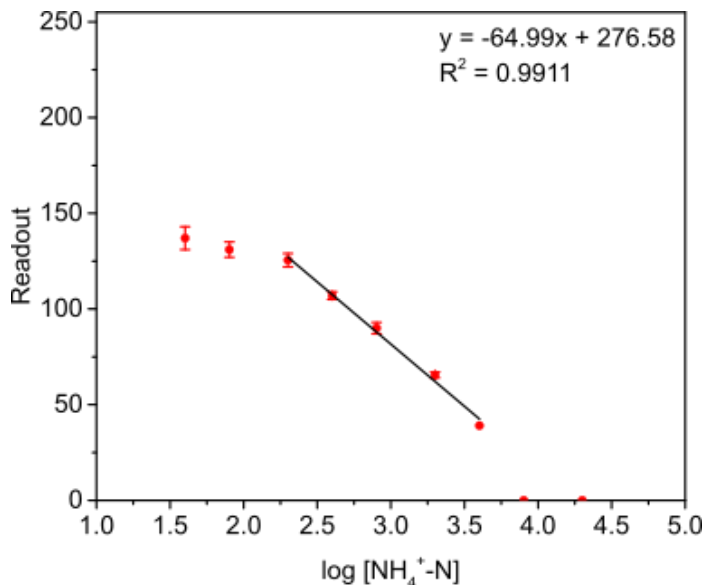


Figure 5.S26 Relationship between ammonium concentrations vs. R value of MOF-808-Cu upon exposure to ammonium hydroxide solutions.

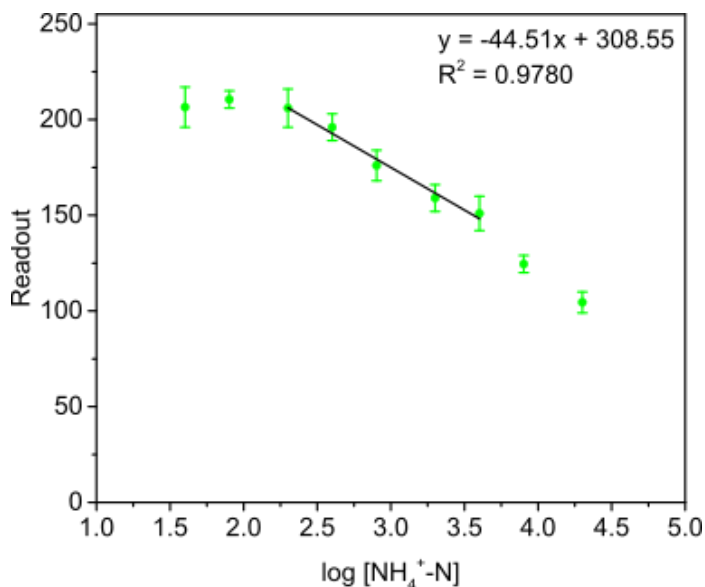


Figure 5.S27 Relationship between ammonium concentrations vs. G value of MOF-808-Cu upon exposure to ammonium hydroxide solutions.

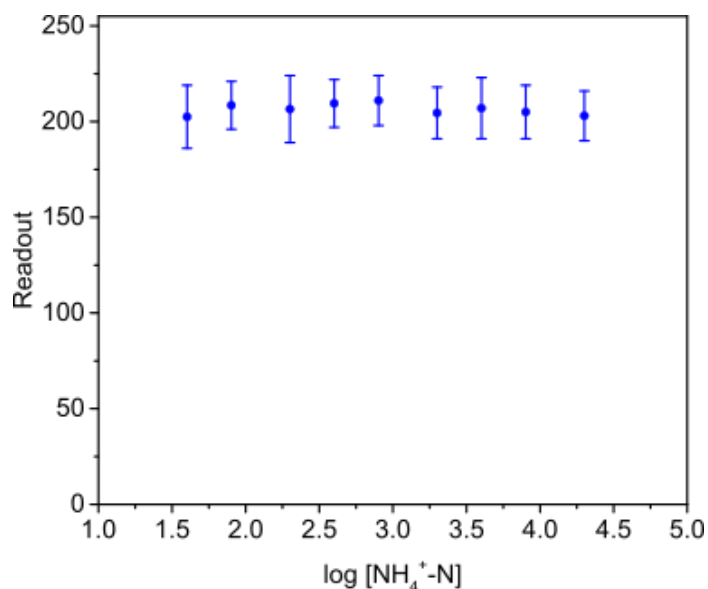


Figure 5.S28 Relationship between ammonium concentrations vs. B value of MOF-808-Cu upon exposure to ammonium hydroxide solutions.

5.S10 Nitrogen Recovery from Fresh Urine with Functionalized MOFs

The relevant performances of all three functional MOFs were studied carefully during treatment. Near-complete conversion of urea was achieved for first three cycles with MOF-808-U with the hydrolysis activity decreasing slightly to 70% after five successive cycles (Figure S27). In the case of MOF-808-OA, ammonium uptake was influenced by the presences of competing ions (e.g., Na⁺, Ca²⁺) (Figure S28). Uptake of urea was also observed with MOF-808-OA, probably due to sorption via Van der Waals interactions between urea and the MOF backbone.^{13–15} Even though adsorbed urea competes with the uptake of ammonium, the total nitrogen capture capacity was not significantly influenced since urea is also a nitrogen rich species. We also found the nitrogen recovery efficiency focusing on the adsorption process (MOF-808-OA) to be efficient (Figure S29).

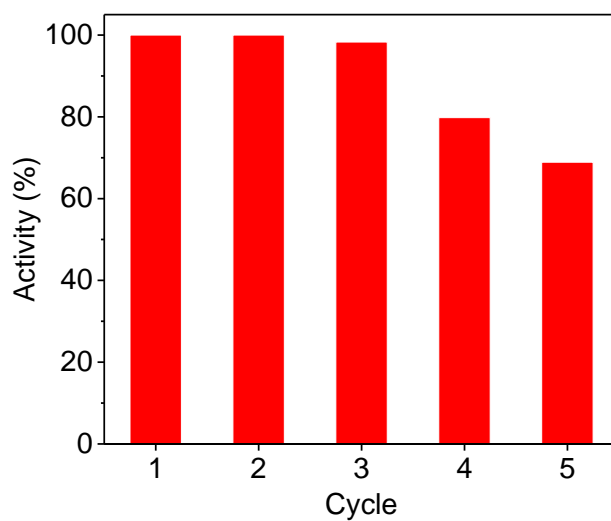


Figure 5.S29 Catalytic activity of MOF-808-U in five successive cycles.

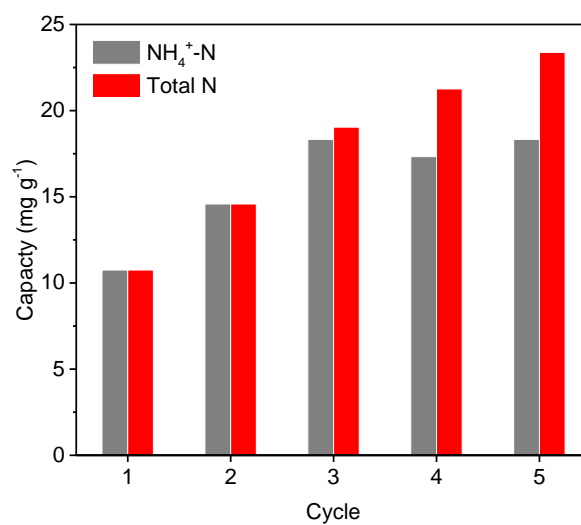


Figure 5.S30 Ammonium and total nitrogen (including urea) capture capacity of MOF-808-OA in five cycles of treatment.

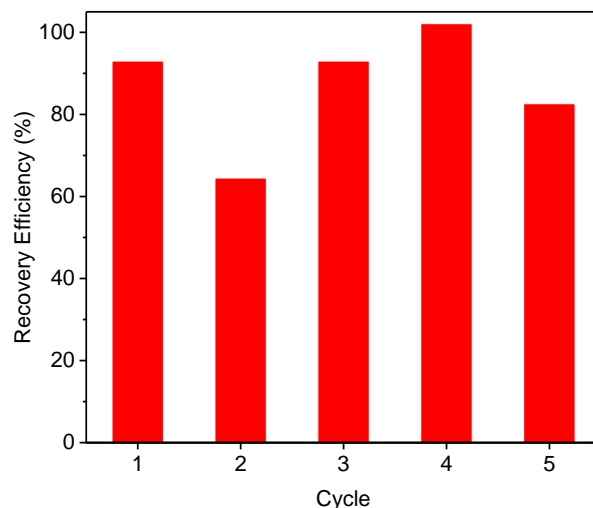


Figure 5.S31 Nitrogen recovery efficiency of MOF-808-OA in five cycles of treatment.

References

- (1) Manto, M. J.; Xie, P.; Keller, M. A.; Liano, W. E.; Pu, T.; Wang, C. Recovery of Ammonium from Aqueous Solutions Using ZSM-5. *Chemosphere* **2018**, *198*, 501–509.
- (2) Weatherburn, M. W. Phenol-Hypochlorite Reaction for Determination of Ammonia. *Anal. Chem.* **1967**, *39* (8), 971–974.
- (3) Cline, R. E.; Fink, R. M. Investigation of Color Reaction between P-Dimethylaminobenzaldehyde and Urea or Ureido Acids. *Anal. Chem.* **1956**, *28* (1), 47–52.
- (4) Jiang, J.; Gándara, F.; Zhang, Y.-B.; Na, K.; Yaghi, O. M.; Klemperer, W. G. Superacidity in Sulfated Metal–Organic Framework-808. *J. Am. Chem. Soc.* **2014**, *136* (37), 12844–12847.
- (5) Guo, L.; Jia, S.; Diercks, C. S.; Yang, X.; Alshimri, S. A.; Yaghi, O. M. Amidation, Esterification, and Thioesterification of a Carboxyl-Functionalized Covalent Organic Framework. *Angew. Chem. Int. Ed.* **2020**, *59* (5), 2023–2027.
- (6) Bergerman, J.; Elliot, J. S. Method for Direct Colorimetric Determination of Oxalic Acid. *Anal. Chem.* **1955**, *27* (6), 1014–1015.
- (7) Furukawa, H.; Gándara, F.; Zhang, Y.-B.; Jiang, J.; Queen, W. L.; Hudson, M. R.; Yaghi, O. M. Water Adsorption in Porous Metal–Organic Frameworks and Related Materials. *J. Am. Chem. Soc.* **2014**, *136* (11), 4369–4381.
- (8) Thompson, A. P.; Aktulga, H. M.; Berger, R.; Bolintineanu, D. S.; Brown, W. M.; Crozier, P. S.; in 't Veld, P. J.; Kohlmeyer, A.; Moore, S. G.; Nguyen, T. D.; Shan, R.; Stevens, M. J.; Tranchida, J.; Trott, C.; Plimpton, S. J. LAMMPS - a Flexible Simulation Tool for Particle-Based Materials Modeling at the Atomic, Meso, and Continuum Scales. *Comput. Phys. Commun.* **2022**, *271*, 108171.

- (9) Rappe, A. K.; Casewit, C. J.; Colwell, K. S.; Goddard, W. A.; Skiff, W. M. UFF, a Full Periodic Table Force Field for Molecular Mechanics and Molecular Dynamics Simulations. *J. Am. Chem. Soc.* **1992**, *114* (25), 10024–10035.
- (10) Lin, S.-T.; Blanco, M.; Goddard, W. A. The Two-Phase Model for Calculating Thermodynamic Properties of Liquids from Molecular Dynamics: Validation for the Phase Diagram of Lennard-Jones Fluids. *J. Chem. Phys.* **2003**, *119* (22), 11792–11805.
- (11) Lin, S.-T.; Maiti, P. K.; Goddard, W. A. Two-Phase Thermodynamic Model for Efficient and Accurate Absolute Entropy of Water from Molecular Dynamics Simulations. *J. Phys. Chem. B* **2010**, *114* (24), 8191–8198.
- (12) Pascal, T. A.; Lin, S.-T.; Iii, W. A. G. Thermodynamics of Liquids: Standard Molar Entropies and Heat Capacities of Common Solvents from 2PT Molecular Dynamics. *Phys. Chem. Chem. Phys.* **2010**, *13* (1), 169–181.
- (13) Cheah, W.-K.; Sim, Y.-L.; Yeoh, F.-Y. Amine-Functionalized Mesoporous Silica for Urea Adsorption. *Mater. Chem. Phys.* **2016**, *175*, 151–157.
- (14) Kameda, T.; Ito, S.; Yoshioka, T. Kinetic and Equilibrium Studies of Urea Adsorption onto Activated Carbon: Adsorption Mechanism. *J. Dispers. Sci. Technol.* **2017**, *38* (7), 1063–1066.
- (15) Pillai, M. G.; Simha, P.; Gugalia, A. Recovering Urea from Human Urine by Bio-Sorption onto Microwave Activated Carbonized Coconut Shells: Equilibrium, Kinetics, Optimization and Field Studies. *J. Environ. Chem. Eng.* **2014**, *2* (1), 46–55.

CONCLUSIONS AND OUTLOOKS

The work in this thesis explored options for decentralized water and wastewater treatment. A newly designed heterojunction Ni-Sb-SnO₂ (NAT/AT) electrode is cost-effective for treating latrine wastewater while simultaneously achieving organic removal and pathogen inactivation. Detailed investigation into pharmaceutical degradation showed promising performance of NAT/AT in oxidizing both parent compounds and their transformation products. Together, the work in chapter 2 and 3 established NAT/AT as an economical and efficient method for treatment practices that is capable of large-scale implementation. Going beyond direct treatment applications, NAT/AT can facilitate another decentralized treatment option using the high oxidation state iron species ferrates by generating ferrates in-situ under circumneutral conditions, which has previously only been done using boron-doped diamond (BDD). In order to deal with the high concentration of ammonium often present in latrine wastewaters that is hard to remove electrochemically using NAT/AT or BDD, functionalized metal-organic frameworks (MOFs) were invoked. Modifications of MOF-808, a highly water-stable MOF, were designed and synthesized. By incorporating different functional groups onto the MOF-808 backbone, three different MOF materials can be used to achieve urea hydrolysis, ammonium capture, and real-time ammonium sensing in sequence.

The work highlighted in this thesis also pointed toward several directions where further research could be conducted for enhanced understanding of the NAT/AT system and for better real-world treatment applications. First, results in chapter 2 showed that compounds with both fast and slow reaction rate constants with ozone could potentially be removed at fast rates, and a new mechanism for anodic ozone activation to hydroxyl radicals has been proposed to explain the acceleration effect. However, chapter 2 and 3 together showed that there are compounds that showed accelerated kinetics at NAT/AT, for example, gabapentin, ibuprofen, and fluconazole, and there are compounds that were not promoted by anodic

ozone activation include nitrobenzene, phenol, and atenolol. Upon initial examination, whether oxidation of a compound is promoted cannot be simply explained using the electron-withdrawing/donating capacity of the ring substituent or the log K_{ow} value of the target compound. Therefore, a more in-depth investigation, starting with a compilation of simple aromatic rings and common substituted benzenes for example, to determine the structure-activity relationship could greatly improve our understanding of the ozone + hydroxyl radical NAT/AT system and help us predict its performance towards specific compounds of interest. Second, in chapter 2 and 3, for treatment of spiked pharmaceuticals in wastewaters, all pharmaceuticals were assumed to be completely dissolved, which may not be accurate in many cases. Investigation into the sorption behaviors of different compounds would give us a better understanding of their degradation in different waste streams. Another aspect to improve the NAT/AT system lies in extending the lifetime of the electrodes while maintaining their performance as best as possible. Like most SnO_2 -based anodes, NAT/AT suffers relatively short service life when compared to BDD. Though a combination of the heterojunction design and an increased number of dip-coating cycles can help increase its stability and lifetime, overall performance in terms of ozone and hydroxyl radical production drops with longer treatment time, which harms degradation efficiency especially for compounds whose removal relies upon ozone and/or anodic ozone activation. Further improvement in this aspect could therefore significantly enhance the practical applicability of NAT/AT in broader treatment scenarios.